

This electronic thesis or dissertation has been downloaded from the King's Research Portal at <https://kclpure.kcl.ac.uk/portal/>



## **In vivo assessment of the developing brain using diffusion magnetic resonance imaging**

Pecheva, Diliana

*Awarding institution:*  
King's College London

The copyright of this thesis rests with the author and no quotation from it or information derived from it may be published without proper acknowledgement.

### **END USER LICENCE AGREEMENT**



**Unless another licence is stated on the immediately following page** this work is licensed

under a Creative Commons Attribution-NonCommercial-NoDerivatives 4.0 International

licence. <https://creativecommons.org/licenses/by-nc-nd/4.0/>

You are free to copy, distribute and transmit the work

Under the following conditions:

- Attribution: You must attribute the work in the manner specified by the author (but not in any way that suggests that they endorse you or your use of the work).
- Non Commercial: You may not use this work for commercial purposes.
- No Derivative Works - You may not alter, transform, or build upon this work.

Any of these conditions can be waived if you receive permission from the author. Your fair dealings and other rights are in no way affected by the above.

### **Take down policy**

If you believe that this document breaches copyright please contact [librarypure@kcl.ac.uk](mailto:librarypure@kcl.ac.uk) providing details, and we will remove access to the work immediately and investigate your claim.

# **IN VIVO ASSESSMENT OF THE DEVELOPING BRAIN USING DIFFUSION MAGNETIC RESONANCE IMAGING**

**Diliana Pecheva**

A thesis submitted in partial fulfilment of the requirement for the degree of

**Doctors of Philosophy of King's College London**

September 2017

Department of Biomedical Engineering

King's College London





## **Abstract**

An estimated 15 million infants are born preterm every year and, thanks to improvements in neonatal care, mortality rates have decreased. However, preterm infants remain at risk of a wide spectrum of neurodevelopmental impairments including cognitive, motor and language deficits. The substantial personal and societal cost of preterm birth underscores the importance of identifying infants at risk, and those who may benefit from early interventional therapies.

Diffusion-weighted magnetic resonance imaging (dMRI) studies have provided valuable insights into the effects of maturation and injury on brain development in infant populations. The cerebral white matter is particularly vulnerable to injury and previous studies of preterm infants have demonstrated that altered white matter microstructure observed at term equivalent age is associated with developmental performance in later life. dMRI analysis of the developing white matter in this population may provide biomarkers of neurodevelopmental impairment.

Through the application of novel approaches to white matter analysis in neonates, this thesis investigates the effects of perinatal risk factors on the developing brain in preterm infants and the relationship between white matter microstructure in the perinatal period and subsequent neurodevelopmental performance. This work evaluated a new approach for neonatal dMRI analysis, tract-specific analysis (TSA). The evaluation of this method demonstrated that TSA provides improved spatial alignment of white matter tracts and better approximation of native space diffusion data than tract-based spatial statistics, a similar, widely used method.

TSA was applied to assess the relationship between diffusion tensor imaging (DTI) metrics in white matter fasciculi in 407 preterm infants at term-equivalent age and neurodevelopmental performance at 20 months, and to assess the effects of prematurity and maturation. Higher motor and cognitive scores assessed using the Bayley Scales of Infant and Toddler Development, 3<sup>rd</sup> edition, were associated with increased fractional anisotropy (FA) and decreased diffusivity in projection, commissural and association fibres, while the associations between language performance and DTI metrics were limited. Higher diffusivity and lower FA was associated with

increased prematurity, and lower diffusivity and increased FA was associated with increasing age at scan, in agreement with previous studies.

Moving beyond the standard diffusion tensor model, novel higher-order diffusion models were applied for the first time to the preterm infant population to provide deeper insight into the relationship between white matter microstructure and perinatal risk factors, neurodevelopmental performance and brain maturation by identifying specific fibre pathways within regions of complex white matter configurations. The diffusion tensor model fails to adequately represent white matter anatomy in regions of crossing fibres. Therefore, fixel-based analysis (FBA) was applied to estimate fibre density and fibre-cross section for each distinct fibre population within a voxel, where a 'fixel' refers to a single fibre population. The association between perinatal risk factors and fibre cross-section was more extensive than with fibre density, implying a greater effect on white matter morphology than microstructure. Higher motor and cognitive scores were associated with increases in fibre cross-section while language performance was positively correlated with fibre density.

Finally, the methods explored in this thesis were applied to assess normal brain maturation in term infants from the Developing Human Connectome Project (dHCP). State-of-the-art diffusion imaging data from the dHCP were analysed to characterise healthy human brain development. TSA was combined with DTI, neurite orientation dispersion and density imaging (NODDI) and fixel-derived metrics. This study presented the first application of NODDI and FBA to healthy term-born infants. The results reveal that lateralisation of white matter fasciculi, observed in adults and associated with functional specialisation, is not present at birth in healthy term-born infants and most likely emerges later in life, also demonstrating a maturation-related increase in intra-axonal density and fibre cross-section in the perinatal period. Analysis of high quality, multi-shell diffusion data from the dHCP demonstrates the potential of advanced dMRI, which may provide a deeper understanding of the environmental and biological factors influencing brain development and the pathophysiology of preterm brain injury.

## **Declaration of Originality**

The work presented in this thesis was conducted by the author at the Centre for the Developing Brain, King's College London between September 2013 and September 2017, all sources are appropriately referenced.

This work has not been submitted for the purpose of obtaining any other degree at this University or any other institution.

## **Acknowledgements**

I would like to thank my supervisors, Professor Serena Counsell and Dr Hui Zhang for their constant support and encouragement. I am hugely grateful to them for the time they have given to guide me through this PhD. It's impossible to express how much their support has meant to me. I would like to thank my amazing colleagues at the Centre for the Developing Brain and the Microstructure Imaging Group at UCL for their friendship and limitless patience. Thank you to Office 1 for putting up with me.

I thank the families who kindly agreed to participate in research studies, and the clinicians and investigators who made the ePrime and the Developing Human Connectome Project studies possible.

Finally, I would like to thank my mother, father and sister, there is no way this would have been possible without your love.

# Table of Contents

ABSTRACT .....	2
DECLARATION OF ORIGINALITY .....	4
ACKNOWLEDGEMENTS .....	5
TABLE OF CONTENTS .....	6
LIST OF FIGURES .....	10
LIST OF TABLES .....	25
ABBREVIATIONS .....	26
PUBLICATIONS .....	28
CONFERENCE ABSTRACTS .....	28
CHAPTER 1 INTRODUCTION .....	30
1.1 MOTIVATION .....	30
1.2 HYPOTHESES AND AIMS .....	31
1.3 THESIS OUTLINE .....	32
CHAPTER 2 MAGNETIC RESONANCE IMAGING .....	34
2.1 NUCLEAR MAGNETIC RESONANCE .....	34
2.2 MAGNETIC RESONANCE IMAGING .....	37
2.3 DIFFUSION-WEIGHTED IMAGING .....	38
2.3.1 Brownian motion and diffusion .....	38
2.3.2 Diffusion-weighted imaging .....	39
2.3.3 Diffusion tensor Imaging .....	40
2.3.4 Compartment models of microstructure .....	42
2.3.5 Spherical deconvolution .....	44
2.3.6 Apparent fibre density .....	45
2.3.7 White matter analysis .....	47
2.3.8 Image registration .....	50
CHAPTER 3 THE DEVELOPING BRAIN .....	52

3.1 NORMAL BRAIN DEVELOPMENT .....	52
3.2 PRETERM BIRTH.....	56
3.2.1 Epidemiology .....	56
3.2.2 Developmental outcome following preterm birth.....	56
3.2.3 Preterm brain injury.....	58
3.2.4 Perinatal risk factors .....	64
3.3 MRI IN NEONATES .....	68
3.3.1 Qualitative T1- and T2-weighted studies.....	68
3.3.2 Volumetric MRI studies.....	69
3.3.3 Diffusion-weighted imaging studies.....	71
CHAPTER 4 TRACT SPECIFIC ANALYSIS IN PRETERM INFANTS. ....	74
4.1 INTRODUCTION .....	74
4.2 METHODS.....	77
4.2.1 Subjects .....	77
4.2.2 Data acquisition.....	<b>Error! Bookmark not defined.</b>
4.2.3 Diffusion weighted image processing .....	78
4.2.4 Evaluation of TSA.....	79
4.3 RESULTS .....	84
4.3.1 Registration comparison .....	84
4.3.2 Data Projection .....	86
4.4 DISCUSSION .....	90
4.4.1 Registration comparison .....	90
4.4.2 Data Projection .....	92
4.4.3 Advantages and limitations of TSA .....	94
4.5 CONCLUSIONS.....	95
CHAPTER 5 WHITE MATTER DIFFUSION PROPERTIES AT TERM EQUIVALENT AGE ARE ASSOCIATED WITH SUBSEQUENT NEURODEVELOPMENTAL PERFORMANCE AT 20 MONTHS .....	96
5.1 INTRODUCTION .....	96

5.2 METHODS.....	97
5.2.1 Subjects.....	97
5.2.2 MR imaging.....	98
5.2.3 Image processing.....	98
5.2.4 Tract-specific analysis .....	99
5.3 RESULTS .....	100
5.3.1 Relationship between dMRI measures and motor performance.....	100
5.3.2 Relationship between dMRI measures and cognitive performance .....	109
5.3.3 Relationship between dMRI measures and language performance .....	116
5.3.4 Relationship between dMRI measures and gestational age at birth .....	118
5.3.5 Relationship between dMRI measures and PMA at scan .....	125
5.4 DISCUSSION .....	133
5.5 CONCLUSIONS.....	137
CHAPTER 6 FIXEL BASED ANALYSIS.....	138
6.1 INTRODUCTION .....	138
6.2 METHODS.....	140
6.2.1 Subjects.....	140
6.2.2 Data Acquisition.....	140
6.2.3 Image processing .....	140
6.2.4 FBA.....	142
6.3 RESULTS .....	145
6.3.1 MRI findings.....	145
6.3.2 Neurodevelopmental performance .....	145
6.3.3 Fixel-based analysis.....	146
6.4 DISCUSSION .....	156
6.5 CONCLUSIONS.....	170
CHAPTER 7 WHITE MATTER IN HEALTHY TERM-BORN INFANTS .....	175
7.1 INTRODUCTION .....	175
7.2 METHODS.....	177

7.2.1 Subjects .....	177
7.2.2 Data Acquisition.....	177
7.2.3 Image Processing .....	178
7.2.4 Estimation of microstructural features .....	178
7.2.5 Tract-specific analysis .....	180
7.3 RESULTS .....	183
7.3.1 Average values.....	183
7.3.2 Inter-hemispheric asymmetries.....	190
7.3.3 Changes in diffusion properties associated with increasing age .....	191
7.3.4 Differences in diffusion properties between male and female subjects.....	203
7.4 DISCUSSION .....	207
7.5 CONCLUSIONS.....	210
CHAPTER 8 SUMMARY AND FUTURE DIRECTIONS.....	211
8.1 KEY FINDINGS .....	211
8.2 CONCLUSIONS.....	213
8.3 FUTURE WORK .....	213
8.3.1 Multimodal imaging.....	213
8.3.2 Future studies of neurodevelopment .....	214
REFERENCES.....	215



## List of Figures

Figure 2.1 Hydrogen protons possess spin, a quantum property that induces a molecular moment (a; black arrow) along the axis of rotation. When an external magnetic field, $B_0$ (grey dotted line) is applied, spins precess about the field and align parallel to it (b), producing a net magnetisation vector, $M_z$ .	35
Figure 2.2 The application of an RF pulse, $B_1$ , causes the net magnetisation vector to spiral towards the transverse plane. For a static observer, the spins precessing about $B_0$ in the z-axis and $B_1$ in the x-axis simultaneously to spiral down to the x-y plane. However, if the observer moves to a rotating reference frame, rotating at the Larmor frequency, they will only see the precession from the z-axis into the x-y plane as an arc.	36
Figure 2.3 Recovery of the longitudinal magnetisation occurs towards equilibrium, with a tissue dependent recover constant $T_1$ (a). b: The transverse magnetisation decays toward zero with a tissue dependent constant $T_2$ (b).	37
Figure 2.4 Diagram shows the pulsed gradient spin echo sequence used for diffusion MR imaging. Two diffusion-encoding gradient ( $G_{diff}$ ) pulses are applied to introduce a phase shift. $\delta$ = duration of the diffusion-encoding gradient, $\Delta$ = diffusion time interval, $G_{phase}$ = phase-encoding gradient, $G_{read}$ = readout gradient, $G_{slice}$ = section-selective gradient, $RF$ = radiofrequency pulse, $t$ = acquisition time. Reproduced from Hagmann et al. (2006).	40
Figure 2.5 Isotropic and anisotropic diffusion in the brain. In the white matter of the corpus callosum (red), diffusion occurs preferentially along the axonal fibres, resulting in anisotropic diffusion (b). In the ventricular cerebro-spinal fluid (CSF; green), diffusion is unhindered and can be described as isotropic (c). Diffusion tensor ellipsoids representing anisotropic and isotropic diffusion are shown in b and c, respectively. Reproduced from Pandit et al. (2013).	41
Figure 2.6 The three compartments of the NODDI model. Diffusion within the intraneurite compartment is restricted and modelled using sticks; diffusion within the extraneurite is hindered and modelled using a zeppelin; the CSF compartment of isotropic diffusion is modelled using an isotropic tensor. Adapted from Slattery et al. (2017).	44
Figure 2.7 A single fibre population within a voxel (A, B) and the expected diffusion-weighted signal profile (C) and the associated FOD. The FOD amplitude is proportional to the radial signal profile and therefore the fibre density of the fibre population. Image adapted from Raffelt et al. (2012a).	46

Figure 2.8 A schematic representation of a fibre bundle cross-section made of numerous axons (grey circles) Anterior commissures voxels represented by the grid. Panels (a), (b) and (c) describe three different ways in which a fibre bundle can change: (a) a reduction in within-voxel fibre density; (b) a macroscopic change in fibre-cross section across voxels; (c) a combination of reductions in both fibre density and cross-section. Image adapted from (Raffelt et al., 2017)...	47
Figure 2.9 A schematic which illustrates the need for tensor reorientation. Panel (a) shows an anisotropic region of a diffusion tensor image. Panel (b) shows the same slice after a 30° rotation about the z-axis with no reorientation of the diffusion tensors. Panel (c) shows the slice after the same rotation, but with each tensor transformed by the same rotation. Image reproduced from Zhang et al. (2007) .....	51
Figure 3.1 Transient fetal organization of the developing cerebral wall during the 20 <sup>th</sup> post-conception week (a), 21 <sup>st</sup> -23 <sup>rd</sup> post-conception weeks (b), 24 <sup>th</sup> -32 <sup>nd</sup> post-conception weeks (c) and after the 32 <sup>nd</sup> post-conception week (d) on a T1-weight image. CP = cortical plate; SP = subplate zone; IZ = intermediate zone; SVZ = subventricular zone, WM = white matter; WMg = gyral white matter. Image modified from Figure 1 in Kostovic and Jovanov-Milosevic (2006)...	53
Figure 3.2 MRI of 19 gestational week post-mortem foetal brain. (a) Average diffusion-weighted image, (b) color-coded orientation map (red: right-left, green: anterior-posterior, blue: superior-inferior orientations), (c) ADC map, (d) FA map, and (e) T1-weighted image. Cg = cingulum; ic = internal capsule; GE = ganglionic eminence; Hip = hippocampus; Tha = thalamus. Image reproduced from Huang et al. (2006) .....	54
Figure 3.3 T1-weighted (left) and T2-weighted (right) images of an infant born at 39.6 weeks GA and imaged after 2 days. The yellow arrows indicate the posterior limb of the internal capsule, which is myelinated at term and is seen as high signal intensity and low signal intensity on the T1- and T2-weighted images, respectively. ....	55
Figure 3.4 Haemorrhagic parenchymal infarct (HPI) in two preterm infants. The top row shows axial T2- (a) and T1-weighted (b) images of an HPI in an infant born at 25.7 weeks GA and imaged at 41.6 weeks PMA. The bottom row shows axial T2- (c) and T1-weighted (d) images of an HPI in an infant born at 30.0 weeks GA and imaged at 42.4 weeks PMA. ....	60
Figure 3.5 Schematic diagram of cystic (A) and non-cystic (B) periventricular leukomalacia exhibit, demonstrating the two component of PVL focal necrosis deep in the white matter and more diffuse injury characterised by a loss of pre-oligodendrocytes and marked astrogliosis. Image modified from Figure 1 in Khwaja and Volpe (2008) .....	61

Figure 3.6 Main structures affected in premature infants with periventricular leukomalacia. ....	62
Figure 3.7 Cystic PVL in a preterm infant. Axial T2- (a) and T1-weighted (b) images of an infant born at 31.2 weeks GA and imaged at 42.7 weeks PMA. ....	63
Figure 3.8 Punctate lesion in an infant born at 28.9 weeks GA and imaged at 41. 6 weeks PMA, shown on T1-weighted image in the axial (a), sagittal (b) coronal view (c). ....	64
Figure 3.9 Absolute tissue volumes of cortical grey matter (CGM), white matter (WM), cerebrospinal fluid (CSF), ventricles, basal ganglia and thalami (BGT), cerebellum, brainstem and whole brain in a cohort of preterm infants imaged between 27-45 weeks PMA. Reproduced from Makropoulos et al. (2016). ....	70
Figure 3.10 Cortical surfaces of preterm neonates at 28, 36 and 44 weeks PMA at scan demonstrating the increase in cortical folding and brain volume during the perinatal period. The surfaces are segmented into the frontal lobe (pink), parietal lobe (magenta), occipital lobe (bright green), medial and inferior temporal gyri (yellow), superior temporal gyrus (blue and dark blue) and the insula (mint green). Reproduced from Makropoulos et al. (2016). ....	70
Figure 4.1 The tract skeletons from TBSS. The left two columns show the tract skeletons evaluated and the right two columns show the tracts overlaid on the whole WM skeleton (shown in grey). ....	82
Figure 4.2 The TSA model fitting results for the left and right CC, CST, IFO, ILF, SLF and UNC. ....	83
Figure 4.3 Median Dice scores for each subject over eight tracts following tensor-based and scalar-based registration. ....	85
Figure 4.4 The variability across subjects' native space tractography for the left and right CST, IFOF, ILF and UNC shown in terms of a. FA values averaged over the entire tract and b. the total number of voxels included. ....	86
Figure 4.5 The mean FA values for each subject across eight tracts as estimated by native space tractography (green), TSA (blue) and TBSS (red). ....	88
Figure 4.6 The distribution of FA values for all subjects across eight tracts as estimated by native space tractography (green), TSA (blue) and TBSS (red). Normalised histograms for each subject (semi-transparent green, blue and red) were averaged and smoothed to represent the general trend (green, blue and red lines). ....	89
Figure 4.7 The Bhattacharyya distance between native space tractography and TSA (blue) and TBSS (red). ....	93

Figure 5.1 Histograms of composite motor, cognitive and language scores from the BSITD-III assessment.....	99
Figure 5.2 The results of the cluster analysis correlating motor scores with FA at each point within the CC, CST, IFOF, ILF, SLF and UNC. Statistically significant regions of positive correlation are shown in red ( $p \leq 0.01$ ), orange ( $0.01 < p \leq 0.02$ ), yellow ( $0.02 < p \leq 0.03$ ), green ( $0.03 < p \leq 0.04$ ) and light blue ( $0.04 < p \leq 0.05$ ). .....	101
Figure 5.3 Partial regression plots showing the linear relationship between motor scores and FA from the regions showing significant correlation for the CC, CST, IFOF, ILF and SLF. Key: FA   X = residuals of FA given the model; Motor score   X = residuals of motor scores given the model. ....	102
Figure 5.4 The results of the cluster analysis correlating motor scores with MD at each point within the CC, CST, IFOF, ILF, SLF and UNC. Statistically significant regions of negative correlation are shown in red ( $p \leq 0.01$ ), orange ( $0.01 < p \leq 0.02$ ), yellow ( $0.02 < p \leq 0.03$ ), green ( $0.03 < p \leq 0.04$ ) and light blue ( $0.04 < p \leq 0.05$ ). .....	103
Figure 5.5 Partial regression plots showing the linear relationship between motor scores and MD from the regions showing significant correlation for the CC, CST, IFOF, ILF and right SLF. Key: MD   X = residuals of MD given the model; Motor score   X = residuals of motor scores given the model. ....	104
Figure 5.6 The results of the cluster analysis correlating motor scores with RD at each point within the CC, CST, IFOF, ILF, SLF and UNC. Statistically significant regions of negative correlation are shown in red ( $p \leq 0.01$ ), orange ( $0.01 < p \leq 0.02$ ), yellow ( $0.02 < p \leq 0.03$ ), green ( $0.03 < p \leq 0.04$ ) and light blue ( $0.04 < p \leq 0.05$ ). .....	105
Figure 5.7 Partial regression plots showing the linear relationship between motor scores and RD from the regions showing significant correlation for the CC, CST, IFOF, ILF and right SLF. Key: RD   X = residuals of RD given the model; Motor score   X = residuals of motor scores given the model. ....	106
Figure 5.8 The results of the cluster analysis correlating motor scores with AD at each point within the CC, CST, IFOF, ILF, SLF and UNC. Statistically significant regions of negative correlation are shown in red ( $p \leq 0.01$ ), orange ( $0.01 < p \leq 0.02$ ), yellow ( $0.02 < p \leq 0.03$ ), green ( $0.03 < p \leq 0.04$ ) and light blue ( $0.04 < p \leq 0.05$ ). .....	107
Figure 5.9 Partial regression plots showing the linear relationship between motor scores and AD from the regions showing significant negative correlation for the CC, CST and right IFOF. Key:	

AD   X = residuals of AD given the model; Motor score   X = residuals of motor scores given the model. ....	107
Figure 5.10 The results of the cluster analysis correlating motor scores with AD at each point within the CST. Statistically significant regions of positive correlation are shown in red ( $p \leq 0.01$ ), orange ( $0.01 < p \leq 0.02$ ), yellow ( $0.02 < p \leq 0.03$ ), green ( $0.03 < p \leq 0.04$ ) and light blue ( $0.04 < p \leq 0.05$ ). ....	108
Figure 5.11 Partial regression plots showing the linear relationship between motor scores and AD from the regions showing significant positive correlation for the CST. Key: AD   X = residuals of AD given the model; Motor score   X = residuals of motor scores given the model.....	108
Figure 5.12 The results of the cluster analysis correlating cognitive scores with FA at each point within the CC, CST, IFOF, ILF, SLF and UNC. Statistically significant regions of positive correlation are shown in red ( $p \leq 0.01$ ), orange ( $0.01 < p \leq 0.02$ ), yellow ( $0.02 < p \leq 0.03$ ), green ( $0.03 < p \leq 0.04$ ) and light blue ( $0.04 < p \leq 0.05$ ).....	109
Figure 5.13 Partial regression plots showing the linear relationship between cognitive scores and FA from the regions showing significant correlation for the CC, CST, IFOF, ILF and SLF. Key: FA   X = residuals of FA given the model; Cognitive score   X = residuals of cognitive scores given the model. ....	110
Figure 5.14 The results of the cluster analysis correlating cognitive scores with MD at each point within the CC, CST, IFOF, ILF, SLF and UNC. Statistically significant regions of negative correlation are shown in red ( $p \leq 0.01$ ), orange ( $0.01 < p \leq 0.02$ ), yellow ( $0.02 < p \leq 0.03$ ), green ( $0.03 < p \leq 0.04$ ) and light blue ( $0.04 < p \leq 0.05$ ).....	111
Figure 5.15 Partial regression plots showing the linear relationship between cognitive scores and MD from the regions showing significant correlation for the CC, CST, IFOF, right ILF and right SLF. Key: MD   X = residuals of MD given the model; Cognitive score   X = residuals of cognitive scores given the model.....	112
Figure 5.16 The results of the cluster analysis correlating cognitive scores with RD at each point within the CC, CST, IFOF, ILF, SLF and UNC. Statistically significant regions of negative correlation are shown in red ( $p \leq 0.01$ ), orange ( $0.01 < p \leq 0.02$ ), yellow ( $0.02 < p \leq 0.03$ ), green ( $0.03 < p \leq 0.04$ ) and light blue ( $0.04 < p \leq 0.05$ ).....	113
Figure 5.17 Partial regression plots showing the linear relationship between cognitive scores and RD from the regions showing significant correlation for the CC, CST, IFOF and ILF. Key: RD	

X = residuals of RD given the model; Cognitive score   X = residuals of cognitive scores given the model. ....	114
Figure 5.18 The results of the cluster analysis correlating cognitive scores with AD at each point within the CC and CST. Statistically significant regions of negative correlation are shown in red ( $p \leq 0.01$ ), orange ( $0.01 < p \leq 0.02$ ), yellow ( $0.02 < p \leq 0.03$ ), green ( $0.03 < p \leq 0.04$ ) and light blue ( $0.04 < p \leq 0.05$ ). ....	115
Figure 5.19 Partial regression plots showing the linear relationship between cognitive scores and AD from the regions showing significant correlation for the CC and CST. Key: AD   X = residuals of AD given the model; Cognitive score   X = residuals of cognitive scores given the model. .	115
Figure 5.20 The results of the cluster analysis correlating language scores with FA at each point within the IFOF and ILF. Statistically significant regions of postive correlation are shown in red ( $p \leq 0.01$ ), orange ( $0.01 < p \leq 0.02$ ), yellow ( $0.02 < p \leq 0.03$ ), green ( $0.03 < p \leq 0.04$ ) and light blue ( $0.04 < p \leq 0.05$ ). ....	116
Figure 5.21 Partial regression plots showing the linear relationship between language scores and FA from the regions showing significant correlation for the ILF and left IFOF. Key: FA   X = residuals of FA given the model; Language score   X = residuals of language scores given the model. ....	116
Figure 5.22 The results of the cluster analysis correlating language scores with MD at each point within the left CST. Statistically significant regions of negative correlation are shown in red ( $p \leq 0.01$ ), orange ( $0.01 < p \leq 0.02$ ), yellow ( $0.02 < p \leq 0.03$ ), green ( $0.03 < p \leq 0.04$ ) and light blue ( $0.04 < p \leq 0.05$ ) and partial regression plot showing from the regions showing significant correlation. Key: MD   X = residuals of MD given the model; Language score   X = residuals of language scores given the model. ....	117
Figure 5.23 The results of the cluster analysis correlating language scores with RD at each point within the left CST and right ILF. Statistically significant regions of negative correlation are shown in red ( $p \leq 0.01$ ), orange ( $0.01 < p \leq 0.02$ ), yellow ( $0.02 < p \leq 0.03$ ), green ( $0.03 < p \leq 0.04$ ) and light blue ( $0.04 < p \leq 0.05$ ). ....	117
Figure 5.24 Partial regression plots showing the linear relationship between language scores and RD from the regions showing significant correlation for the left CST and right ILF. Key: RD   X = residuals of RD given the model; Language score   X = residuals of language scores given the model. ....	117

Figure 5.25 The results of the cluster analysis correlating GA at birth with FA at each point within the CC, CST, IFOF, ILF, SLF and UNC. Statistically significant regions of positive correlation are shown in red ( $p \leq 0.01$ ), orange ( $0.01 < p \leq 0.02$ ), yellow ( $0.02 < p \leq 0.03$ ), green ( $0.03 < p \leq 0.04$ ) and light blue ( $0.04 < p \leq 0.05$ ).	118
Figure 5.26 Partial regression plots showing the linear relationship between GA at birth and FA from the regions showing significant correlation for the CC, IFOF, ILF and SLF. Key: FA   X = residuals of FA given the model; GA   X = residuals of GA given the model	119
Figure 5.27 The results of the cluster analysis correlating GA at birth with MD at each point within the CC, CST, IFOF, ILF, SLF and UNC. Statistically significant regions of negative correlation are shown in red ( $p \leq 0.01$ ), orange ( $0.01 < p \leq 0.02$ ), yellow ( $0.02 < p \leq 0.03$ ), green ( $0.03 < p \leq 0.04$ ) and light blue ( $0.04 < p \leq 0.05$ ).	120
Figure 5.28 Partial regression plots showing the linear relationship between GA at birth and MD from the regions showing significant correlation for the CC, CST, IFOF and ILF. Key: MD   X = residuals of MD given the model; GA   X = residuals of GA given the model	121
Figure 5.29 The results of the cluster analysis correlating GA at birth with RD at each point within the CC, CST, IFOF, ILF, SLF and UNC. Statistically significant regions of negative correlation are shown in red ( $p \leq 0.01$ ), orange ( $0.01 < p \leq 0.02$ ), yellow ( $0.02 < p \leq 0.03$ ), green ( $0.03 < p \leq 0.04$ ) and light blue ( $0.04 < p \leq 0.05$ ).	122
Figure 5.30 Partial regression plots showing the linear relationship between GA at birth and RD from the regions showing significant correlation for the CC, CST, IFOF and ILF. Key: RD   X = residuals of RD given the model; GA   X = residuals of GA given the model.	123
Figure 5.31 The results of the cluster analysis correlating GA at birth with AD at each point within the CC, CST, IFOF, ILF, SLF and UNC. Statistically significant regions of negative correlation are shown in red ( $p \leq 0.01$ ), orange ( $0.01 < p \leq 0.02$ ), yellow ( $0.02 < p \leq 0.03$ ), green ( $0.03 < p \leq 0.04$ ) and light blue ( $0.04 < p \leq 0.05$ ).	124
Figure 5.32 Partial regression plots showing the linear relationship between GA at birth and AD from the regions showing significant correlation for the CC, IFOF, ILF and SLF. Key: AD   X = residuals of AD given the model; GA   X = residuals of GA given the model.	124
Figure 5.33 The results of the cluster analysis correlating PMA at scan with FA at each point within the CC, CST, IFOF, ILF, SLF and UNC. Statistically significant regions of positive correlation are shown in red ( $p \leq 0.01$ ), orange ( $0.01 < p \leq 0.02$ ), yellow ( $0.02 < p \leq 0.03$ ), green ( $0.03 < p \leq 0.04$ ) and light blue ( $0.04 < p \leq 0.05$ ).	125

Figure 5.34 Partial regression plots showing the linear relationship between PMA at scan and FA from the regions showing significant correlation for the CC, CST, IFOF, ILF, SLF and UNC. Key: FA   X = residuals of FA given the model; PMA   X = residuals of PMA given the model. ....	126
Figure 5.35 The results of the cluster analysis correlating PMA at scan with MD at each point within the CC, CST, IFOF, ILF, SLF and UNC. Statistically significant regions of negative correlation are shown in red ( $p \leq 0.01$ ), orange ( $0.01 < p \leq 0.02$ ), yellow ( $0.02 < p \leq 0.03$ ), green ( $0.03 < p \leq 0.04$ ) and light blue ( $0.04 < p \leq 0.05$ ).....	127
Figure 5.36 Partial regression plots showing the linear relationship between PMA at scan and MD from the regions showing significant correlation for the CC, CST, IFOF, ILF, SLF and UNC. Key: RD   X = residuals of RD given the model; PMA   X = residuals of PMA given the model. ....	128
Figure 5.37 The results of the cluster analysis correlating PMA at scan with RD at each point within the CC, CST, IFOF, ILF, SLF and UNC. Statistically significant regions of negative correlation are shown in red ( $p \leq 0.01$ ), orange ( $0.01 < p \leq 0.02$ ), yellow ( $0.02 < p \leq 0.03$ ), green ( $0.03 < p \leq 0.04$ ) and light blue ( $0.04 < p \leq 0.05$ ).....	129
Figure 5.38 Partial regression plots showing the linear relationship between PMA at scan and RD from the regions showing significant correlation for the CC, CST, IFOF, ILF, SLF and UNC. Key: RD   X = residuals of RD given the model; PMA   X = residuals of PMA given the model. ....	130
Figure 5.39 The results of the cluster analysis correlating PMA at scan with AD at each point within the CC, CST, IFOF, ILF, SLF and UNC. Statistically significant regions of negative correlation are shown in red ( $p \leq 0.01$ ), orange ( $0.01 < p \leq 0.02$ ), yellow ( $0.02 < p \leq 0.03$ ), green ( $0.03 < p \leq 0.04$ ) and light blue ( $0.04 < p \leq 0.05$ ).....	131
Figure 5.40 Partial regression plots showing the linear relationship between PMA at scan and AD from the regions showing significant correlation for the CC, CST, IFOF, ILF, SLF and UNC. Key: AD   X = residuals of AD given the model; PMA   X = residuals of PMA given the model. ....	132
Figure 6.1 Axial, sagittal and coronal views of T2-weighted image of infant with small HPOI, indicated by the yellow arrows. ....	143
Figure 6.2 Histograms of motor, cognitive and language scores from the BSITD-III assessment .....	143
Figure 6.3 The results of fixel-based analysis assessing the relationship between FD and PMA at scan. The top and third rows show fixels with significant positive correlation (corrected $p \leq 0.05$ ) between FD and PMA at scan. The second and bottom rows show the streamlines passing	



through significant fixels, coloured by direction (red: left-right; green: anterior-posterior; blue: inferior-superior). .....	146
Figure 6.4 Coronal view of fixels showing significant positive correlation between FD and PMA at scan (red-yellow) overlaid on the template fixel mask (black) with a close-up of fixels projecting to the laterally to the cortex.....	147
Figure 6.5 The results of fixel-based analysis assessing the relationship between FC and PMA at scan. The top and third rows show fixels with significant positive correlation (corrected $p \leq 0.05$ ) between FC and PMA at scan. The second and bottom rows show the streamlines passing through significant fixels, coloured by direction (red: left-right; green: anterior-posterior; blue: inferior-superior). .....	148
Figure 6.6 Coronal view of fixels showing significant positive correlation between FC and PMA at scan (red-yellow) overlaid on the template fixel mask (black) with a close-up of fixels projecting to the cortex. While multiple fixels within a voxel are identified as statistically significant, they are not the same value, with medial projections having a lower p-value than lateral projections. ....	149
Figure 6.7 The results of fixel-based analysis assessing the relationship between FDC and PMA at scan. The top and third rows show fixels with significant positive correlation (corrected $p \leq 0.05$ ) between FC and PMA at scan. The second and bottom rows show the streamlines passing through significant fixels, coloured by direction (red: left-right; green: anterior-posterior; blue: inferior-superior). .....	150
Figure 6.8 The results of fixel-based analysis assessing the relationship between FD and GA at birth. The top row shows fixels with significant positive correlation (corrected $p \leq 0.05$ ) between FD and GA at birth. The bottom row shows the streamlines passing through significant fixels, coloured by direction (red: left-right; green: anterior-posterior; blue: inferior-superior). .....	151
Figure 6.9 The results of fixel-based analysis assessing the relationship between FC and GA at birth. The top row shows fixels with significant positive correlation (corrected $p \leq 0.05$ ) between FC and GA at birth. The bottom row shows the streamlines passing through significant fixels, coloured by direction (red: left-right; green: anterior-posterior; blue: inferior-superior). .....	151
Figure 6.10 Axial view of fixels showing significant positive correlation between FC and GA at birth (red-yellow) overlaid on the fixel template mask (black) with a close-up of fixels within the centrum semiovale, identifying fixels within the SLF as statistically significant. ....	152
Figure 6.11 The results of fixel-based analysis assessing the relationship between FDC and GA at birth. The top row shows fixels with significant positive correlation (corrected $p \leq 0.05$ ) between	

FDC and GA at birth. The bottom row shows the streamlines passing through significant fixels, coloured by direction (red: left-right; green: anterior-posterior; blue: inferior-superior).....	153
Figure 6.12 The results of fixel-based analysis assessing the relationship between FD and the number of days on mechanical ventilation. The top row shows fixels with significant negative correlation (corrected $p \leq 0.05$ ) between FD and days on ventilation. The bottom row shows the streamlines passing through significant fixels, coloured by direction (red: left-right; green: anterior-posterior; blue: inferior-superior). .....	154
Figure 6.13 Axial view of fixels showing significant positive correlation between FD and the number of days on mechanical ventilation (red-yellow) overlaid on the fixel template mask (black) with a close-up of fixels within the cerebellum. ....	155
Figure 6.14 The results of fixel-based analysis assessing the relationship between FC and the number of days on mechanical ventilation. The top and third rows show fixels with significant negative correlation (corrected $p \leq 0.05$ ) between FC and days on ventilation. The second and bottom rows show the streamlines passing through significant fixels, coloured by direction (red: left-right; green: anterior-posterior; blue: inferior-superior). ....	156
Figure 6.15 Sagittal view of the fixels showing significant positive negative between FC and the number of days on mechanical ventilation (red-yellow) overlaid on the template fixel mask (black) with a close-up demonstrating that, within the centrum semiovale, it is fibres from the CST that show a significant correlation with days on ventilation, and not association fibres or lateral projections of the CC. ....	157
Figure 6.16 The results of fixel-based analysis assessing the relationship between FDC and the number of days on mechanical ventilation. The top and third rows show fixels with significant negative correlation (corrected $p \leq 0.05$ ) between FDC and days on ventilation. The second and bottom rows show the streamlines passing through significant fixels, coloured by direction (red: left-right; green: anterior-posterior; blue: inferior-superior). ....	158
Figure 6.17 The results of fixel-based analysis assessing the relationship between FC and the number of days requiring total parenteral nutrition (TPN). The top row shows fixels with significant negative correlation (corrected $p \leq 0.05$ ) between FC and days on TPN. The bottom row shows the streamlines passing through significant fixels, coloured by direction (red: left-right; green: anterior-posterior; blue: inferior-superior). ....	159

Figure 6.18 Coronal view of the fixels showing significant positive negative between FC and the number of days requiring total parenteral nutrition (TPN) (red-yellow) overlaid on the template fixel mask (black) with a close-up of a region of crossing fibres within the brain stem. ....	159
Figure 6.19 The results of fixel-based analysis assessing the relationship between FC and birth weight z scores. The top and third rows show fixels with significant positive correlation (corrected $p \leq 0.05$ ) between FC and birth weight z scores. The second and bottom rows show the streamlines passing through significant fixels, coloured by direction (red: left-right; green: anterior-posterior; blue: inferior-superior).....	160
Figure 6.20 Sagittal view of fixels showing significant positive correlation between FC and birthweight z scores (red-yellow) overlaid on the fixel template mask (black) with a close-up within the cingulum.....	161
Figure 6.21 The results of fixel-based analysis assessing the relationship between FDC and birth weight z scores. The top and third rows show fixels with significant positive correlation (corrected $p \leq 0.05$ ) between FDC and birth weight z scores. The second and bottom rows show the streamlines passing through significant fixels, coloured by direction (red: left-right; green: anterior-posterior; blue: inferior-superior). ....	162
Figure 6.22 The results of fixel-based analysis assessing differences between male and female subjects. The top and third rows show fixels with FC significantly greater (corrected $p \leq 0.05$ ) in male subjects than in female subjects. The second and bottom rows show the streamlines passing through significant fixels, coloured by direction (red: left-right; green: anterior-posterior; blue: inferior-superior). ....	163
Figure 6.23 Axial view of the fixels showing significant differences in FC between male and female subjects (red-yellow) overlaid on the template fixel mask with a close-up of the fixels within the cingulum. The cingulum can be difficult to identify due to partial volume effects from the CC, however it is possible to distinguish the two using fixel-based analysis.....	164
Figure 6.24 The results of fixel-based analysis assessing the relationship between FC and motor performance. The top row shows fixels with significant positive correlation (corrected $p \leq 0.05$ ) between FC and motor scores from the BSITD-III. The bottom row shows the streamlines passing through significant fixels, coloured by direction (red: left-right; green: anterior-posterior; blue: inferior-superior). ....	165
Figure 6.25 Coronal view of the fixel showing significant positive correlation between motor scores and FC (red-yellow) overlaid on the template fixel mask (black) with a close-up of the brainstem	

demonstrating that only fixels within the pons, and not the CST, are significantly correlated with motor scores. ....	165
Figure 6.26 The results of fixel-based analysis assessing the relationship between FDC and motor performance. The top row shows fixels with significant positive correlation (corrected $p \leq 0.05$ ) between FDC and motor scores from the BSITD-III. The bottom row shows the streamlines passing through significant fixels, coloured by direction (red: left-right; green: anterior-posterior; blue: inferior-superior).....	166
Figure 6.27 The results of fixel-based analysis assessing the relationship between FC and cognitive performance. The top row shows fixels with significant positive correlation (corrected $p \leq 0.05$ ) between FC and cognitive scores from the BSITD-III. The bottom row shows the streamlines passing through significant fixels, coloured by direction (red: left-right; green: anterior-posterior; blue: inferior-superior). ....	167
Figure 6.28 The results of fixel-based analysis assessing the relationship between FDC and cognitive performance. The top row shows fixels with significant positive correlation (corrected $p \leq 0.05$ ) between FDC and cognitive scores from the BSITD-III. The bottom row shows the streamlines passing through significant fixels, coloured by direction (red: left-right; green: anterior-posterior; blue: inferior-superior). ....	168
Figure 6.29 The results of fixel-based analysis assessing the relationship between FD and language performance. The top row shows fixels with significant positive correlation (corrected $p \leq 0.05$ ) between FD and language scores from the BSITD-III. The bottom row shows the streamlines passing through significant fixels, coloured by direction (red: left-right; green: anterior-posterior; blue: inferior-superior). ....	169
Figure 6.30 The results of fixel-based analysis assessing the relationship between FDC and language performance. The top row shows fixels with significant positive correlation (corrected $p \leq 0.05$ ) between FDC and language scores from the BSITD-III. The bottom row shows the streamlines passing through significant fixels, coloured by direction (red: left-right; green: anterior-posterior; blue: inferior-superior). ....	169
Figure 7.1 A representative subject from the study group, male infant born at 39.6 weeks and scanned at 39.9 weeks PMA. The top and middle rows show DTI and NODDI scalar maps in native space, the bottom row shows WM and CSF FODs overlaid on WM density and CSF density images, respectively. ....	179

Figure 7.2 Template tractography and TSA model fitting results for the left and right CC, CST, IFO, ILF, SLF and UNC. ....	181
Figure 7.3 Unilateral skeleton for CC; (a) cross-sectional view of the CC tractography (blue), skeleton (green-yellow) and skeleton boundary (pink); (b) lateral (top) and medial (bottom) view of the CC skeleton; (c) lateral (top) and medial (bottom) view of the skeleton boundary.....	182
Figure 7.4 Group-averaged values for FA, AD, RD, MD, <i>vic</i> , ODI and FD for the CC. ....	184
Figure 7.5 Group-averaged values for FA, AD, RD, MD, <i>vic</i> , ODI and FD for the CST. ....	185
Figure 7.6 Group-averaged values for FA, AD, RD, MD, <i>vic</i> , ODI and FD for the IFOF. ....	186
Figure 7.7 Group-averaged values for FA, AD, RD, MD, <i>vic</i> , ODI and FD for the ILF. ....	187
Figure 7.8 Group-averaged values for FA, AD, RD, MD, <i>vic</i> , ODI and FD for the SLF. ....	188
Figure 7.9 Group-averaged values for FA, AD, RD, MD, <i>vic</i> , ODI and FD for the UNC.....	189
Figure 7.10 The regions where AD, RD and MD are greater in the left SLF and ILF (shown in red). ....	190
Figure 7.11 The region where FA is greater in the right SLF.....	190
Figure 7.12 The regions where <i>vic</i> and ODI are greater in the right SLF, IFOF and ILF (shown in red). ....	191
Figure 7.13 The results of the cluster analysis correlating PMA with FA at each point within the CC, CST, IFOF, ILF, SLF and UNC. Statistically significant regions of positive correlation are shown in red ( $p \leq 0.01$ ), orange ( $0.01 < p \leq 0.02$ ), yellow ( $0.02 < p \leq 0.03$ ), green ( $0.03 < p \leq 0.04$ ) and light blue ( $0.04 < p \leq 0.05$ ). ....	192
Figure 7.14 Scatter plots showing the linear relationship between FA and PMA from the regions showing significant correlation for the CC, CST, IFOF, ILF, SLF and UNC. ....	193
Figure 7.15 The results of the cluster analysis correlating PMA with MD at each point within the CC, CST, IFOF, ILF, SLF and UNC. Statistically significant regions of negative correlation are shown in red ( $p \leq 0.01$ ), orange ( $0.01 < p \leq 0.02$ ), yellow ( $0.02 < p \leq 0.03$ ), green ( $0.03 < p \leq 0.04$ ) and light blue ( $0.04 < p \leq 0.05$ ). ....	194
Figure 7.16 Scatter plots showing the linear relationship between MD and PMA from the regions showing significant correlation for the CC, CST, IFOF, ILF, SLF and UNC. ....	195
Figure 7.17 The results of the cluster analysis correlating PMA with RD at each point within the CC, CST, IFOF, ILF, SLF and UNC. Statistically significant regions of negative correlation are	

shown in red ( $p \leq 0.01$ ), orange ( $0.01 < p \leq 0.02$ ), yellow ( $0.02 < p \leq 0.03$ ), green ( $0.03 < p \leq 0.04$ ) and light blue ( $0.04 < p \leq 0.05$ ).	196
Figure 7.18 Scatter plots showing the linear relationship between RD and PMA from the regions showing significant correlation for the CC, CST, IFOF, ILF, SLF and UNC.	197
Figure 7.19 The results of the cluster analysis correlating PMA with AD at each point within the CC, CST, IFOF, ILF, SLF and UNC. Statistically significant regions of negative correlation are shown in red ( $p \leq 0.01$ ), orange ( $0.01 < p \leq 0.02$ ), yellow ( $0.02 < p \leq 0.03$ ), green ( $0.03 < p \leq 0.04$ ) and light blue ( $0.04 < p \leq 0.05$ ).	198
Figure 7.20 Scatter plots showing the linear relationship between AD and PMA from the regions showing significant correlation for the CC, CST, IFOF, ILF, SLF and UNC.	199
Figure 7.21 The results of the cluster analysis correlating PMA with <i>vic</i> at each point within the CC, CST, IFOF, ILF, SLF and UNC. Statistically significant regions of positive correlation are shown in red ( $p \leq 0.01$ ), orange ( $0.01 < p \leq 0.02$ ), yellow ( $0.02 < p \leq 0.03$ ), green ( $0.03 < p \leq 0.04$ ) and light blue ( $0.04 < p \leq 0.05$ ).	200
Figure 7.22 Scatter plots showing the linear relationship between <i>vic</i> and PMA from the regions showing significant correlation for the CC, CST, IFOF, ILF, SLF and UNC.	201
Figure 7.23 Scatter plots showing the relationship between ODI and PMA averaged over the whole tract skeleton for the CC, CST, IFOF, ILF, SLF and UNC. TSA found no statistically significant relationship was found between ODI and PMA.	202
Figure 7.24 The results of the cluster analysis correlating PMA with FD at each point within the the CC, CST, IFOF, ILF, SLF and UNC. Statistically significant regions of positive correlation are shown in red ( $p \leq 0.01$ ), orange ( $0.01 < p \leq 0.02$ ), yellow ( $0.02 < p \leq 0.03$ ), green ( $0.03 < p \leq 0.04$ ) and light blue ( $0.04 < p \leq 0.05$ ).	203
Figure 7.25 Scatter plots showing the linear relationship between FD and PMA from the regions showing significant correlation for the CC, CST, IFOF, ILF, SLF and UNC.	204
Figure 7.26 The results of the cluster analysis correlating PMA with FC at each point within the the CC, CST, IFOF, ILF, SLF and UNC. Statistically significant regions of postive correlation are shown in red ( $p \leq 0.01$ ), orange ( $0.01 < p \leq 0.02$ ), yellow ( $0.02 < p \leq 0.03$ ), green ( $0.03 < p \leq 0.04$ ) and light blue ( $0.04 < p \leq 0.05$ ).	205
Figure 7.27 Scatter plots showing the linear relationship between FC and PMA from the regions showing significant correlation for the CC, CST, IFOF, ILF, SLF and UNC.	206



## List of Tables

Table 4.1 A summary of the key aspects of the TSA and TBSS pipelines.....	76
Table 4.2 Perinatal characteristics of the study group. ....	78
Table 4.3 ROI placement for tractography.....	79
Table 4.4 p-values from the Wilcoxon signed rank test comparing Dice scores from the tensor-based and scalar-based registration. ....	84
Table 4.5 . p-values from the Wilcoxon signed rank test comparing mean FA values between native space and TBSS, native space and TSA, and TSA and TBSS. ....	87
Table 4.6 Summary of the Bhattacharyya distances.....	91
Table 5.1 Characteristics of the study group. ....	98
Table 5.2 Focal brain injury observed on T1- and T2-weighted MR imaging. ....	99
Table 5.3 Summary of results from tract-specific analysis. All significant results are bilateral, unless the hemisphere is explicitly stated.....	133
Table 6.1 Characteristics of the study group. ....	141
Table 6.2 Summary of results from fixel-based analysis. All significant results are bilateral, unless the hemisphere is explicitly stated.....	171
Table 7.1 The perinatal characteristics of the study group.....	177
Table 7.2 Summary of results from tract-specific analysis. All significant results are bilateral. ....	207



## Abbreviations

Abbreviation	Meaning
$^1\text{H}$	Hydrogen proton
AD	Axial diffusivity
AFD	Apparent fibre density
ALIC	Anterior limb of the internal capsule
CC	Corpus callosum
cm-rep	Continuous medial representation
CP	Cortical plate
CSD	Constrained spherical deconvolution
CSF	cerebro
CST	Corticospinal tract
dMRI	Diffusion-weighted magnetic resonance imaging
DWI	Diffusion-weighted imaging
EPI	Echo planar imaging
FA	Fractional anisotropy
FBA	Fixel-based analysis
FC	Fibre cross-section
FD	Fibre density
FDC	Fibre density and cross-section
FOD	Fibre orientation distribution
FWER	Family-wise error correction
GA	Gestational age
GM	Grey matter
GMH	Germinal matrix haemorrhage
HARDI	High angular resolution diffusion imaging
HMOA	Hindrance modulated orientational anisotropy
IFOF	Inferior fronto-occipital fasciculus
ILF	Inferior longitudinal fasciculus
IUGR	Intrauterine growth restriction
IVH	Intraventricular haemorrhage
IZ	Intermediate zone
MD	Mean diffusivity
MRI	Magnetic resonance imaging
NODDI	Neurite orientation dispersion and density imaging
PDF	Probability distribution function
PGSE	Pulsed gradient spin echo
PLIC	Posterior limb of the internal capsule
PVL	Periventricular leukomalacia
RD	Radial diffusivity
RF	Radio frequency
ROI	Region of interest
ROP	Retinopathy of prematurity
SD	Spherical deconvolution
SE	Spin echo
SLF	Superior longitudinal fasciculus
SP	Subplate
SVZ	Subventricular zone
TBSS	Tract-based spatial statistics
TE	Echo time
TPN	Total parenteral nutrition

TR	Repetition time
TSA	Tract-specific analysis
UNC	Uncinate fasciculus
VBM	Voxel-based morphometry
VZ	Ventricular zone
WM	White matter

## Publications

**Pecheva D**, Yushkevich P, Batalle D, Hughes E, Aljabar P, Wurie J, Hajnal JV, Edwards AD, Alexander DC, Counsell SJ, Zhang H. *A tract-specific approach to assessing white matter in preterm infants*. NeuroImage. 2017 Apr 27.

## Conference abstracts

**Pecheva D**, Zhang H, Barnett M, Chew A, Falconer S, Rutherford M, Kennea N, Hajnal JV, Alexander DC, Edwards AD, Counsell SJ. *White matter diffusion properties at term equivalent age are associated with subsequent motor performance in infants born preterm*.

Magna cum Laude Award.

25th Annual Meeting of the International Society for Magnetic Resonance in Medicine (ISMRM-ESMRMB 2017) 22-27<sup>th</sup> April 2017, Honolulu, HI, USA.

**Pecheva D**, Zhang H, Pietsch M, Barnett M, Chew A, Falconer S, Rutherford M, Kennea N, Hajnal JV, Alexander DC, Tournier JD, Edwards AD, Counsell SJ. *A novel, fibre-bundle specific assessment of the effects of maturation, ventilation and prematurity on white matter and preterm infants*.

Pediatric Academic Societies Meeting (PAS 2017), San Francisco, CA, USA.

**Pecheva D**, Zhang H, Barnett M, Chew A, Falconer S, Rutherford M, Kennea N, Hajnal JV, Alexander DC, Edwards AD, Counsell SJ. *White matter diffusion properties at term equivalent age are associated with subsequent motor and cognitive performance in a large cohort of infants born preterm*.

British Chapter ISMRM Postgraduate Meeting 2017 (BCISMRM 2017), London, UK.

Guerra G, **Pecheva D**, Pietsch M, Batalle D, Zhang H, Alexander DC, Rutherford M, Kinnea N, Hajnal JV, Nosarti C, Tournier JD, Edwards AD, Counsell SJ. *Mapping cerebello-cortical pathways in preterm infants*.

British Chapter ISMRM Postgraduate Meeting 2017 (BCISMRM 2017), London, UK.

**Pecheva D**, Zhang H, Ball G, Rutherford M, Kennea N, Hajnal JV, Alexander DC, Edwards AD, Counsell SJ. *Tract-specific analysis of white matter fasciculi in a large cohort of preterm infants*.

24th Annual Meeting of the International Society for Magnetic Resonance in Medicine (ISMRM-ESMRMB 2016) 5-13<sup>th</sup> May 2016, Singapore.

**Pecheva D**, Zhang H, Ball G, Rutherford M, Kennea N, Hajnal JV, Alexander DC, Edwards AD, Counsell SJ. *Tract-specific analysis of white matter fasciculi in a large cohort of preterm infants*.

Pediatric Academic Societies Meeting (PAS 2016), Baltimore, MD, USA.

Salvan P, Tournier JD, Batalle D, Aljabar P, **Pecheva D**, Arichi T, Edwards AD, Counsell SJ. *Language ability in children born preterm is associated with arcuate fasciculus structure at term equivalent*.

Pediatric Academic Societies Meeting (PAS 2016), Baltimore, MD, USA.

**Pecheva D**, Zhang H, Ball G, Rutherford M, Kennea N, Hajnal JV, Alexander DC, Edwards AD, Counsell SJ. *A tract-specific approach to white matter analysis in a large cohort of preterm infants*.

3<sup>rd</sup> place prize for poster presentation.

British Chapter ISMRM Postgraduate Meeting 2016 (BCISMRM 2016), London, UK.

**Pecheva D**, Yushkevich P, Batalle D, Hughes E, Aljabar P, Wurie J, Hajnal JV, Edwards AD, Alexander DC, Counsell SJ, Zhang H. *A tract-specific approach to assessing white matter microstructure in preterm newborn infants*.

21st Annual Meeting of the Organization for Human Brain Mapping (OHBM 2015), Honolulu, HI, USA.

# Chapter 1 Introduction

## 1.1 Motivation

Preterm birth affects 1 in 10 births worldwide (Howson et al., 2013), with approximately half of extremely preterm infants experiencing some neurological impairment (Moore et al., 2012; Serenius et al., 2016). The adverse consequences of prematurity encompass a wide range of impairments including cognitive, behavioural (Bayless and Stevenson, 2007; Bhutta et al., 2002; Delobel-Ayoub et al., 2009; Joseph et al., 2016; Marlow et al., 2005b), motor (Marlow et al., 2007; Williams et al., 2010; Wood et al., 2005) and language impairments (Allin et al., 2008; Guarini et al., 2009; Wolke and Meyer, 1999; Wolke et al., 2008). Moreover, perinatal risk factors such as the need for respiratory support, parenteral nutrition, necrotising enterocolitis, growth restriction and infection are common in the preterm population and can exacerbate the deleterious effects of prematurity (Berger et al., 2009; Bernstein et al., 2000; Brouwer et al., 2017; Hintz et al., 2005; Kady and Gardosi, 2004; Kaukola et al., 2006; Kobaly et al., 2008; Lin and Stoll, 2006; Lodha et al., 2014; Longo et al., 2013; Padilla et al., 2014; Rees et al., 2007; Short et al., 2003; Stephens et al., 2009; Vohr et al., 2000; Wu, 2002).

The cerebral white matter (WM) is particularly vulnerable to injury in preterm infants (Volpe, 2003, 2009a, b). Focal white matter lesions including cystic periventricular leukomalacia and haemorrhagic parenchymal infarct, are associated with neurological impairments (de Vries and Groenendaal, 2002; Klebermass-Schrehof et al., 2012; Patra et al., 2006; Radic et al., 2015a; Resch et al., 2000). While such injuries have decreased in recent years (Groenendaal et al., 2010; Hamrick et al., 2004; Larroque et al., 2003; van Haastert et al., 2011), advanced magnetic resonance imaging (MRI) techniques have revealed WM injury in the absence of overt pathology (Anjari et al., 2007; Huppi et al., 1998a; Rose et al., 2008; Thompson et al., 2011).

Diffusion-weighted MRI (dMRI), principally diffusion tensor imaging (DTI) (Basser et al., 1994), has been used to study the effects of prematurity on the developing brain (Arzoumanian et al., 2003; Ball et al., 2010; Partridge et al., 2004) and the association between WM microstructure at term-equivalent age and developmental outcome (Counsell et al., 2008; De Bruine et al., 2013;

Drobyshevsky et al., 2007; van Kooij et al., 2012b). With the move towards larger cohort imaging studies such as the Evaluation of Preterm Imaging Study (ePrime) and the Developing Human Connectome Project (dHCP), there is a need to employ analysis tools appropriate for large datasets. Tract-specific analysis (TSA) (Yushkevich et al., 2008) is a WM analysis method that may offer benefits over other commonly used methods such as tract-based spatial statistics (Smith et al., 2006) or methods relying on manually drawn regions of interest, but has not been evaluated for use in neonatal populations.

More recently, higher order diffusion models that can better characterise complex fibre configurations by explicitly modelling the dispersion and density of neurites (Zhang et al., 2012) and the density and cross-section of distinct fibre populations (Raffelt et al., 2017) have been developed. However, only a handful of neonatal studies have employed these models. Neurite orientation dispersion and density imaging (NODDI) (Zhang et al., 2012) has been applied previously to study preterm infants (Batalle et al., 2017; Eaton-Rosen et al., 2015; Melbourne et al., 2016), but there are no NODDI studies of normal brain development in healthy infants. Novel imaging methods developed for the dHCP (Hughes et al., 2016; Hutter et al., 2017) present a unique opportunity to study normal human brain development by applying advanced diffusion models, such as NODDI, to state-of-the-art dMRI data. Fixel-based analysis (FBA) (Raffelt et al., 2017) which provides fibre-bundle specific measures for individual fibre populations (referred to as a 'fixel') within voxels containing multiple fibre populations, has not been applied previously to a neonatal population.

## **1.2 Hypotheses and aims**

This thesis aims to apply advanced diffusion MRI analysis approaches to study brain development and WM injury in the preterm brain, and to evaluate normal development in the neonatal period in healthy term-born infants. Using TSA, FBA, and NODDI I evaluate the effects of perinatal risk factors on the developing brain in preterm infants; examine the relationship between WM microstructure in the perinatal period and subsequent neurodevelopmental performance in preterm infants; and evaluate lateralisation in healthy term-born infants.

I test the following hypotheses;

- i. White matter microstructure in preterm infants at term equivalent age is related to neurodevelopmental performance at 20 months in preterm infants (Chapter 5).
- ii. Exposure to perinatal clinical risk factors is associated with impaired white matter development in preterm infants at term equivalent age (Chapter 6).
- iii. Lateralisation of white matter fasciculi is evident in the brain of healthy term infants soon after birth (Chapter 7).

### 1.3 Thesis outline

The rest of this thesis is summarised below:

**Chapter 2** provides an overview of the main principles of MRI and dMRI and relevant WM analysis techniques.

**Chapter 3** provides an overview of brain maturation, the impact of preterm birth on brain development and neurodevelopmental outcome, and the use of MRI and dMRI to study neonatal populations.

**Chapter 4** presents an extensive methodological evaluation of TSA, demonstrating TSA's suitability for infant studies and the advantages offered over current popular analysis techniques.

**Chapter 5** explores the relationship between white matter diffusion properties using TSA and DTI at term equivalent age and neurodevelopmental performance at 2 years in a cohort of 407 preterm infants. This analysis demonstrated anatomically-specific relationships between motor, cognitive and language performance and WM fasciculi.

**Chapter 6** presents the first application of FBA to a neonatal population. The effects of perinatal risk factors such as respiratory illness, nutrition and growth restriction on WM, and the association between WM and neurodevelopmental outcome were assessed. This analysis provides detailed

information on how such factors affect distinct fibre populations within WM regions of complex configurations and identifies associations between WM tracts and neurodevelopmental outcome.

**Chapter 7** applies TSA to dHCP diffusion data to assess lateralisation and maturation-dependent changes in DTI, NODDI and fixel-derived measures in term-born infants. The results demonstrate little to no hemispheric differences in WM, indicating that lateralisation emerges later in life. Maturation-dependent changes in WM tracts concur with previous DTI studies and novel findings demonstrate increases in the intra-axonal compartment and fibre cross-section.

**Chapter 8** summarises the key findings in this thesis and outlines potential future work.



## Chapter 2 Magnetic Resonance Imaging

This chapter describes the principal concepts of magnetic resonance imaging, diffusion-weighted imaging and current analysis methods.

### 2.1 Nuclear magnetic resonance

Nuclear magnetic resonance first described almost 80 years ago (Bloch, 1946; Purcell et al., 1946) is the basis of magnetic resonance imaging (MRI). Atomic and subatomic nuclei possess the quantum property of spin angular momentum. Nuclei with non-zero spin, such as the hydrogen proton ( $^1\text{H}$ ) which has spin of  $\frac{1}{2}$ , possess a magnetic dipole moment.  $^1\text{H}$  is used in MRI due its abundance in the body. When no magnetic field is present, the axes of the magnetic dipole moments are oriented randomly. When a constant external magnetic field,  $B_0$ , is applied along a particular direction the magnetic moments align in one of two energy states – parallel or antiparallel to  $B_0$ . In a three-dimensional coordinate system (x, y, z), the direction of  $B_0$  is chosen as the z-axis. There will be slightly more spins aligned parallel to  $B_0$  as this is the lower energy state, resulting in a net magnetisation,  $M_0$ , in the direction of  $B_0$ . The external magnetic field creates torque on the spins, acting perpendicular to both the field and the direction of the angular momentum, which causes them to precess about the axis of  $B_0$ . The spins precess at the Larmor frequency,  $\omega$ , given by

$$\omega = \gamma B_0$$

where  $\gamma$  is gyromagnetic ratio, a proportionality constant that is fixed for a nucleus given by the ratio of its magnetic moment to its angular momentum. For  $^1\text{H}$  this is equal to 42.6 MHz/T.

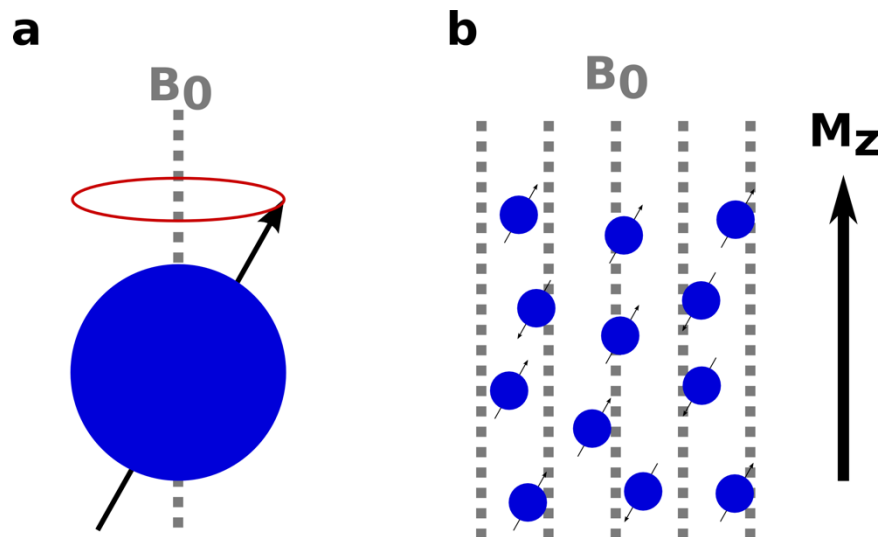


Figure 2.1 Hydrogen protons possess spin, a quantum property that induces a molecular moment (a; black arrow) along the axis of rotation. When an external magnetic field,  $B_0$  (grey dotted line) is applied, spins precess about the field and align parallel to it (b), producing a net magnetisation vector,  $M_z$ .

Resonance occurs when another magnetic field,  $B_1$ , is applied oscillating at the Larmor frequency and perpendicular to  $B_0$ , along the x-axis. Resonance results in the absorption of electromagnetic energy by the spins. The spins now precess about  $B_0$  and  $B_1$ , resulting in a spiral motion of the net magnetisation from the z-axis to the x-y plane. Simultaneously as the spins align with new magnetic field  $B_1$ , they are brought in phase with each other, whereas previously they were not, creating transverse magnetisation. The angle by which  $M_0$  is flipped away from the z-axis, known as the flip angle, is determined by duration and strength of the radio frequency (RF) pulse  $B_1$ . If this is witnessed by a static, external observer, they would see the spins precessing about  $B_0$  in the z-axis and  $B_1$  in the x-axis simultaneously to spiral down to the x-y plane. However, if the observer moves to a rotating reference frame, rotating at the Larmor frequency, the observer will no longer see the precession about the z-axis and only see the precession from the z-axis into the x-y plane as an arc. The net magnetisation is now rotating in the x-y plane, and a rotating magnetic field induces an electric current in charged particles. The current induced by the rotating magnetisation is the MR signal measured by a receiver coil.

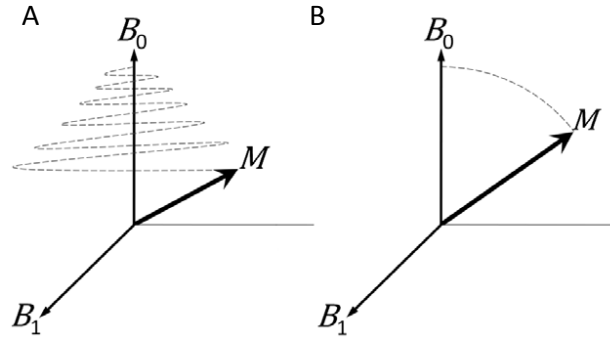


Figure 2.2 The application of an RF pulse,  $B_0$ , causes the net magnetisation vector to spiral towards the transverse plane. For a static observer, the spins precessing about  $B_0$  in the z-axis and  $B_1$  in the x-axis simultaneously to spiral down to the x-y plane. However, if the observer moves to a rotating reference frame, rotating at the Larmor frequency, they will only see the precession from the z-axis into the x-y plane as an arc.

When the RF pulse is switched off, the system will return to equilibrium and the spins will return to their previous state. As the spins realign with  $B_0$ , the longitudinal magnetisation,  $M_z$ , returns and transverse magnetisation,  $M_{xy}$ , decays. These are independent processes. The rate of the return of the longitudinal magnetisation is characterised by the time constant T1:

$$M_z = M_0 \left( 1 - e^{-t/T_1} \right).$$

The rate of the decay of the transverse magnetisation is characterised by the time constant T2:

$$M_{xy} = M_0 e^{-t/T_2}.$$

Both T1 and T2 are tissue-specific and T2 is always shorter than T1. Immediately after the RF pulse the spins are in phase but due to spin-spin interactions they begin to dephase, known as free-induction decay. The presence of inhomogeneities in  $B_0$  will result in differences in the precession frequencies of spins at different locations also contributing to spin dephasing.

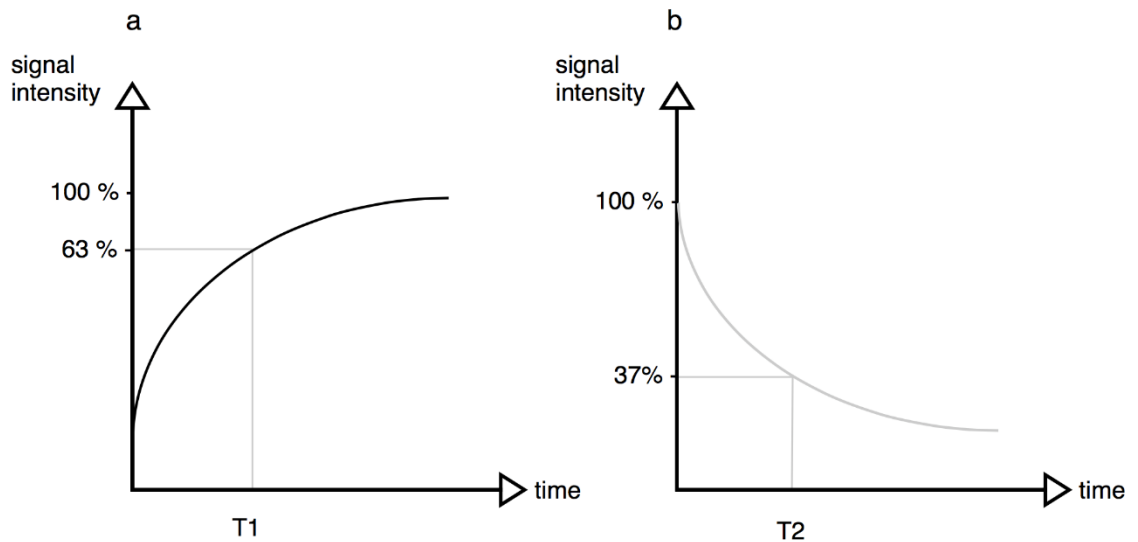


Figure 2.3 Recovery of the longitudinal magnetisation occurs towards equilibrium, with a tissue dependent recover constant  $T_1$  (a). b: The transverse magnetisation decays toward zero with a tissue dependent constant  $T_2$  (b).

## 2.2 Magnetic resonance imaging

To produce an image, the MR signal must be spatially localised. Magnetic gradients are used to spatially encode the MR signal (Lauterbur, 1973). By spatially varying the magnetic field, spins will precess at different rates depending on their location. By applying a gradient,  $G_z$ , in z-direction at the same time as the RF pulse, the RF pulse transmitted will excite only spins at certain location that correspond to that resonant frequency. By transmitting an RF pulse with a given bandwidth of frequencies we can select a slice at a specific location and determine the slice thickness. Following slice selection, it is necessary to encode spatial information within the slice. Another gradient,  $G_y$  is applied immediately after the RF pulse, the phase-encoding gradient, which applies a permanent phase shift to the spins. Multiple successive phase encoding gradients of differing strengths are needed to determine the location of spins along the y-axis. A frequency encoding gradient,  $G_x$ , also known as the readout gradient, is applied in the x-direction. This results in a mixture of frequencies corresponding to the location of the spins. The digitised MR signal is stored in k-space, a 2-dimensional matrix which represents spatial frequencies present. An image is constructed using a 2-dimensional inverse Fourier transform. It is possible to construct an image using a 3-dimensional Fourier transform by not introducing a slice-encoding gradient and instead applying a second phase-encoding gradient in the z-direction. Single-shot echo planar imaging

(EPI) is an imaging technique that fills k-space after a single RF pulse. The k-space lines are filled in by rapidly reversing the readout gradient, switching from positive to negative.

Contrast between tissues is achieved by varying the time between RF pulses – the repetition time (TR) and the time between the RF pulse and readout – the echo time (TE). A long TR reduces T1 contrast. If two tissues have different T1s, a long TR will allow the longitudinal magnetisation of both to recover almost fully, whereas a short TR will enhance T1 contrast. A short TE reduces T2 contrast and long TE enhances T1. T2-weighted images are normally acquired using a spin-echo (SE) sequence. After the application of the 90° RF pulse, begin to dephase due to T2\* effects. At a time of TE/2, a second 180° RF pulse is applied which rephases spins at time TE producing a signal decay governed by T2. Applying multiple rephasing RF pulses, an echo train, allows us to take multiple readouts from a single 90° RF excitation pulse.

## 2.3 Diffusion-weighted imaging

### 2.3.1 Brownian motion and diffusion

Diffusion is the constant motion of particles suspended in a liquid due to thermal energy, even under thermodynamic equilibrium. Given an environment without restrictions, a particle will traverse a random walk, with direction changes following collisions with other particles. This process was described by botanist Robert Brown in 1828 who observed the random movement of pollen grains in water. Later, Albert Einstein (1905) and Marian Smoluchowski (1906) each derived mathematical characterisations of Brownian motion independently via different methods, which were confirmed experimentally by Jean Baptiste Perrin in 1908. Einstein described the mass motion of particles undergoing free diffusion as a 3-dimensional Gaussian distribution

$$P(\mathbf{r}) = \frac{1}{\sqrt{(4\pi Dt)^3}} e^{-\|\mathbf{r}\|^2 / 4Dt}$$

where  $\mathbf{r}$  is a 3-dimensional displacement vector,  $t$  the diffusion time, and  $D$  is the diffusion coefficient which is  $2.5 \mu\text{m}^2/\text{ms}$  for water at room temperature. The root-mean-square displacement is given by

$$\sqrt{\langle \|\mathbf{r}\|^2 \rangle} = \sqrt{6Dt}$$

where  $\langle \rangle$  denote the averaging operator. This describes isotropic diffusion, in the absence of structural impediments to diffusion. However, in the brain the presence of axons, neuronal cell

bodies, glial cells and macromolecules comprise a heterogeneous environment which hinders and restricts diffusion. In the presence of these impediments, the measured root-mean-square displacement will be lower than predicted for water at room temperature. The term apparent diffusion coefficient was used to convey that the observed measure is influenced by the tissue microstructure. Diffusion is restricted if it is confined by physical boundaries, such as the diffusion of molecules in the intra-axonal space, causing the diffusion to become non-Gaussian. Hindered diffusion on the hand, where molecules are obstructed such as in the extra-axonal space, does follow the Gaussian distribution displacement (Assaf et al., 2004; Basser, 1995).

### 2.3.2 Diffusion-weighted imaging

Diffusion-weighted imaging (DWI) is a non-invasive imaging technique that is sensitised to the diffusion of water to generate contrast in MR images. To measure the diffusion of water molecules the pulsed gradient spin-echo (PGSE) sequence was proposed by Stejskal and Tanner (1965). The diffusion of water molecules was measured using two symmetric diffusion gradients added to either side of an EPI sequence. The first gradient is a spin dephasing gradient and the phase of each spin depends on its location with respect to the gradient. The spins are inverted by the 180° RF pulse and the second diffusion gradient applied, identical to the previous one, rephasing the spins. For the spins that are translocated due to diffusion there will be a non-zero net phase shift, whereas for those that undergo no diffusion there will be no phase shift. A non-zero phase shift will result in attenuation of the spin-echo signal. The signal attenuated by the diffusion gradients,  $S$ , is given by the Stejskal-Tanner equation

$$S = S_0 e^{-bD}$$

where  $S_0$  is the signal without the application of diffusion gradients,  $D$  is the apparent diffusion coefficient and  $b$  is a measure of the diffusion-weighting applied, given by

$$b = (\gamma\delta)^2 \left( \Delta - \frac{\delta}{3} \right) \|G\|^2$$

where  $\gamma$  is the gyromagnetic ratio,  $\delta$  is the diffusion gradient pulse duration,  $G$  is the diffusion gradient and  $\Delta$  is the time between gradients.

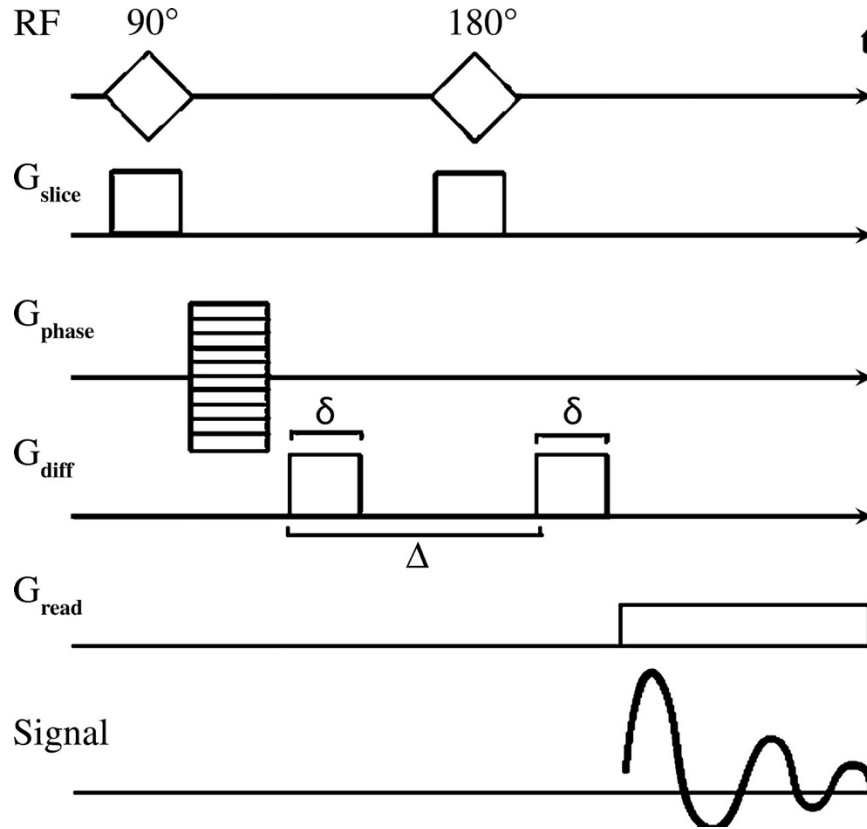


Figure 2.4 Diagram shows the pulsed gradient spin echo sequence used for diffusion MR imaging. Two diffusion-encoding gradient ( $G_{diff}$ ) pulses are applied to introduce a phase shift.  $\delta$  = duration of the diffusion-encoding gradient,  $\Delta$  = diffusion time interval,  $G_{phase}$  = phase-encoding gradient,  $G_{read}$  = readout gradient,  $G_{slice}$  = section-selective gradient,  $RF$  = radiofrequency pulse,  $t$  = acquisition time. Reproduced from Hagmann et al. (2006).

### 2.3.3 Diffusion tensor Imaging

The organisation of tissue microstructure will affect how water molecules diffuse, with coherently organised microstructure resulting in anisotropic diffusion (Hajnal et al., 1991; Moseley et al., 1990; Thomsen et al., 1987). Within white matter (WM), water molecules diffuse more slowly perpendicular to the fibres than parallel to them. Under these conditions, the apparent diffusion coefficient will be different depending in the direction in which it is measured. To account for this (Basser et al., 1994) proposed that diffusion is characterised using the diffusion tensor, a  $3 \times 3$  symmetric, positive-definite matrix:

$$D = \begin{pmatrix} D_{xx} & D_{xy} & D_{xz} \\ D_{xy} & D_{yy} & D_{yz} \\ D_{xz} & D_{yz} & D_{zz} \end{pmatrix}$$

The apparent diffusion coefficient is evaluated for a given direction  $u$  as  $u^T D u$ . This gives the diffusion-attenuated signal

$$S = S_0 e^{-b g^T D g}$$

along the gradient direction  $g$ . The diagonal elements give the diffusivities along the x-, y- and z-axes and the off-diagonal elements give the correlation between them. The diffusion tensor  $D$  has six independent elements and therefore requires a minimum of one non-diffusion weighted image and six diffusion-weighted images, although usually more are acquired.

The diffusion tensor is the covariance matrix of a 3-dimensional Gaussian probability distribution function (PDF) representing the distance that a molecule will diffuse to with equal probability. The isosurface of this PDF is an ellipsoid described by the eigensystem of  $D$ . The eigenvalues ( $\lambda_1, \lambda_2, \lambda_3$ ) of  $D$  represent the diffusivities along the three principal axes of the tensor, given by the eigenvectors ( $e_1, e_2, e_3$ ), where the eigenvector,  $e_1$ , associated with the largest eigenvalue,  $\lambda_1$ , defines the orientation of the tensor. In an anisotropic medium, the orientation of the tensor is taken to be aligned with the main fibre population orientation.

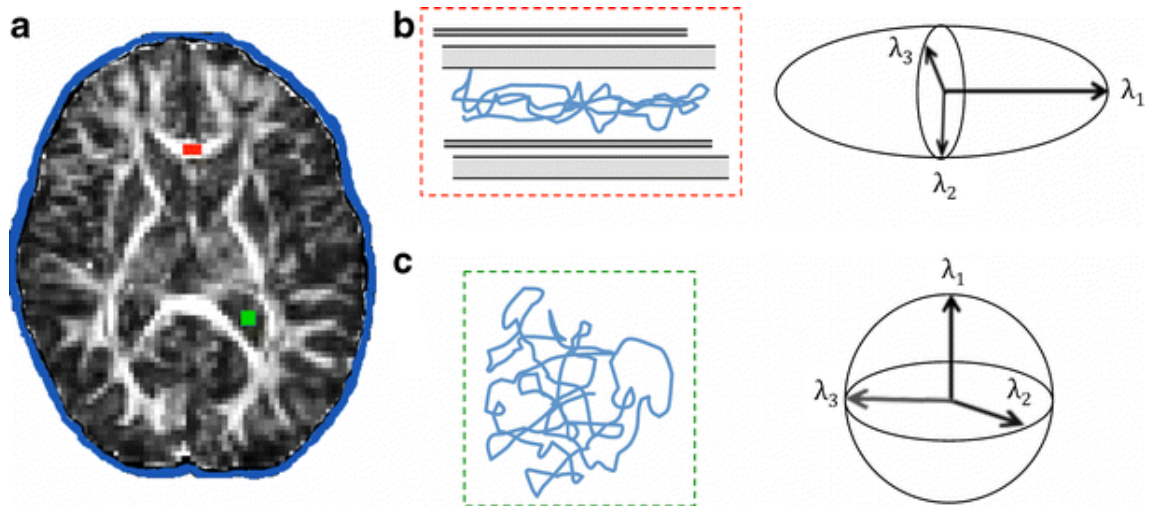


Figure 2.5 Isotropic and anisotropic diffusion in the brain. In the white matter of the corpus callosum (*red*), diffusion occurs preferentially along the axonal fibres, resulting in anisotropic diffusion (**b**). In the ventricular cerebro-spinal fluid (CSF; *green*), diffusion is unhindered and can be described as isotropic (**c**). Diffusion tensor ellipsoids representing anisotropic and isotropic diffusion are shown in **b** and **c**, respectively. Reproduced from Pandit et al. (2013).

The diffusion tensor provides scalar, rotationally invariant indices (Basser and Pierpaoli, 1996; Pierpaoli and Basser, 1996). Indices derived from  $\lambda_1, \lambda_2, \lambda_3$  are, by definition, independent of orientation. The magnitude of the diffusivity along the main fibre orientation as estimated by DTI is given by  $\lambda_1$ , termed the axial diffusivity (AD). The average of the other two eigenvalues, the radial diffusivity (RD), give the magnitude of diffusivity across the fibres. The mean diffusivity (MD) is the average of all three eigenvalues and provides a measure of the overall diffusivity within a



voxel. Fractional anisotropy (FA) is the variance of the three eigenvalues normalised by the magnitude of the tensor; normalising by the magnitude of the tensor accounts for differences in the overall magnitude of diffusivity within a voxel. FA takes values between 0 and 1, and measures the degree to which diffusion within the voxel is isotropic. FA is given by

$$FA = \sqrt{\frac{3}{2} \frac{\sqrt{(\lambda_1 - \bar{\lambda})^2 + (\lambda_2 - \bar{\lambda})^2 + (\lambda_3 - \bar{\lambda})^2}}{\sqrt{\lambda_1^2 + \lambda_2^2 + \lambda_3^2}}}$$

where  $\bar{\lambda}$  is the average of the three eigenvalues.

While DTI has proven to be a powerful technique for studying the brain, a major limitation is that it is only able to depict a single fibre orientation within a voxel. DTI fails to represent appropriately the tissue microstructure in the presence of crossing fibres and DTI-derived measures lack tissue specificity as multiple microstructural features can affect them. Moreover, in a restricted environment, diffusion is no longer Gaussian and the tensor model deviates from the signal.

#### 2.3.4 Compartment models of microstructure

Compartment models provide a biophysical interpretation of the diffusion-weighted signal and attempt to characterise the complexity of cerebral tissue by decomposing the signal into compartments describing diffusion within distinct microstructural constituents.

Stanisz et al. (1997) first introduced the three-compartment model comprising a restricted intra-axonal compartment, anisotropic hindered extra-axonal compartment and a restricted isotropic compartment describing diffusion within cellular structures such as glial cells. Behrens et al. (2003) presented a method to account for multiple fibre populations using the ball and stick model where diffusion along axons is represented by sticks and outside the axons diffusion is an isotropic ball. CHARMED (Assaf and Basser, 2005) models the intra-axonal space using cylinders with a distribution of radii given by the  $\Gamma$ -distribution and extra-axonal space as tensor with a principle direction aligned with the cylinders. This was extended to provide an estimate of axon diameter in the AxCaliber framework (Assaf et al., 2008; Barazany et al., 2009). Alexander (2008) simplified CHARMED by using a single axon radius and symmetric tensor and was used in the ActiveAx framework to estimate axon diameter in biological tissue (Alexander et al., 2010; Dyrby et al., 2013) and axon diameter mapping in the presence orientation dispersion (Zhang et al.,

2011). Recent work shows that the gradient amplitudes attainable with current clinical scanners are not able to estimate axon diameter accurately (Drobnjak et al., 2016; Nilsson et al., 2017).

An in-depth study of compartment models was carried out by (Panagiotaki et al., 2012) to determine the necessary model components where multiple compartment representations are possible for diffusion signal in WM. Models for three compartments are explored. The intra-axonal compartment modelled as sticks (cylinders with zero radius), cylinders (with non-zero radius), or cylinders with a distribution of radii given by the  $\Gamma$ -distribution, the extra-axonal compartment modelled via variants of the tensor – an isotropic ball, a zeppelin (tensor with  $\lambda_2 = \lambda_3$ ) and fully anisotropic tensor ( $\lambda_1 > \lambda_2 > \lambda_3$ ); the restricted isotropic compartment represented by uniformly distributed sticks or cylinders, or a sphere with either zero or non-zero radius. The authors demonstrate that three-compartment models perform better than two compartment models, specifically non-zero radius cylinders to represent the intra-axonal compartment, anisotropic tensor model for the extra-axonal compartment, and sphere representation of the isotropic restricted compartment in fixed rat tissue, and was supported by results from in vivo human tissue (Ferizi et al., 2014).

Neurite orientation density and dispersion imaging (NODDI) (Zhang et al., 2012) simplified the model in (Zhang et al., 2011) to provide measures of neurite density and orientation dispersion. The model consists of three compartments modelling the intra-, extracellular and cerebrospinal fluid (CSF) environments. The intraneurite compartment captures the diffusion inside dendrites and axons, collectively termed neurites. The intraneurite compartment is modelled using sticks to represent unhindered diffusion along the neurites and highly restricted diffusion perpendicular the neurites. The orientation distribution can vary from highly parallel, reflecting the coherent organisation of WM fibres such as in the posterior limb of the internal capsule (PLIC) or the corpus callosum (CC), to highly dispersed, such as in regions of crossing fibres like the centrum semiovale or the complex configuration of the cortex. The Watson distribution is used to model the orientation distribution. The extraneurite compartment represents the space occupied by glial cells and neuronal somas (in grey matter), where diffusion is hindered. As the diffusion is not restricted, it is modelled as an anisotropic Gaussian distribution using a zeppelin. The CSF compartment is modelled as isotropic Gaussian diffusion. This modelled has been widely applied across neuroimaging studies, including in connectivity, WM and grey matter (GM) analysis of

preterm infants (Batalle et al., 2017; Eaton-Rosen et al., 2015; Melbourne et al., 2016). However, NODDI has yet to be applied to study typical development in healthy newborns.

More recently, Kaden et al. (2016a); (2016b) proposed a two-compartment model which uses the spherical mean of the diffusion signal over all gradient directions to fit microstructural parameters independent of fibre orientation, crossings and dispersion. Lampinen et al. (2017) used spherical tensor encoding to derive measures of microscopic anisotropic diffusivity, tissue mean diffusivity and free water diffusion, however the spherical tensor encoding technique required for this method is not yet applicable on most clinical systems. The DIAMOND model (Scherrer et al., 2016) combined compartmental and statistical modelling to represent restricted, hindered and isotropic compartments using three peak-shaped matrix-variate distributions. DIAMOND estimates the number of tissue compartments in each voxel and provides compartment-specific measures of FA, AD, RD, MD and a measure of heterogeneity within the compartment. This model was recently applied to assess cortical maturation in the preterm cortex demonstrating a decrease in the radial organisation of the cortex (Eaton-Rosen et al., 2017).

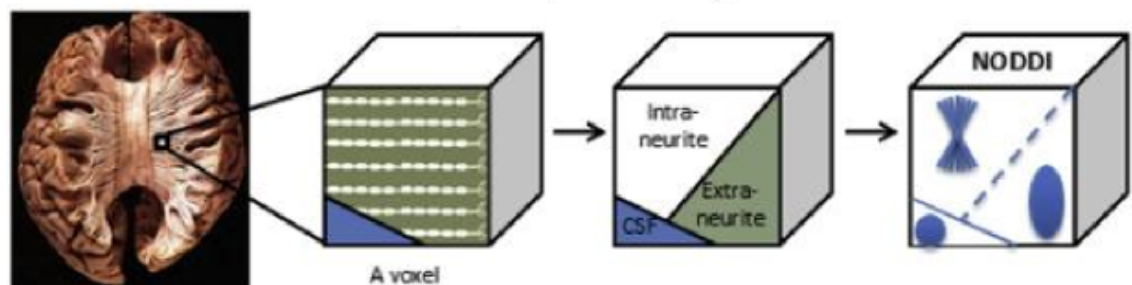


Figure 2.6 The three compartments of the NODDI model. Diffusion within the intraneurite compartment is restricted and modelled using sticks; diffusion within the extraneurite is hindered and modelled using a zeppelin; the CSF compartment of isotropic diffusion is modelled using an isotropic tensor. Adapted from Slattery et al. (2017).

### 2.3.5 Spherical deconvolution

Spherical deconvolution (SD) is a technique which estimates the fibre orientation distribution (FOD) in the presence of multiple fibre orientations (Alexander, 2005; Anderson, 2005; Dell'Acqua et al., 2007; Descoteaux et al., 2009; Tournier et al., 2004). It was initially introduced for single-shell high angular resolution diffusion imaging (HARDI) data (Tuch et al., 2002) and is able to estimate FODs regardless of the number of fibre populations within a voxel. It is assumed that

each fibre bundle has the same diffusion properties, apart from the orientation, and that no exchange occurs between bundles over the time-scale of DWI acquisition. The signal emanating from each fibre bundle is independent and they can be summed. The diffusion-attenuated profile for an anisotropic fibre bundle is represented by a response function. The response function is low amplitude along the axis where diffusion is high, and high amplitude in the radial plane, where diffusion is low. SD assumes a fixed response function, typically estimated from a region of highly anisotropic WM assumed to contain only a single fibre population. The signal measured can be expressed as the convolution of the response function and the FOD. Therefore, the FOD can be recovered using deconvolution. SD is an ill-posed problem and susceptible to noise, producing biologically implausible negative peaks. This problem was first tackled using a low-pass filter but this limited angular resolution (Tournier et al., 2004) and later, a non-negativity constraint was included, constrained SD (CSD), which prevented negative lobes in the FOD (Tournier et al., 2007). However, an inaccurate estimation of the response function can result in spurious peaks in the FOD (Parker et al., 2013). Dell'Acqua et al. (Dell'Acqua et al., 2007; Dell'acqua et al., 2010) presented an alternative CSD algorithm that was more robust to perturbations in the response function. Moreover, single-tissue SD does not account for partial volume effects from GM and CSF, which has been shown to affect up to half of all WM voxels (Roine et al., 2014). This produces spurious peaks in the FOD in the presence of CSF or GM. Exploiting the different diffusion dependencies of different tissues at multiple b-values multi-tissue CSD was introduced to derive tissue-specific response functions, where GM and CSF response functions are both isotropic, leading to improved estimation of the FOD (Jeurissen et al., 2014).

### **2.3.6 Apparent fibre density**

CSD has led to the development of fibre-bundle-specific measures. Raffelt et al. (2012b) introduced a measure of apparent fibre density (AFD) of individual fibre populations estimated from the FOD. AFD is based on the assumptions that the intra-axonal water is restricted in the direction perpendicular to the fibre orientation, the extra-axonal diffusion-weighted signal is attenuated at high b-values, and the diffusion-weighted signal from the restricted compartment is preserved under typical DW gradient pulse durations used in vivo. Consequently, the radial DW signal is approximately proportional to the volume of the intra-axonal compartment (Raffelt et al., 2012b). Since the FOD amplitude is proportional to the radial diffusion-weighted signal it provides a measure of fibre density determined as a proportion of the volume occupied by the fibre

population (Raffelt et al., 2012b), as illustrated by Figure 1.5. This measure would detect within-voxel changes related to the volume of restricted water along a specific direction. AFD also accounts for differences in macroscopic WM structure across subjects. FODs are modulated according to changes in local volume, such as expansion or contraction, that occur during registration. This presents a measure pertaining to both microscopic changes in fibre density and macroscopic morphological changes that occur across voxels.

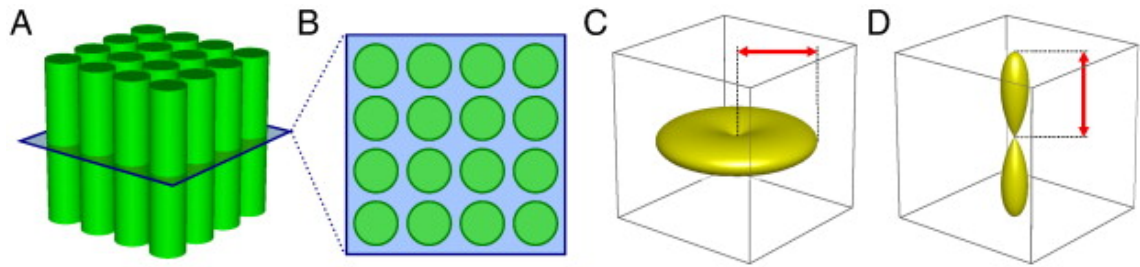


Figure 2.7 A single fibre population within a voxel (A, B) and the expected diffusion-weighted signal profile (C) and the associated FOD. The FOD amplitude is proportional to the radial signal profile and therefore the fibre density of the fibre population. Image adapted from Raffelt et al. (2012a).

Raffelt et al. (2017) makes a distinction between the changes in microstructure that occur within a voxel and the macroscopic changes in morphology that occur across voxels. They introduced a measure of fibre density (FD) derived solely from unmodulated FOD amplitude so as to describe changes in WM microstructure without the effects of macroscopic morphological changes. Changes in WM microstructure which would result in a reduction in FD can be visualised in Figure 2.8a. Nonetheless, macroscopic alterations in morphology are likely to occur across WM during development, as depicted in Figure 2.8b, and need to be accounted for.

In addition to FD, Raffelt et al. (2017) provide a measure of macroscopic differences in morphology based on the local deformations that are applied during registration. Changes in brain morphology have previously been investigated using voxel-based morphometry (VBM) (Ashburner and Friston, 2000) and tensor-based morphometry (Gaser et al., 2001; Leow et al., 2006). Local changes in volume can be investigated using the information from a subject's nonlinear deformation to a template. At each voxel, the determinant of the Jacobian describes the expansion or contraction of the subject image relative to a target. This method focuses on the changes in fibre bundle that occur perpendicular the main fibre orientation as a reduced fibre

bundle cross-section would imply a reduced number of axons as illustrated in Figure 2.8b. Using FOD registration, it is possible to assess changes in volume with respect to specific fibre orientations. This provides a fibre bundle-specific measure of fibre cross-section (FC) based on the Jacobian determinant following registration of FOD images.

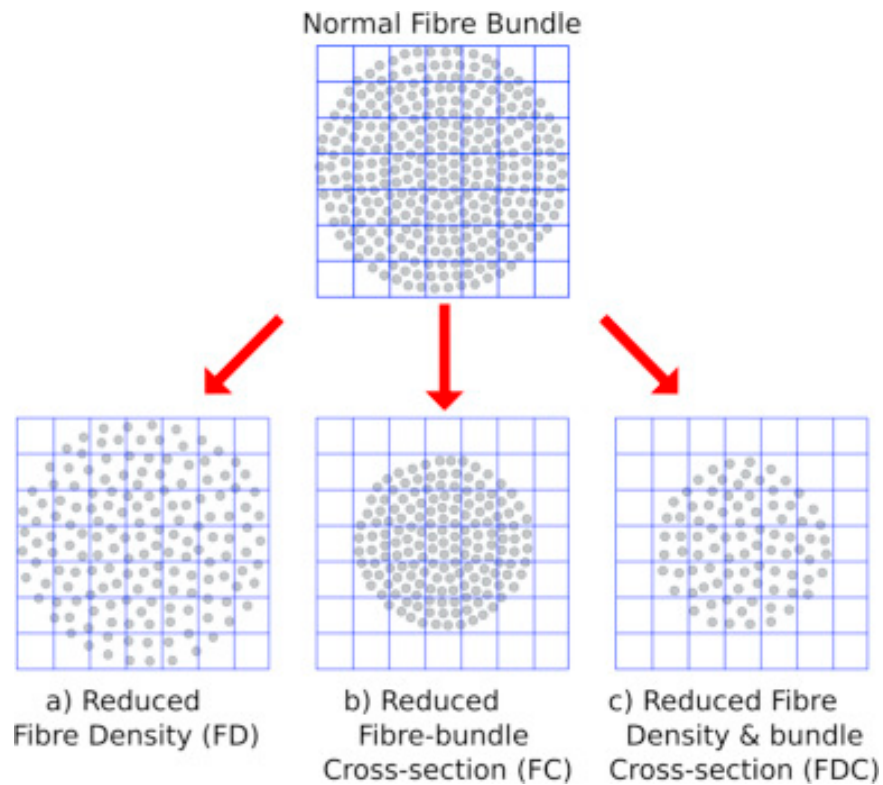


Figure 2.8 A schematic representation of a fibre bundle cross-section made of numerous axons (grey circles) Anterior commissures voxels represented by the grid. Panels (a), (b) and (c) describe three different ways in which a fibre bundle can change: (a) a reduction in within-voxel fibre density; (b) a macroscopic change in fibre-cross section across voxels; (c) a combination of reductions in both fibre density and cross-section. Image adapted from (Raffelt et al., 2017).

A similar measure based on FOD amplitude is the hindrance modulated orientational anisotropy (HMOA) index. HMOA is calculated as the absolute amplitude of each FOD lobe normalized to the highest FOD amplitude measurable in a biological sample (Dell'Acqua et al., 2013). This provides a measure of radial diffusion hindrance and fibre-bundle-specific anisotropy.

### 2.3.7 White matter analysis

#### 2.3.7.1 Diffusion tractography

Tractography is used to delineate WM pathways throughout the brain. As water molecules diffuse preferentially along the length of WM fibre it is possible to infer the trajectory of WM tracts. The

first implementations were based on the DT model and implemented a deterministic approach (Basser et al., 2000; Conturo et al., 1999; Jones et al., 1999; Mori et al., 1999; Poupon et al., 2000). In these methods WM fibres are traced by tracking along the direction of principal diffusion. Tracking is initiated at the centre of a voxel and the streamline propagates along the direction of the largest eigenvector for a given step-size and the orientation is estimated at the new location. Tracking terminates when a region of low anisotropy, below a predefined threshold, is encountered or an angle greater than a given curvature threshold. The dependence on anisotropy can mean that reliable tracking in the neonatal brain can be difficult due to the lower FA in neonates compared to the adult brain. Inherent noise and the presence of complex fibre configurations mean that errors in the estimation of the fibre direction will be propagated along a streamline, resulting in potentially incorrect reconstructions of WM tracts (Jones, 2003).

Probabilistic tractography methods were developed to quantify the uncertainty associated with fibre tracking and by using models that allow for multiple fibre estimates which can track through regions of crossing fibres (Behrens et al., 2007; Behrens et al., 2003; Parker and Alexander, 2005; Parker et al., 2003; Tournier et al., 2003). Multiple streamlines are propagated from a seed region within a voxel along a direction selected at random from a distribution of possible directions. Regions through which a high density of streamlines pass are considered more likely to be connected to the seed-point.

Both deterministic and probabilistic tractography techniques have been used in neonatal populations to delineate tracts of interest. Tracts can be segmented by specifying regions of interest (ROIs) as start, end and waypoints for streamlines to pass through. This can be done manually or using automated methods. Manually drawn ROIs in the infant's native space have been used with probabilistic tracking algorithms (Bassi et al., 2011; Bassi et al., 2008; Counsell et al., 2007) and with deterministic tractography (Adams et al., 2010; Dubois et al., 2006), or both (Berman et al., 2005). A number of automated methods have been used to segment tracts, such as ROIs defined in a group-averaged template and propagating these to each subject's tensor images (Lebel et al., 2008), using a WM atlas (Aeby et al., 2009), and using cortical parcellations on structural MRI propagated to diffusion space as start and end points (Pandit et al., 2014; Pannek et al., 2010; Robinson et al., 2010).

The major limitation of deterministic tractography implemented using the principal direction of the diffusion tensor is the inability to track more than a single fibre orientation within a voxel. As discussed previously, this is problematic in regions of crossing fibres. Using probabilistic tractography with DTI data can to some extent alleviate this restriction by allowing for multiple streamlines to track from a single seed point and capture more dispersed trajectories (Jones, 2008). When HARDI data is available, multiple fibre populations can be resolved, and probabilistic CSD tractography has been successfully applied in neonatal populations to resolve complex WM configurations such as cerebellar tracts (Pieterman et al., 2017).

### **2.3.7.2 Skeletonisation methods and fibre clustering**

Tract-based spatial statistics (TBSS) (Smith et al., 2006) is an automated multi-subject whole-brain WM analysis method. It was introduced to overcome difficulties in achieving anatomical correspondence across subjects while carrying out whole-brain analysis without the need for spatial smoothing. Each subject's FA images are nonlinearly aligned and averaged together to create a mean FA map. The mean FA image is skeletonised so that WM tracts are represented by a line or surface. This dimensionality reduction reduces the problem of multiple comparisons during statistical analyses. Skeletonisation is achieved by non-maximum-suppression in the direction perpendicular to local tract orientation. The skeleton produced consists of the voxels with maximum FA values, corresponding to the centre of WM tracts. Each subject's FA values are then projected onto the skeleton. This is done by searching within each subject's FA map for the closest maximum FA in the direction perpendicular to the skeleton. This projection step is to correct for any remaining misalignment between the centre of WM tracts in the subject and the FA skeleton. After data projection, statistical analysis is performed on the skeleton. TBSS has been used in a number of developmental studies (Anjari et al., 2007; Ball et al., 2010; Counsell et al., 2008; Rose et al., 2008; van Kooij et al., 2012b). Other methods have also taken similar dimensionality reduction approaches (Corouge et al., 2006; Goodlett et al., 2009; O'Donnell et al., 2009; Verde et al., 2014) with applications to paediatric populations (Feldman et al., 2012; Gilmore et al., 2007a; Yeatman et al., 2012). However, unlike TBSS's whole-brain approach, these methods construct single tract skeleton representations of WM fasciculi as a single arc. Tract-specific analysis (TSA) (Yushkevich et al., 2008), on the other hand, represents individual WM tracts as surfaces. WM tracts are modelled using continuous medial representations (cm-rep), which define each tract's skeleton as a medial surface. The cm-rep model is described by a



coordinate system where each point has a position, and radius value describing tract thickness defining the tract boundary and diffusion data is projected onto the skeleton. Statistical analysis is carried out on the skeleton similar to TBSS.

#### **2.3.7.3 Region of interest analysis**

A commonly employed technique for WM analysis in neonatal studies is the manual delineation of ROIs (Bartha et al., 2007; Gao et al., 2009; Huppi et al., 1998a; Mukherjee et al., 2002; Partridge et al., 2004). ROIs produce accurate segmentations of anatomical structures; however, this requires expert knowledge of brain anatomy and can be time-consuming, especially if studying a large cohort and/or multiple structures. Furthermore, this technique is entirely dependent on the operator and therefore susceptible to bias and reproducibility errors (Pannek et al., 2012).

#### **2.3.8 Image registration**

Image registration is a key step in many group analyses of diffusion-weighted images. To localise WM differences, images must be brought into a common space to ensure anatomical correspondence across subjects. Removing inter-subject differences in shape and size ensures the remaining differences between subjects represent variation in diffusion properties. Therefore, WM analyses depend on the successful alignment of WM tracts and the quality of registration affects the extent to which results are driven by genuine group differences or misalignments.

Most registration algorithms for diffusion-weighted images can be categorised into one of two groups. One approach uses scalar values such as FA or T1/ T2 intensities (Avants et al., 2008; Jenkinson et al., 2012; Rueckert et al., 1999), and the other uses higher-order information from the diffusion tensor, such as the principal eigenvector or full tensor information (Geng et al., 2010; Van Hecke et al., 2007; Xu et al., 2003; Yeo et al., 2009; Zhang et al., 2006). Registration based on rotationally invariant scalar indices such as FA avoids the complicated but necessary step of reorienting the diffusion data. The need for tensor reorientation to maintain anatomical consistency between adjacent structures is illustrated by Figure 2.9. However, using diffusion tensors for registration was shown to improve registration overall (Park et al., 2003) and explicit optimisation of tensor reorientation further improves alignment (Zhang et al., 2006) and detection of WM differences (Zhang et al., 2007).

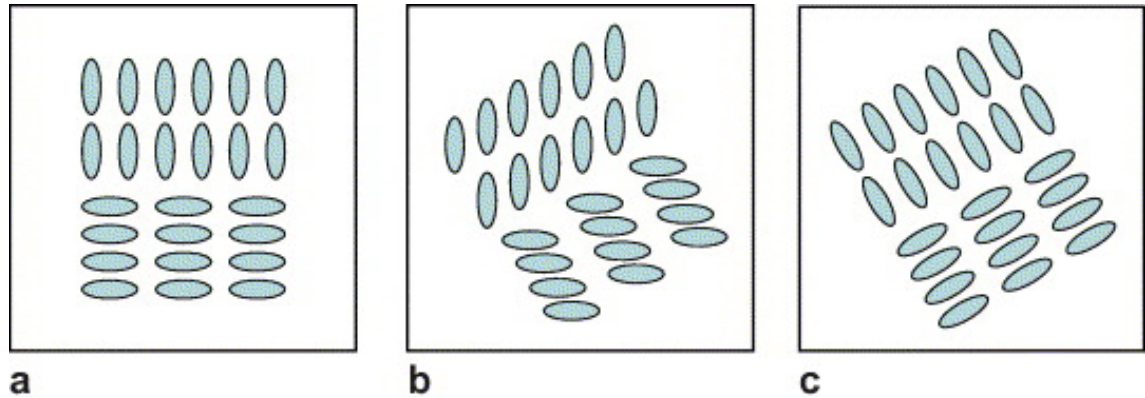


Figure 2.9 A schematic which illustrates the need for tensor reorientation. Panel (a) shows an anisotropic region of a diffusion tensor image. Panel (b) shows the same slice after a  $30^\circ$  rotation about the z-axis with no reorientation of the diffusion tensors. Panel (c) shows the slice after the same rotation, but with each tensor transformed by the same rotation. Image reproduced from Zhang et al. (2007)

More recently Raffelt et al. (2011) introduced FOD registration to overcome the limitation of DTI in regions of crossing fibres by leveraging crossing fibre information. FOD registration improved inter-subject spatial alignment over FA based registration, however this study did not include a comparison with tensor-driven registration algorithms.

Neonatal dMRI data presents a specific challenge due to the lower resolution and contrast compared with adult data. Few studies have directly assessed the performance of different registration algorithms in neonatal populations. Ball et al. (2010) demonstrated that introducing an additional 6 degrees-of-freedom linear registration prior to affine and nonlinear warps and registering to a study-specific group-average template improved alignment in preterm neonates when using the FA-based FNIRT algorithm. Wang et al. (2011) evaluated the performances of eight registration algorithms in a population of neonates with infantile Krabbe disease and demonstrated that the tensor-based DTI-TK registration, based on the algorithm in (Zhang et al., 2006), outperformed other scalar- and tensor-based techniques. However, this study only included 10 subjects and assessed alignment in only 4 WM regions.

## **Chapter 3 The Developing brain**

This chapter provides an overview of brain maturation, discusses the impact of preterm birth on brain development and on neurodevelopmental outcome, and describes the use of MRI to study neonatal populations.

### **3.1 Normal brain development**

During the first half of gestation, human brain development is characterised by neuronal proliferation and migration. During the second half of gestation the transient laminar zones of the foetal brain reorganise into permanent cortical pathways. Cellular proliferation occurs initially around 2 months gestation; neuronal and radial glia proliferation peaks between 3-4 months and glial multiplication begins around 5 months gestation and continues well after birth, beyond the first year of life. Neurons produced in the ventricular zone (VZ) and subventricular zone (SVZ) migrate to the cortical plate (CP) via the subplate (SP). Neuronal migration peaks between 12-20 weeks of gestation (de Graaf-Peters and Hadders-Algra, 2006). Around the 20<sup>th</sup> week of gestation the laminar structures of the foetal brain are (from the ventricles to the pia) the VZ, SVZ, intermediate zone (IZ), SP and the CP (Kostovic and Jovanov-Milosevic, 2006).

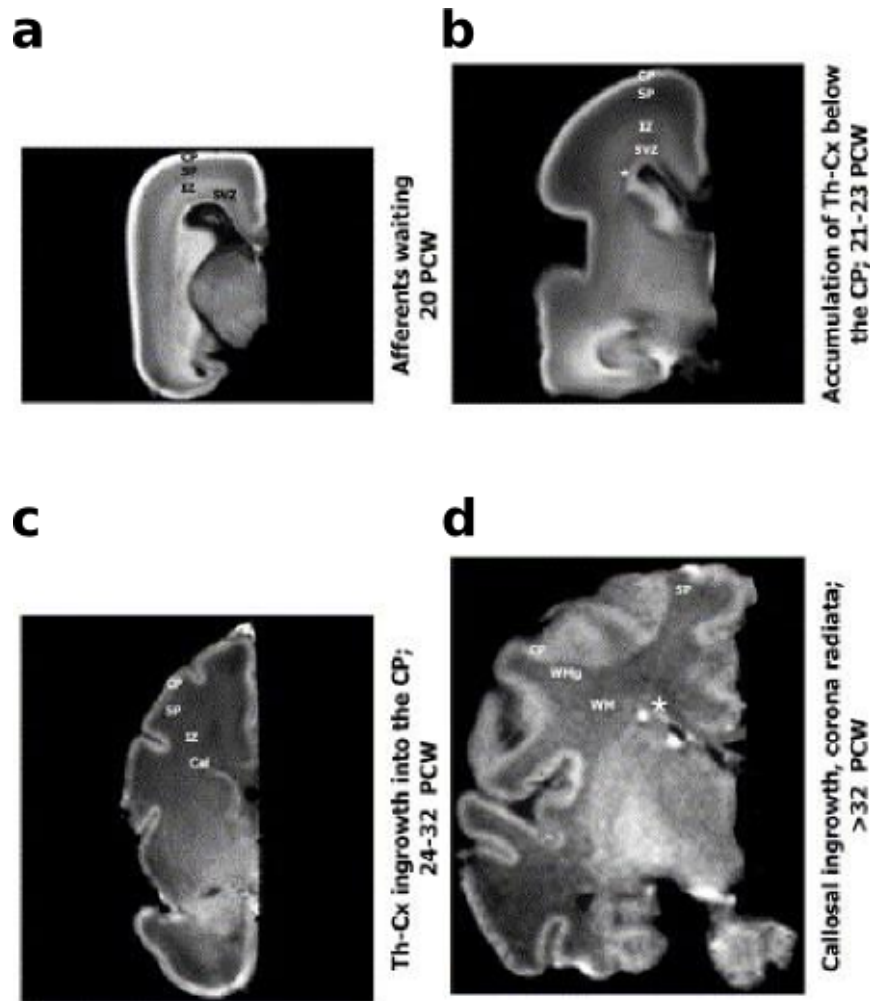


Figure 3.1 Transient fetal organization of the developing cerebral wall during the 20<sup>th</sup> post-conception week (a), 21<sup>st</sup>-23<sup>rd</sup> post-conception weeks (b), 24<sup>th</sup>-32<sup>nd</sup> post-conception weeks (c) and after the 32<sup>nd</sup> post-conception week (d) on a T1-weight image. CP = cortical plate; SP = subplate zone; IZ = intermediate zone; SVZ = subventricular zone, WM = white matter; WMg = gyral white matter. Image modified from Figure 1 in Kostovic and Jovanov-Milosevic (2006).

These zones are visible on conventional and diffusion MR imaging (Figure 3.1 and Figure 3.2) (Huang et al., 2009; Huang et al., 2006; Kostovic and Jovanov-Milosevic, 2006; Maas et al., 2004). The SP is the thickest of these zones (Kostovic et al., 2002), where afferent fibres 'wait' prior to growing into the CP. It is characterised by migratory neurons, axons, and glial cells within a hydrophilic extracellular matrix (Kostovic and Judas, 2010). The central and periventricular regions contain crossing thalamocortical, corticofugal, callosal and association fibres (Judas et al., 2005). Towards 24 weeks gestation, thalamocortical afferent neurons have passed through the PLIC and through the periventricular crossroads and IZ to the superficial part of the SP where they wait before entering the CP (Kostovic and Jovanov-Milosevic, 2006). Neuronal differentiation and synaptogenesis first occur in the SP and continue in the CP (Kostovic and Judas, 2006). Between the 24<sup>th</sup> and 32<sup>nd</sup> weeks of gestation the thalamocortical afferents reach the CP. After the 25<sup>th</sup> week, the VZ and SVZ decrease substantially (Vasung et al., 2016). Synapses appear in

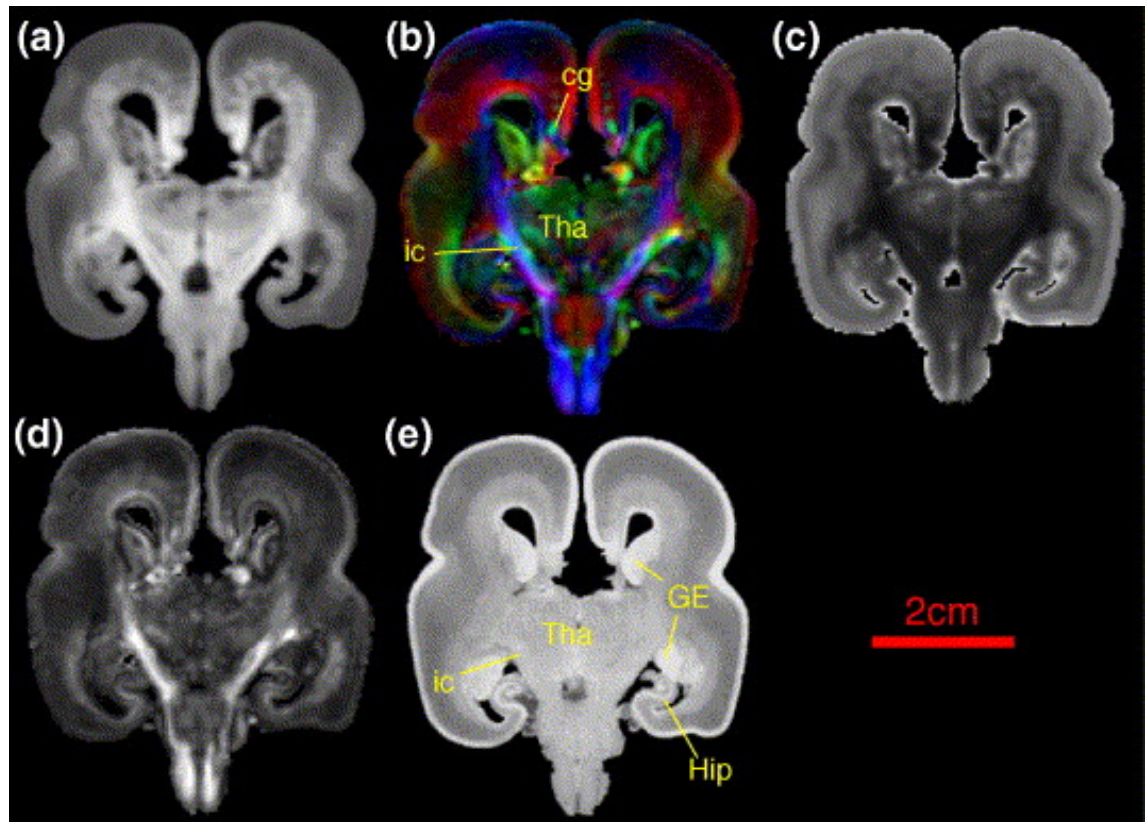


Figure 3.2 MRI of 19 gestational week post-mortem foetal brain. (a) Average diffusion-weighted image, (b) color-coded orientation map (red: right-left, green: anterior-posterior, blue: superior-inferior orientations), (c) ADC map, (d) FA map, and (e) T1-weighted image. Cg = cingulum; ic = internal capsule; GE = ganglionic eminence; Hip = hippocampus; Tha = thalamus. Image reproduced from Huang et al. (2006)

the CP between 26 and 28 weeks gestation (Kostovic and Judas, 2010). Dendritic differentiation and the formation of synapses within the CP establish the permanent thalamocortical pathways in the brain.

As commissural, projection and association fibres proliferate into the CP, the SP decreases after 31 weeks (de Graaf-Peters and Hadders-Algra, 2006) and the laminar structures disappear towards term. During this period the supratentorial brain volume increases 4-fold and growth rate is fastest in the CP (Scott et al., 2011). The ventricles also decrease with respect to total cerebral volume. Primary sulci and gyri appear around 31–34 weeks gestation (Kostovic et al., 2014a) and the CP begins to differentiate into the six cortical layers. Between 35 and 37 weeks there is a period of growth of interhemispheric connections, followed by the growth of long range intrahemispheric connections. There is an over-production of interhemispheric axons and axonal

branches prenatally (Innocenti and Price, 2005). This is followed by axonal pruning in the CC during the first and second postnatal months (Kostovic and Jovanov-Milosevic, 2006). Also during the first postnatal month, short cortico-cortical connections develop and there is an increase in the number of cortical synapses (Kostovic and Jovanov-Milosevic, 2006).

Myelination is an important part of WM maturation. Processes of mature oligodendrocytes wrap around axons to increase the conduction velocity of electrical impulses. The myelin sheath is composite of multiple segments of oligodendrocyte processes and each oligodendrocyte can contribute myelin to an estimated 50 axons (Barkovich, 2000). Myelination follows a heterogeneous spatiotemporal pattern. The rostral brain stem, cerebellar peduncles and PLIC are myelinated at birth, the splenium of the CC and optic radiations begin myelinating shortly after, around 6 and 8 weeks post-term, respectively, and the frontal, parietal and occipital WM much later, between 8-12 months (Brody et al., 1987; Kinney et al., 1988; Paus et al., 2001; Yakovlev and Lecours, 1967). Myelin appears as high signal intensity on T1-weighted images and low signal on T2-weighted images (Figure 3.3).

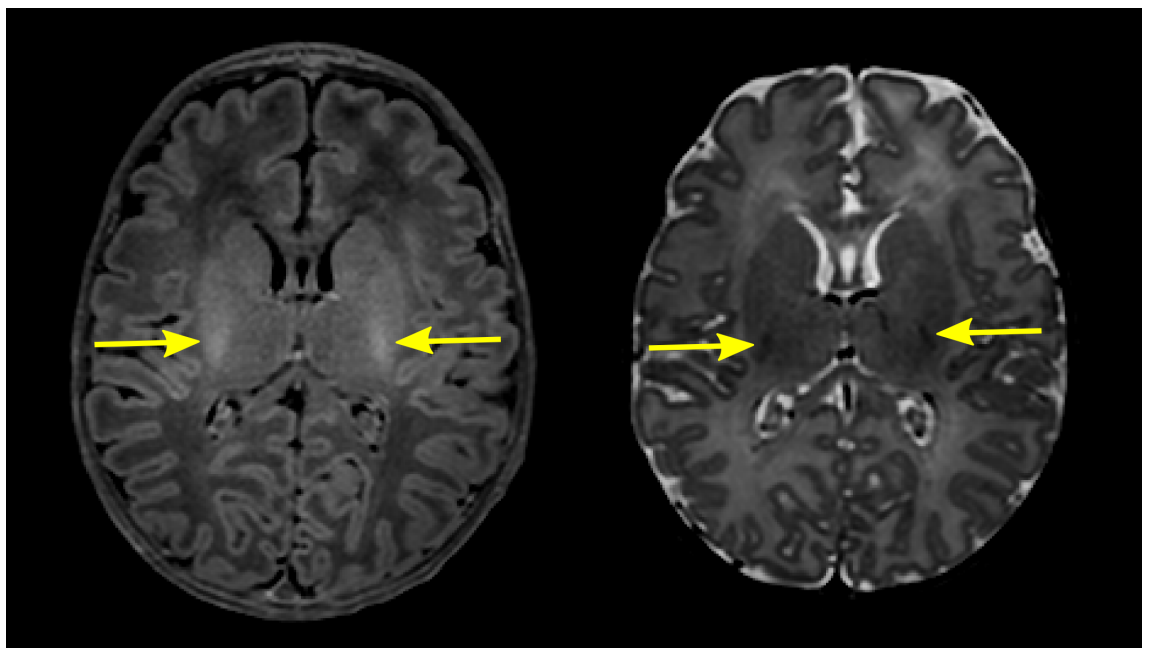


Figure 3.3 T1-weighted (left) and T2-weighted (right) images of an infant born at 39.6 weeks GA and imaged after 2 days. The yellow arrows indicate the posterior limb of the internal capsule, which is myelinated at term and is seen as high signal intensity and low signal intensity on the T1- and T2-weighted images, respectively.

## **3.2 Preterm birth**

### **3.2.1 Epidemiology**

Preterm birth is defined as birth before 37 weeks completed gestation. Preterm birth can be categorised according to gestational age; infants born at less than 28 weeks GA are considered extremely preterm, infants born between 28 and 32 weeks GA are considered very preterm, and infants born between 32 and 37 weeks are considered moderate to late preterm. More than 1 in 10 babies are born preterm around the world, and complications due to prematurity result in over 1 million neonatal deaths every year (Howson et al., 2013). In the UK, 8% of babies are born preterm, and this figure is rising, as is the incidence of preterm birth around the world (Beck et al., 2010; Blencowe et al., 2012). No clear aetiology has been identified, nonetheless several factors have been associated with increased risk of preterm birth. These include maternal history of preterm birth, multiple pregnancies, infection, genetic factors, and lifestyle-dependent factors such as excessive physical exertion, smoking, or alcohol consumption (Blondel et al., 2006; Gravett et al., 2010; Menon, 2008; Muglia and Katz, 2010; Plunkett and Muglia, 2008).

### **3.2.2 Developmental outcome following preterm birth**

There are an estimated 15 million preterm births worldwide every year (Blencowe et al., 2012), resulting in a huge, and increasing, disease burden (Murray et al., 2012). Improvements in neonatal care have led to a decrease in mortality (Stoll et al., 2015) and more infants are surviving without disability (Moore et al., 2012), however preterm infants are still at greater risk of neurodevelopmental impairments than their term counterparts (Rogers and Hintz, 2016; Saigal and Doyle, 2008). Cognitive, motor and language deficits in the preterm population result in substantial economic costs in terms of health-care and educational needs (Mangham et al., 2009), and significant personal costs for individuals and their families. The severity of disability increases with prematurity (Larroque et al., 2008) and adverse effects persist into adulthood (Bauml et al., 2017; Lindstrom et al., 2007). Morbidities often co-occur (Marlow et al., 2005a) and are likely to potentiate each other (Danks et al., 2017).

#### **3.2.2.1 Motor impairment**

Prematurity can present lasting significant motor impairments, with cerebral palsy being the most severe manifestation. The prevalence of cerebral palsy increases with decreasing gestational age

(GA); a meta-analysis by Himpen et al. (2008) reported the prevalence of cerebral palsy as 15% at 22–27 weeks, 6% at 28–31 and 1% at 32–36 weeks GA. Other risk factors include male sex, low birthweight and multiple births (Smithers-Sheedy et al., 2016). Overall rates of cerebral palsy have decreased (Platt et al., 2007; Reid et al., 2011) and this has been primarily due to the reduction of cystic periventricular leukomalacia (van Haastert et al., 2011). Nonetheless, motor impairments persist in the absence of cerebral palsy (Williams et al., 2010). Motor impairment within the preterm population range in types: fine and gross motor function, visuomotor integration, manual dexterity, ball skills, and balance skills (Cooke, 2005; de Kieviet et al., 2009; Goyen and Lui, 2002; Goyen et al., 1998; Marlow et al., 2007). Although the severity of these deficits is likely to be lesser than that experienced by children with cerebral palsy, it can adversely affect their self-esteem, peer relationships and academic achievement (Marlow et al., 2007)

### **3.2.2.2 Cognitive impairment**

Cognitive deficits following preterm birth vary in severity and across functional domains. While neonatal care for preterm infants has improved greatly, cognitive functional impairments persist. Increasing prematurity has detrimental effects on cognitive performance (Cooke, 2005; Joseph et al., 2016; Marlow et al., 2005b) and even late preterm infants perform worse than their term-born peers in cognitive assessment at preschool age (Shah et al., 2016; Spittle et al., 2017). Differences in executive function persist into adulthood (Allin et al., 2008; Lefebvre et al., 2005; Nosarti et al., 2007). In addition, preterm infants are also at higher risk of emotional and behavioural problems such as hyperactivity/inattention, emotional symptoms, and peer problems, which are also related to poor cognitive performance (Bhutta et al., 2002; Delobel-Ayoub et al., 2009; Hornman et al., 2016).

### **3.2.2.3 Language impairment**

Language ability can be impaired in individuals born preterm (Barre et al., 2011; Vohr, 2014). Increased prematurity has been associated with decreased language performance (Skiold et al., 2012) and preterm subjects perform worse than term born subjects (Allin et al., 2008; Doyle et al., 2010; Wolke and Meyer, 1999) even when controlling for IQ (Guarini et al., 2009). However, language and cognitive performance are interrelated and cognitive delay may account for language and phonetic deficits but probably not speech impairments (Wolke et al., 2008). Language development trajectories can vary during early childhood, however there is a positive



association between language abilities assessed at 2 and 4 years (Spencer-Smith et al., 2015), and the majority of children who score in the normal range at 3 years remain within the normal range at 5 years (Woods et al., 2014). Environmental factors such as socioeconomic status and maternal education become increasingly important to language development as children grow up (Reilly et al., 2010) and there is evidence that preterm adolescents have the potential to catch-up with term-born peers given a favourable socioeconomic status and in the absence of neurosensory disability (Luu et al., 2011).

#### **3.2.2.4 Neurosensory impairment**

Visual and hearing impairments can also occur as a result of prematurity. Retinopathy of prematurity (ROP) occurs due to aberrant retinal vascularisation and can lead to visual loss and, in extreme outcomes, blindness (Hellstrom et al., 2013). The risk factors are excessive oxygen, low GA, low birthweight and reduced postnatal growth (Chen and Smith, 2007; Klevebro et al., 2016). Other factors such as hypoxia, hypercarbia, nutritional deficits, intraventricular haemorrhage and acidosis can also increase the risk of ROP (Repka, 2002).

Auditory deficits can also occur. Hearing impairment requiring amplification is reported to affect 1–9% of extremely low birthweight infants (Rogers and Hintz, 2016; Vohr, 2016). The EPICure study reported that in a population of infants born at less than 25 weeks GA, 3% had sensorineural hearing impairment not amenable to correction with hearing aids, 3% had hearing impairment that could be corrected with hearing aids, and 4% had mild hearing impairment (Marlow et al., 2005b). Hearing loss can present extra challenges by adversely affecting language development (Tomblin et al., 2015), however early intervention can improve language skills (Vohr et al., 2008; Watkin et al., 2007).

#### **3.2.3 Preterm brain injury**

Brain development is determined by both genetic and environmental cues. Preterm birth disrupts the pattern of normal brain development and, in infants born preterm, many of the events described in Section 3.1 may occur ex utero. The timing of neurodevelopmental events render cerebral pathways vulnerable to injury. Volpe (2009b) introduced the term the encephalopathy of prematurity to capture the myriad of insults and developmental events that occur during brain development following preterm birth. Brain injury in preterm infants can include periventricular

leukomalacia, germinal matrix haemorrhage, haemorrhagic parenchymal infarct, intraventricular haemorrhage and impaired global WM and GM development (Volpe, 2009a) . Neonatal MRI provides a non-invasive method to investigate in vivo the effects of prematurity and injury on cerebral macro- and microstructure. .

### **3.2.3.1 Germinal matrix haemorrhage, intraventricular haemorrhage and haemorrhagic parenchymal infarction**

The germinal matrix is a highly vascular, periventricular region made up of glial and neuronal precursor cells. The germinal matrix has a rich capillary network. The inability to maintain stable cerebral blood flow and the vulnerability of the germinal matrix mean the preterm brain is particularly vulnerable to haemorrhages within the first 48hrs of life (Ballabh, 2010). If a haemorrhage in the germinal matrix is substantial it may develop into intraventricular haemorrhage (IVH) and could result in ventricular dilation (Murphy et al., 2002). IVH is a common diagnosis in preterm infants, occurring in almost a third of infants (Radic et al., 2015b). The severity of IVH can be graded with Papile's grading system, where Grade I refers to germinal matrix haemorrhage (GMH), Grade II to IVH without ventricular dilation, Grade III to IVH with dilation and Grade IV, shown in Figure 3.4, refers to when IVH leads to damage to neighbouring parenchyma (Papile et al., 1978). MRI studies have shown IVH can lead to reduced cortical GM volume (Vasileiadis et al., 2004) decreased cerebellar volumes (Peterson et al., 2000; Tam et al., 2011). Motor and cognitive abilities were positively correlated with total cerebral tissue volume, and cerebellar and thalamic volumes were positively correlated with motor performance in infants with IVH and ventricular dilation (Jary et al., 2012). Infants with grades I and II were shown to have lower FA in the superior cerebellar peduncles and the motor corticospinal tract (Morita et al., 2015). The incidence of cerebral palsy, deafness, and blindness has been shown to be higher in infants with IVH grades III and IV compared with infants with IVH grade I and II and infants without IVH in a cohort of preterm infants born between 24-28 weeks (Bolisetty et al., 2014; Radic et al., 2015a). Poorer developmental scores are related to increasing grade of IVH (de Vries and Groenendaal, 2002; Klebermass-Schrehof et al., 2012) however, even low grades of IVH can have a detrimental impact on neurodevelopment (Klebermass-Schrehof et al., 2012; Patra et al., 2006).

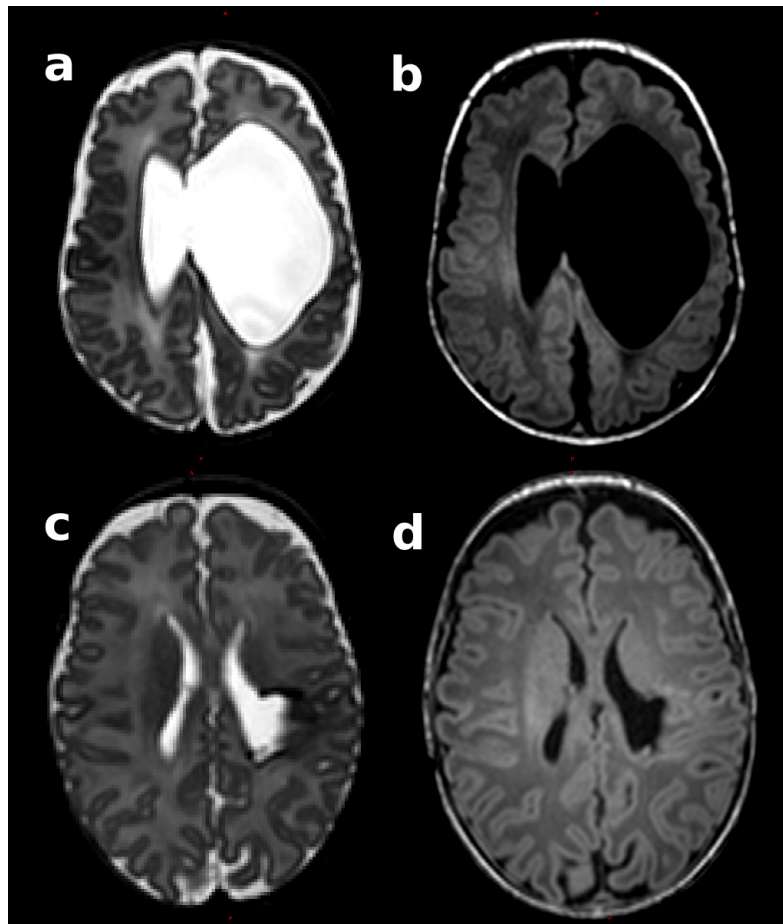


Figure 3.4 Haemorrhagic parenchymal infarct (HPI) in two preterm infants. The top row shows axial T2- (a) and T1-weighted (b) images of an HPI in an infant born at 25.7 weeks GA and imaged at 41.6 weeks PMA. The bottom row shows axial T2- (c) and T1-weighted (d) images of an HPI in an infant born at 30.0 weeks GA and imaged at 42.4 weeks PMA.

### 3.2.3.2 Periventricular leukomalacia

Although there has been a decline in the incidence of cystic periventricular leukomalacia (PVL), it remains the most severe type of injury within the preterm population leading to major motor and cognitive deficits (Hamrick et al., 2004; van Haastert et al., 2011; Volpe, 2001, 2003). The causes of PVL include ischemia, inflammation, intrauterine infection, excitotoxicity, and free-radical attack (Dammann and Leviton, 1997; Khwaja and Volpe, 2008; Resch et al., 2000; Rezaie and Dean, 2002; Saliba and Marret, 2001). PVL is characterised by two components – focal necrosis in the periventricular WM, and a diffuse component of injury to premyelinating oligodendrocytes across the central WM (Volpe, 2009b). The necrotic foci may be macroscopic and visible on conventional MRI and ultrasound, and can evolve into cystic lesions, leading to cystic PVL. When the necroses are microscopic and not visible using imaging, they often form glial scars in the absence of macroscopic cysts, this is termed non-cystic PVL (Volpe, 2009a). The diffuse component is

marked by astrogliosis, microgliosis (Volpe, 2009b) and a loss of oligodendrocyte progenitor processes (Billiards et al., 2008). Disruptions to oligodendrocyte maturation result in subsequent impaired myelination.

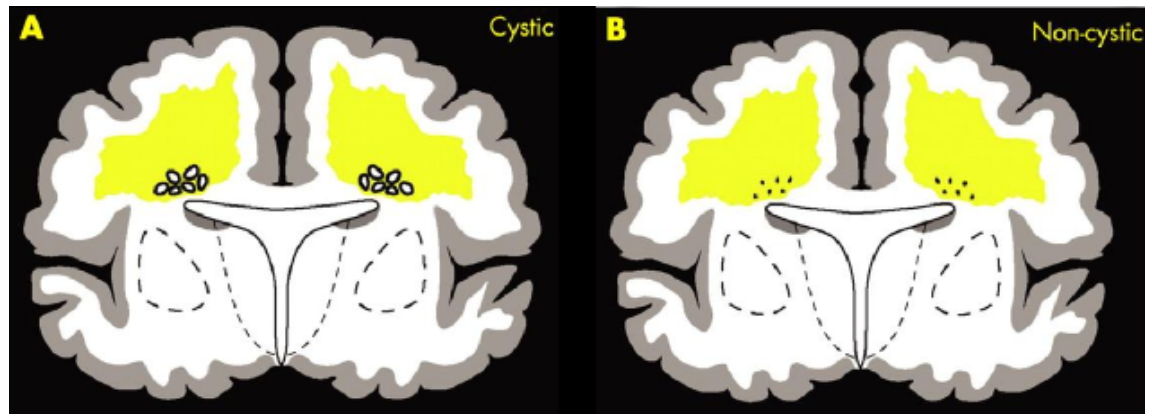


Figure 3.5 Schematic diagram of cystic (A) and non-cystic (B) periventricular leukomalacia exhibit, demonstrating the two component of PVL focal necrosis deep in the white matter and more diffuse injury characterised by a loss of pre-oligodendrocytes and marked astrogliosis. Image modified from Figure 1 in Khwaja and Volpe (2008)

Premyelinating oligodendrocytes are particularly susceptible to injury (Volpe et al., 2011). Injury to premyelinating oligodendrocytes can be acute, comprising of cell death. (Back et al., 2005; Bell et al., 2005; Haynes et al., 2003). Late oligodendrocyte progenitors are distinctly vulnerable to hypoxia-ischemia and inflammation whereas cells in the earlier and later stages of the oligodendrocyte lineage are more robust (Back and Miller, 2014). This results in a defective regeneration response of oligodendrocytes. Following the degeneration of some late oligodendrocyte progenitors, surviving oligodendrocyte progenitors proliferate and replenish the depleted cells. However the regenerated late oligodendrocyte progenitors lack processes and the capacity to differentiate into mature myelin-producing cells (Back and Miller, 2014; Billiards et al., 2008; Buser et al., 2012).

Volumetric MRI studies have shown that PVL is accompanied by volume loss in the CC, thalamus, basal ganglia, cortex and cerebellum (Andiman et al., 2010; Argyropoulou et al., 2003; Inder et al., 1999; Kersbergen et al., 2015; Lee et al., 2011; Lin et al., 2001; Pierson et al., 2007). dMRI studies have shown PVL results in reduced FA in the corticospinal tract and thalamus. Kersbergen et al. (2015) found reduced FA in the corticospinal tract and reduced thalamic volumes in preterm infants with cystic PVL compared with preterm infants without focal brain injury and normal motor

performance at 15 months. Nagasunder et al. (2011) observed reduced volume and FA in the thalamus in preterm born children with PVL compared with term-born children. DTI studies have reported that WM FA values are related to motor ability in preterm survivors with PVL. Lower FA in the posterior CC and corticospinal tract was associated with greater motor dysfunction in adults and children with PVL (Lee et al., 2011), and FA values were significantly lower in the corticospinal tract in toddlers with cerebral palsy compared with non-impaired toddlers (Murakami et al., 2008).

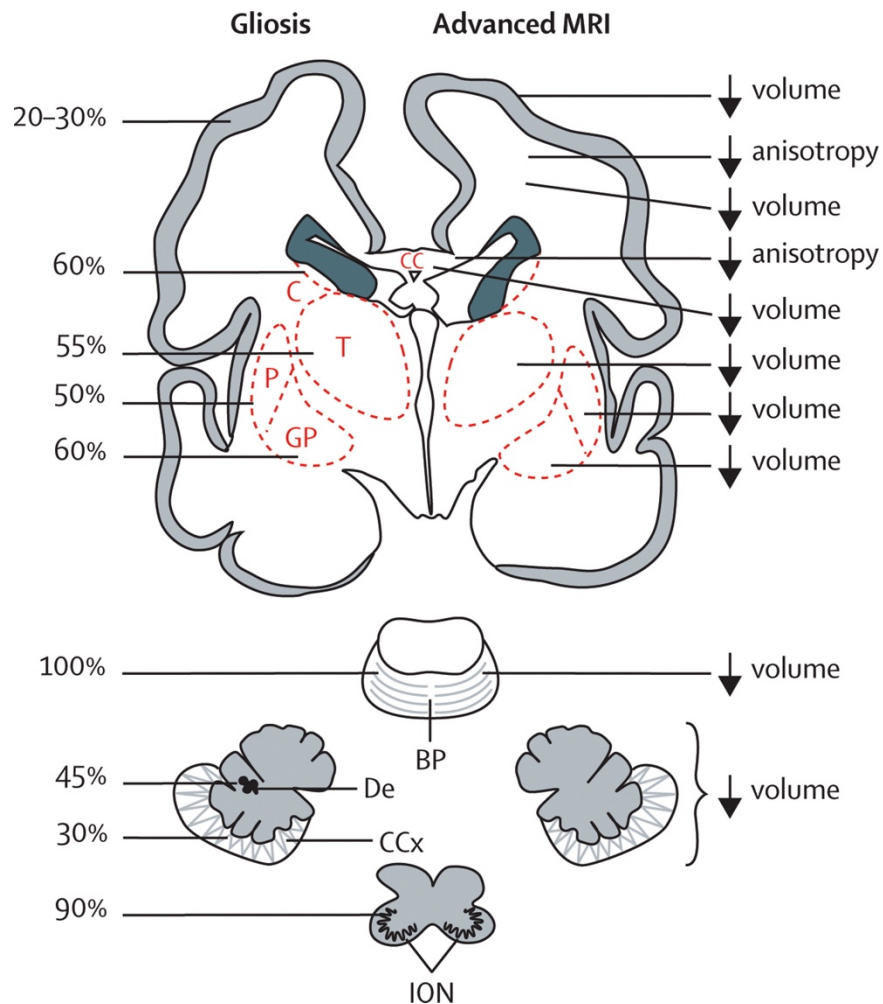


Figure 3.6 Main structures affected in premature infants with periventricular leukomalacia. Coronal sections of the cerebrum, pons, cerebellum, and medulla (inferior olivary nuclei) are shown. The left side shows the frequency of gliosis detected by neuropathological studies. The right side shows the major abnormalities detected by volumetric and diffusion-based MRI. BP =basis pontis. C=caudate. CC=corpus callosum. CCx=cerebellar cortex. De=dentate. GP=globus pallidus. ION=inferior olivary nuclei. P=putamen. T=thalamus. Reproduced from Volpe (2009a).

The occurrence of lesions in the periventricular parenchyma during the early preterm period may affect any combination of callosal, associative, thalamocortical or projection fibres as these fibres all traverse this region. Lesions affect growing axons and also the cells responsible for axonal

guidance to specific regions of the brain (Kostovic and Judas, 2006) and cell proliferation and migration (Kostovic et al., 2014b). Acute damage to cells may disturb the axonal guidance and the formation of appropriate cerebral connections.

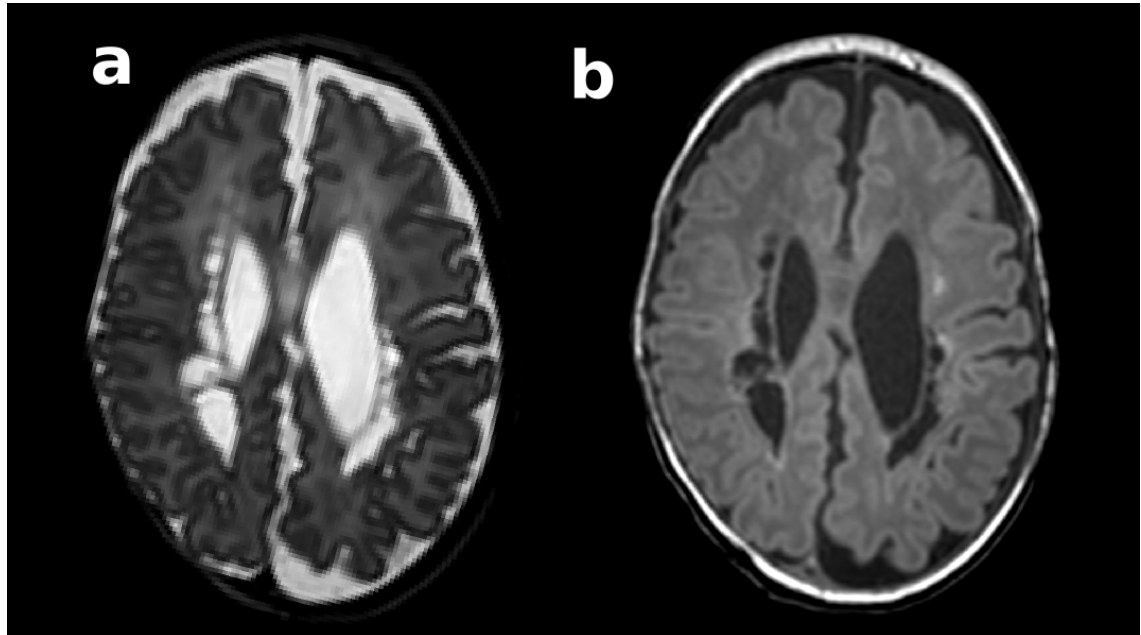


Figure 3.7 Cystic PVL in a preterm infant. Axial T2- (a) and T1-weighted (b) images of an infant born at 31.2 weeks GA and imaged at 42.7 weeks PMA.

### 3.2.3.3 Punctate lesions

Punctate lesions commonly occur in preterm infants (Childs et al., 2001; Dyet et al., 2006; Inder et al., 2003; **Leijser** et al., 2009; Ramenghi et al., 2007). They can be identified as high signal intensity on T1-weighted MRI and low-signal intensity on T2-weighted MRI, as shown in Figure 3.8. These lesions often occur in the centrum semiovale, corticospinal tract, optic radiations and posterior periventricular WM (Bassi et al., 2011; Cornette et al., 2002; Dyet et al., 2006; Groppo et al., 2014; Kersbergen et al., 2014a; Wagenaar et al., 2017). Punctate lesions result in reduced FA beyond the spatial extent of the lesions themselves (Bassi et al., 2011; Li et al., 2017; Tusor et al., 2017), and have been associated with impaired myelination and cortical folding (Ramenghi et al., 2007) and reduced thalamic volume (Tusor et al., 2017; Wisnowski et al., 2015). The aetiology and clinical significance of punctate lesions remain unclear. Some studies show that developmental impairments were associated with the presence of six or more lesions (de Bruine et al., 2011a; Miller et al., 2003; Sie et al., 2005), however some studies did not observe an association between punctate lesions and outcome (Cornette et al., 2002; Kersbergen et al.,

2014a). Tusor et al. (2017) reported that motor disability was more common in infants with punctate WM lesions observed predominantly in the centrum semiovale and corona radiata, compared to infants without lesions, while punctate lesions in the frontal WM have been associated with impaired cognitive outcome at 18 months (Guo et al., 2017).

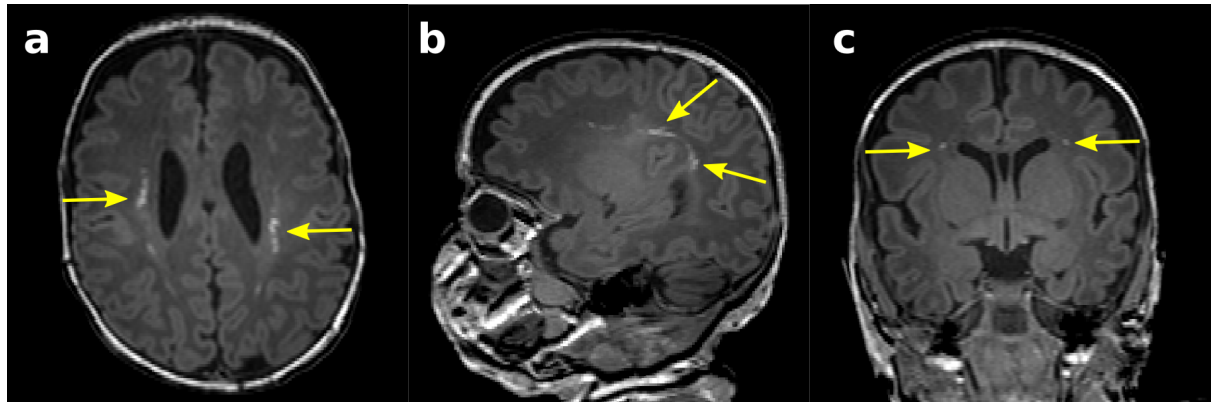


Figure 3.8 Punctate lesion in an infant born at 28.9 weeks GA and imaged at 41. 6 weeks PMA, shown on T1-weighted image in the axial (a), sagittal (b) coronal view (c).

#### 3.2.3.4 Grey Matter Injury

Prematurity has been associated with abnormal GM growth (Back, 2015). MRI studies have shown reduced cortical and deep GM volumes (Ball et al., 2012; Boardman et al., 2006; Srinivasan et al., 2007), and reduced cortical folding and surface area (Ajayi-Obe et al., 2000; Dubois et al., 2008a; Engelhardt et al., 2015). In comparison with term-born infants, preterm infants at term-equivalent age have increased cortical FA and MD (Ball et al., 2013), while lower GA, lower birthweight and slower weight gain have been associated with higher FA in the preterm cortex (Vinall et al., 2013). Preterm birth can result in long-term GM alteration such as decreased cortical volume and gyrification in children and adolescents (Kesler et al., 2004; Lodygensky et al., 2005; Nosarti et al., 2002; Zhang et al., 2015)

#### 3.2.4 Perinatal risk factors

In addition to the degree of prematurity, there are several clinical factors that can adversely affect brain development during the preterm period.

#### **3.2.4.1 Intrauterine growth restriction**

Intrauterine growth restriction (IUGR) is major cause of morbidity and mortality (Bernstein et al., 2000; Kady and Gardosi, 2004) and is associated with neurodevelopmental impairments including motor and cognitive delay (Padilla et al., 2011; Tolsa et al., 2004; Torrance et al., 2010). MRI studies have demonstrated that in comparisons with appropriate for gestational age preterm infants IUGR preterm infants have reduced cortical GM volume (Dubois et al., 2008a; Inder et al., 2005; Tolsa et al., 2004), reduced occipital cerebral tissue volume (Thompson et al., 2007), reduced thalamic and basal ganglion volume (Bruno et al., 2017), and decreased FA in the splenium and genu of the corpus callosum and increased FA in the corona radiata (Padilla et al., 2014).

#### **3.2.4.2 Respiratory illness**

Respiratory illness in preterm infants affects between 14-20% of infants born before 30 weeks GA and infants with birth weight less 1500g (Baraldi and Filippone, 2007; Groenendaal et al., 2010), increasing to 68% in infants born between 22-26 weeks GA (Costeloe et al., 2012). It has been associated with impaired developmental outcome (Kobaly et al., 2008; Lodha et al., 2014; Natarajan et al., 2012; Short et al., 2003; Vohr et al., 2000). Conventional MRI studies have reported cerebral tissue volume reductions (Boardman et al., 2007; Inder et al., 2005; Thompson et al., 2007), and TBSS studies have demonstrated alterations in WM microstructure. Decreased FA was observed in preterm infants who required oxygen therapy at 36 weeks' gestation compared with preterm infants who didn't in the left inferior longitudinal fasciculus (Anjari et al., 2009). A larger study found an association between increased length of neonatal respiratory support and increasing diffusivities and decreasing FA across WM (Ball et al., 2010)

#### **3.2.4.3 Parenteral nutrition**

Parenteral nutrition forms an integral component of neonatal care for preterm infants when a patient's nutritional needs are not being met due to gastrointestinal immaturity or disease (Hay, 2013). Reduced energy and protein intake during the first week of life has been associated with impaired cognitive and motor performance (Stephens et al., 2009), while greater rate of weight gain is associated with improved neurodevelopmental outcome in low birth weight infants (Claas et al., 2011; Ehrenkranz et al., 2006; Franz et al., 2009). Total parenteral nutrition (TPN) has been associated with qualitatively assessed brain abnormalities on conventional MRI (Brouwer et al.,



2017; Kidokoro et al., 2013), and Beauport et al. (2017) found that increased combined parenteral and enteral intake of total energy, fat, and carbohydrates within the first two weeks of life was associated with reduced risk of cerebral abnormalities at TEA. These studies employed the scoring system for cerebral abnormalities outlined in Kidokoro et al. (2013) which combines sub-scores of WM, cortical GM, deep GM and cerebellar abnormalities assessed on T1- and T2-weighted scans.

#### **3.2.4.4 Necrotising enterocolitis**

Necrotising enterocolitis (NEC) is characterised by acute and chronic intestinal inflammation. The pathogenesis remains unclear however, the most common risk factors are low birthweight and low GA (Lin and Stoll, 2006). NEC occurs in approximately 9% of infants (Stoll et al., 2015; Wojkowska-Mach et al., 2014). It is a leading cause of mortality and morbidity in preterm infants, with survival to discharge in extremely low birth weight infants who undergo operation for NEC at only 51% (Blakely et al., 2005). Neurodevelopmental impairment has been reported in 45% of children who had neonatal NEC (Rees et al., 2007), and those who undergo surgery are at greater risk of neurodevelopmental impairment than infants treated medically or those without NEC (Hintz et al., 2005). Merhar et al. (2014) reported increased WM injury, graded according to the qualitative scoring system described by Miller et al. (2005), in preterm infants treated surgically compared with those treated medically. NEC has also been associated with increased rates of IVH (Lee et al., 2014), higher FA in the cortex (Vinall et al., 2013), and reduced FA and increased MD in the splenium of the corpus callosum (Brossard-Racine et al., 2017).

#### **3.2.4.5 Chorioamnionitis**

Chorioamnionitis refers to the acute inflammation of the membranes and the chorion of the placenta. This usually occurs due to ascending microbial infection following membrane rupture. Chorioamnionitis is a cause of preterm labour, (Goldenberg et al., 2008; Goldenberg et al., 2000), with occurrence increasing with decreasing GA, observed in 66% at 20 to 24 weeks of gestation decreasing to 16% at 34 weeks (Lahra and Jeffery, 2004). The effects of chorioamnionitis on an infant's development remain unclear, with conflicting results from a number of studies. Several studies suggest that chorioamnionitis has a protective effect on respiratory distress syndrome (Lahra et al., 2009b) and chronic lung disease (Lahra et al., 2009a), and a protective effect on mortality rates after adjusting for other perinatal risk factors (Hendson et al., 2011). While other

studies report chorioamnionitis is a risk factor for cystic PVL and cerebral palsy (Jacobsson et al., 2002; Wu, 2002; Wu and Colford, 2000; Wu et al., 2003), impaired neuromotor performance (Berger et al., 2009), abnormal neurologic outcome (Kaukola et al., 2006). DTI studies of histological chorioamnionitis have also produced differing results. An ROI study found with no difference in DTI measures between preterm infants with chorioamnionitis and preterm infants without exposure to chorioamnionitis (Chau et al., 2009), while a TBSS study reported lower FA values across the WM in exposed infants (Anblagan et al., 2016).

#### **3.2.4.6 Patent ductus arteriosus**

The ductus arteriosus is a foetal blood vessel that connects the right ventricular outflow tract to the descending aorta, and should close within the first 24 hours of life in term infants. However in 8 in 1000 preterm infants the duct fails to close (Forsey et al., 2009). Treatment for PDA can be either medical treatment with cyclooxygenase inhibitors or surgical ligation. Infants treated, either medically or surgically, scored worse on neurodevelopmental assessments than infants not treated for PDA, with infants treated surgically performing worse than infants treated medically (Bourgoin et al., 2016; Janz-Robinson et al., 2015; Madan et al., 2009). There were differences between the three groups in GA, birthweight and respiratory condition, however the risk of impaired neurodevelopmental remained significantly higher in the PDA treated group after correcting for these factors (Bourgoin et al., 2016; Janz-Robinson et al., 2015). MRI studies have reported conflicting findings on the effects of PDA on the brain. Padilla et al. (2015) reported reduced brain volumes in infants treated medically for PDA compared with preterm infants treated medically and infants not treated for PDA, but the study also found regions of increased cortical GM volume in infants treated surgically compared with infants not treated for PDA. PDA has been associated with reductions in cerebellar volume and pontine diameter (Argyropoulou et al., 2003). However, Lemmers et al. (2016) found no significant brain volumes differences or differences in FA and diffusivities in the PLIC between infants treated surgically, infants treated medically and infants without PDA. Conversely, Rogers et al. (2016) found reduced FA in the anterior limb of the internal capsule (ALIC) in preterm infants medically treated for PDA compared with preterm infants without PDA.

### **3.2.4.7 Infection and sepsis**

Preterm infants are at risk of infection during the perinatal period (Adams-Chapman and Stoll, 2006). 65% of extremely low birthweight infants have at least one infection, such as sepsis, meningitis or NEC (Stoll et al., 2004), and compared with uninfected extremely low birthweight infants are significantly more likely to experience motor, cognitive and visual impairments (Alshaikh et al., 2014; Chau et al., 2012; Stoll et al., 2004), while mortality is significantly higher in infants with sepsis than in uninfected infants (Stoll et al., 2002a, b). Infection in preterm infants has been associated with increased WM injury. Infants with PVL had significantly higher rates of culture-positive infection (Graham et al., 2004) and increased incidence of WM injury was observed in infants with recurrent infection compared with infants with one or no infection (Glass et al., 2008). In newborn mice, moderate systemic inflammation during the period equivalent to preterm in human resulted in an increase in the number of non-myelinated axons and reduced axon diameter (Favrais et al., 2011). DTI studies of infants with culture-positive infection reveal reduced WM FA and increased MD compared with uninfected preterm infants, after correcting for WM injury and GA at birth (Chau et al., 2012), a slower rate of increase of WM FA between 25 and 45 weeks PMA (Adams et al., 2010), and reduced cerebellar FA (Tam et al., 2009).

## **3.3 MRI in neonates**

MRI allows in vivo assessment of brain development. The application of MRI to neonatal populations has brought new insights into normal and preterm brain maturation, the effects of perinatal risk factors and the relationship between cerebral macro- and microstructure and neurodevelopmental outcome. This section provides a brief overview of MR studies in the preterm brain, and more detailed discussions follow in Chapters 4-7.

### **3.3.1 Qualitative T1- and T2-weighted studies**

As mentioned in Section 3.2.3, MRI can be used to assess brain injury associated with prematurity (Inder et al., 2003; Rutherford et al., 2010). Brain injury observed on conventional MRI is associated with developmental impairment (Brouwer et al., 2017; Miller et al., 2005; Reidy et al., 2013; Rutherford et al., 1998; Shah et al., 2006; Spittle et al., 2009; Woodward et al., 2006; Woodward et al., 2005). Such studies typically employ a qualitative assessment of a combination of several image characteristics, including signal abnormality in the WM, ventricular dilation, cystic

lesions, thinning of the CC and the presence of GM abnormalities. Nonetheless these methods are subjective, dependent on the assessor's experience and are unable to identify infants at risk of developmental impairment in the absence of overt injury. Quantitative MRI can provide objective assessment of changes in brain tissue associated with maturation, prematurity, injury and developmental performance in preterm populations.

### **3.3.2 Volumetric MRI studies**

Volumetric MRI studies of preterm infants demonstrate that total brain volume increases between 23-48 weeks PMA (Ajayi-Obe et al., 2000; Huppi et al., 1998b; Kapellou et al., 2006; Kuklisova-Murgasova et al., 2011; Makropoulos et al., 2016; Peterson et al., 2003; Soria-Pastor et al., 2009). Absolute volumes of cortical GM, deep GM, WM and the ventricles increase, as shown by Figure 3.9 and Figure 3.10 (Makropoulos et al., 2016), but relative volumes, as a percentage of total brain volume, of the brainstem, WM and ventricles decrease and relative values of the cortical GM and cerebellum increase (Makropoulos et al., 2016; Nishida et al., 2006).

However, preterm infants have reduced cortical GM, deep GM and WM volumes and increased CSF volume compared to term-born infants at TEA (Boardman et al., 2006; Inder et al., 2005; Thompson et al., 2007; Zacharia et al., 2006), and the extent of cerebral tissue volume reduction and increase in CSF volume is associated with the degree of prematurity (Inder et al., 2005; Soria-Pastor et al., 2009). Furthermore, differences in brain volume persist into adolescence (Nosarti et al., 2002; Peterson et al., 2000).

Brain tissue volumes estimated during the perinatal period are related to developmental performance in preterm infants. Decreased total brain volume, cortical and deep GM volume, cerebellar volume and increased CSF and ventricular volumes are associated with impaired motor function and developmental delay (Inder et al., 2005; Lind et al., 2011; Peterson et al., 2003; Peterson et al., 2000).

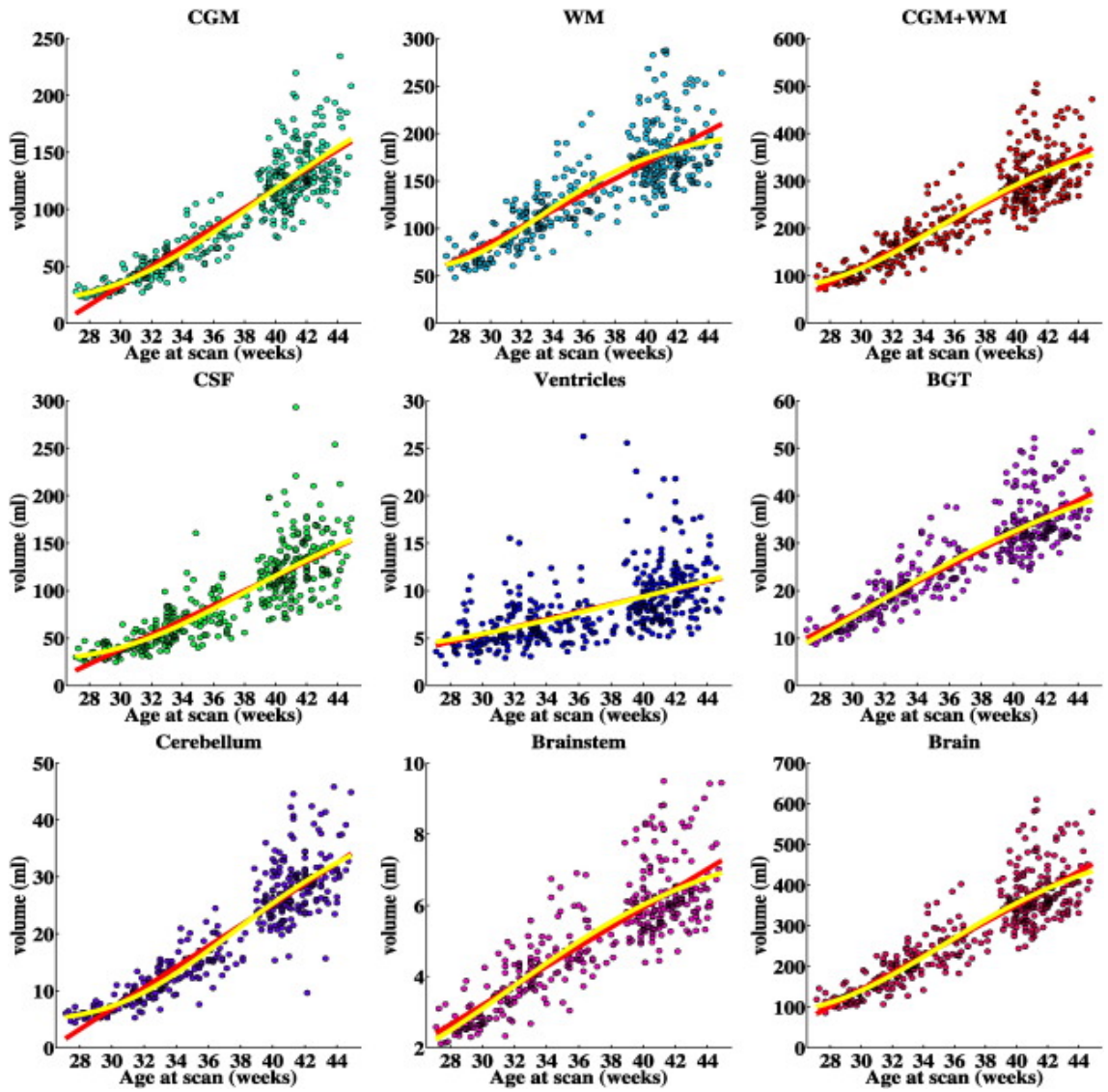


Figure 3.9 Absolute tissue volumes of cortical grey matter (CGM), white matter (WM), cerebrospinal fluid (CSF), ventricles, basal ganglia and thalami (BGT), cerebellum, brainstem and whole brain in a cohort of preterm infants imaged between 27-45 weeks PMA. Reproduced from Makropoulos et al. (2016).

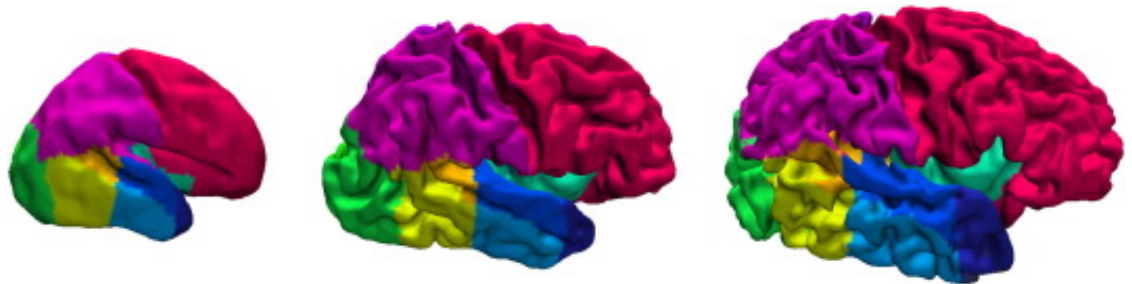


Figure 3.10 Cortical surfaces of preterm neonates at 28, 36 and 44 weeks PMA at scan demonstrating the increase in cortical folding and brain volume during the perinatal period. The surfaces are segmented into the frontal lobe (pink), parietal lobe (magenta), occipital lobe (bright green), medial and inferior temporal gyri (yellow), superior temporal gyrus (blue and dark blue) and the insula (mint green). Reproduced from Makropoulos et al. (2016).

### 3.3.3 Diffusion-weighted imaging studies

dMRI provides a quantitative tool to study in vivo microstructural changes associated with maturation and injury in neonatal populations. A number of analysis approaches have been employed to study brain maturation including ROI approaches, tractography and TBSS. The perinatal period is characterised by a pattern of decreasing diffusivity and increasing FA in the cerebral WM in preterm infants (Akazawa et al., 2016; de Bruine et al., 2011b; Kersbergen et al., 2014b; Miller et al., 2002; Partridge et al., 2004; van Pul et al., 2012) and term infants (Akazawa et al., 2016; Dubois et al., 2006; Oishi et al., 2011). FA continues to increase and diffusivity decreases during the first 2 years after birth in term (Forbes et al., 2002; Gao et al., 2009; Geng et al., 2012) and preterm infants (Young et al., 2016).

WM maturation follows a heterogeneous spatiotemporal pattern, with different fasciculi maturing at different times and different rates (Braga et al., 2015; Dubois et al., 2008c; Dubois et al., 2006; Gao et al., 2009; Kulikova et al., 2015; Nossin-Manor et al., 2013; Nossin-Manor et al., 2015; Oishi et al., 2011; Rose et al., 2014) in a posterior-to-anterior and a central-to-peripheral direction of maturation. A post-mortem study of WM organisation between 17-40 weeks gestation revealed that projection fibres such as the corticospinal and corticothalamic tracts were identifiable as early as 17 weeks gestation and long-range intrahemispheric association fibres can be delineated from 20 weeks, while short-range cortico-cortical pathways emerge around 24 weeks gestation (Takahashi et al., 2012).

Lower FA and increased diffusivity are found across the WM in preterm infants compared with term-born infants (Anjari et al., 2007; Huppi et al., 1998a; Rose et al., 2008; Thompson et al., 2011) and increased prematurity is associated with lower FA and higher diffusivity (Arzoumanian et al., 2003; Ball et al., 2010; Dudink et al., 2007; Hasegawa et al., 2011; Partridge et al., 2004). Furthermore infants with WM injury identified on conventional MRI show reduced anisotropy and increased diffusivity across the WM in comparison to preterm infants with normal MRI scans (Cheong et al., 2009; Counsell et al., 2003a; Counsell et al., 2006; Huppi et al., 2001; Liu et al., 2012; van Pul et al., 2012) and the rates of increase in FA associated with maturation are slower (Adams et al., 2010).

WM diffusion measures at TEA have been related to later neurodevelopmental performance later in life. Increased FA and decreased diffusivity in the WM are associated with improved motor, cognitive and language performance (Arzoumanian et al., 2003; Counsell et al., 2008; De Bruine et al., 2013; Duerden et al., 2015; Krishnan et al., 2007; Rose et al., 2007; Salvan et al., 2017; van Kooij et al., 2012b) and improved visual function (Bassi et al., 2008; Berman et al., 2009; Groppo et al., 2014). These associations persist into childhood and adolescence, with poorer cognitive and motor abilities associated with reduced FA in the WM (Eikenes et al., 2011; Murray et al., 2016; Skranes et al., 2009; Skranes et al., 2007; Vollmer et al., 2017).

#### **3.3.4 MR Relaxometry**

MR relaxometry estimates T1, T2, and  $T2^*$  relaxation times. Quantitative maps of relaxation parameters provide measures of tissue content, as they are influenced by tissue density, water content and macromolecular composition (Deoni, 2010). The decrease in T1 and T2 relaxation times observed during the first year of life is assumed to be driven by the increase in lipids and other macromolecules due to myelination, pre-myelination events and a decrease in water content (Paus et al., 2001). Relaxometry techniques have been used to derive myelin-related measures, in particular myelin water fraction (MWF), by decomposing the MR signal into its constituent components from distinct water compartments. MWF has been shown to correlate well with myelin content estimated from histology (Laule et al., 2008; Laule et al., 2006; Webb et al., 2003). MWF has been used to demonstrate the pattern of myelination during the first year of life in healthy infants (Dean et al., 2016; Deoni et al., 2012; Deoni et al., 2011). Studies in preterm infants during the perinatal period have shown a decrease in T2 (Counsell et al., 2003b), increases in MWF in the thalamus and posterior WM (Melbourne et al., 2016), longer T2 in very preterm infants compared to late preterm infants (Knight et al., 2018), and compared to term-born infants (Hagmann et al., 2009; Pannek et al., 2013).

#### **3.3.5 MR Spectroscopy**

MR spectroscopy has been used to measure metabolic markers of normal and preterm brain development. Metabolites measured with MR spectroscopy include N-acetyl-aspartate (NAA), which is found in mature neurons and axons, creatine (Cr), an energy metabolite, choline (Cho), a membrane metabolite, glutamate (Glu), the most abundant excitatory neurotransmitter in the brain, and lactate which is produced under conditions of inflammation and anaerobic metabolism

(Moffett et al., 2007; Shih et al., 2004). Studies in preterm infants reveal changes in brain metabolites associated with maturation, prematurity and neurodevelopmental performance. Studies have shown NAA/Cho ratio increases and Lac/NAA and Lac/Cr ratios decrease with increasing age at scan in the thalamus, basal ganglia, calcarine GM, corticospinal tract, parietal, frontal and posterior WM (Augustine et al., 2008; Card et al., 2013; Xu et al., 2011). MR spectroscopy measurements in preterm infants at TEA showed a positive correlation between NAA/Cho ratio and GA at birth in the posterior WM (Kendall et al., 2014) and reduced NAA/Cho and NAA/Cr ratios in the frontal WM compared with term-born infants (Hyodo et al., 2017). Reduced NAA/Cr was also observed in the basal ganglia in preterm infants with WM injury compared to preterm infants without WM injury (Card et al., 2013). Increased Lac/Cr and Lac/Cho levels in the basal ganglia were also associated with increased illness severity at birth as measured by Apgar score at 1 and 5 minutes and Clinical Risk Index for Babies II (Card et al., 2013; Ezz-Eldin et al., 2015).

Changes in metabolites of preterm infants measured at TEA have been associated with later neurodevelopmental performance. Preterm infants with normal developmental performance at 18 months showed higher NAA/Cho ratio in the right and left thalami compared with preterm infants with mild neurodevelopmental delay (Hyodo et al., 2017). Increased NAA/Cho ratio and decreased Cho/Cr ratio in the posterior cerebral WM were associated with higher composite and scaled gross motor scores assessed with the Bayley Scales of Infants and Toddler Development, 3<sup>rd</sup> edition (BSID-III), at 1 year of age, after correcting for GA at birth (Kendall et al., 2014). Similar correlations were seen with composite language and cognitive scores but were not significant after correcting for GA at birth (Kendall et al., 2014). Cerebellar NAA/Cho ratio were significantly positively correlated with composite cognitive BSID-III scores at 2 years (Van Kooij et al., 2012a).



## Chapter 4 Tract specific analysis in preterm infants

Tract-specific analysis (TSA) is a WM analysis method that may offer potential benefits over other widely-used methods such as region-of-interest approaches or tract-based spatial statistics (TBSS). TSA produces a skeleton representation of WM tracts and projects the group's diffusion data onto the skeleton for statistical analysis. In this chapter, the performance of TSA for analysing preterm infant data is evaluated against results obtained from native space tractography and TBSS. The results demonstrate that the registration employed in TSA provides better WM tract alignment than a previous TBSS protocol optimised for neonatal spatial normalisation, and that TSA projects FA values in close agreement with values derived from native space tractography.

This work is published in Pecheva et al., "A tract-specific approach to assessing white matter in preterm infants." *NeuroImage* (2017).

### 4.1 Introduction

dmRI is increasingly being used to study brain development and injury in infants. Using metrics derived from DTI (Basser et al., 1994) we have gained valuable insights into the effects of maturation and injury on WM in healthy and patient infant populations. A number of approaches have been used to analyse DTI data during development. Manually-drawn ROIs (Gao et al., 2009; Huppi et al., 1998a) or tractography using manually-placed waypoints (Bassi et al., 2008; Dubois et al., 2008c; Dubois et al., 2006) are generally assumed to produce anatomically accurate results but these methods become prohibitively labour-intensive for large cohort studies. Subsequently a number of methods have been developed for automatic segmentation of WM tracts (Suarez et al., 2012; Zhang et al., 2010b). However, establishing correspondence between subjects' WM tracts can be problematic due to inter-subject variability in anatomy and DTI characteristics, which can result in differences in tractography or segmentation. It is possible to average the DTI metrics over the entire tract (Lebel et al., 2008) but localised differences may be missed. Correspondence can be achieved by sampling at equivalent levels along tracts (Groeschel et al., 2014; Verde et

al., 2014) or parameterising WM tracts by arc length, essentially reducing entire tracts to a single, core line (Corouge et al., 2006; Goodlett et al., 2009; O'Donnell et al., 2009; Verde et al., 2014; Yeatman et al., 2012). These methods have been used to study neurodevelopment in toddlers (Geng et al., 2012; Goodlett et al., 2009), WM heritability in twin neonates (Lee et al., 2015), infantile Krabbe disease (Gupta et al., 2015), and prenatal exposure to selective serotonin reuptake inhibitors (Jha et al., 2016). However, these methods are more suitable for tubular rather than sheet-like tracts. Collapsing tracts such as the corticospinal tract into a single line, especially in the region of the fanning cortical projections, fails to appropriately represent the tract macrostructure and averaging over such a large area may obscure microstructural changes. Moreover, bundles such as the corpus callosum need to be separated into tubular regions and cannot be analysed as a whole.

Exploiting the sheet-like structure of many WM tracts, tract-based spatial statistics (TBSS) was introduced (Smith et al., 2006) and initiated the practice of projecting volumetric data onto a WM skeleton. Although it has proven to be a valuable analysis tool for studying development (Anjari et al., 2007; Ball et al., 2010; Counsell et al., 2008; Rose et al., 2008; van Kooij et al., 2012b), recent studies have discussed the potential pitfalls of TBSS (Bach et al., 2014; de Groot et al., 2013; Edden and Jones, 2011; Schwarz et al., 2014; Van Hecke et al., 2010; Zalesky, 2011). A particular limitation of TBSS is a lack of anatomical specificity due to the construction of the skeleton for the entire WM, rather than separately for each individual WM tract. Although TBSS is useful when there is no a priori hypothesis regarding the anatomical location of an effect of interest, it makes it impossible to distinguish between adjacent WM tracts such as the inferior longitudinal and inferior-fronto-occipital fasciculi.

Tract-specific analysis (TSA) (Yushkevich et al., 2008) is an alternative WM analysis method that creates skeleton models of individual WM tracts onto which diffusion data can be projected for statistical analysis. In TSA, subjects are registered to a study-specific template using a tensor-based algorithm (Zhang et al., 2006). Following registration, tracts of interest are delineated from the template using deterministic tractography and manually-drawn ROIs. From the tractography results, a medial surface is determined for each tract that simultaneously defines its skeleton and boundary (Yushkevich and Zhang, 2013). The skeleton also describes local tract thickness via the radius function defined as equal to the radius of the maximal inscribed sphere within the

boundary centred at that point on the skeleton. Diffusion data from every subject is then projected onto the skeleton, similarly to TBSS. TSA samples data to be projected onto each point of the skeleton by searching along the unit normal from that point to the tract boundary. The tract boundary defines the stopping criteria. This aims to limit potential voxel misassignment from neighbouring tracts. The TSA framework allows for either a maximum-value or mean-value data projection strategy. In the maximum-value strategy, the tensor with the highest FA value is selected. In the mean-value strategy, the average tensor is computed and from this average tensor, scalars such as FA are computed. Statistical analysis of projected diffusion data is then carried out at each point on the skeleton. The key aspects of the TSA and TBSS pipelines and their differences are summarised in .

Table 4.1 A summary of the key aspects of the TSA and TBSS pipelines.

Aspect	TSA	TBSS
Registration	Tensor-based	Scalar-based (FA)
Search direction	Perpendicular to the skeleton surface	Direction of maximum change within a local 3x3x3 voxel neighbourhood.
Choice of voxel to project	Maximum FA tensor or mean tensor	Maximum FA tensor
Stopping criteria	Tract boundary	Skeleton distance map
Statistical resolution	Point on surface	Voxel
Multiple comparisons	Suprathreshold analysis	Threshold-free cluster enhancement

TSA offers potential advantages as an analysis tool. It is automated therefore reducing the time cost and inter-rater variability which affect manual-input methods. It characterises WM tracts as surfaces rather than aggregating tracts into a single core line thereby capturing the overall tract morphology. Theoretically TSA also offers improvements over TBSS by (i) employing a tensor-based rather than scalar-based registration; (ii) defining tracts individually and so making it possible to distinguish between adjacent tracts; and (iii) having a data projection search stopping criteria intended to limit crossing over into neighbouring tracts. TSA has been successfully applied

to study pathologies such as paediatric chromosome 22q11.2 deletion syndrome (Yushkevich et al., 2008) and amyotrophic lateral sclerosis (Zhang et al., 2010a), and changes in DTI metrics over the lifespan (Chen et al., 2016), however has not been previously applied to study infant populations. Moreover, the performance of TSA has not been assessed extensively.

The aim of this chapter is to evaluate the performance of TSA within the context of preterm infant data. We compare TSA with native space tractography as a gold standard, and with TBSS, a similar and widely-used method. Despite some known limitations, TBSS remains a widely-used tool. Our evaluation of TSA involves (i) an assessment of TSA's ability to align WM tracts from different subjects; and (ii) assessment of the accuracy of its data projection step in comparison to TBSS.

## **4.2 Methods**

### **4.2.1 Subjects**

Permission for this study was granted by Queen Charlotte's and Hammersmith Hospitals Research Ethics Committee (07/H0704/99) and written parental consent was acquired prior to imaging. MR data were collected from 53 preterm subjects who were imaged between February and July 2013. All images were reviewed by an experienced perinatal neuroradiologist and cases with major focal lesions were excluded. Five data-sets were excluded; 2 unilateral haemorrhagic infarction, 1 cerebellar infarct, 1 cerebellar haemorrhage and 1 infant had temporal and cerebellar haemorrhages with cerebellar hypertrophy. 48 subjects (23 female) born at a median (range) gestational age (GA) of 30.6 (24.0-32.9) weeks and imaged at a median age of 41.9 (38.6-47.1 weeks) weeks post-menstrual age (PMA) were analysed in this study. The perinatal characteristics of the study group are summarised in Table 4.2.

### **4.2.2 Data acquisition**

MR imaging was performed on a 3-T MR system sited on the neonatal intensive care unit. T1- and T2-weighted MR imaging and single shot echo planar dMRI data were acquired using an 8-channel phased array head coil. The pulse sequence parameters were as follows. 3D MPRAGE: repetition time (TR) = 17 ms, echo time (TE) = 4.6 ms, flip angle 13°, voxel size: 0.82 × 0.82 × 0.8. mm T2 weighted fast-spin echo imaging: TR = 8670 ms, TE = 160 ms, flip angle 90°, slice

thickness 2 mm with 1 mm overlapping slices, in-plane resolution  $1.14 \times 1.14$  mm. dMRI was acquired in the transverse plane in 32 non-collinear directions using the following parameters: TR = 8000 ms, TE = 49 ms, voxel size: 2mm isotropic, b-value: 750 s/mm<sup>2</sup>, SENSE factor of 2.

All examinations were supervised by a paediatrician experienced in MR imaging procedures. Infants were sedated with oral chloral hydrate (25-50 mg/kg) prior to scanning and pulse oximetry, temperature, and electrocardiography data were monitored throughout. Ear protection was used, comprising earplugs moulded from a silicone-based putty (President Putty, Coltene Whaledent, Mahwah, NJ, USA) placed in the external auditory meatus and neonatal earmuffs (MiniMuffs, Natus Medical Inc., San Carlos, CA, USA).

Table 4.2 Perinatal characteristics of the study group.

<b>Perinatal clinical characteristic</b>	
Median (range) gestational age at birth	30.64 (24-32.86) weeks
Median (range) postmenstrual age at scan	41.93 (38.57 – 47.14) weeks
Median (range) day age at scan	84 (142 – 48) days
Median (range) birthweight	1218 (655-1960) grams
Median (range) days of ventilation	0 (0 – 40) days
Small for gestational age* (number of infants)	13

#### 4.2.3 Diffusion weighted image processing

Diffusion-weighted images were visually inspected in 3 orthogonal planes for the presence of motion artefact and corrupt diffusion weighted volumes were excluded before tensor fitting. 33 subjects had no volumes excluded, eight subjects had one volume excluded, three subjects had two volumes excluded, three subjects had three volumes excluded and one subject had four volumes excluded. Non-brain tissue was removed using BET (Smith, 2002), images were corrected for eddy current artefacts using *eddy* (Andersson and Sotiropoulos, 2015) and the tensor model was fitted using dtifit from FSL (FMRIB, Oxford, <http://fsl.fmrib.ox.ac.uk>). Signal-to-noise-ratio (SNR) was calculated for each subject from the raw DW data. A 5×5 voxel ROI was manually placed in the central corona radiata of the b=0 volume and SNR was calculated as the mean signal divided by the standard deviation. For each subject deterministic tractography based

on the FACT approach (Mori et al., 1999) (part of DTI-TK <http://dti-tk.sf.net>) was used to delineate WM tracts in native space. Each subject's FA map was thresholded at 0.1 and whole brain tractography was seeded from each voxel with tracking parameters: maximum angle threshold of 45 and minimum FA threshold of 0.1. ROIs used to delineate tracts in native space were drawn manually for each subject, according to the protocol outlined in Wakana et al. (2007) . Separate ROIs were drawn for TSA. Placement of the ROIs is described in Table 3. The tracts delineated were the bilateral corticospinal tract (CST), inferior fronto-occipital fasciculus (IFOF), inferior longitudinal fasciculus (ILF), superior longitudinal fasciculus (SLF), uncinate fasciculus (UNC) and genu and splenium of the corpus callosum (CC), to include commissural, projection and association tracts in our comparison.

#### **4.2.4 Evaluation of TSA**

To evaluate TSA, we assessed two key aspects of the pipeline that are comparable in both TSA and TBSS. To determine how well TSA is able to align subjects' WM tracts we compared the standard TSA registration with an existing protocol that was optimised for neonatal spatial normalisation (Ball et al., 2010). To determine how accurately the TSA skeletons represent subjects' WM tracts we compared the mean FA values in each tract and the distributions of FA values over the whole tract projected by TSA with those calculated from native space tractography, which we take to be the ground truth.

Table 4.3 ROI placement for tractography.

<b>Tract</b>	<b>First ROI</b>	<b>Second ROI</b>	<b>Exclusion ROI</b>
CC genu	The CC is identified in the mid-sagittal plane and only the genu is selected	N/A	Exclude fibres that project posteriorly along the fornix.
CC splenium	The CC is identified in the mid-sagittal plane and only the splenium is selected.	N/A	Exclude fibres that project inferiorly along association fibres.
CC (whole)	The CC is identified in the mid-sagittal plane.	N/A	Exclude fibres passing through the cingulum and fornix.
CST	CST is identified in the axial plane at the level of the decussation of the superior cerebellar peduncle.	Projections to the cortex are identified in the axial plane at the level of the central semiovale.	Exclude fibres crossing into the opposite hemisphere and into the cerebellum.
IFOF	The occipital lobe is selected in the coronal plane identified halfway between the posterior edge of the cingulum and the posterior of the brain.	The entire hemisphere in the coronal plane at the level of the genu of the CC identified in the mid-sagittal slice.	Exclude fibres crossing medially through the anterior commissure.
ILF	The entire hemisphere is selected in the coronal plane at the posterior edge of the cingulum identified at the mid-sagittal slice.	The entire temporal lobe identified in the coronal plane at the level where the frontal and temporal lobe are no longer connected.	Exclude fibres that track medially into the fornix and CC.
SLF	The SLF is identified in the coronal plane at the lowest axial level in which the fornix can be identified as a single structure.	Projections that pass through the coronal plane at the level of the splenium of the CC identified in the mid-sagittal slice.	Exclude fibers that project into the external capsule.
UNC	The entire temporal lobe identified in the coronal plane at the level where the frontal and temporal lobe are no longer connected.	All the projections into the frontal lobe.	Exclude fibres which project into the anterior limb of the external capsule and posteriorly.

#### **4.2.4.1 Registration comparison**

WM tracts delineated in native space were warped using the transformations from TSA's tensor-based registration, DTI-TK, and the scalar-based registration from an optimised neonatal protocol to their respective template spaces. The scalar-based registration is an adaptation of the FNIRT (FMRIB, Oxford, <http://fsl.fmrib.ox.ac.uk>) registration used in TBSS (Ball et al., 2010). Each subject's tracts were converted into binary ROIs which were compared using Dice scores. For each of the two registration methods, a Dice score was calculated pairwise between each subject and all other subjects, measuring the degree of overlap between two subjects' WM tracts at the voxel level. The median Dice score was calculated per tract for each subject. The Wilcoxon signed rank test was used to compare the differences between the Dice scores from the two registrations.

#### **4.2.4.2 Data Projection**

To determine how accurately TSA projects each subject's diffusion data, we compared projected FA values, in template space following registration, with those calculated from the subjects' native space tractography. We also compared TSA's data projection step with the data projection step carried out in TBSS, to determine how TSA performs with respect to a similar and widely used method. While previous studies have investigated the accuracy of data projection step in TBSS in terms of alleviating misregistrations (Zalesky, 2011) and voxel misassignment following projection (Bach et al., 2014), none have investigated how template space data projected onto the skeleton representation of WM deviates from native space data for either method. For each subject, we calculated the mean of the FA values as well as the distribution of FA values over a tract derived from native space tractography, and projected by TSA and TBSS. This was done for the left and right CST, IFOF, ILF, UNC and genu and splenium of the CC. We take the FA values calculated from each subjects' native space tractography as our ground truth. For each subject, and across all eight tracts, we calculated the Bhattacharyya distances between the distribution of values over the tract derived from native space tractography and TSA, and between native space tractography and TBSS. The Wilcoxon signed rank test was used to compare the difference in the resulting paired Bhattacharyya distances. The tract-averaged FA values provide a summary of the differences between the methods, whereas the Bhattacharyya distance calculation assesses the difference between TSA and TBSS's deviation from the native space data over the entire distribution of FA values within a tract.



Some of the differences in projected values will be due to differences in registration since TBSS uses a different registration to TSA. As we are only interested in the data projection step, TSA's registration was incorporated into the TBSS pipeline. TBSS was also adapted to make the TBSS skeleton "tract specific" to allow a comparison with TSA and native space tractography. The tracts from the deterministic tractography identified in the TSA template were warped to the TBSS mean FA template. A binary segmentation of each tract was then overlapped with the TBSS skeleton. The voxels in the TBSS skeleton that overlap with the binary segmentation of a particular tract were assigned to that tract. This produced a mean FA value and distribution of FA values for the different tracts for each subject.

**Tensor-registered TBSS skeleton**

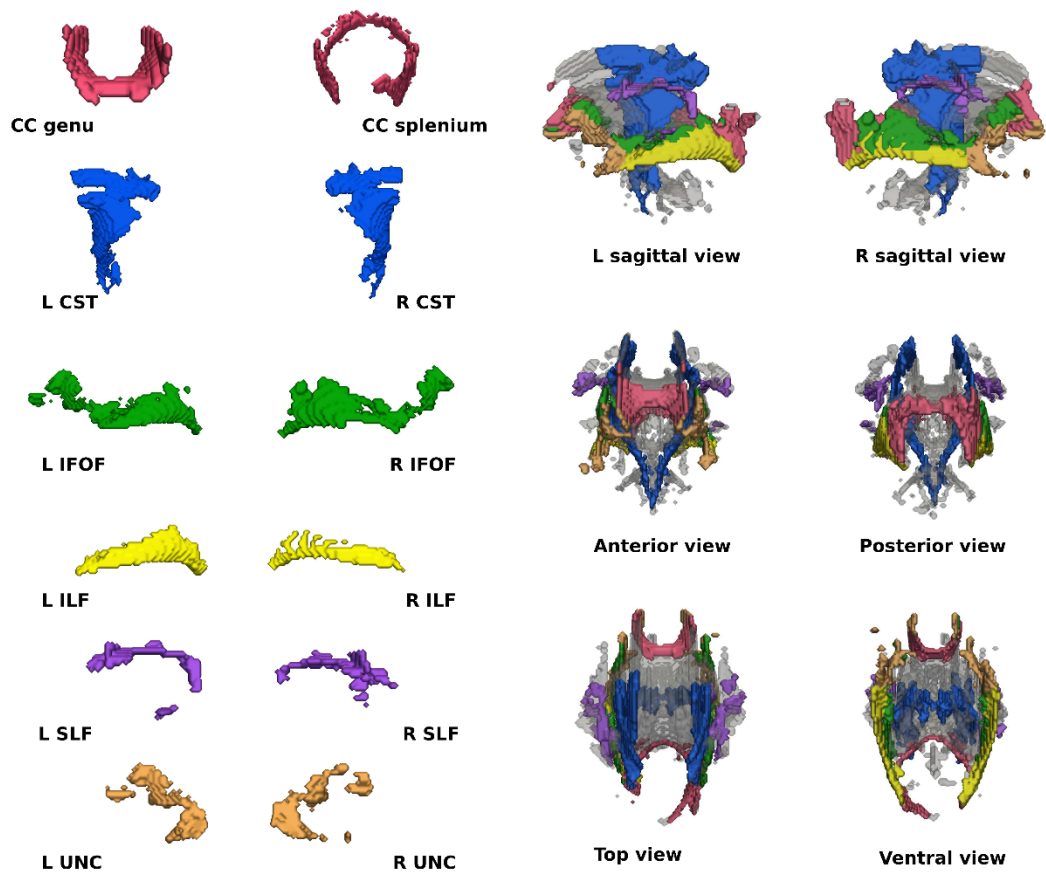


Figure 4.1 The tract skeletons from TBSS. The left two columns show the tract skeletons evaluated and the right two columns show the tracts overlaid on the whole WM skeleton (shown in grey).

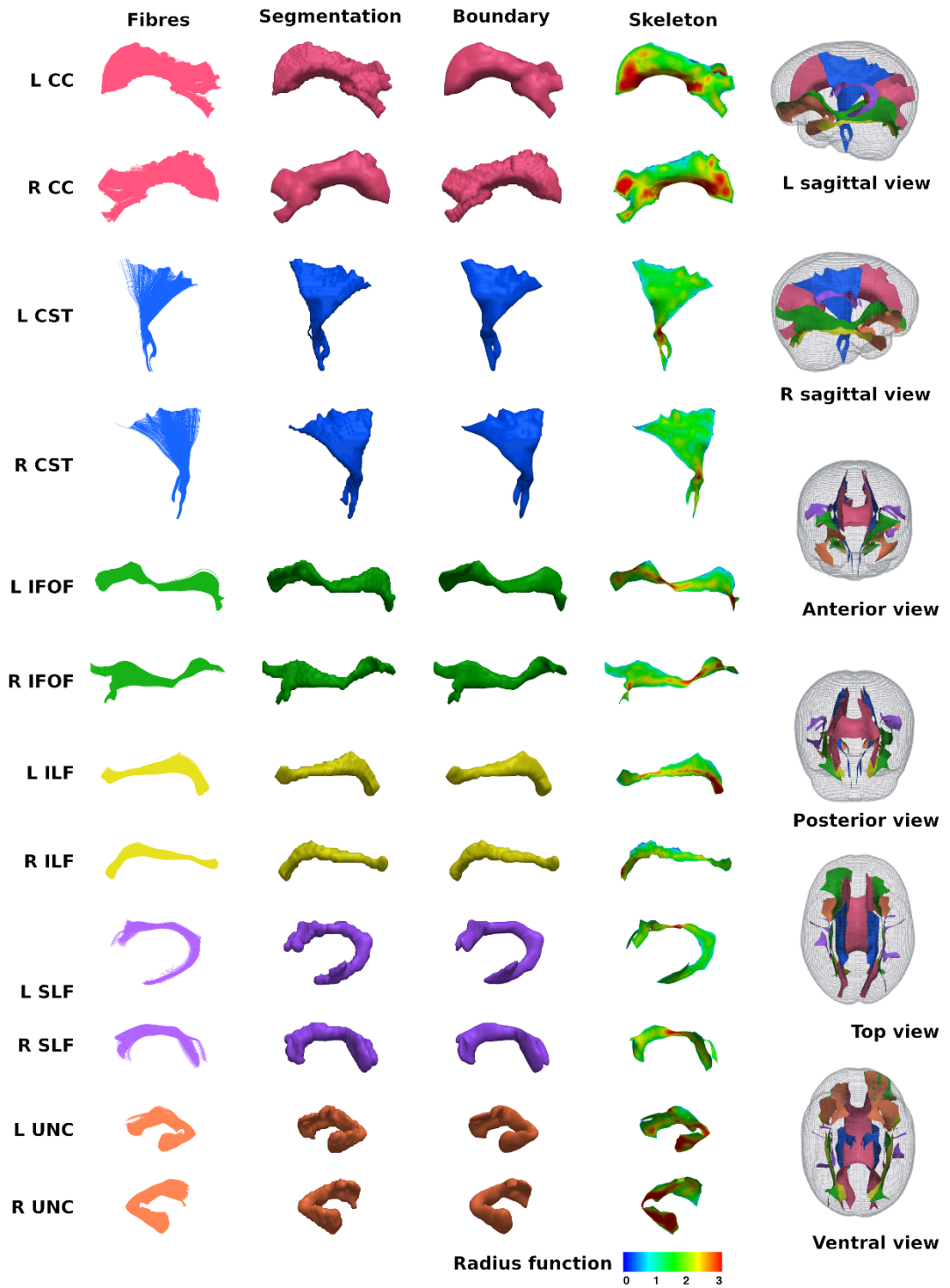


Figure 4.2 The TSA model fitting results for the left and right CC, CST, IFO, ILF, SLF and UNC.

## 4.3 Results

The results from the segmentation for the TBSS skeleton is shown in Figure 4.1, and the results from the TSA skeleton model fitting are shown in Figure 4.2.

### 4.3.1 Registration comparison

Figure 4.3 shows the median Dice scores following tensor-based and scalar-based registration for the eight tracts, representing the degree of alignment between subjects. For each tract, the Dice scores for the tensor-based registration were higher ( $p < 0.001$ , summarised in Table 4.4) than those for the scalar-based registration, demonstrating that TSA's tensor-based registration provides better alignment consistently over all tracts. However, it should be noted that for the subjects with the very lowest Dice scores the two registration techniques have very similar scores. Although native space tractography produced anatomically plausible results for these subjects and in these tracts, they contained fewer voxels resulting in a lower degree of overlap with other subjects' tracts. Indeed, there was notable variability across subjects within the native space tracts in terms of both FA values and number of voxels (Figure 4.4), however SNR was variable across subjects with mean SNR=22.2 (range=11.3 – 48.6).

Table 4.4 p-values from the Wilcoxon signed rank test comparing Dice scores from the tensor-based and scalar-based registration.

Tract	p-value
CC genu	$1.63 \times 10^{-9}$
CC splenium	$1.63 \times 10^{-9}$
L CST	$1.63 \times 10^{-9}$
R CST	$1.74 \times 10^{-9}$
L IFOF	$1.85 \times 10^{-9}$
R IFOF	$1.63 \times 10^{-9}$
L ILF	$1.63 \times 10^{-9}$
R ILF	$2.10 \times 10^{-9}$
L SLF	$1.74 \times 10^{-9}$
R SLF	$1.63 \times 10^{-9}$
L UNC	$1.63 \times 10^{-9}$
R UNC	$2.54 \times 10^{-9}$

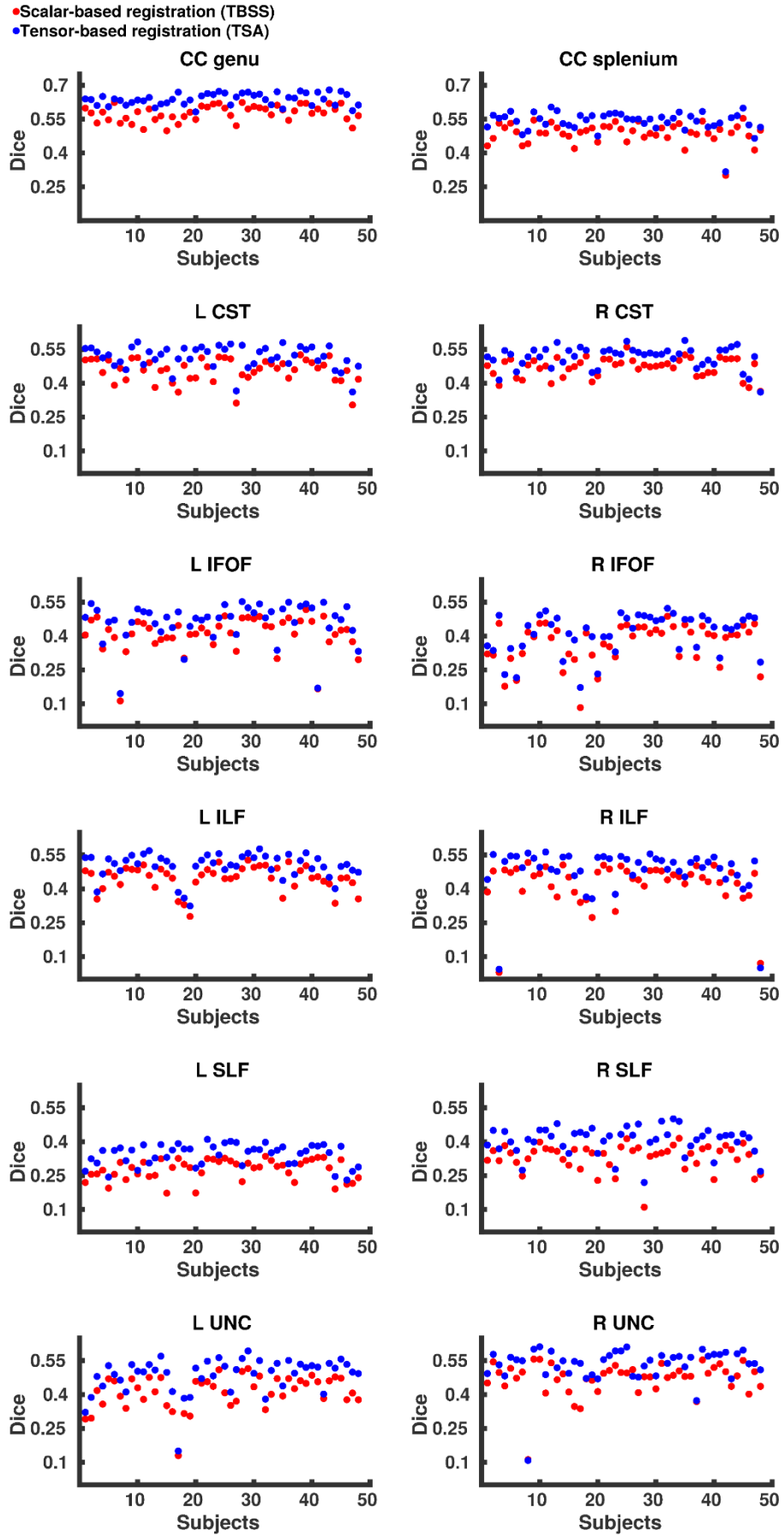


Figure 4.3 Median Dice scores for each subject over eight tracts following tensor-based and scalar-based registration.

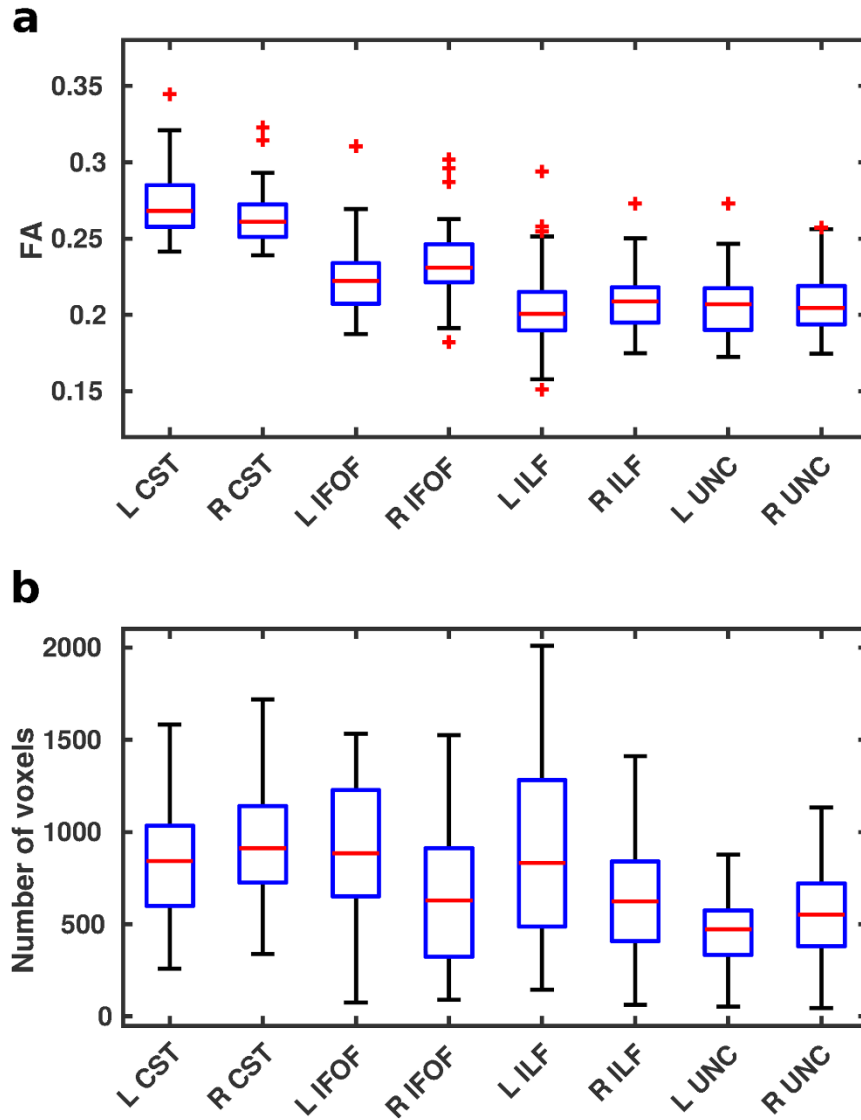


Figure 4.4 The variability across subjects' native space tractography for the left and right CST, IFOF, ILF and UNC shown in terms of a. FA values averaged over the entire tract and b. the total number of voxels included.

#### 4.3.2 Data Projection

The means and distributions of FA values from different WM tracts are shown in Figure 4.5 and Figure 4.6, respectively. Figure 4.5 shows the mean values per subject for each tract as derived from native space tractography and TSA. Overall TSA projects FA values similar to those obtained from the native space tractography, however these were still significantly different from native space-derived FA values in all but three tracts – left CST, right IFOF and right SLF (Table 4.5). TBSS projects FA values significantly higher than those produced by both native space tractography and TSA.

Table 4.5 . p-values from the Wilcoxon signed rank test comparing mean FA values between native space and TBSS, native space and TSA, and TSA and TBSS.

Tract	Native space vs TBSS (p-value)	Native space vs TSA (p-value)	TSA vs TBSS (p-value)
CC genu	$1.63 \times 10^{-9}$	$9.84 \times 10^{-9}$	$1.63 \times 10^{-9}$
CC splenium	$1.63 \times 10^{-9}$	0.0058	$1.63 \times 10^{-9}$
L CST	$1.63 \times 10^{-9}$	0.87	$1.63 \times 10^{-9}$
R CST	$1.63 \times 10^{-9}$	$2.41 \times 10^{-4}$	$1.63 \times 10^{-9}$
L IFOF	$1.63 \times 10^{-9}$	$1.69 \times 10^{-8}$	$1.63 \times 10^{-9}$
R IFOF	$1.63 \times 10^{-9}$	0.74	$1.63 \times 10^{-9}$
L ILF	$1.63 \times 10^{-9}$	$1.63 \times 10^{-9}$	$1.63 \times 10^{-9}$
R ILF	$1.63 \times 10^{-9}$	$3.22 \times 10^{-6}$	$1.63 \times 10^{-9}$
L SLF	$1.63 \times 10^{-9}$	$2.23 \times 10^{-9}$	$1.63 \times 10^{-9}$
R SLF	$1.63 \times 10^{-9}$	0.18	$1.63 \times 10^{-9}$
L UNC	$1.63 \times 10^{-9}$	$1.90 \times 10^{-8}$	$1.63 \times 10^{-9}$
R UNC	$1.63 \times 10^{-9}$	$5.69 \times 10^{-9}$	$1.63 \times 10^{-9}$

Figure 4.6 shows the normalised histograms for each subject from the native space tractography, TSA and TBSS across eight tracts. Overall the distributions of FA values across the tracts derived from TSA are in close agreement with those obtained from native space. Although the TSA and native space tractography distributions are similar, there are some differences, most noticeably for the left IFOF and ILF where TSA overestimates FA values. The Bhattacharyya distances between native space tractography and TSA, and native space tractography and TBSS are shown for each subject in Figure 4.7 and summarised in Table 4.6. The Bhattacharyya distances between native space tractography and TBSS were significantly greater ( $p < 0.001$ ), than that between native space tractography and TSA, which were close to zero for every tract.

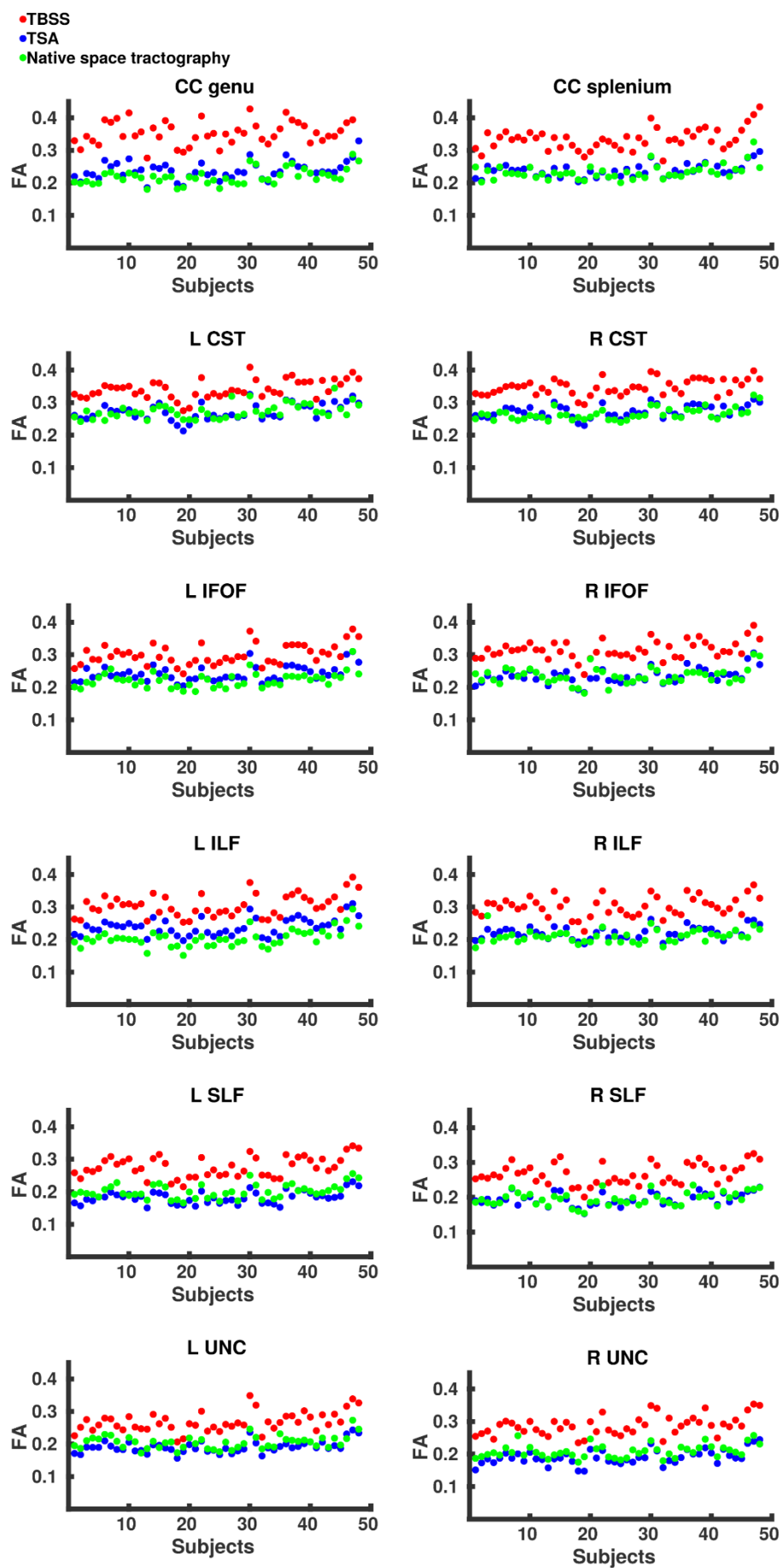


Figure 4.5 The mean FA values for each subject across eight tracts as estimated by native space tractography (green), TSA (blue) and TBSS (red).

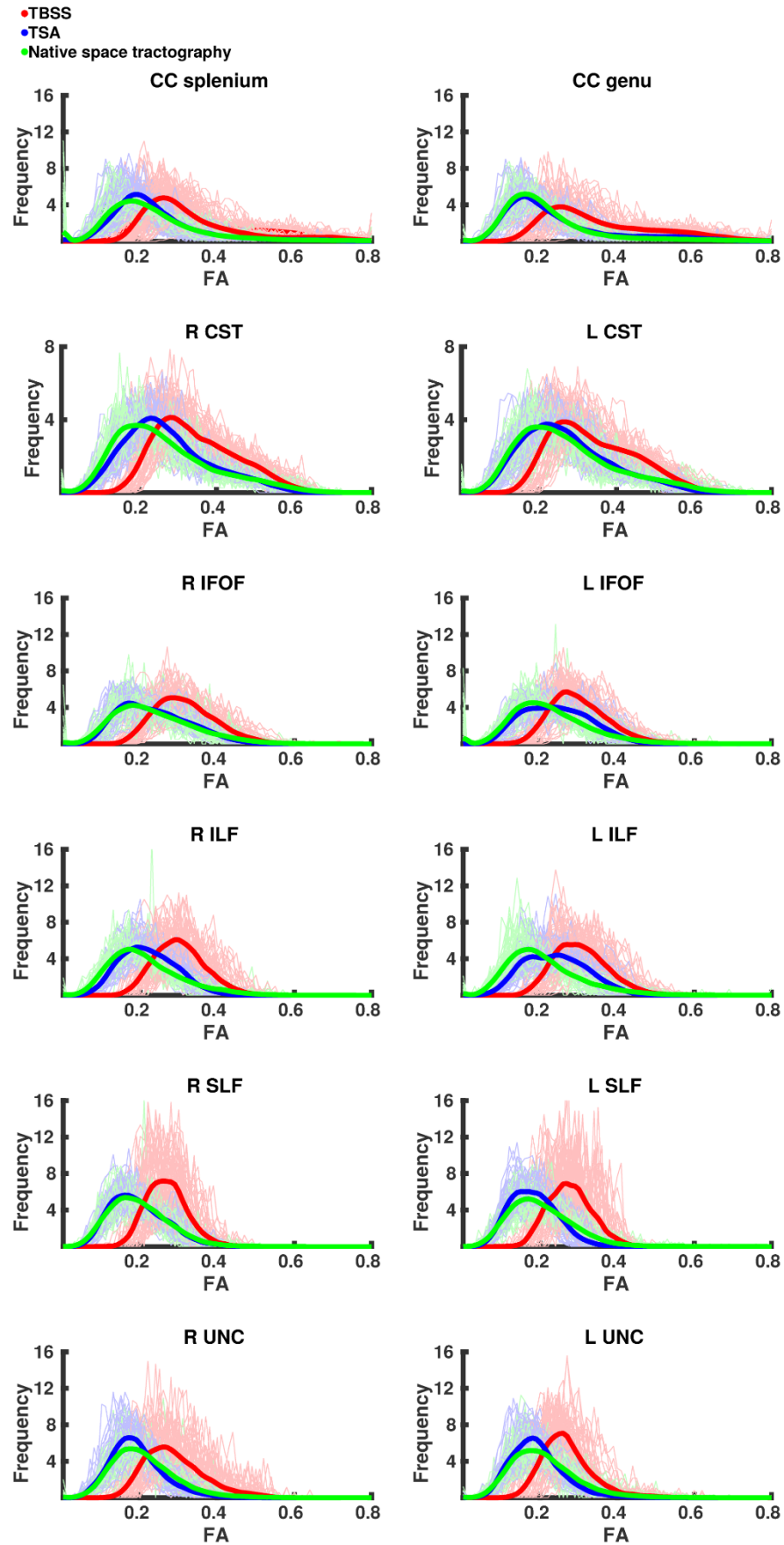


Figure 4.6 The distribution of FA values for all subjects across eight tracts as estimated by native space tractography (green), TSA (blue) and TBSS (red). Normalised histograms for each subject (semi-transparent green, blue and red) were averaged and smoothed to represent the general trend (green, blue and red lines).



## 4.4 Discussion

We have evaluated the performance of TSA in analysing preterm infant dMRI data in comparison to TBSS, with native space tractography as our gold standard. The registration comparison shows that TSA's tensor-based registration improves WM tract alignment over TBSS's scalar-based registration. The results from the data projection step show that TSA can approximate native space tractography FA values more closely than TBSS.

### 4.4.1 Registration comparison

The improvements in alignment seen with TSA's registration are likely to be due to both leveraging the full tensor information and how the template is constructed. Scalar-based registration algorithms discard orientation information, making it difficult to distinguish neighbouring tracts with similar FA values but different orientations, and utilising orientation information during registration significantly improves alignment (Van Hecke et al., 2007). Tensor-based algorithms use the full tensor features resulting in better alignment of the dominant diffusion orientation (Zhang et al., 2007) which may help distinguish neighbouring tracts (Bach et al., 2014). The tensor-based algorithm from TSA has previously been shown to improve registration in adults (Keihaninejad et al., 2013). However infant population registrations require further consideration because the lower contrast and resolution in neonatal scans can be problematic for registration (Ball et al., 2010). Wang et al. (2011) showed that the registration used in TSA outperformed other registration algorithms, including FNIRT, in neonates with Krabbe disease. Their analysis included 10 subjects, was limited to 4 WM regions and did not test the same FNIRT protocol as that used in this study. Here we build on these results in a larger study group and across a wider range of WM fasciculi using a more appropriate metric of assessment.

The registration methods explored here both use a template that is averaged from the study cohort, which improves image alignment accuracy (Van Hecke et al., 2011). The scalar-based registration evaluated here was improved for neonatal populations by introducing an extra linear registration step and registering all the subjects to the mean FA map created after first registering to the most representative subject. This improved alignment over standard TBSS registration, which previously failed for some subjects (Bassi et al., 2008). TSA's algorithm uses an iteratively refined template averaged from all subjects' tensor images. Keihaninejad et al. (2012) showed

that alignment was improved when registering to an iteratively refined template over registering to the mean FA.

Table 4.6 Summary of the Bhattacharyya distances.

Tract		TSA	TBSS	p-value
CC genu	Mean	0.044	0.354	$1.63 \times 10^{-9}$
	SD	0.008	0.091	
CC splenium	Mean	0.043	0.244	$1.63 \times 10^{-9}$
	SD	0.012	0.051	
L CST	Mean	0.031	0.151	$1.85 \times 10^{-9}$
	SD	0.011	0.041	
R CST	Mean	0.036	0.197	$1.63 \times 10^{-9}$
	SD	0.01	0.049	
L ILF	Mean	0.079	0.429	$1.63 \times 10^{-9}$
	SD	0.025	0.106	
R ILF	Mean	0.06	0.388	$1.63 \times 10^{-9}$
	SD	0.033	0.083	
L IFOF	Mean	0.057	0.258	$1.63 \times 10^{-9}$
	SD	0.021	0.058	
R IFOF	Mean	0.047	0.253	$2.88 \times 10^{-9}$
	SD	0.034	0.073	
L SLF	Mean	0.059	0.368	$1.63 \times 10^{-9}$
	SD	0.022	0.087	
R SLF	Mean	0.034	0.348	$1.63 \times 10^{-9}$
	SD	0.015	0.083	
L UNC	Mean	0.044	0.290	$1.63 \times 10^{-9}$
	SD	0.041	0.086	
R UNC	Mean	0.047	0.299	$1.74 \times 10^{-9}$
	SD	0.037	0.065	

Our analysis presents a novel approach to assessing registration accuracy in the neonatal population. Previous studies have focused on using image similarity measures and tissue label overlap scores to assess registration performance. However it has been shown that these are not reliable criteria for establishing registration accuracy and that only local labeled ROIs are able to appropriately distinguish registration performance (Rohlfing, 2012).

We report similar Dice score results to those seen in previous registration comparison studies. Klein et al. (2009) reported similar values in overlap measures in an evaluation of 14 different registration methods with adult subjects. They obtained slightly higher measure of overlap only when looking at larger regions which cover a greater extent of the brain. It should be noted that by looking at smaller local ROIs even small disagreements in overlap can lower the Dice score. Moreover, we are looking at a relatively large age range which may explain the high variability observed in native space tracts.

#### **4.4.2 Data Projection**

We present the first analysis of the concordance between template space data projected onto WM skeletons derived from TSA and TBSS and native space data. The closer agreement between FA values derived from native space tractography and FA values projected by TSA demonstrates that the TSA skeleton model is able to represent more accurately individual subjects' tracts than TBSS. The discrepancy between TSA-projected, TBSS-projected and native space-derived FA values is most likely due to (i) dimensionality reduction in TBSS and TSA from volumetric tracts to voxel-wise skeleton and surface skeleton, respectively; (ii) the projection of the maximum FA value; and (iii) misregistrations between the template and subject. The closer agreement between the values projected by TSA and native space tractography than those projected by TBSS may be due to better-defined stopping criteria for the data projection search in TSA. The search for the maximum FA value in TBSS can cross over into neighbouring tracts (Bach et al., 2014) and the different maturation rates for different tracts during early development (Nossin-Manor et al., 2015) may compound this. Moreover, the data projection in TBSS aligns voxels with the same FA rather than voxels from the same anatomical structure (Zalesky, 2011).

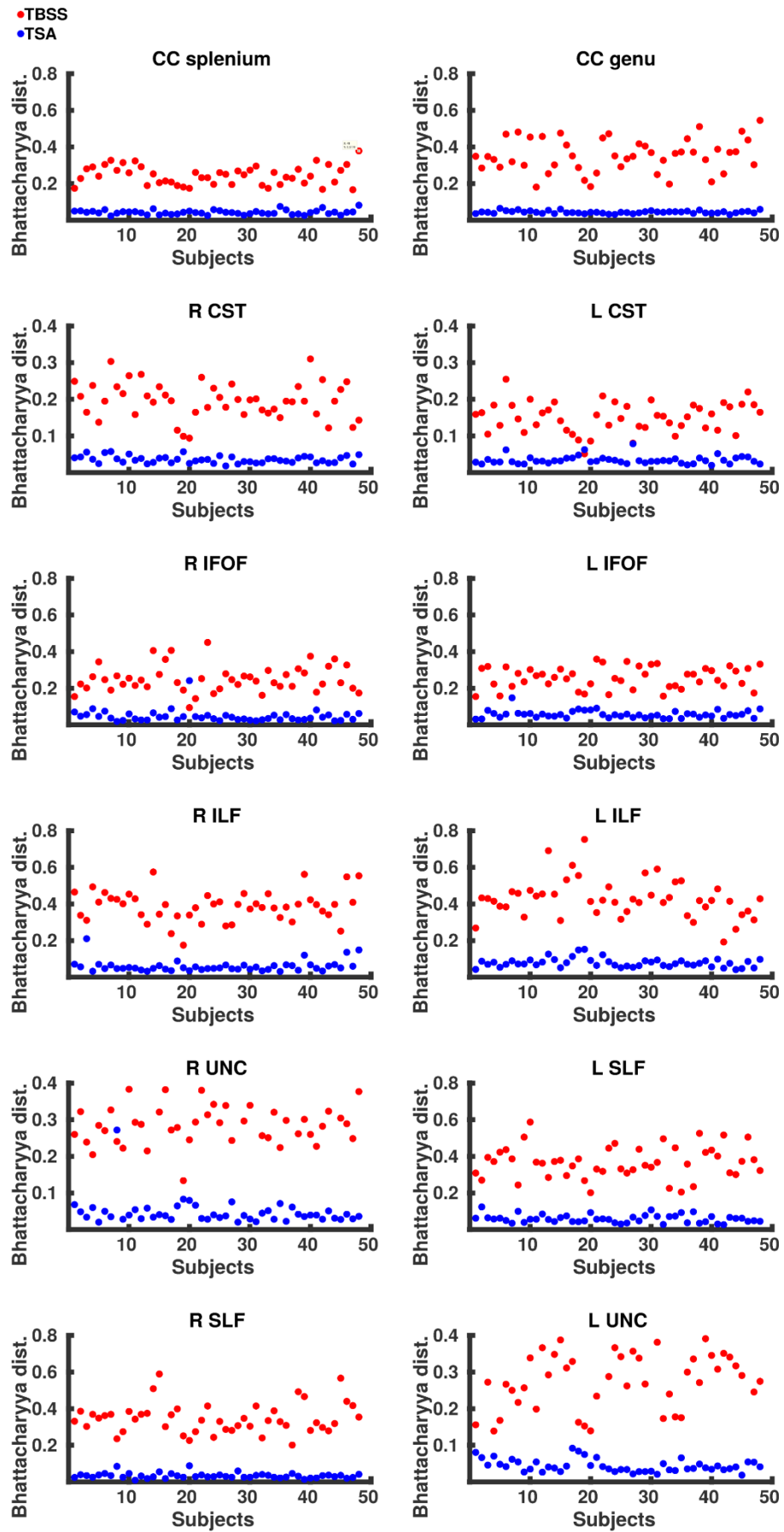


Figure 4.7 The Bhattacharyya distance between native space tractography and TSA (blue) and TBSS (red).

#### 4.4.3 Advantages and limitations of TSA

TSA has several advantages as an analysis tool. It is automated; its surface representations of tracts approximate closely native space diffusion data and TSA offers improved alignment between WM tracts.

A major benefit of TSA is that it is anatomically specific, like other tracts-of-interest methods. Tract-of-interest approaches using tractography have been previously used to study development, averaging DTI values over the whole tract (Berman et al., 2005; Braga et al., 2015; Miller et al., 2002). The axonal configuration of a tract may vary along its length resulting in different diffusion properties at different locations. WM development follows an asynchronous spatiotemporal pattern (Oishi et al., 2011) and differences in FA between subjects born preterm and controls and have been shown to be non-uniform along WM tracts (Groeschel et al., 2014; Travis et al., 2015; Yeatman et al., 2012). In this respect, TSA offers the benefits of anatomically specific analysis with the ability to highlight regions of statistical significance at locations along a tract, and is less likely to obscure localised differences. The downside to using TSA is that the investigator must assume a priori where they expect to observe a change of interest. When no such information is available exploratory, whole-brain analyses like TBSS may be more appropriate.

A possible application of TSA could be to study subjects where tractography is unsuccessful due to brain injury. As the tract skeletons are defined in the template it would be possible to project such subjects' diffusion data onto the skeleton, as long as the registration was successful.

A limitation of TSA, as assessed here, is the geometry it is able to describe. The choice made here, the FACT algorithm for tractography, is motivated by its suitability to the diffusion data at hand (32 gradient directions and a b-value of 750 s/mm<sup>2</sup>).

We have also omitted tracts that have a tubular structure, such as the fornix and cingulum. This is because TSA is ill-suited to such structures. The tract skeleton is determined by thinning the tract-boundary down to a medial surface. This strategy is poorly defined when there are multiple directions in which it is possible to thin, as would be the case for cylindrical structures. For such

tracts, it would be more appropriate to use methods such as those developed by (Corouge et al., 2006; O'Donnell et al., 2009; Yeatman et al., 2012).

A limitation of the analysis presented here is the definition of seed masks for native space tractography. Seed masks were defined by thresholding each subject's FA image at 0.1. While this covered a reasonable portion of the central WM and excluded the cortex, seed and propagation masks derived from tissue segmentations of anatomical scans have been demonstrated to improve the biological accuracy of tractograms (Guevara et al., 2011; Smith et al., 2012). However, for the FACT tracking algorithm, the differences in streamline density and termination points when using a seeding mask derived the diffusion-weighted images and a T1-derived WM mask were minor (Smith et al., 2012), therefore unlikely to affect the overall conclusions of this study.

As part of our evaluation of TSA we have analysed only DTI-derived measures, however the framework allows data from other diffusion models, such as NODDI (Zhang et al., 2012) or g-ratio mapping (Stikov et al., 2015), to be projected onto the skeletons.

## **4.5 Conclusions**

The performance of TSA was evaluated against native space tractography, which serves as the gold standard, using TBSS as a benchmark, for the preterm population. This work demonstrates that TSA is a suitable method for infant studies using dMRI when particular tracts are to be targeted. The framework allows numerous WM tracts to be analysed and, by design, can easily be applied to large cohort studies.

## **Chapter 5 White matter diffusion properties at term equivalent age are associated with subsequent neurodevelopmental performance at 20 months**

This chapter explores the relationship between DTI measures in white matter fasciculi at term equivalent age using TSA in a large cohort of preterm infants. Preterm birth is associated with a high prevalence of neurodevelopmental impairment, related to white matter microstructure in the perinatal period. This analysis demonstrates a correlation between DTI measures and motor and cognitive performance across commissural, projection and association fibres, whereas the relationship between DTI measures and language performance is limited. Furthermore, TSA shows localised effects of prematurity on white matter and widespread maturation-dependent changes.

### **5.1 Introduction**

Between 38-58% of children born extremely preterm have impaired neurodevelopmental outcome (Moore et al., 2012; Serenius et al., 2016), resulting in substantial personal and societal costs. Preterm born individuals experience wide-ranging difficulties including cognitive, behavioural (Bayless and Stevenson, 2007; Bhutta et al., 2002; Delobel-Ayoub et al., 2009; Joseph et al., 2016; Marlow et al., 2005b), motor (Marlow et al., 2007; Williams et al., 2010; Wood et al., 2005), and language impairments (Allin et al., 2008; Guarini et al., 2009; Wolke and Meyer, 1999; Wolke et al., 2008). The neuropathological substrates underlying these impairments remain unclear. Therefore, it is important to identify quantitative measures related to the risk and degree of developmental impairment, and to recognise those infants who may benefit from early interventional therapies. DTI has proven to be an effective tool for detecting WM changes at term-equivalent age (TEA) associated with neurodevelopmental outcome in early childhood (Ball et al., 2015), and has potential as a biomarker for determining efficacy of potential therapies (Milgrom et al., 2010; O'Gorman et al., 2015; Tusor et al., 2012).

The majority of studies investigating the relationship between WM microstructure and outcome have been either ROI-based, tractography-based, or TBSS studies. While tractography and ROI-based studies demonstrate anatomically specific relationships between WM properties and neurodevelopmental performance, they have been limited either in the number of tracts or ROIs investigated (Bassi et al., 2008; De Bruine et al., 2013; Krishnan et al., 2007; Rose et al., 2009; Rose et al., 2007; Roze et al., 2012; Thompson et al., 2012; van Kooij et al., 2011) or have assessed a limited number of subjects (Drobyshevsky et al., 2007). TBSS studies (Counsell et al., 2008; Duerden et al., 2015; Tusor et al., 2012; van Kooij et al., 2012b) are able to assess a large study group and explore whole-brain WM. TBSS, however, has some limitations which have been discussed previously in Chapter 4. A recent study (Young et al., 2016) combined TBSS with the JHU-neonate-SS atlas (Oishi et al., 2011) to achieve an anatomically specific skeleton, however this study reported outcome in only 19 subjects.

The aim of this chapter is to assess the relationship between DTI measures in multiple WM fasciculi at term-equivalent age and motor, cognitive and language performance at 20 months in a large cohort of preterm infants using TSA. Based on previous investigations (Counsell et al., 2008) it is expected that increasing FA and decreasing diffusivities will be associated with improved neurodevelopmental performance.

## **5.2 Methods**

### **5.2.1 Subjects**

Permission for this study was granted by Queen Charlotte's and Hammersmith Hospitals Research Ethics Committee (07/H0704/99) as part of the E-Prime study of preterm brain development. Written parental consent was acquired prior to imaging. We studied 407 infants (206 male) born between 23.6-32.9 (median 30.3) weeks gestational age (GA) and imaged between 37.9-45.9 (median 42.6) weeks postmenstrual age (PMA). The characteristics of the study group are summarised in Table 5.1. T1- and T2-weighted MR images were assessed for the presence of focal brain injury. Motor, cognitive and language performances were assessed using composite scores from the Bayley Scales for Infant and Toddler Development, 3<sup>rd</sup> edition, (BSID-III) at 20 months of age.



Table 5.1 Characteristics of the study group.

<b>Characteristic</b>	
Median (range) gestational age at birth (weeks)	30.3 (23.6-32.9)
Median (range) postmenstrual age at scan (weeks)	42.6 (37.9-45.9)
Median (range) PMA at BSITD-III assessment corrected for prematurity (months)	20 (18-29)
Median (range) birth weight (grams)	1295 (552-2600)
Median (range) days of ventilation (days)	0 (0-40)
Bronchopulmonary dysplasia (no., %)	85 (20.8)
Median (range) days of total parenteral nutrition (days)	6 (0-89)
NEC requiring surgery (no, %)	5 (1.2)
Chorioamnionitis (no., %)	21 (5.2)
PDA requiring medical or surgical treatment (no., %)	20 (4.9)
Median (range) index of multiple deprivation	17.7 (1.7-60.6)

### 5.2.2 MR imaging

MR imaging was performed on a 3T MR system sited on the neonatal intensive care unit. T1- and T2-weighted MR imaging and single shot echo planar dMRI data were acquired under the supervision of a paediatrician experienced in MR imaging procedures as described in Chapter 4.

### 5.2.3 Image processing

Diffusion-weighted images were visually inspected for the presence of motion artefacts and corrupt diffusion weighted volumes were excluded before tensor fitting. 284 subjects had no volumes excluded, 56 subjects had one volume excluded, 30 subjects had two volumes excluded, 12 subjects had three volumes excluded, 7 subjects had four volumes excluded, 9 subjects had five volumes excluded, 1 subject had six volumes excluded, 3 subjects had 7 volumes excluded, 3 subjects had 8 volumes excluded, and 1 subjects had 9 volumes excluded. Non-brain tissue was removed using BET (Smith, 2002), images were corrected for eddy current artefacts using *eddy\_correct* and the tensor model was fitted using *dtifit*, both from FSL (FMRIB, Oxford, <http://fsl.fmrib.ox.ac.uk>).

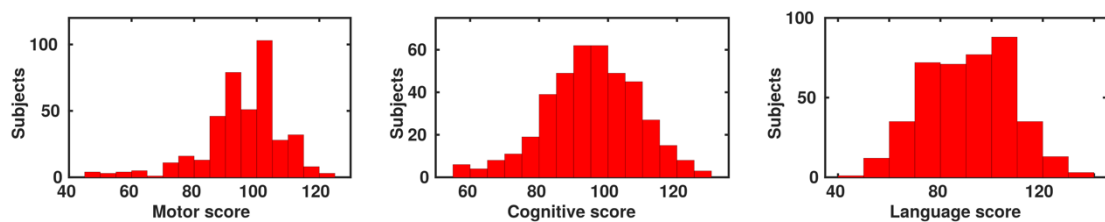


Figure 5.1 Histograms of composite motor, cognitive and language scores from the BSITD-III assessment.

Table 5.2 Focal brain injury observed on T1- and T2-weighted MR imaging.

Lesions (n=35)	No. (%)
Periventricular leukomalacia	9 (2.2)
Haemorrhagic parenchymal infarction	10 (2.5)
Cerebellar haemorrhages	4 (1.0)
Other cystic lesions*	7 (1.7)
Other haemorrhagic lesions**	4 (1.0)
Residual GMH	1 (0.3)

\*Other cystic lesions: left temporal lobe cyst; right anterior periventricular white matter cyst; long cyst adjacent to left ventricle; left posterior periventricular white matter cyst (n=2); right posterior periventricular WM; left caudo-thalamic cyst.

\*\*Other haemorrhagic lesions: haemorrhage in left corona radiata; haemorrhage in occipital cortex; haemorrhages in occipital horn and cerebellum; haemorrhage in right posterior periventricular white matter.

#### 5.2.4 Tract-specific analysis

A study-specific template was created by registering all subjects without focal lesions together to create an iteratively-refined average tensor image (n = 372) (Zhang et al., 2006). The subjects with focal lesions (n=35) were registered to this template. The TSA medial representation model was used to create tract-wise WM skeletons in the template for the bilateral corticospinal tract (CST), inferior fronto-occipital fasciculus (IFOF), inferior longitudinal fasciculus (ILF), superior longitudinal fasciculus (SLF), uncinate fasciculus (UNC) and corpus callosum (CC), as described in Chapter 4. Each subject's registered DTI data were projected onto the WM skeletons. Linear regression analysis carried out on the tract skeletons to assess the relationship between the BSITD-III composite scores for motor, cognitive and language performance at 20 months and FA, AD, RD, MD with GA, PMA, sex and socioeconomic status as covariates. Socioeconomic status (SES) was defined by the index of multiple deprivation. The correlation between prematurity at birth and DTI metrics was also analysed, with PMA and sex as covariates, and the correlation between PMA at scan and DTI measures, with GA and sex as covariates. Multiple comparisons

correction was carried out using non-parametric permutation-based suprathreshold cluster analysis (Nichols and Holmes, 2002) with family-wise error rate (FWER) correction.

## **5.3 Results**

The results for the BSID-III scores are shown in Figure 5.1. Details of focal brain injury observed on T1- and T2-weighted MR imaging are summarised in Table 5.2. The median (range) composite motor, cognitive and language scores were 97 (46-121), 95 (55-130) and 91 (47-135) respectively.

### **5.3.1 Relationship between dMRI measures and motor performance**

There was a significant positive correlation between FA and motor performance in the CST, IFOF, ILF and SLF bilaterally and the body and splenium of the CC, and forceps major shown in Figure 5.2 and Figure 5.3. There was a significant negative correlation between RD, MD and motor performance in the CST, IFOF, ILF bilaterally, the right SLF, and the body and splenium of the CC, shown in Figure 5.4 Figure 5.7. There was a significant negative correlation between AD and motor performance in the body of the CC, right IFOF and the CST bilaterally at the level of the SLF, shown in Figure 5.8 and Figure 5.9, however this was not extensive. There was also a significant positive correlation between AD and motor performance in the poster limb of the internal capsule (PLIC) bilaterally, shown in Figure 5.10 and Figure 5.11. This was the only instance of positive correlation between AD and any outcome measure.

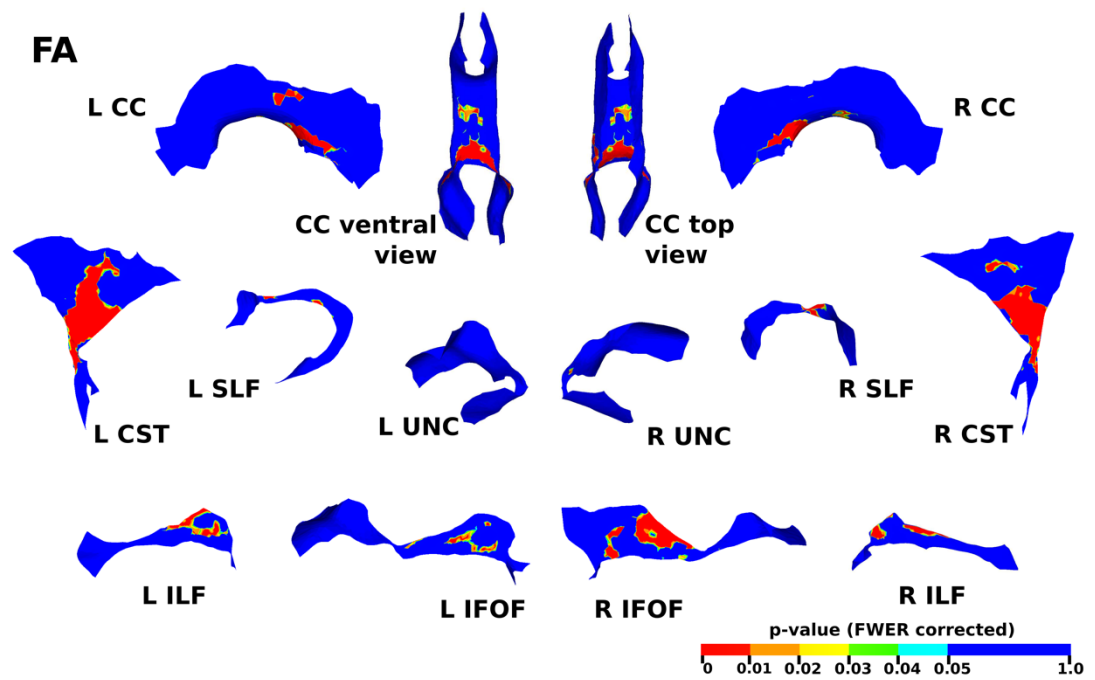


Figure 5.2 The results of the cluster analysis correlating motor scores with FA at each point within the CC, CST, IFOF, ILF, SLF and UNC. Statistically significant regions of positive correlation are shown in red ( $p \leq 0.01$ ), orange ( $0.01 < p \leq 0.02$ ), yellow ( $0.02 < p \leq 0.03$ ), green ( $0.03 < p \leq 0.04$ ) and light blue ( $0.04 < p \leq 0.05$ ).

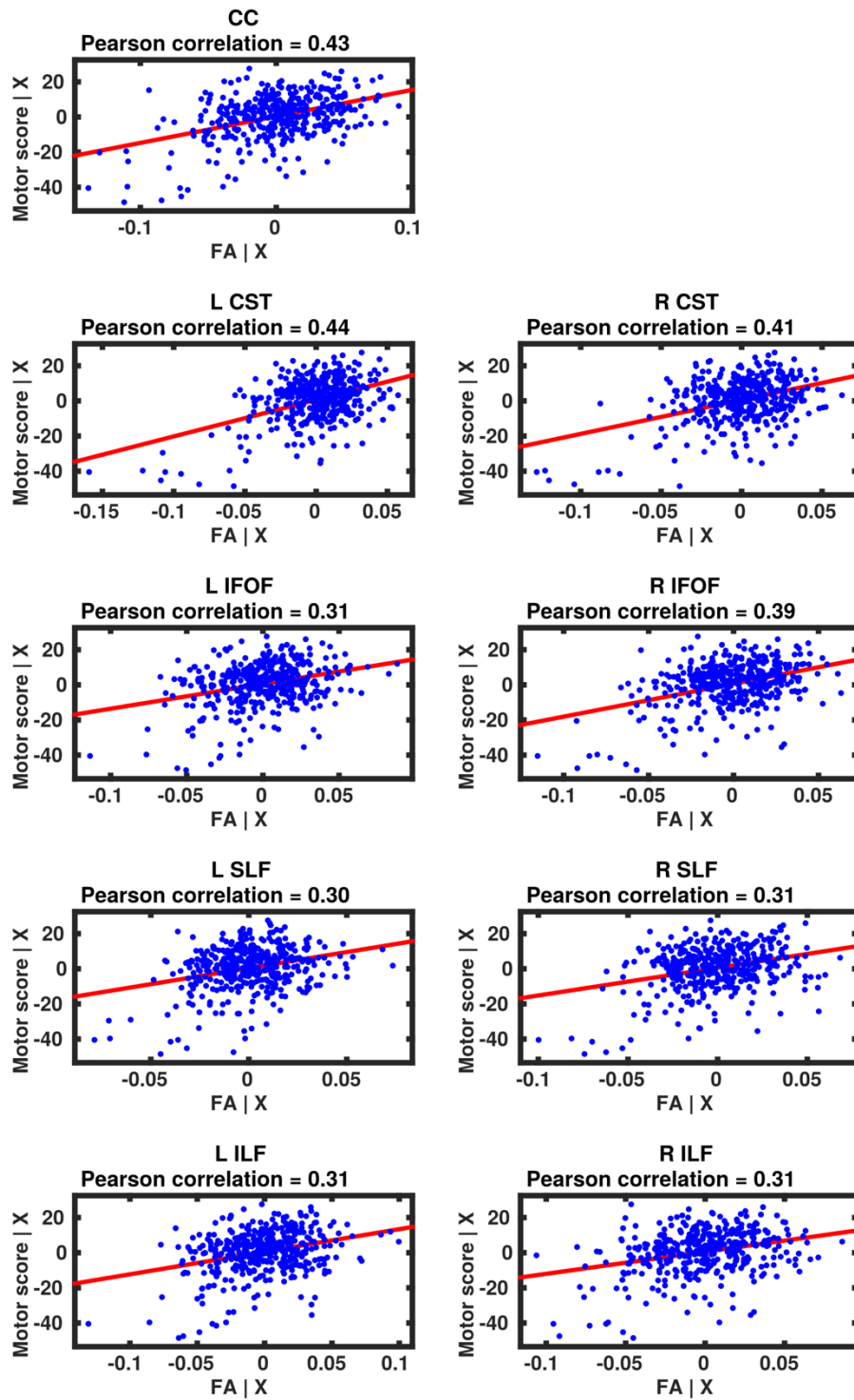


Figure 5.3 Partial regression plots showing the linear relationship between motor scores and FA from the regions showing significant correlation for the CC, CST, IFOF, ILF and SLF. Key: FA | X = residuals of FA given the model; Motor score | X = residuals of motor scores given the model.

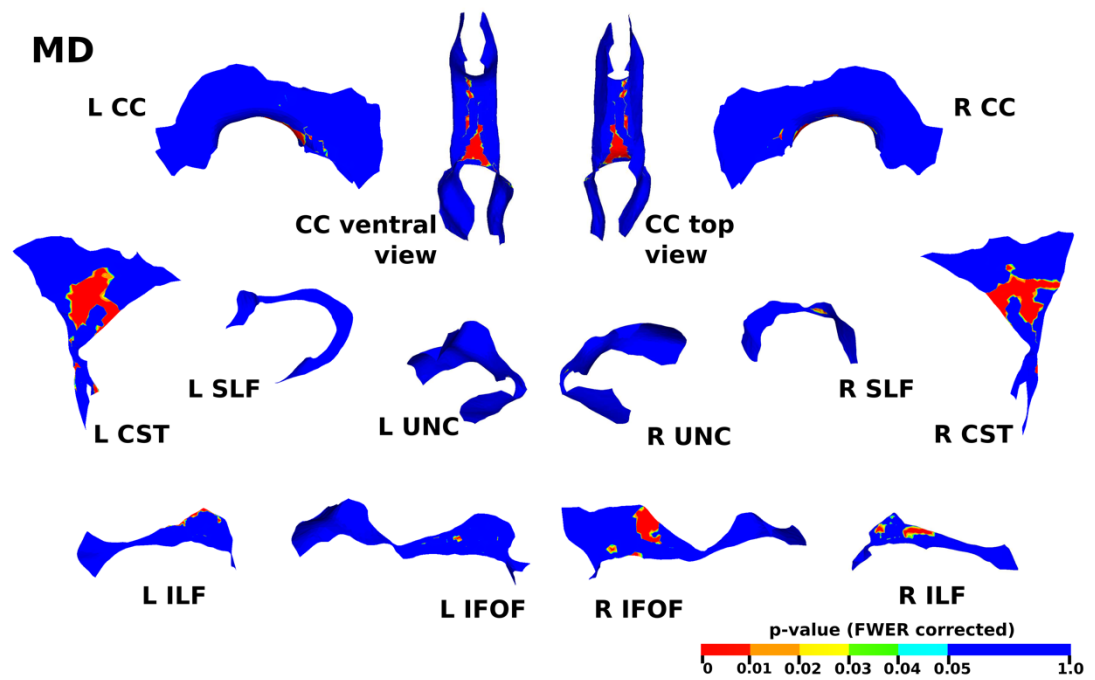


Figure 5.4 The results of the cluster analysis correlating motor scores with MD at each point within the CC, CST, IFOF, ILF, SLF and UNC. Statistically significant regions of negative correlation are shown in red ( $p \leq 0.01$ ), orange ( $0.01 < p \leq 0.02$ ), yellow ( $0.02 < p \leq 0.03$ ), green ( $0.03 < p \leq 0.04$ ) and light blue ( $0.04 < p \leq 0.05$ ).

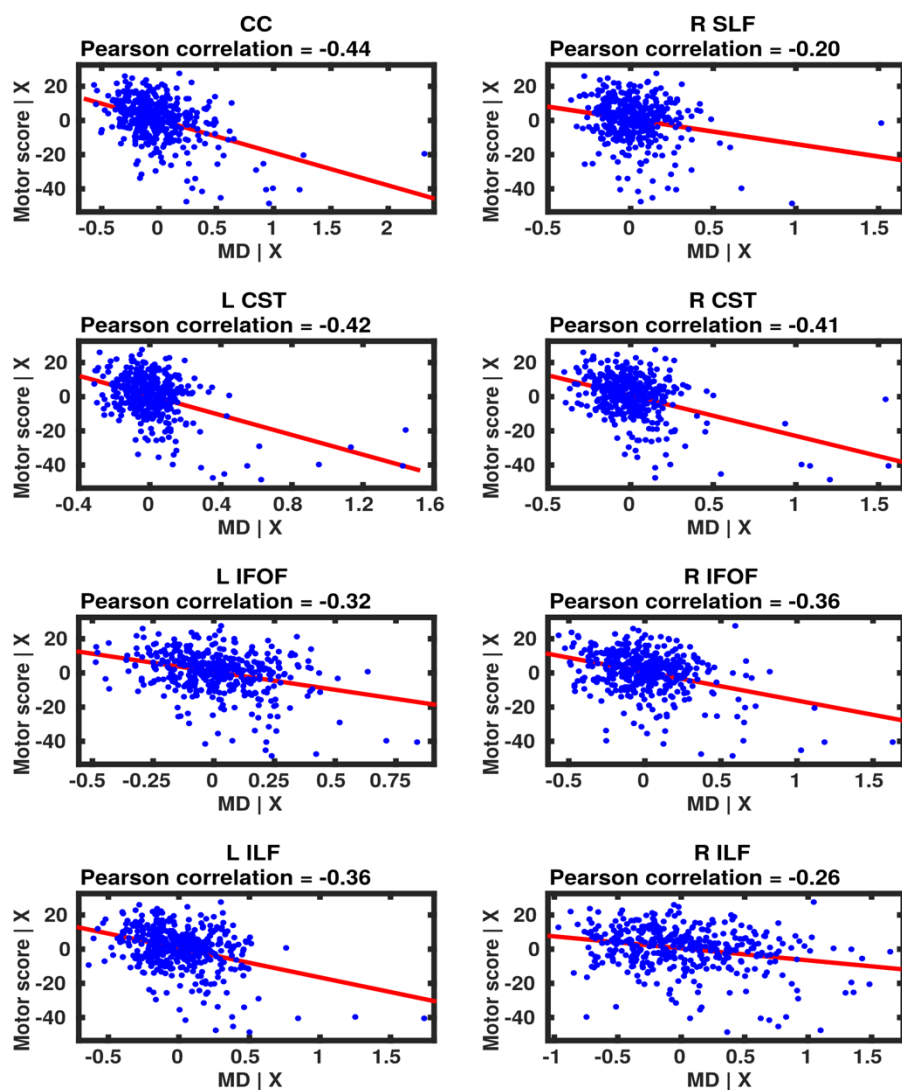


Figure 5.5 Partial regression plots showing the linear relationship between motor scores and MD from the regions showing significant correlation for the CC, CST, IFOF, ILF and right SLF. Key: MD | X = residuals of MD given the model; Motor score | X = residuals of motor scores given the model.

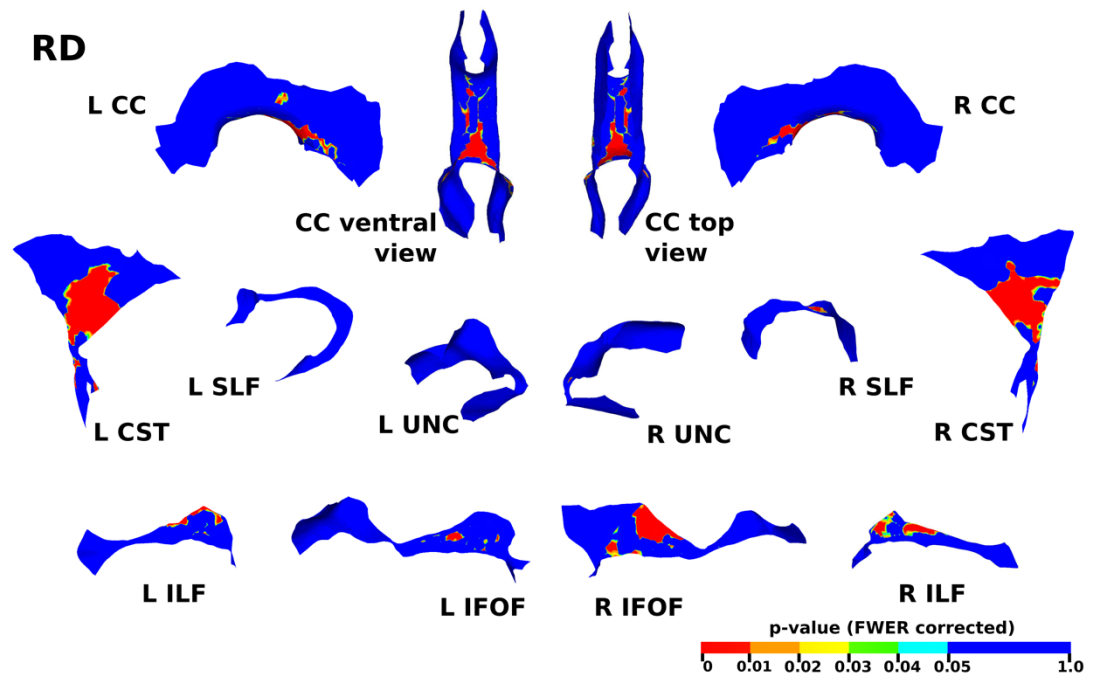


Figure 5.6 The results of the cluster analysis correlating motor scores with RD at each point within the CC, CST, IFOF, ILF, SLF and UNC. Statistically significant regions of negative correlation are shown in red ( $p \leq 0.01$ ), orange ( $0.01 < p \leq 0.02$ ), yellow ( $0.02 < p \leq 0.03$ ), green ( $0.03 < p \leq 0.04$ ) and light blue ( $0.04 < p \leq 0.05$ ).



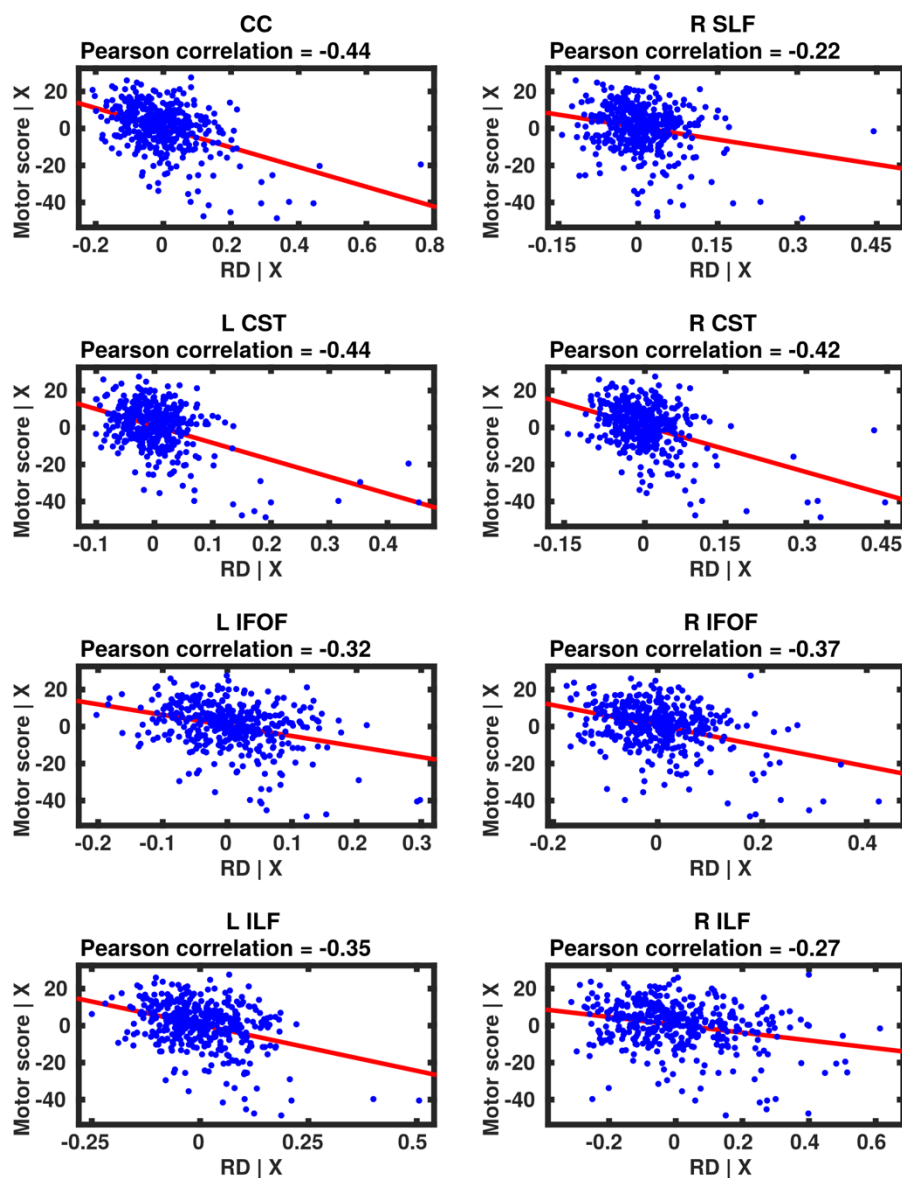


Figure 5.7 Partial regression plots showing the linear relationship between motor scores and RD from the regions showing significant correlation for the CC, CST, IFOF, ILF and right SLF. Key: RD | X = residuals of RD given the model; Motor score | X = residuals of motor scores given the model.

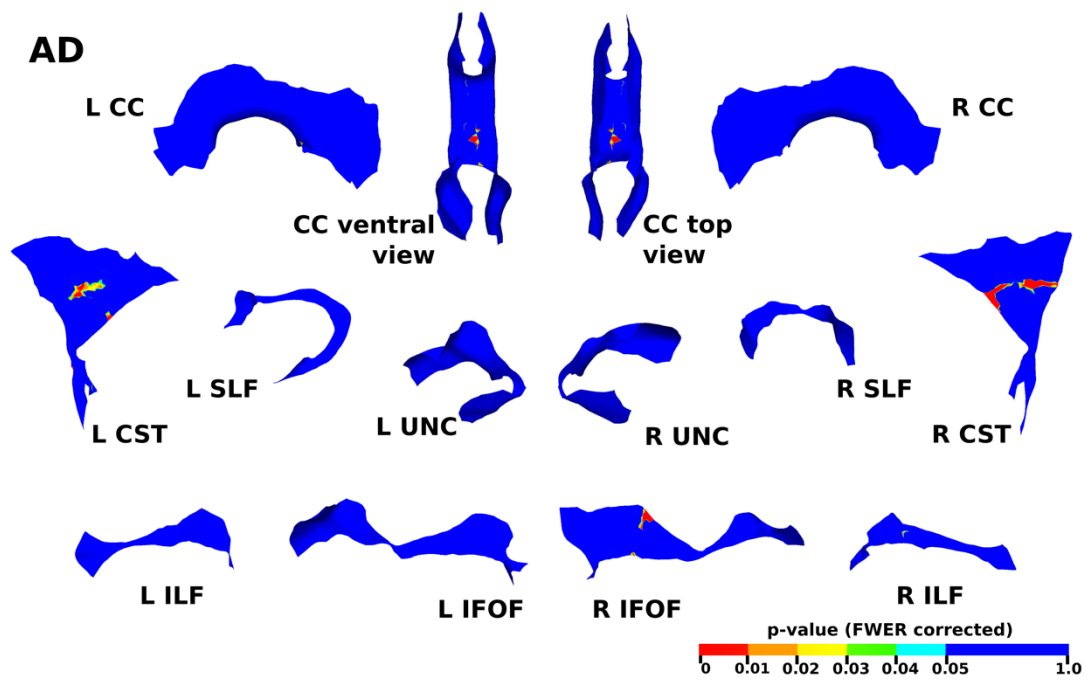


Figure 5.8 The results of the cluster analysis correlating motor scores with AD at each point within the CC, CST, IFOF, ILF, SLF and UNC. Statistically significant regions of negative correlation are shown in red ( $p \leq 0.01$ ), orange ( $0.01 < p \leq 0.02$ ), yellow ( $0.02 < p \leq 0.03$ ), green ( $0.03 < p \leq 0.04$ ) and light blue ( $0.04 < p \leq 0.05$ ).

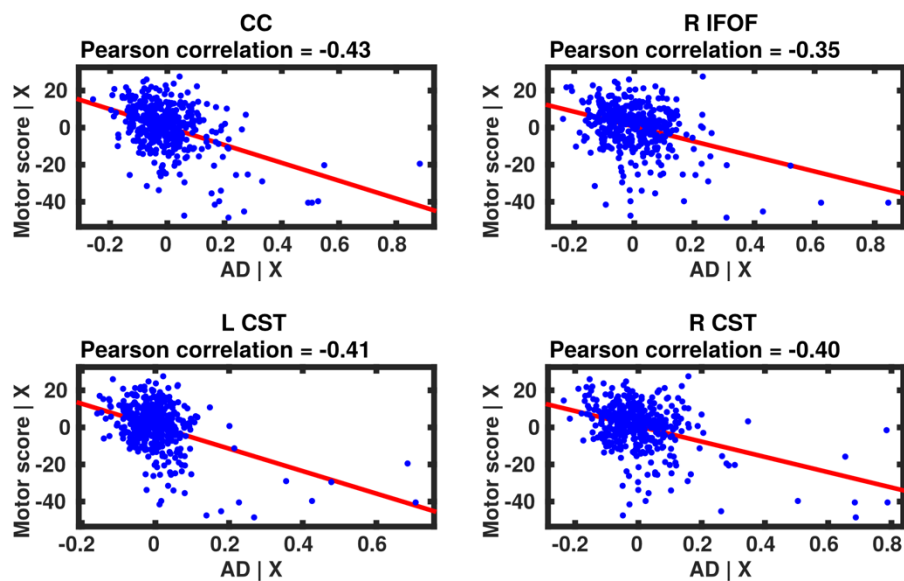


Figure 5.9 Partial regression plots showing the linear relationship between motor scores and AD from the regions showing significant negative correlation for the CC, CST and right IFOF. Key: AD | X = residuals of AD given the model; Motor score | X = residuals of motor scores given the model.

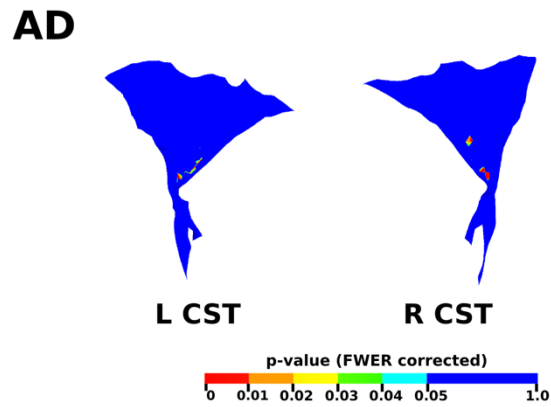


Figure 5.10 The results of the cluster analysis correlating motor scores with AD at each point within the CST. Statistically significant regions of positive correlation are shown in red ( $p \leq 0.01$ ), orange ( $0.01 < p \leq 0.02$ ), yellow ( $0.02 < p \leq 0.03$ ), green ( $0.03 < p \leq 0.04$ ) and light blue ( $0.04 < p \leq 0.05$ ).

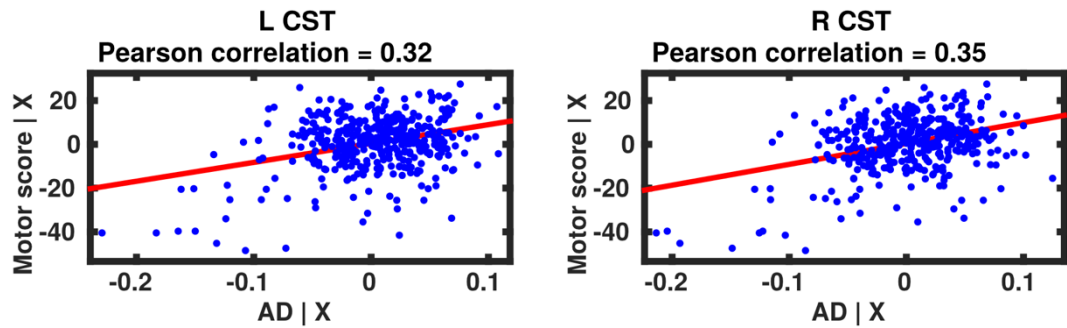


Figure 5.11 Partial regression plots showing the linear relationship between motor scores and AD from the regions showing significant positive correlation for the CST. Key: AD | X = residuals of AD given the model; Motor score | X = residuals of motor scores given the model.

### 5.3.2 Relationship between dMRI measures and cognitive performance

There was a significant positive correlation between FA and cognitive performance in the CST, IFOF, ILF, SLF bilaterally and in the splenium of the CC, shown in Figure 5.12 and Figure 5.13. A significant negative correlation between MD and cognitive scores was found in the PLIC and in CST bilaterally at the level of the SLF, and small regions in the IFOF bilaterally, the right SLF and the right ILF, shown in Figure 5.14 and Figure 5.15. There was a negative correlation between RD and cognitive performance in the CST, IFOF, ILF bilaterally and in the body of the CC, shown in Figure 5.16 and Figure 5.17. AD was negatively correlated with cognitive scores only in the CST bilaterally at the level of the SLF and a small region of the body of the CC, shown in Figure 5.18 and Figure 5.19.

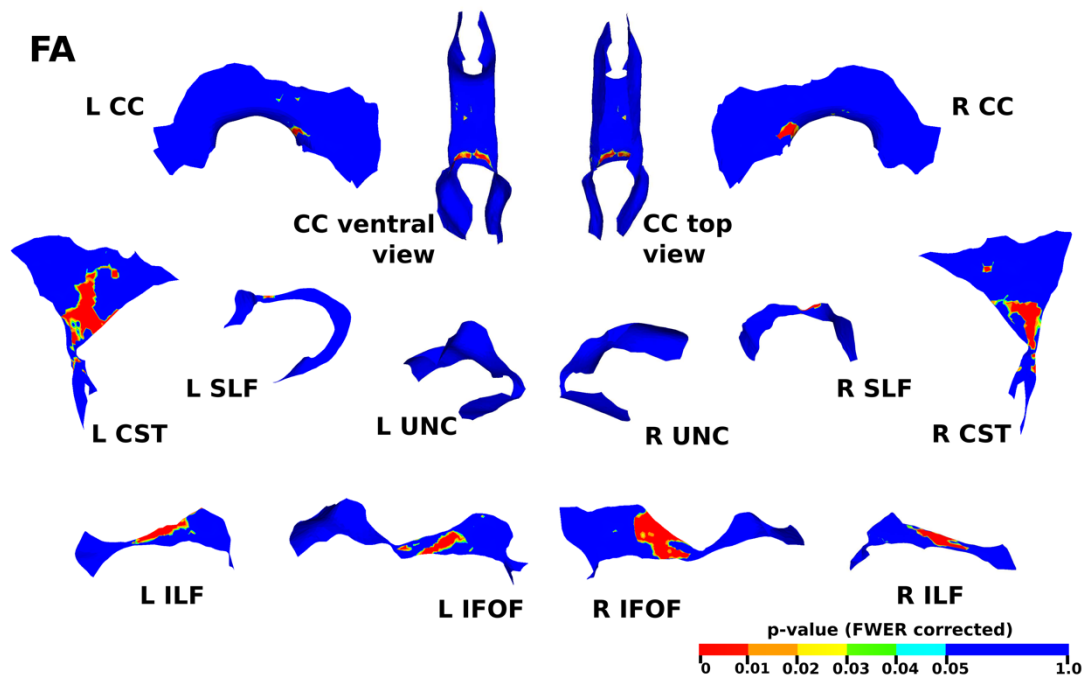


Figure 5.12 The results of the cluster analysis correlating cognitive scores with FA at each point within the CC, CST, IFOF, ILF, SLF and UNC. Statistically significant regions of positive correlation are shown in red ( $p \leq 0.01$ ), orange ( $0.01 < p \leq 0.02$ ), yellow ( $0.02 < p \leq 0.03$ ), green ( $0.03 < p \leq 0.04$ ) and light blue ( $0.04 < p \leq 0.05$ ).

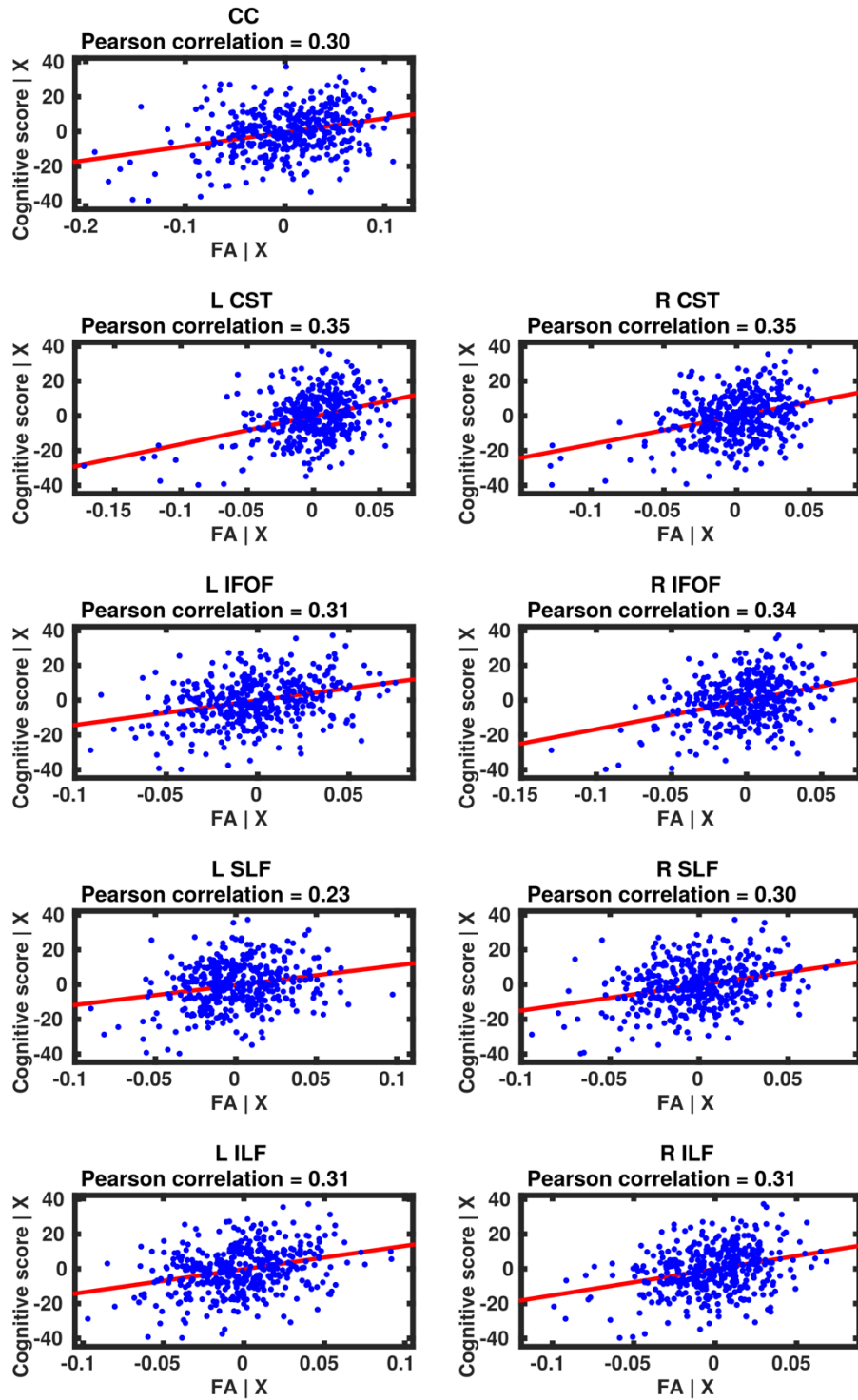


Figure 5.13 Partial regression plots showing the linear relationship between cognitive scores and FA from the regions showing significant correlation for the CC, CST, IFOF, ILF and SLF. Key: FA | X = residuals of FA given the model; Cognitive score | X = residuals of cognitive scores given the model.

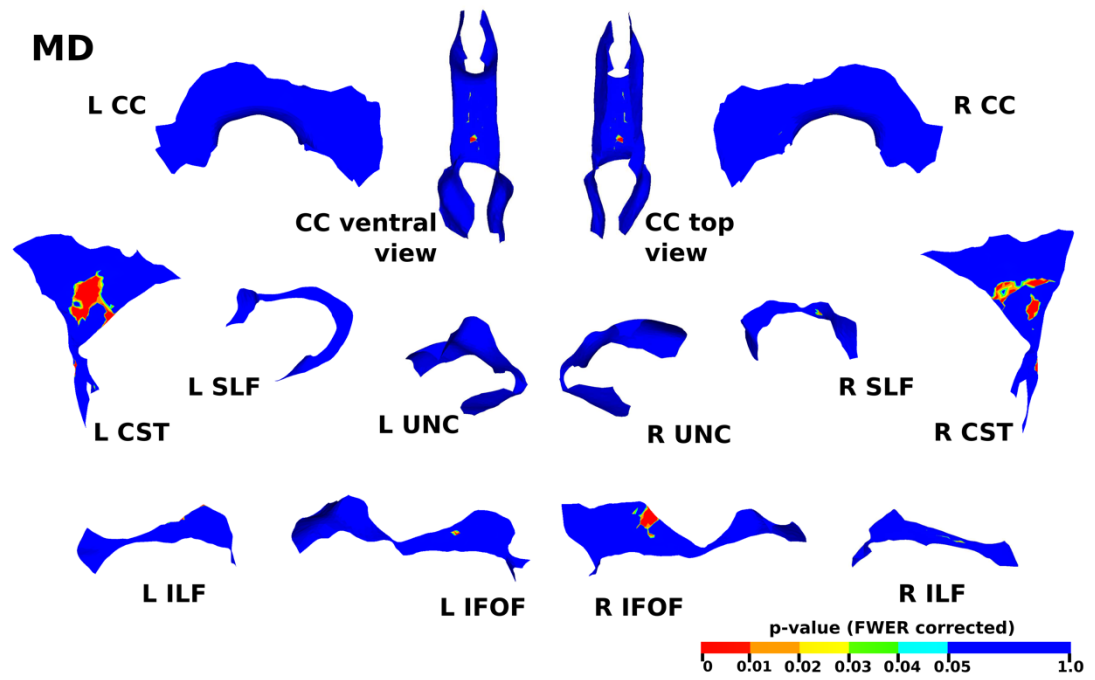


Figure 5.14 The results of the cluster analysis correlating cognitive scores with MD at each point within the CC, CST, IFOF, ILF, SLF and UNC. Statistically significant regions of negative correlation are shown in red ( $p \leq 0.01$ ), orange ( $0.01 < p \leq 0.02$ ), yellow ( $0.02 < p \leq 0.03$ ), green ( $0.03 < p \leq 0.04$ ) and light blue ( $0.04 < p \leq 0.05$ ).

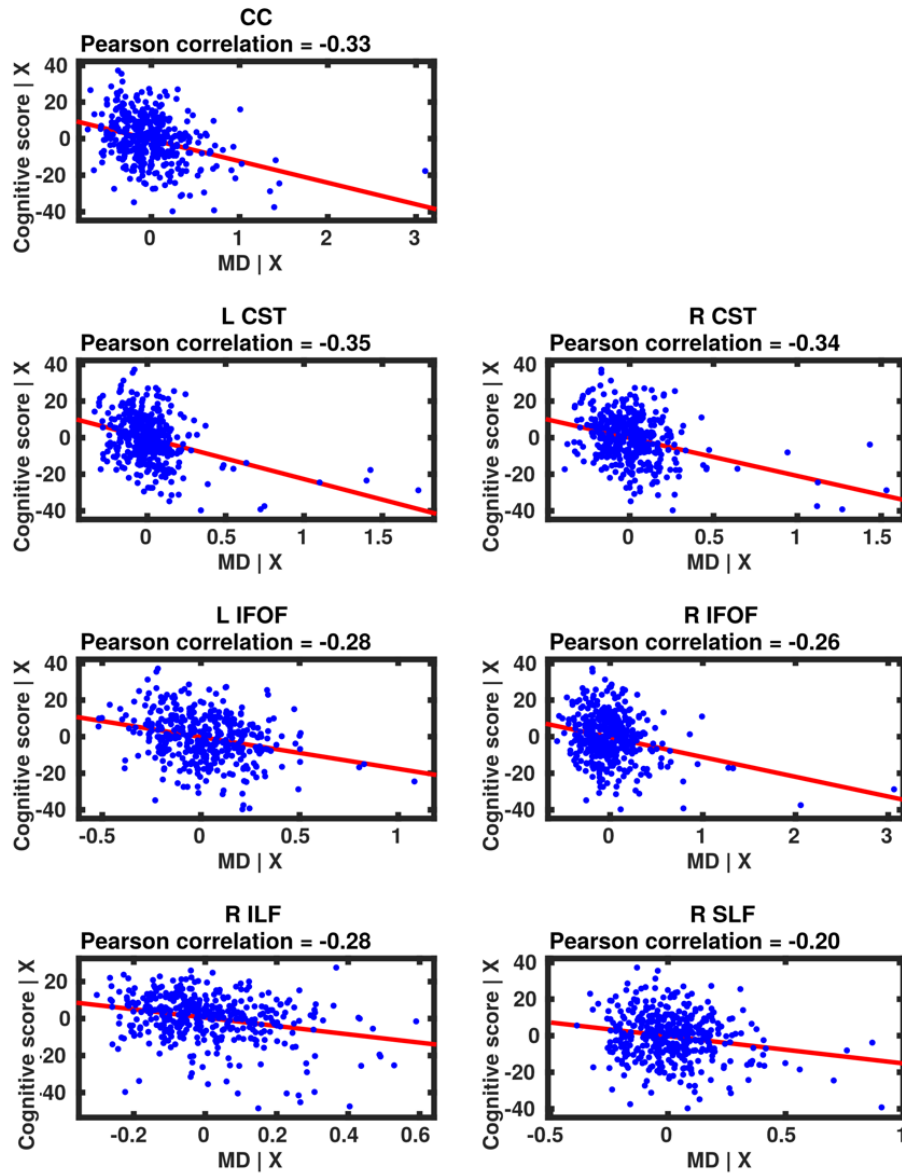


Figure 5.15 Partial regression plots showing the linear relationship between cognitive scores and MD from the regions showing significant correlation for the CC, CST, IFOF, right ILF and right SLF. Key: MD | X = residuals of MD given the model; Cognitive score | X = residuals of cognitive scores given the model.

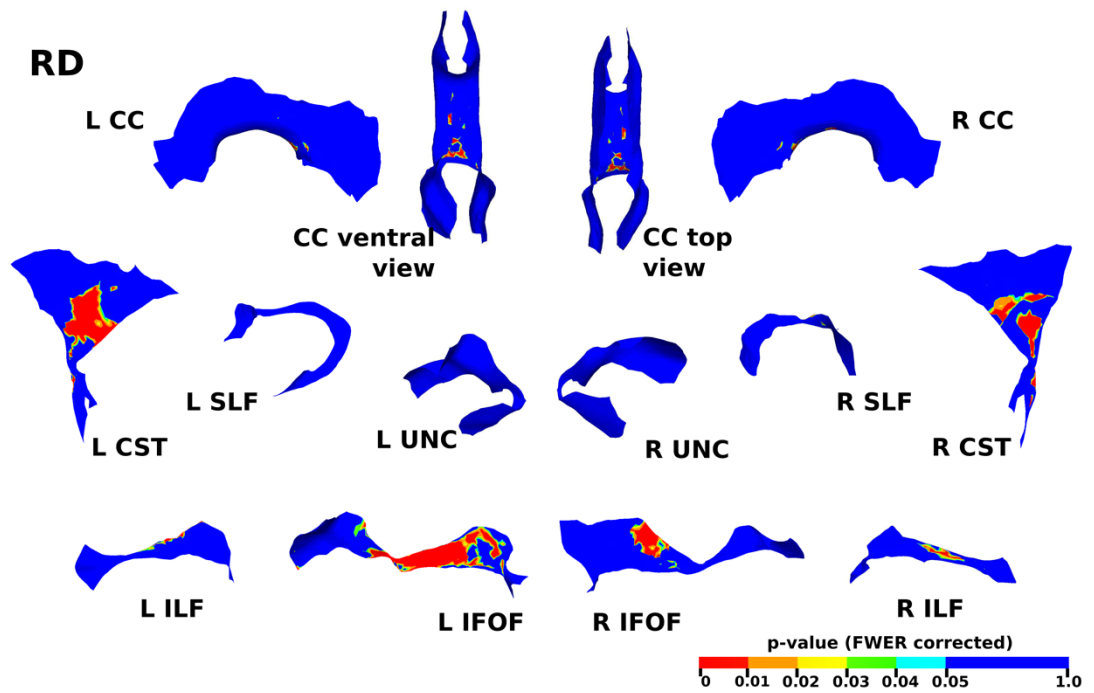


Figure 5.16 The results of the cluster analysis correlating cognitive scores with RD at each point within the CC, CST, IFOF, ILF, SLF and UNC. Statistically significant regions of negative correlation are shown in red ( $p \leq 0.01$ ), orange ( $0.01 < p \leq 0.02$ ), yellow ( $0.02 < p \leq 0.03$ ), green ( $0.03 < p \leq 0.04$ ) and light blue ( $0.04 < p \leq 0.05$ ).



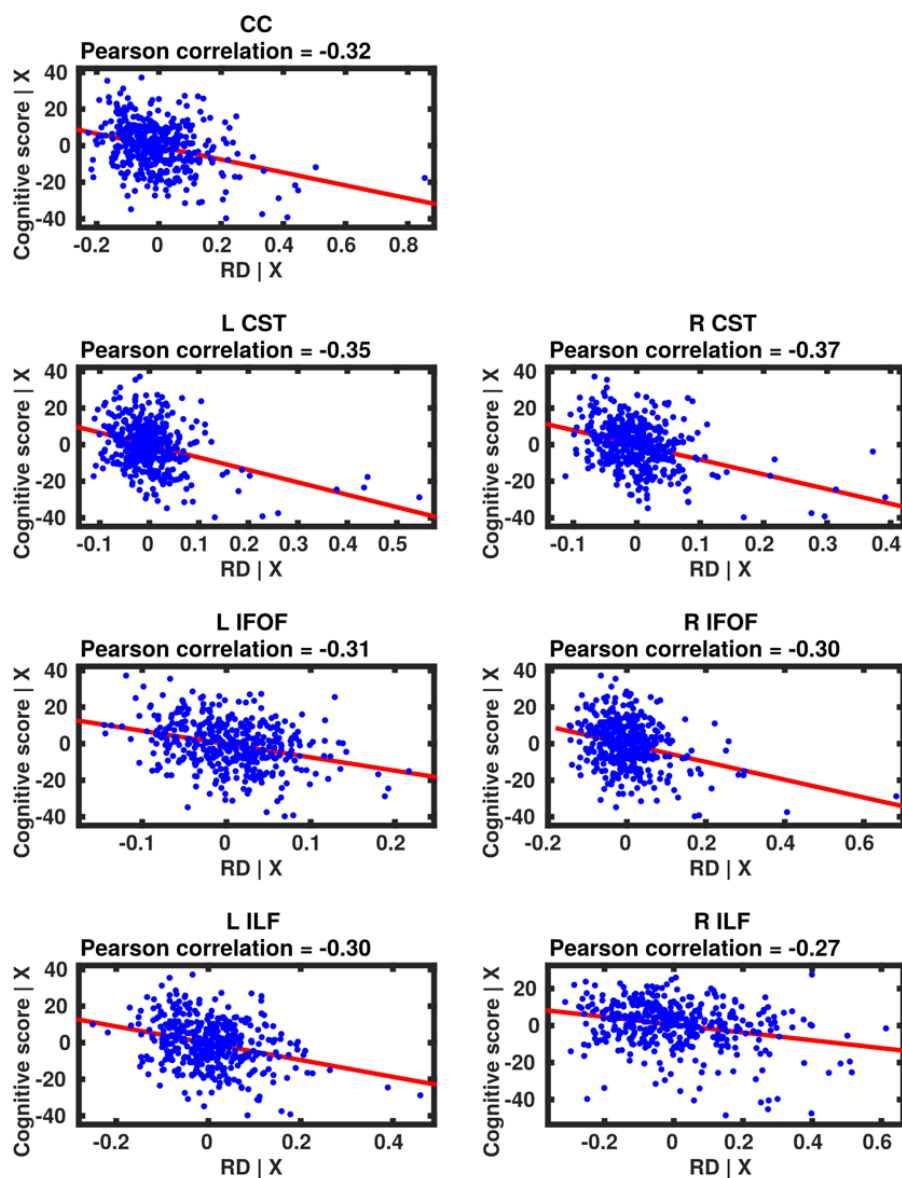


Figure 5.17 Partial regression plots showing the linear relationship between cognitive scores and RD from the regions showing significant correlation for the CC, CST, IFOF and ILF. Key: RD | X = residuals of RD given the model; Cognitive score | X = residuals of cognitive scores given the model.

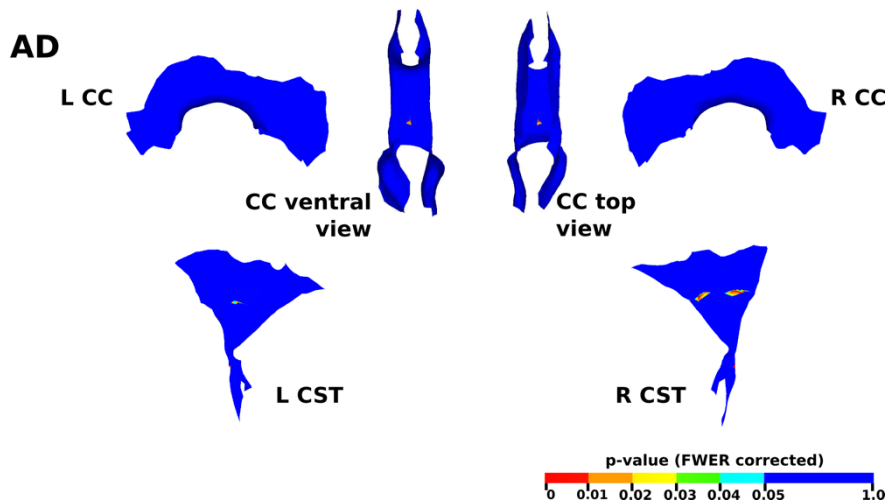


Figure 5.18 The results of the cluster analysis correlating cognitive scores with AD at each point within the CC and CST. Statistically significant regions of negative correlation are shown in red ( $p \leq 0.01$ ), orange ( $0.01 < p \leq 0.02$ ), yellow ( $0.02 < p \leq 0.03$ ), green ( $0.03 < p \leq 0.04$ ) and light blue ( $0.04 < p \leq 0.05$ ).

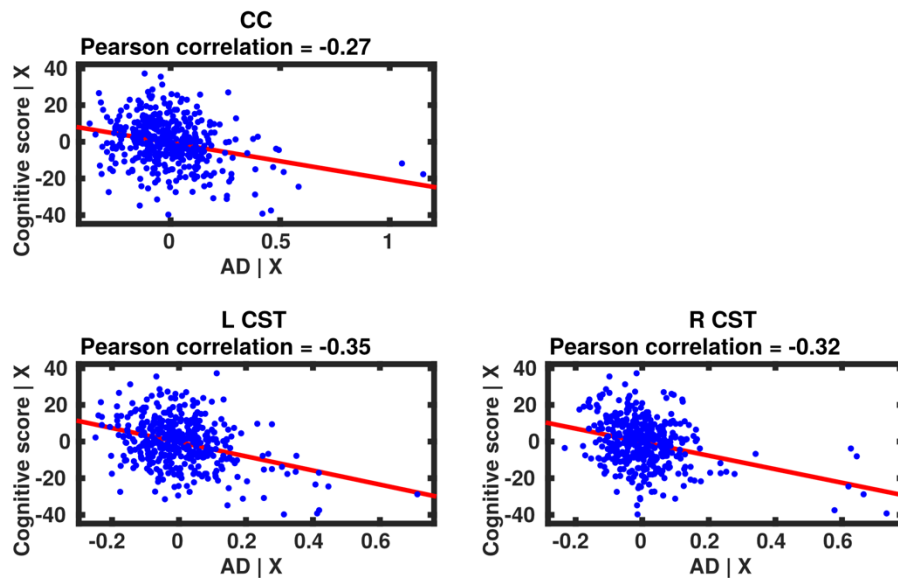


Figure 5.19 Partial regression plots showing the linear relationship between cognitive scores and AD from the regions showing significant correlation for the CC and CST. Key: AD | X = residuals of AD given the model; Cognitive score | X = residuals of cognitive scores given the model.

### 5.3.3 Relationship between dMRI measures and language performance

Significant correlations between DTI measures and language scores were limited. There was a significant positive correlation between FA and language scores in small regions in the left IFOF and the ILF bilaterally, shown in Figure 5.20 and Figure 5.21, a negative correlation with MD in the left CST and right ILF and negative correlation between RD in left CST, shown in Figure 5.22 and Figure 5.24. AD was not significantly associated with language performance in any region.

#### FA

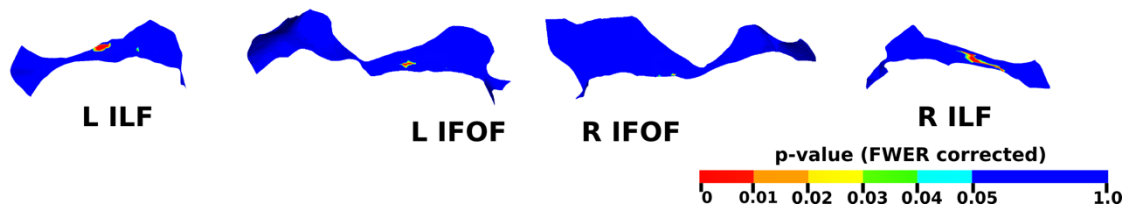


Figure 5.20 The results of the cluster analysis correlating language scores with FA at each point within the IFOF and ILF. Statistically significant regions of positive correlation are shown in red ( $p \leq 0.01$ ), orange ( $0.01 < p \leq 0.02$ ), yellow ( $0.02 < p \leq 0.03$ ), green ( $0.03 < p \leq 0.04$ ) and light blue ( $0.04 < p \leq 0.05$ ).

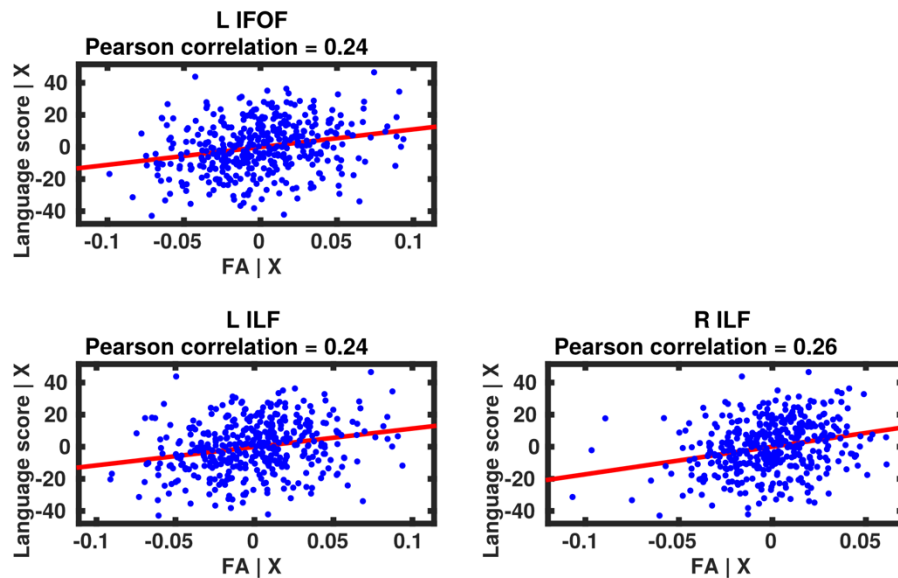


Figure 5.21 Partial regression plots showing the linear relationship between language scores and FA from the regions showing significant correlation for the ILF and left IFOF. Key: FA | X = residuals of FA given the model; Language score | X = residuals of language scores given the model.

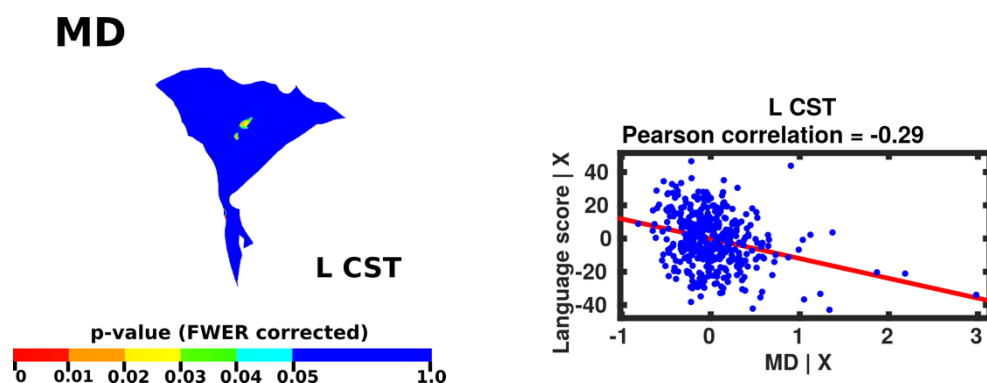


Figure 5.22 The results of the cluster analysis correlating language scores with MD at each point within the left CST. Statistically significant regions of negative correlation are shown in red ( $p \leq 0.01$ ), orange ( $0.01 < p \leq 0.02$ ), yellow ( $0.02 < p \leq 0.03$ ), green ( $0.03 < p \leq 0.04$ ) and light blue ( $0.04 < p \leq 0.05$ ) and partial regression plot showing from the regions showing significant correlation. Key: MD | X = residuals of MD given the model; Language score | X = residuals of language scores given the model.

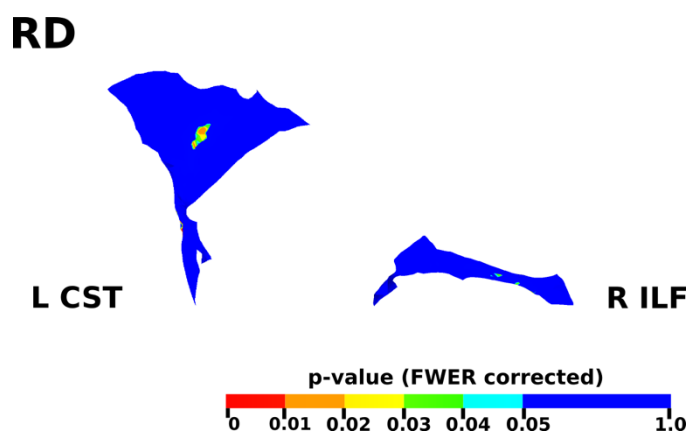


Figure 5.23 The results of the cluster analysis correlating language scores with RD at each point within the left CST and right ILF. Statistically significant regions of negative correlation are shown in red ( $p \leq 0.01$ ), orange ( $0.01 < p \leq 0.02$ ), yellow ( $0.02 < p \leq 0.03$ ), green ( $0.03 < p \leq 0.04$ ) and light blue ( $0.04 < p \leq 0.05$ ).

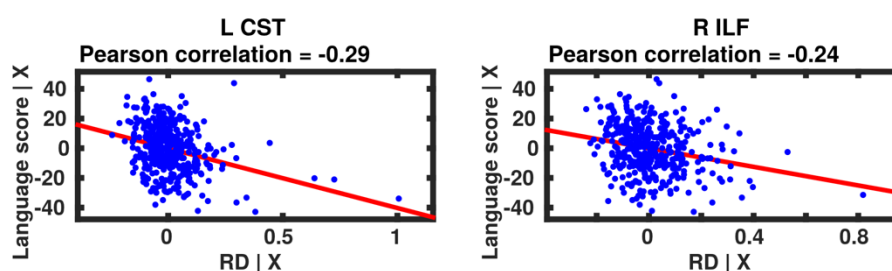


Figure 5.24 Partial regression plots showing the linear relationship between language scores and RD from the regions showing significant correlation for the left CST and right ILF. Key: RD | X = residuals of RD given the model; Language score | X = residuals of language scores given the model.

### 5.3.4 Relationship between dMRI measures and gestational age at birth

Gestational age at birth was correlated positively with FA in the IFOF, ILF, SLF bilaterally and the body of the CC, shown in Figure 5.25 and Figure 5.26. There was a similar pattern of negative correlation between RD and MD and GA at birth in the IFOF and ILF bilaterally, the right SLF and the body of the CC, and only very small regions of the CST, shown in Figure 5.27 to Figure 5.30. Negative correlation between AD and GA was found only in the IFOF and ILF bilaterally, shown in Figure 5.31 and Figure 5.32.

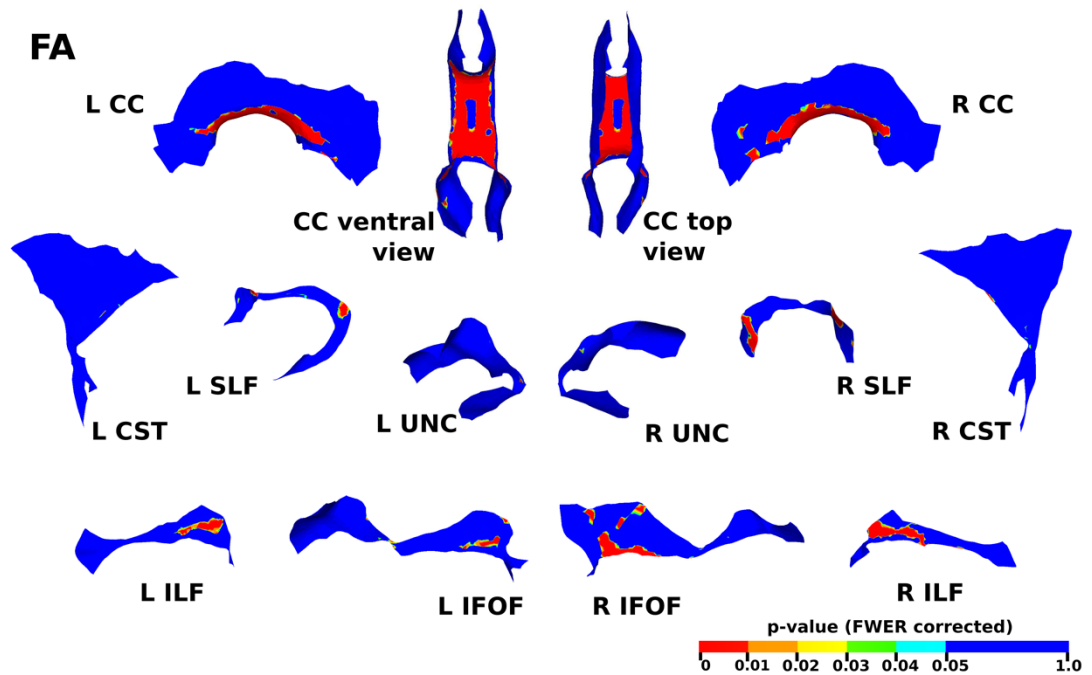


Figure 5.25 The results of the cluster analysis correlating GA at birth with FA at each point within the CC, CST, IFOF, ILF, SLF and UNC. Statistically significant regions of positive correlation are shown in red ( $p \leq 0.01$ ), orange ( $0.01 < p \leq 0.02$ ), yellow ( $0.02 < p \leq 0.03$ ), green ( $0.03 < p \leq 0.04$ ) and light blue ( $0.04 < p \leq 0.05$ ).

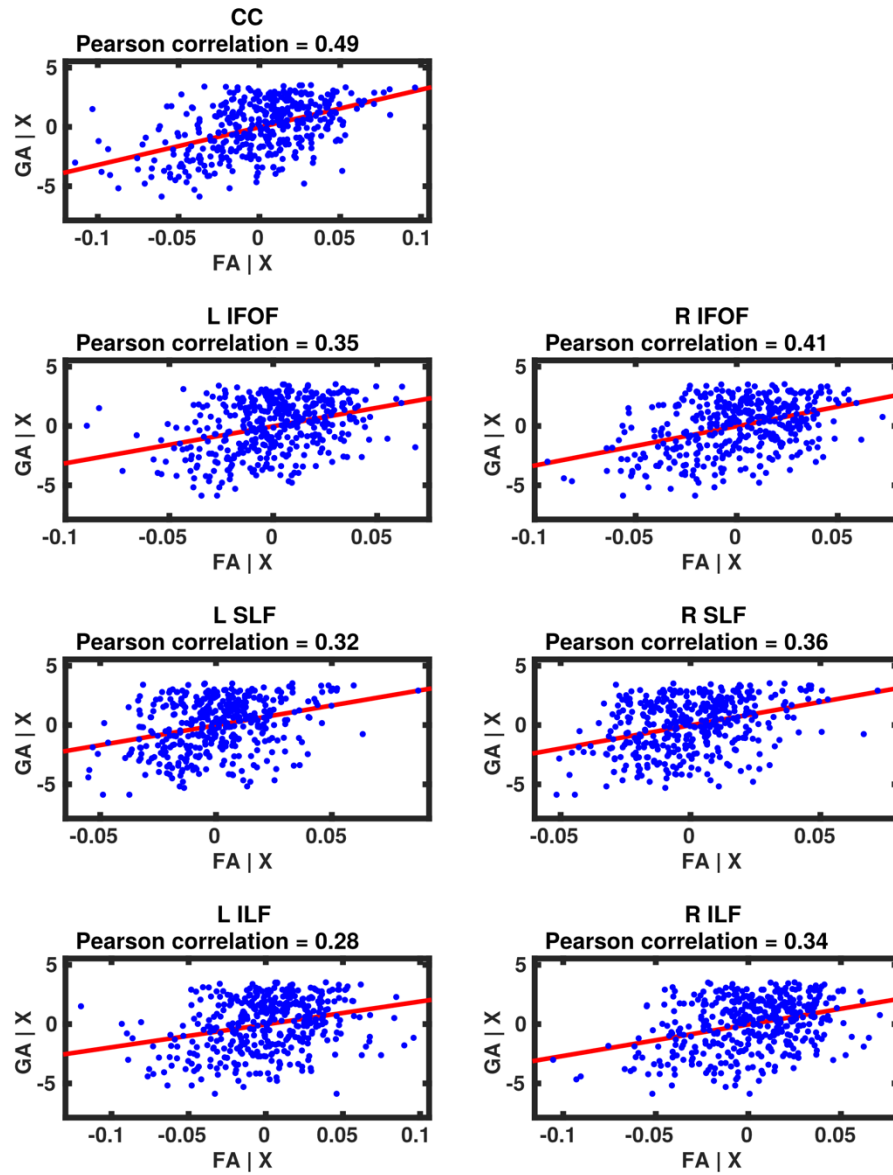


Figure 5.26 Partial regression plots showing the linear relationship between GA at birth and FA from the regions showing significant correlation for the CC, IFOF, ILF and SLF. Key:  $FA | X$  = residuals of FA given the model;  $GA | X$  = residuals of GA given the model

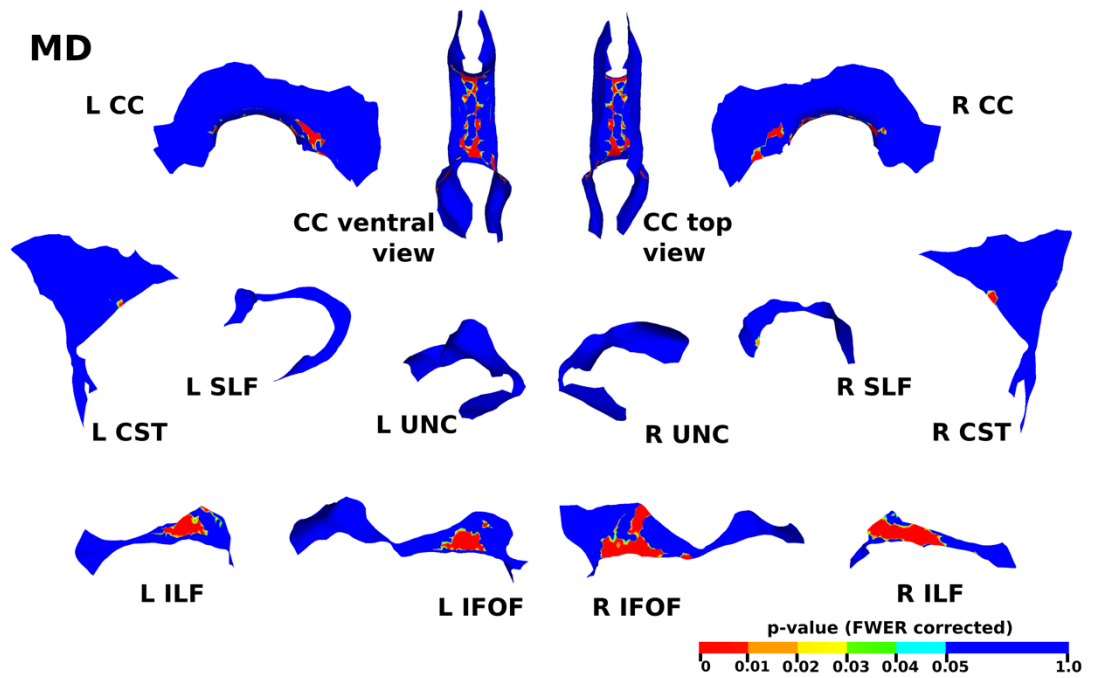


Figure 5.27 The results of the cluster analysis correlating GA at birth with MD at each point within the CC, CST, IFOF, ILF, SLF and UNC. Statistically significant regions of negative correlation are shown in red ( $p \leq 0.01$ ), orange ( $0.01 < p \leq 0.02$ ), yellow ( $0.02 < p \leq 0.03$ ), green ( $0.03 < p \leq 0.04$ ) and light blue ( $0.04 < p \leq 0.05$ ).

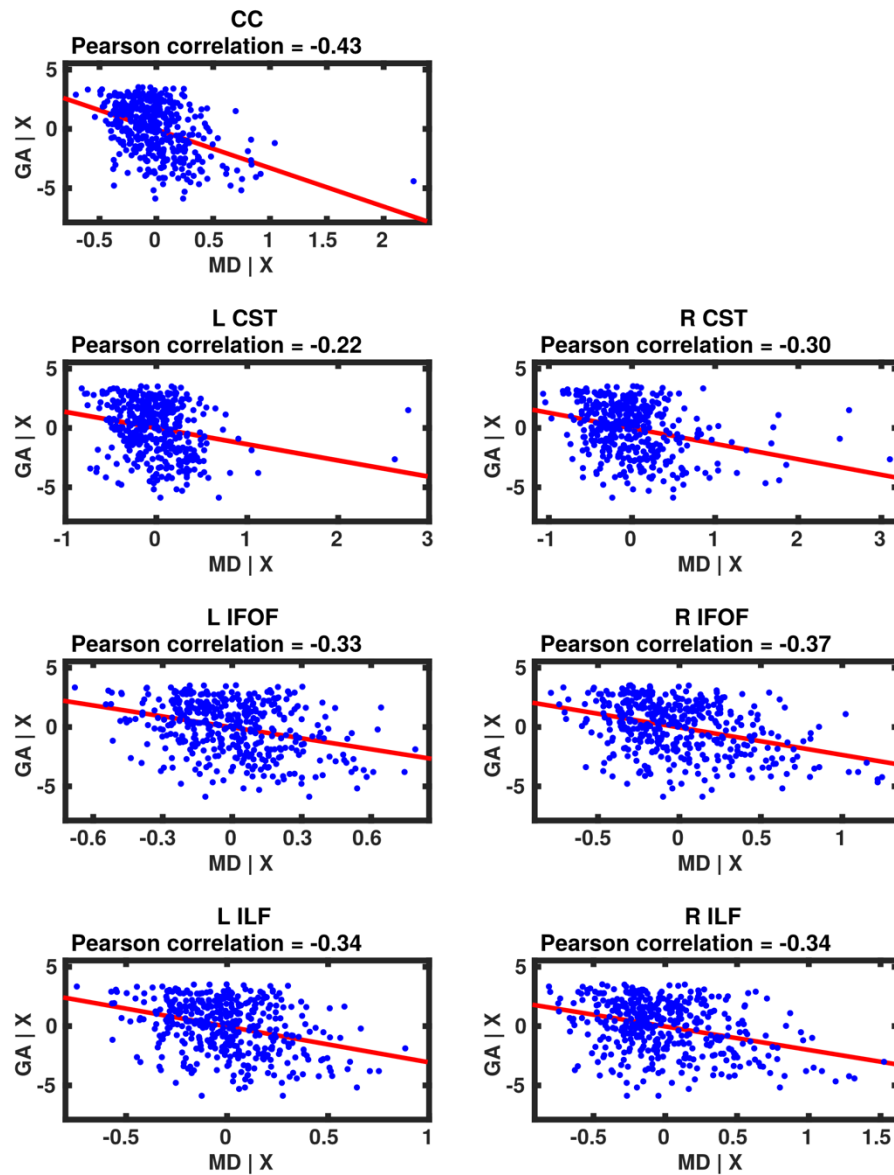


Figure 5.28 Partial regression plots showing the linear relationship between GA at birth and MD from the regions showing significant correlation for the CC, CST, IFOF and ILF. Key: MD | X = residuals of MD given the model; GA | X = residuals of GA given the model



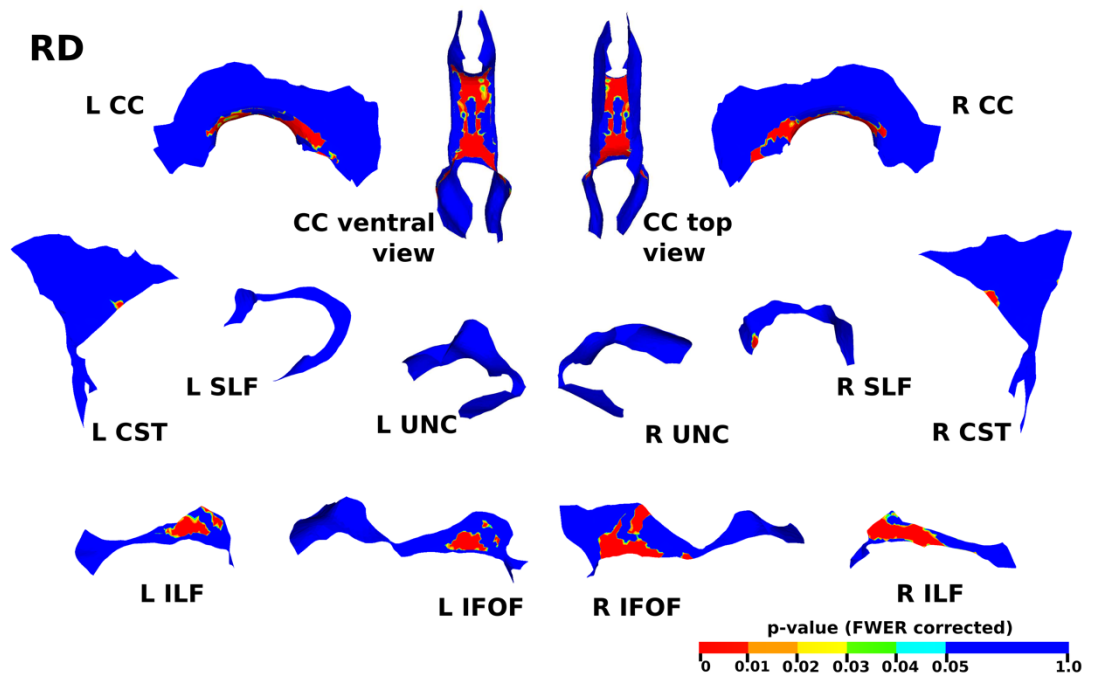


Figure 5.29 The results of the cluster analysis correlating GA at birth with RD at each point within the CC, CST, IFOF, ILF, SLF and UNC. Statistically significant regions of negative correlation are shown in red ( $p \leq 0.01$ ), orange ( $0.01 < p \leq 0.02$ ), yellow ( $0.02 < p \leq 0.03$ ), green ( $0.03 < p \leq 0.04$ ) and light blue ( $0.04 < p \leq 0.05$ ).

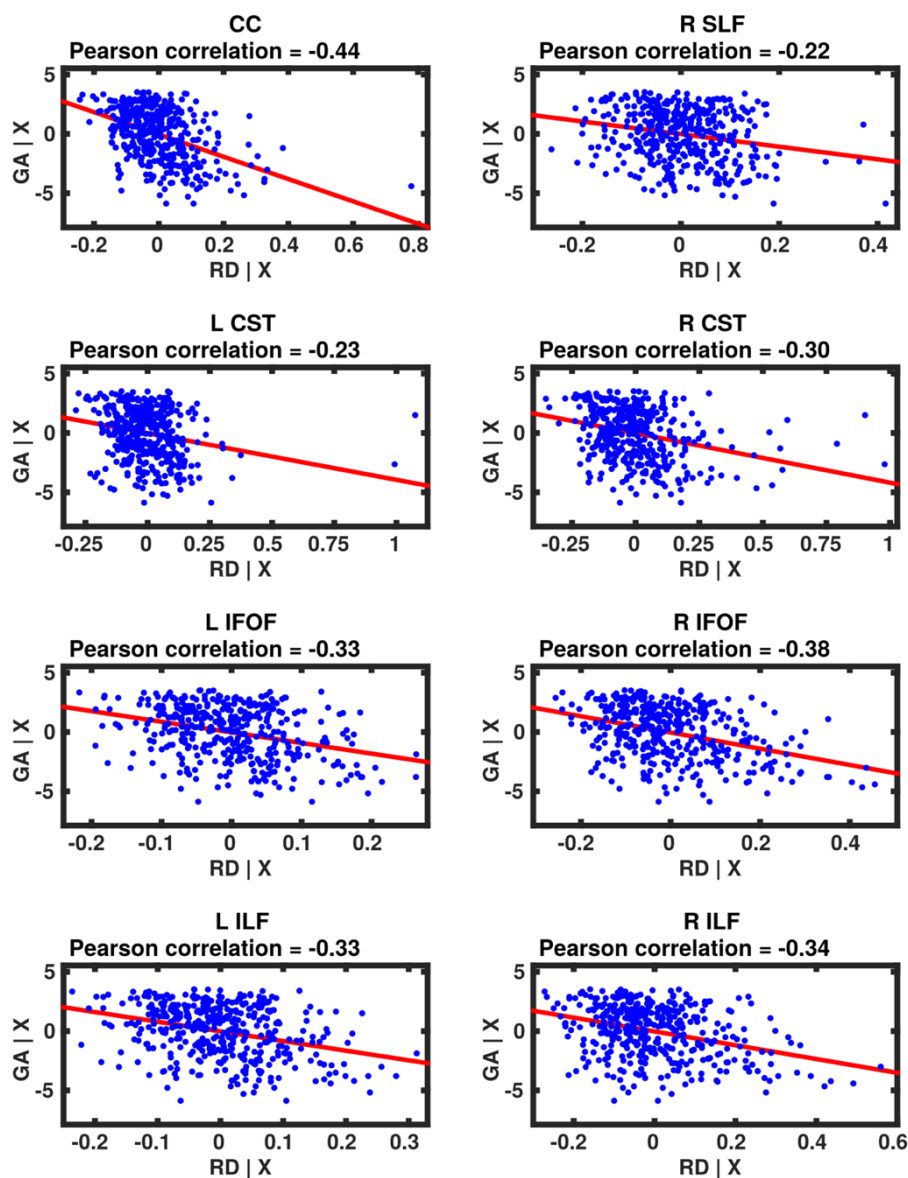


Figure 5.30 Partial regression plots showing the linear relationship between GA at birth and RD from the regions showing significant correlation for the CC, CST, IFOF and ILF. Key: RD | X = residuals of RD given the model; GA | X = residuals of GA given the model.

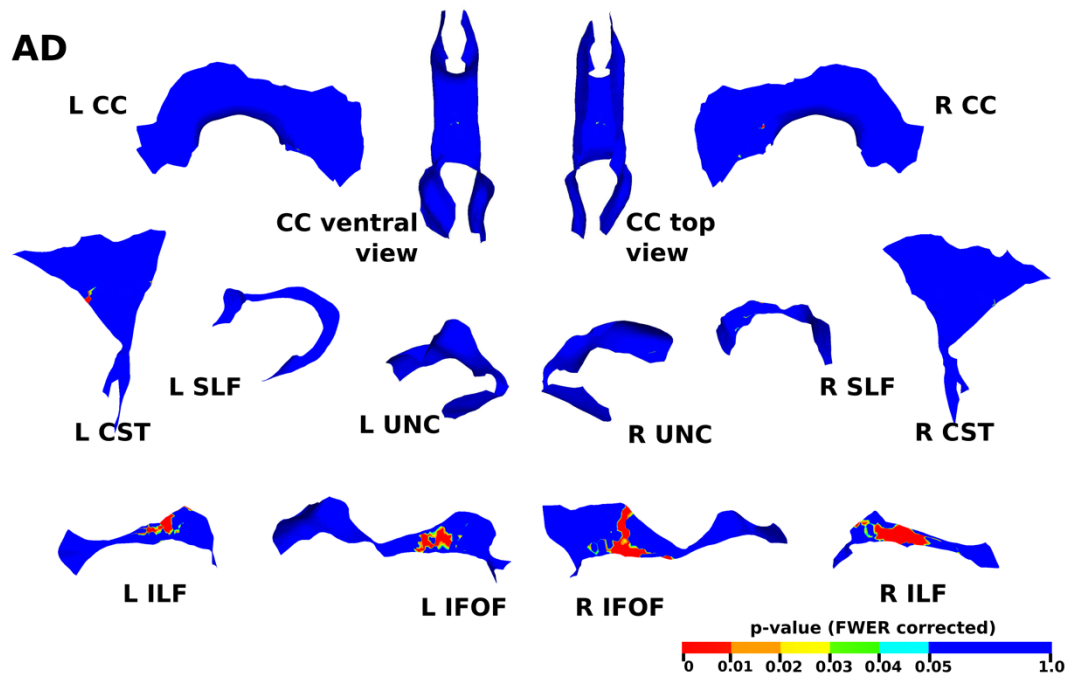


Figure 5.31 The results of the cluster analysis correlating GA at birth with AD at each point within the CC, CST, IFOF, ILF, SLF and UNC. Statistically significant regions of negative correlation are shown in red ( $p \leq 0.01$ ), orange ( $0.01 < p \leq 0.02$ ), yellow ( $0.02 < p \leq 0.03$ ), green ( $0.03 < p \leq 0.04$ ) and light blue ( $0.04 < p \leq 0.05$ ).

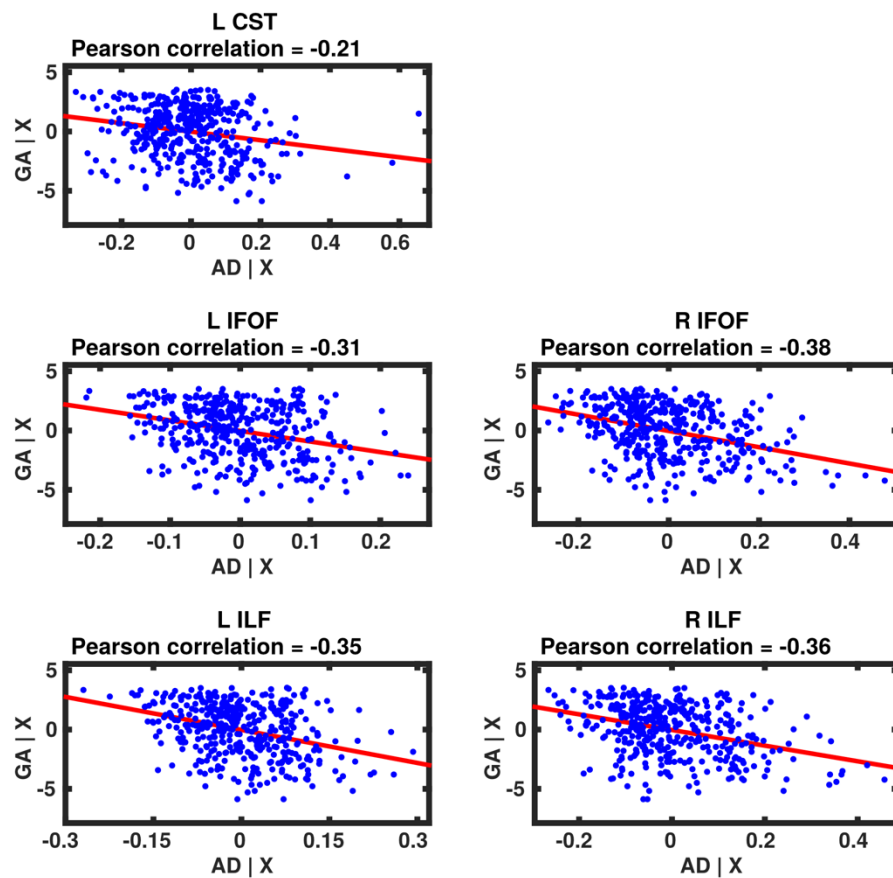


Figure 5.32 Partial regression plots showing the linear relationship between GA at birth and AD from the regions showing significant correlation for the CC, IFOF, ILF and SLF. Key: AD | X = residuals of AD given the model; GA | X = residuals of GA given the model.

### 5.3.5 Relationship between dMRI measures and PMA at scan

PMA at scan was significantly correlated with all DTI measures in all tracts. There was a positive correlation between FA and PMA, and negative correlation between PMA and MD, RD and AD, shown in Figure 5.33Figure 5.40. The correlation was widespread across all measures but to a lesser extent in AD than FA, MD and RD.

All the results are summarised in Table 5.3.

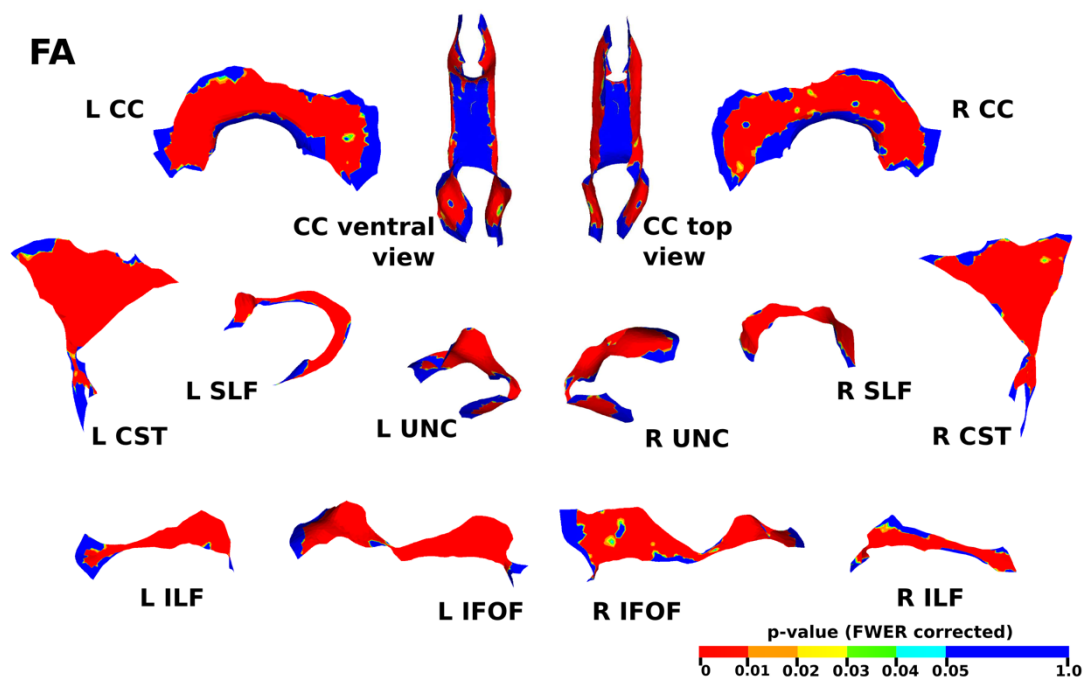


Figure 5.33 The results of the cluster analysis correlating PMA at scan with FA at each point within the CC, CST, IFOF, ILF, SLF and UNC. Statistically significant regions of positive correlation are shown in red ( $p \leq 0.01$ ), orange ( $0.01 < p \leq 0.02$ ), yellow ( $0.02 < p \leq 0.03$ ), green ( $0.03 < p \leq 0.04$ ) and light blue ( $0.04 < p \leq 0.05$ ).

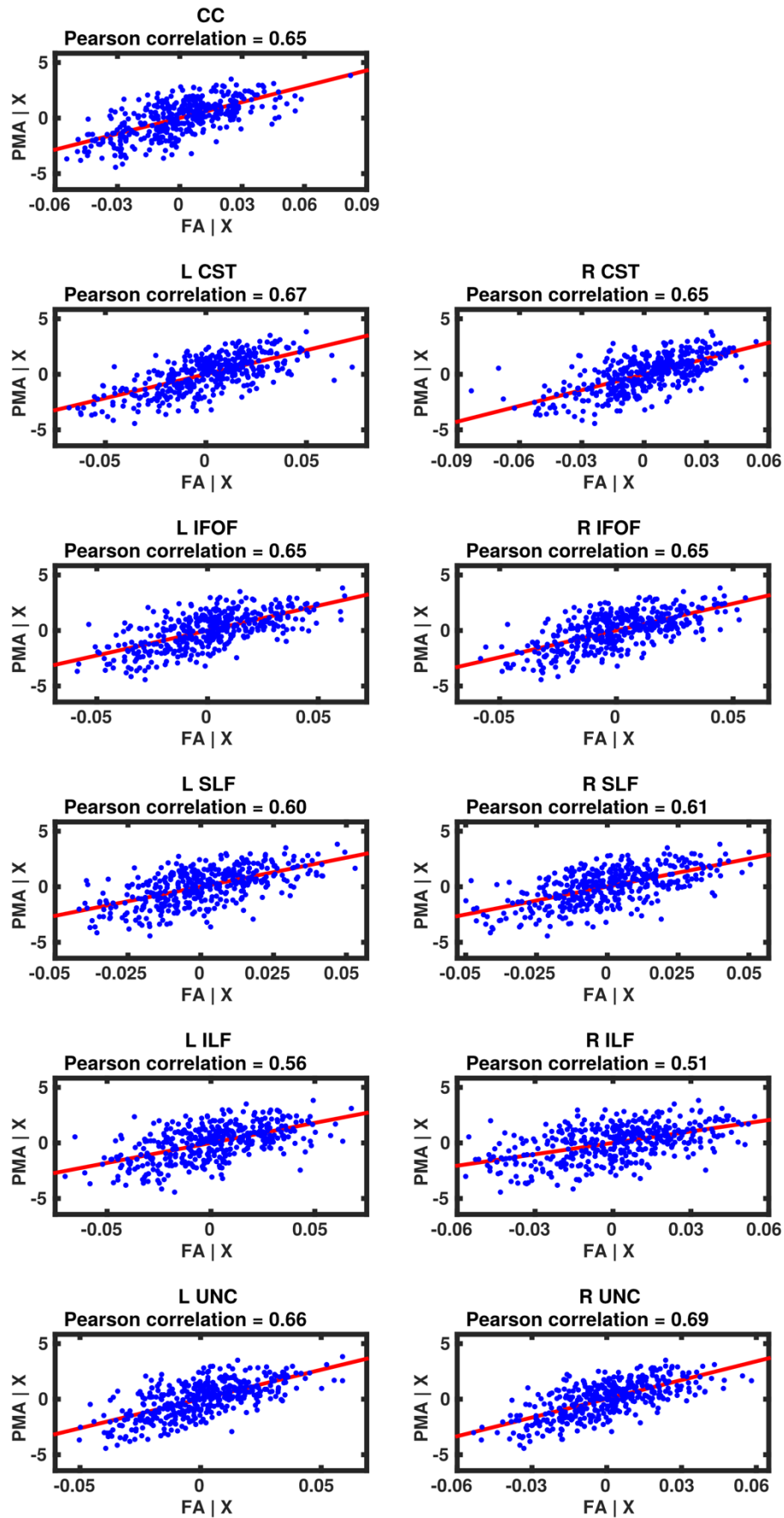


Figure 5.34 Partial regression plots showing the linear relationship between PMA at scan and FA from the regions showing significant correlation for the CC, CST, IFOF, ILF, SLF and UNC. Key:  $FA | X$  = residuals of FA given the model;  $PMA | X$  = residuals of PMA given the model.

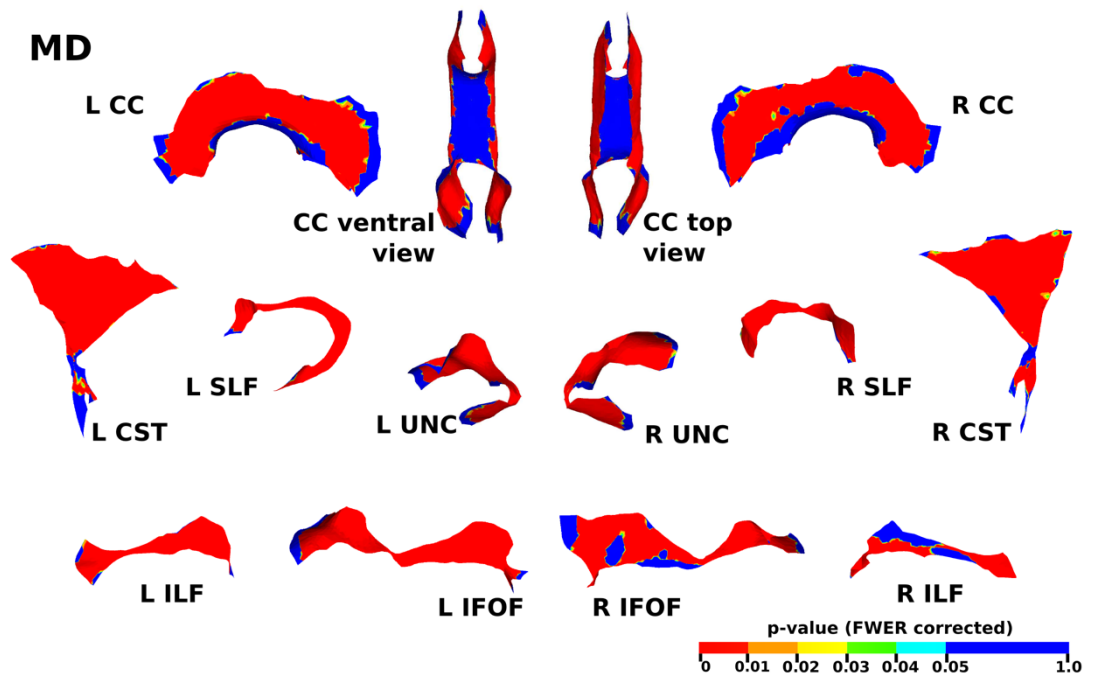


Figure 5.35 The results of the cluster analysis correlating PMA at scan with MD at each point within the CC, CST, IFOF, ILF, SLF and UNC. Statistically significant regions of negative correlation are shown in red ( $p \leq 0.01$ ), orange ( $0.01 < p \leq 0.02$ ), yellow ( $0.02 < p \leq 0.03$ ), green ( $0.03 < p \leq 0.04$ ) and light blue ( $0.04 < p \leq 0.05$ ).

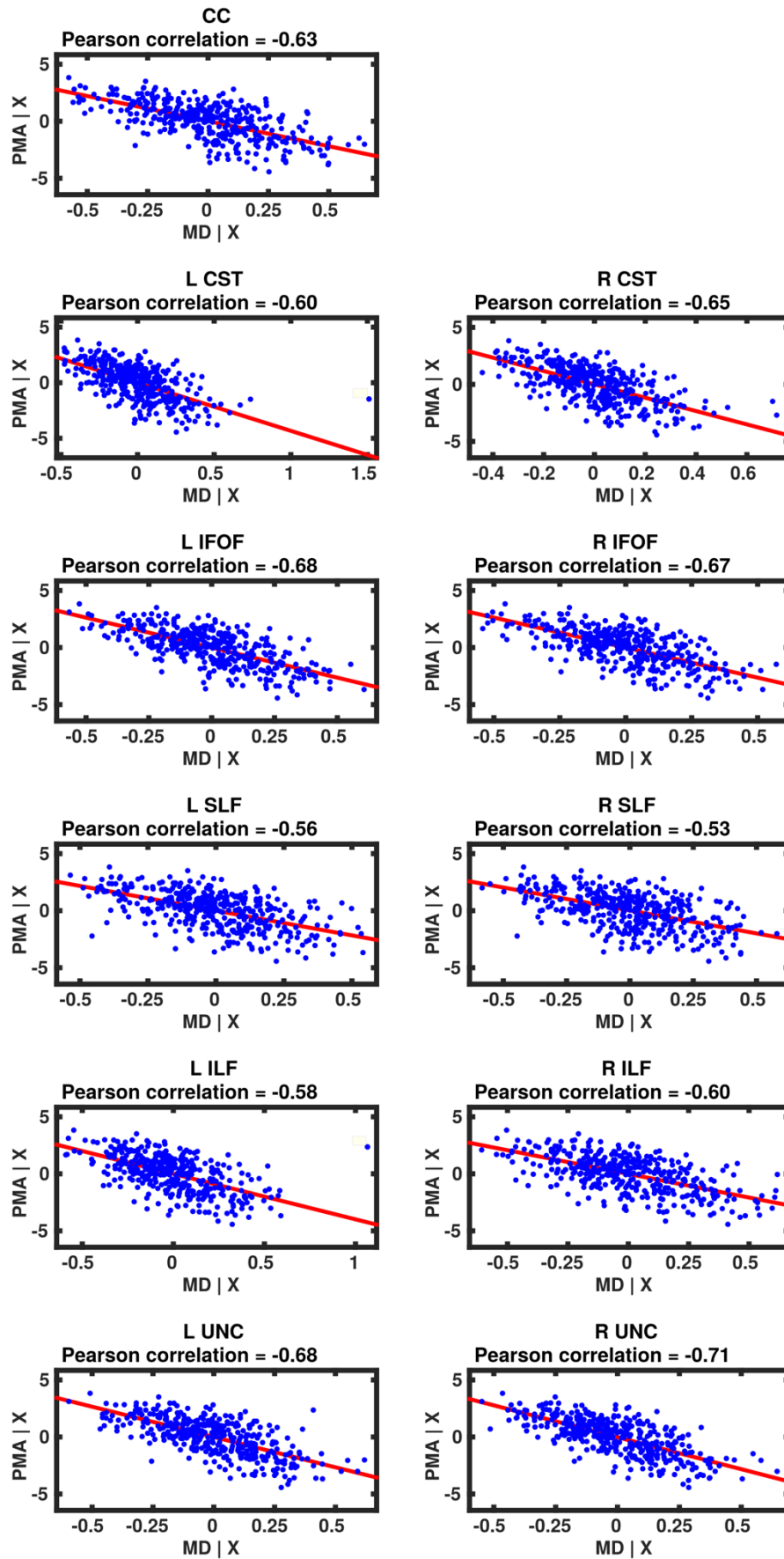


Figure 5.36 Partial regression plots showing the linear relationship between PMA at scan and MD from the regions showing significant correlation for the CC, CST, IFOF, ILF, SLF and UNC. Key: RD | X = residuals of RD given the model; PMA | X = residuals of PMA given the model.

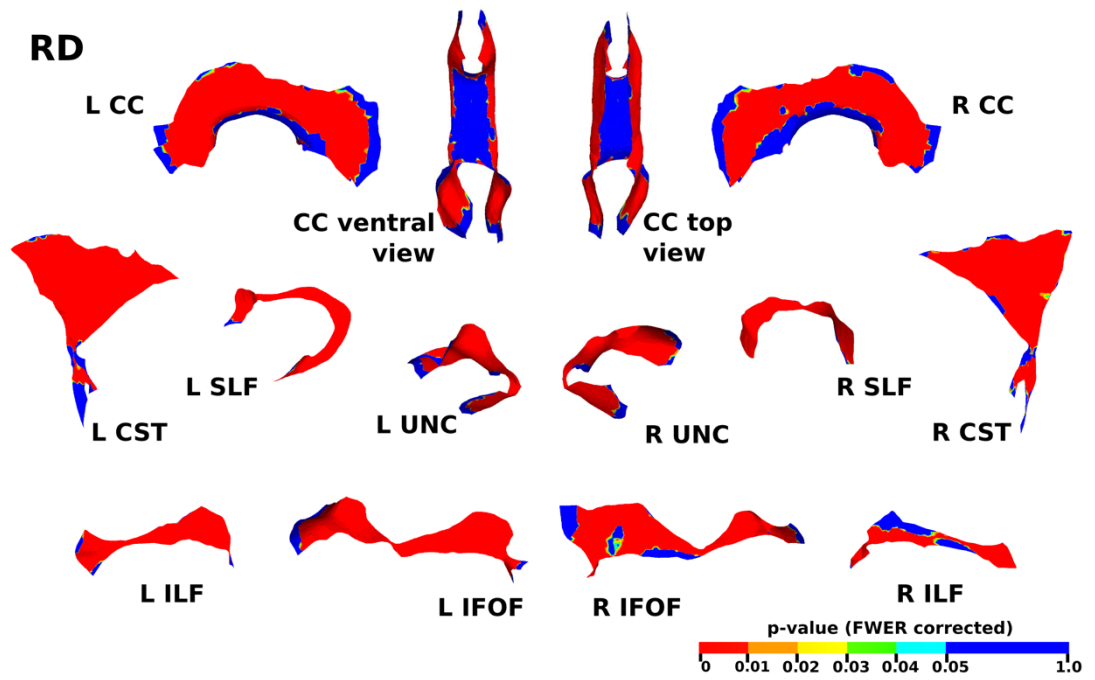


Figure 5.37 The results of the cluster analysis correlating PMA at scan with RD at each point within the CC, CST, IFOF, ILF, SLF and UNC. Statistically significant regions of negative correlation are shown in red ( $p \leq 0.01$ ), orange ( $0.01 < p \leq 0.02$ ), yellow ( $0.02 < p \leq 0.03$ ), green ( $0.03 < p \leq 0.04$ ) and light blue ( $0.04 < p \leq 0.05$ ).



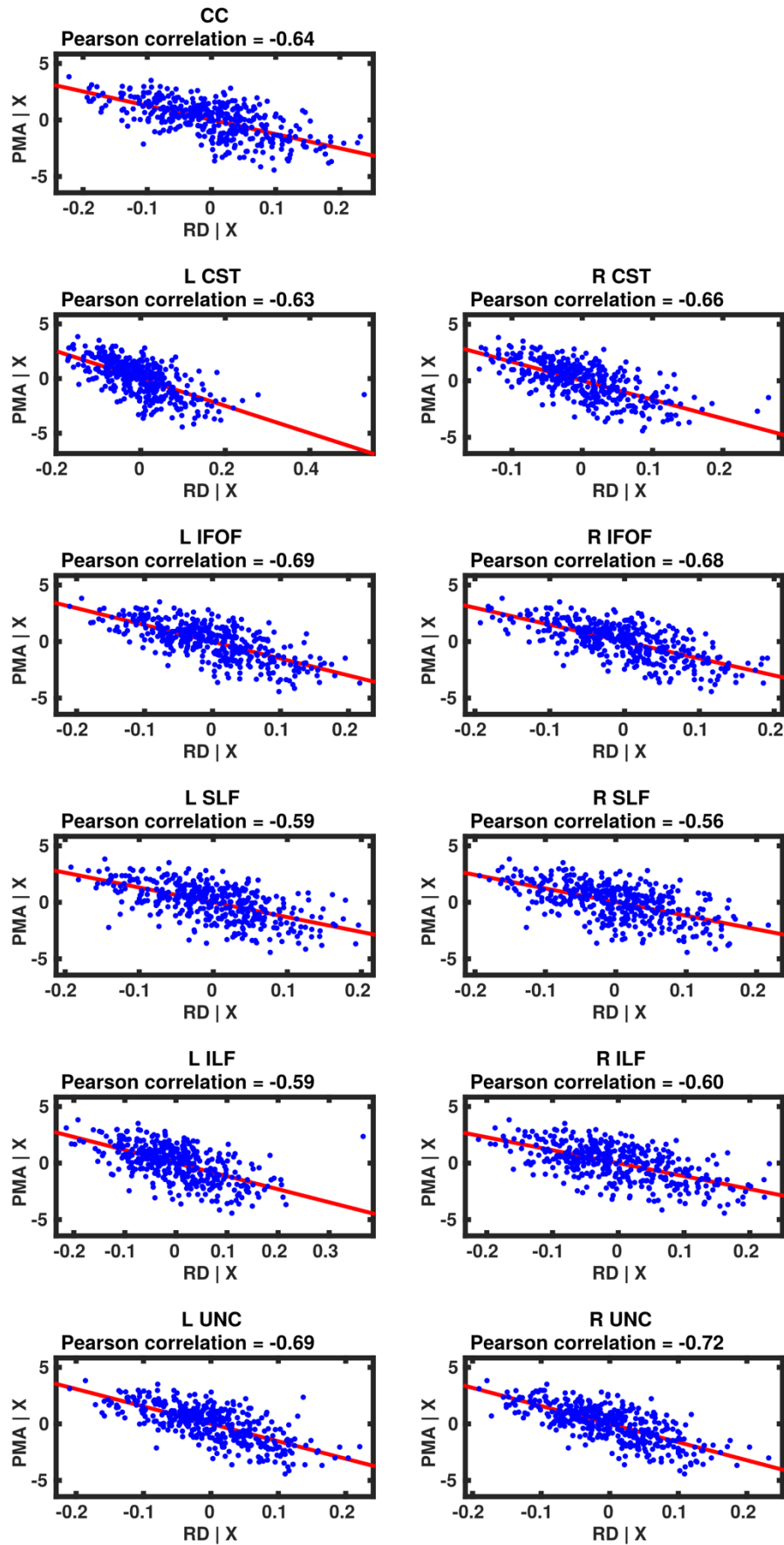


Figure 5.38 Partial regression plots showing the linear relationship between PMA at scan and RD from the regions showing significant correlation for the CC, CST, IFOF, ILF, SLF and UNC. Key: RD | X = residuals of RD given the model; PMA | X = residuals of PMA given the model.

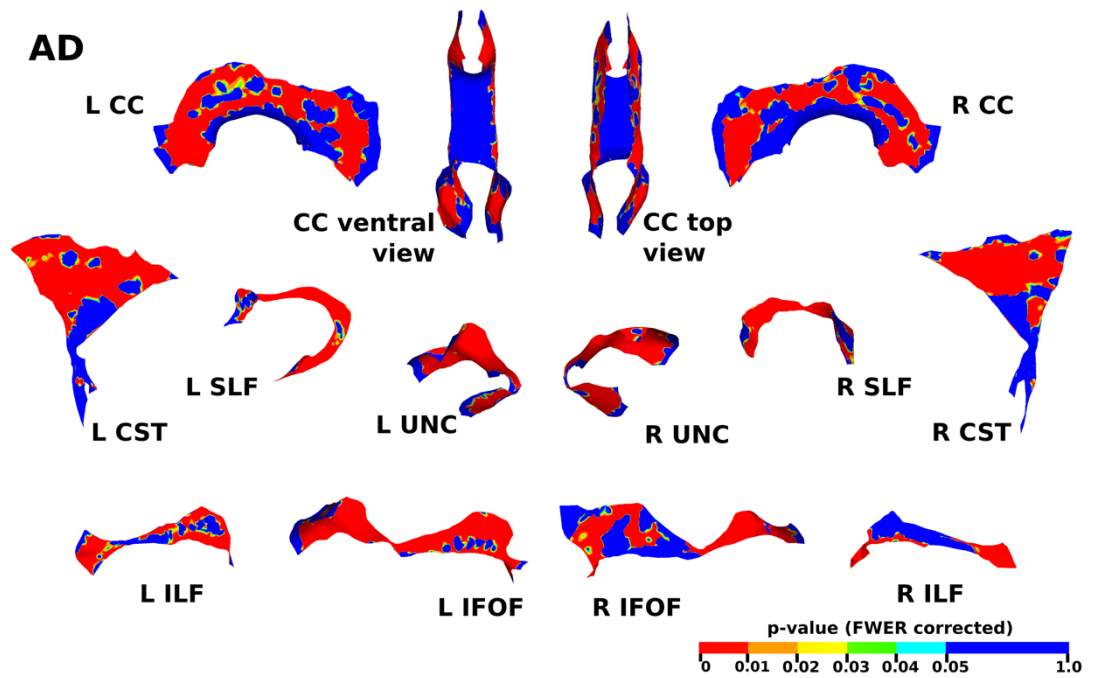


Figure 5.39 The results of the cluster analysis correlating PMA at scan with AD at each point within the CC, CST, IFOF, ILF, SLF and UNC. Statistically significant regions of negative correlation are shown in red ( $p \leq 0.01$ ), orange ( $0.01 < p \leq 0.02$ ), yellow ( $0.02 < p \leq 0.03$ ), green ( $0.03 < p \leq 0.04$ ) and light blue ( $0.04 < p \leq 0.05$ ).

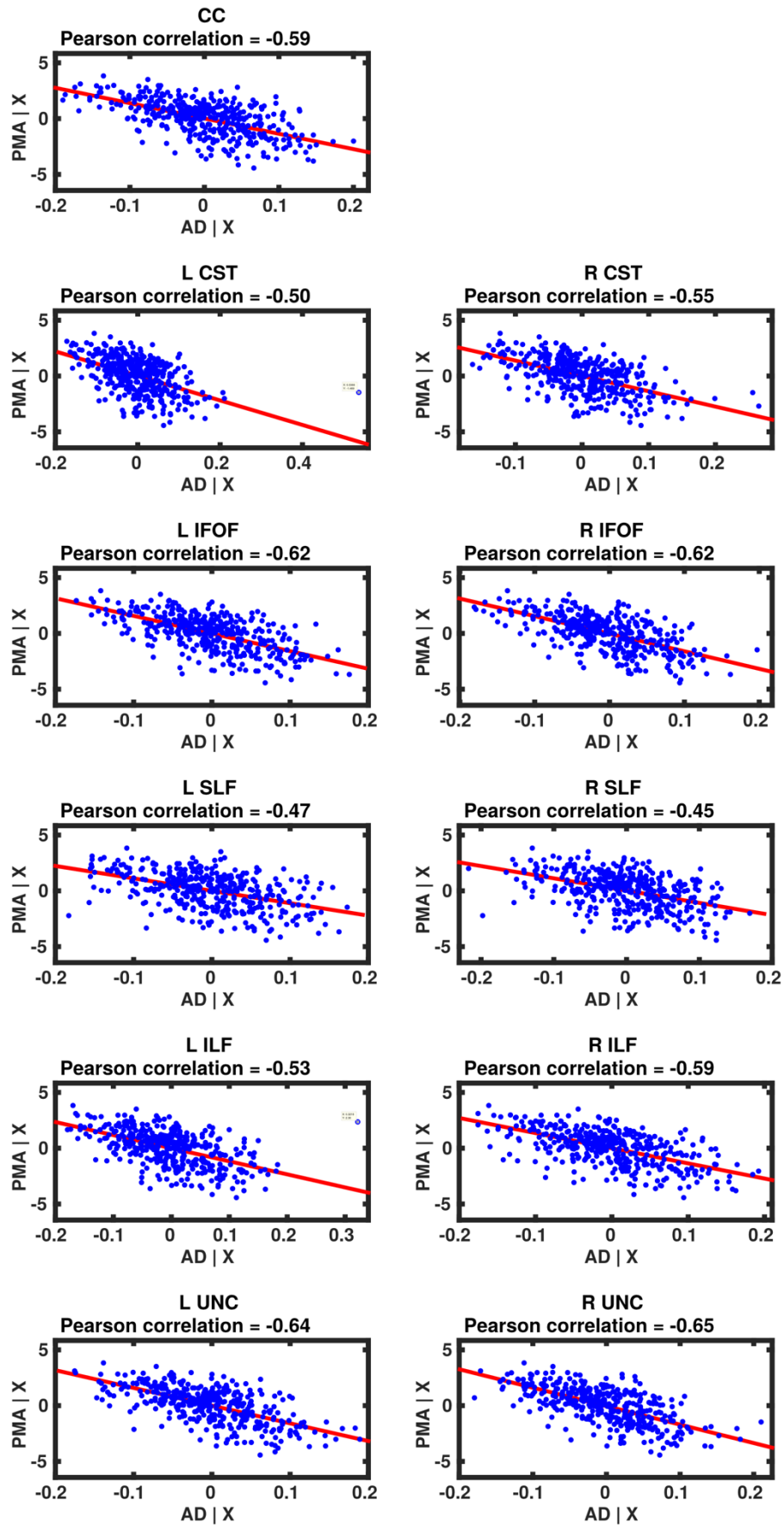


Figure 5.40 Partial regression plots showing the linear relationship between PMA at scan and AD from the regions showing significant correlation for the CC, CST, IFOF, ILF, SLF and UNC. Key: AD | X = residuals of AD given the model; PMA | X = residuals of PMA given the model.

Table 5.3 Summary of results from tract-specific analysis. All significant results are bilateral, unless the hemisphere is explicitly stated.

Variable of interest	FA (positive correlation)	MD (negative correlation)	RD (negative correlation)	AD (negative correlation)	AD (positive correlation)
Motor performance	splenium CC body CC CST IFOF ILF SLF	splenium CC body CC CST IFOF ILF R SLF	splenium CC body CC CST IFOF ILF R SLF	body CC CST R IFOF	PLIC
Cognitive performance	splenium CC CST IFOF ILF SLF	CST IFOF R ILF R SLF	body CC CST IFOF ILF	body CC (very small) CST	NS
Language performance	L IFOF IFOF	L CST R ILF	L CST	NS	NS
GA at birth	body CC IFOF ILF SLF	body CC IFOF ILF R SLF	body CC IFOF ILF R SLF	IFOF ILF	NS
PMA at scan	CC CST IFOF ILF SLF UNC	CC CST IFOF ILF SLF UNC	CC CST IFOF ILF SLF UNC	CC CST IFOF ILF SLF UNC	NS

## 5.4 Discussion

This study demonstrates a significant correlation between WM microstructural measures at term equivalent age and neurodevelopmental performance in early childhood. Overall, increasing motor and cognitive scores at 20 months are related to increased FA and decreased diffusivities at TEA. The results show that this relationship is tract-specific, most prominent in the CC, CST and posterior ILF and IFOF, and localised to particular regions within tracts. The most extensive correlation with developmental performance is seen with FA and RD, while AD showed only limited correlations with performance. On the other hand, the relationship between language performance and DTI measures was not as pronounced, limited to small regions within the CST, ILF and IFOF. Gestational age at birth was correlated with DTI measures in the central and posterior WM, while PMA at scan was correlated with all four DTI measures across all tracts.

This study demonstrates that the microstructural properties of both projection, commissural and association fibres are associated with motor and cognitive performance. Previous studies have shown that reduced FA in the CC and CST, specifically the PLIC, are associated with lower motor scores (De Bruine et al., 2013; Rose et al., 2007) while van Kooij et al. (2012b) showed that DTI measures in association tracts were also correlated with motor performance, similar to the findings here. This analysis provides evidence that cognitive performance is associated with DTI measures in the CC and CST in preterm infants at TEA as reported by (Duerden et al., 2015), and that the relationship between association fibres and cognition observed in later life are present at TEA (Allin et al., 2011; Kelly et al., 2016; Skranes et al., 2007; Vollmer et al., 2017). The regions where DTI measures correlated with cognitive and motor scores were similar, particularly in the CC, CST, IFOF and ILF. This suggests that either alterations in WM microstructure occur coincidentally in multiple tracts that independently modulate motor and cognitive functions, or that development of these two functional domains is related, as has been proposed in term-born children (Davis et al., 2010; Pangelinan et al., 2011).

Correlations between language performance and DTI measures were very limited. These results are similar to Duerden et al. (2015) who found no relationship between DTI and language, but did find a relationship between DTI and motor and cognitive performances. These findings differ to those reported in school-aged children, where language and reading ability was shown to have

widespread relationship with FA in major association fibres (Feldman et al., 2012). Language development is heavily influenced by environmental factors and at the age range studied language abilities can vary. Nonetheless, Salvan et al. (2017) demonstrated that FA values in the arcuate fasciculus, but not in the CST or SLF, at TEA are related to language ability at 2 years. Salvan et al. (2017) used high b-value, HARDI data and CSD tractography in native space to delineate the arcuate fasciculus and showed that it has numerous projections that fan out into the cortex through areas of crossing fibres. This geometry is not captured here due to the limitations of low angular resolution diffusion imaging and deterministic tractography in regions of complex fibre configurations. In addition, projections are likely to vary substantially across subjects and would most likely be averaged out when analysis is carried out in template space. Of note, the entire temporal lobe projections of the right SLF were not reconstructed in this study.

While statistically significant, the correlation between DTI measures and BSID-III scores was modest. GA at birth and SES are known predictors of neurodevelopmental performance (Ball et al., 2015; Greene et al., 2013; Serenius et al., 2013), however a number of additional perinatal risk factors such as nutrition (Stephens et al., 2009), respiratory illness (Anderson and Doyle, 2006; Lodha et al., 2014), and growth restriction (Padilla et al., 2011; Torrance et al., 2010) can influence outcome (discussed in detail in Section 3.2.4) but were not included in the model. Factors such as ROP, postnatal infection and sepsis have been associated with impaired developmental performance (Adams-Chapman and Stoll, 2006; Drost et al., 2018; Schlapbach et al., 2011), while treatment with postnatal steroids has been shown to have differing effects on neurodevelopmental outcome depending on treatment regimens (Doyle et al., 2017a, b; Parikh et al., 2015; Patra et al., 2015). Unfortunately, a limitation of this study is that data on these factors were not collected in the perinatal period and so the relationship between these perinatal risk factors and DTI measures or BSID-III scores were not assessed. Furthermore, GM diffusion properties have been related to neurodevelopmental performance (Ball et al., 2013). It is possible that a more comprehensive model, incorporating WM and GM properties and a wider range of clinical variables, may better explain the variation in neurodevelopmental performance observed in preterm infants.

Prematurity has been shown to result in altered WM DTI measures in comparison to term-born infants (Anjari et al., 2007; Counsell et al., 2006; Huppi et al., 1998a; Neil et al., 1998) and these

changes are related to the degree of prematurity (Anjari et al., 2009; Dudink et al., 2007). TSA shows that reduced FA and increased diffusivity in the body of the CC and the posterior ILF and IFOF are associated with increased prematurity. No relationship was found between GA at birth and DTI measures in the CST. This is supported by previous results in smaller tractography studies (Adams et al., 2010; de Bruine et al., 2011b) and ROI analysis which found no differences in the PLIC between extremely preterm infants and term controls at TEA (Skiold et al., 2010). In contrast, in a TBSS study Ball et al. (2010) found widespread DTI changes associated with the degree of prematurity at birth including in the CST, and Dudink et al. (2007) and Anjari et al. (2009) found increases in FA associated with increased GA at birth in the PLIC. These studies did not include subjects with focal WM injury, whereas the studies which did not find a significant relationship between DTI measures and GA included subjects with focal injury, as did this study. Reduced FA and increased diffusivity in the PLIC and CST has been observed in infants with WM injury (Counsell et al., 2006; Huppi et al., 2001; Lee et al., 2011; Liu et al., 2012) and rates of the change in FA and MD are slower in preterm infants with WM abnormalities than in preterm infants with normal appearing WM (Adams et al., 2010). Together these results suggest that disruptions to the CST occur in the presence of overt WM injury that are independent of GA at birth.

Our results show a maturation-dependent increase in FA and decrease in diffusivity that concurs with previous studies in preterm infants (Bonifacio et al., 2010; Kersbergen et al., 2014b; Miller et al., 2002; Nossin-Manor et al., 2015; Partridge et al., 2004). The wide range of age at scan studied here, 37-46 weeks PMA, is a period of rapid development across the whole brain where transient circuitry organises into permanent cerebral pathways (Kostovic and Jovanov-Milosevic, 2006). By this time neuronal proliferation and migration have largely finished and the dominant neurogenic processes are axonal pathway development, cortical neuronal differentiation and synaptogenesis (Kostovic and Judas, 2006) across the whole brain. This is reflected in the extent of the correlation seen across every tract. Notably, the only region where PMA does not correlate with any DTI measure was within the body of the CC, however diffusion measures in this region were strongly correlated with GA at birth. These results suggest that the microstructural organisation of the body of the CC is unchanging during the period studied here but is disrupted by prematurity. Indeed Young et al. (2016) observed that the CC displays the slowest rate of change in FA during the first month of life out of nine WM tracts. Across all results, changes in RD were greater than changes in AD, confirming previous findings (Adams et al., 2010; Anjari et al., 2007; Chau et al.,

2013; Partridge et al., 2004; Rose et al., 2014) that changes in FA are driven primarily by reduction in RD. At TEA, the PLIC is one of the few myelinated regions in therefore it is likely that these changes reflect premyelination events such as increases in axon diameter and decreased membrane permeability, oligodendrocyte proliferation and maturation resulting in more coherent axonal organization and overall reduction in free water (Beaulieu, 2002; Wimberger et al., 1995). Nonetheless we are limited in the conclusions we can draw with respect to the underlying microstructure. The standard diffusion tensor can model only a single fibre population. The presence of multiple fibre populations within a single WM voxel (Jeurissen et al., 2013) confound biophysical interpretations of DTI measures (Wheeler-Kingshott and Cercignani, 2009). More advanced dMRI models that are able to resolve multiple fibre populations (Alexander, 2005; Anderson, 2005; Dell'Acqua et al., 2007; Descoteaux et al., 2009; Tournier et al., 2004) and quantify neurite morphology (Zhang et al., 2012) are unfortunately not applicable here due to the relatively low angular resolution and low b value of the diffusion data (32 gradient directions and a b-value of 750 s/mm<sup>2</sup>).

## 5.5 Conclusions

TSA was applied to assess the relationship between WM diffusion properties derived from DTI at TEA in a cohort of 407 preterm infants and neurodevelopmental performance at 20 months. This analysis demonstrated anatomically-specific relationships between motor, cognitive and language performance and WM fasciculi. Higher motor and cognitive scores were associated with increased FA and decreased diffusivity in projection, commissural and association fibres, however there was little to no correlation between language performance and DTI metrics. Lower gestational age was associated with decreased FA and increased diffusivity, and a maturation-dependent increase in FA and decrease in diffusivity was observed across the WM.



## Chapter 6 Fixel based analysis

White matter voxels contain multiple fibre populations. Despite the sensitivity of the diffusion tensor model to WM changes during the perinatal period, it is an inadequate representation of crossing fibre configurations. Fixel based analysis (FBA), where a single fibre populations is referred to as a fixel, is a novel analysis framework which provides parameters of fibre density and fibre cross-section for individual fibre populations within a voxel. This chapter demonstrates the feasibility of applying FBA to the preterm neonatal population. FBA is applied to assess changes in fibre density and fibre cross-section associated with perinatal risk factors and neurodevelopmental outcome.

### 6.1 Introduction

Measures derived from the diffusion tensor model are sensitive to developmental changes and alterations in WM related to prematurity and perinatal risk factors. Nonetheless this model is an over simplification of the underlying anatomy. WM voxels contain complex fibre configurations, with up to 90% of voxels containing multiple distinct fibre populations (Behrens et al., 2007; Jeurissen et al., 2013) but the diffusion tensor expresses a single principal direction and therefore it is unable to characterise more than one fibre orientation. This is especially important for tensor-based tractography methods as it can lead to false negatives in regions of low FA due to complex fibre architecture. Tensor-based algorithms track the dominant fibre orientation and capture the gross structure of a tract (Mori and van Zijl, 2002) however branching structures such as the lateral projections of the CC or the CST are likely to be missed (Tournier et al., 2011).

Higher order diffusion models can better characterise fibre orientations in the presence of multiple fibre populations. These models rely on the acquisition of high angular resolution diffusion-weighted imaging (HARDI) data to better characterise the diffusion profile. An increased number of diffusion-weighted gradient directions and higher b-values are required to resolve crossing fibres (Tournier et al., 2013). CSD is one such method, which provides estimates of FODs of

multiple fibre populations within a voxel. CSD has been applied previously to preterm neonatal populations to study WM tracts with complex configurations that are not possible to resolve with DTI. Salvan et al. (2017) demonstrated the relationship between the diffusion properties of the arcuate fasciculus at TEA and language performance at 2 years old. Using high b-value, high angular resolution diffusion imaging and CSD tractography the authors were able to capture the lateral projections of the arcuate fasciculus. Pieterman et al. (2017) were able to, for the first time, delineate the cortico-ponto-cerebellar and cerebello-thalamo-cortical tracts in vivo using HARDI data analysed with CSD in infants scanned as early as 29 weeks PMA. Delineating connections between the cerebellum and the supratentorial brain regions is particularly challenging due to the crossing fibres at the level of the pons and mesencephalon, and the high degree of fanning in the cerebrum. However, these methods only reported voxel-averaged DTI measures in their assessments of WM microstructure.

Fixel-based analysis (FBA) is a novel framework which provides quantitative measures associated with a single fibre population derived from FOD estimations (Raffelt et al., 2017), rather than voxel-averaged measures such as FA which are likely to be influenced by multiple fibre populations within a voxel. A single fibre population in a voxel is referred to as a fixel. FBA provides measures of fixel-specific fibre density (FD) and fibre cross-section (FC). FD quantifies the volume of the restricted intra-axonal compartment along a particular fibre population direction (Raffelt et al., 2017). This provides an assessment of WM microstructure. As described in full in Chapter 2 (Section 2.3.6), the volume of the restricted intra-axonal compartment is proportional to the FOD amplitude and FD is calculated by integrating the FOD lobes. For assessment of fibre-bundle morphology, FC measures relative changes in local WM fibre bundle cross-section in the plane perpendicular to the main fibre orientation. FC is based on nonlinear deformations applied during spatial normalisation, similar to tensor-based morphometry.

Previous dMRI studies assessing WM in infants have solely investigated voxel-averaged measures (Anjari et al., 2007; Counsell et al., 2008; De Bruine et al., 2013; Duerden et al., 2015; van Kooij et al., 2012b), such as DTI, and not fibre population specific measures. Studies investigating brain morphology have only examined whole brain volumes or whole tissue volumes (Ball et al., 2012; Boardman et al., 2007; Boardman et al., 2006; Inder et al., 2005; Peterson et al., 2003; Srinivasan et al., 2007) but not local change in individual fibre-bundles.

The aims in this chapter are to (i) demonstrate the feasibility of FBA in the neonatal preterm population; (ii) investigate the relationship between fixel-based measures of WM and perinatal risk factors; (iii) and to investigate the relationship between fixel-based measures of WM at TEA and neurodevelopmental performance at 20 months.

## **6.2 Methods**

### **6.2.1 Subjects**

We studied 50 infants (28 male) born at 24.0–32.9 (median 30.4) weeks GA and imaged at 38.6–47.1 (median 42.1) weeks PMA. Infants were recruited as part of the ePrime study of preterm brain development. Written parental consent was obtained prior to imaging. T1- and T2-weighted MR images were assessed for the presence of focal brain injury. Motor, cognitive and language performances were assessed using the BSITD-III at 20 months. The characteristics of the subjects studied are summarised in Table 6.1. A two-sample Kolmogorov-Smirnov test was applied to test for differences between the whole cohort (n=50) and the subset of subjects assessed using the BSITD-III (n=45).

### **6.2.2 Data Acquisition**

All MR imaging data were acquired under the supervision of a paediatrician experienced in MR imaging procedures. T1- and T2-weighted were acquired as described in Chapter 3. dMRI was acquired on a 3-Tesla MR system sited on the neonatal intensive care unit in 64 non-collinear directions with a b-value of 2500 s/mm<sup>2</sup> and 4 non-diffusion-weighted images using the following parameters: TR = 9000 ms, TE = 62 ms, voxel size: 2mm isotropic, SENSE factor of 2.

### **6.2.3 Image processing**

The data were pre-processed by removal of motion-corrupted volumes, PCA-based denoising (Veraart et al., 2016), distortion correction and outlier replacement (Andersson et al., 2016), bias field correction (Tustison et al., 2010) and intensity normalisation across datasets. FOD images were computed for each subject using multi-shell multi-tissue CSD (Jeurissen et al., 2014). Tissue-specific group-average response functions for WM and CSF were estimated using both b=0 and b=2500 s/mm<sup>2</sup> shells. WM FODs are assumed to be anisotropic and are modelled using

spherical harmonic series of order 8, whereas CSF is assumed to be isotropic and FODs are modelled using spherical harmonic series of order 0. GM FODs are also assumed to be isotropic and modelled using spherical harmonic series of order 0, however no response function was calculated for GM. The WM response function was estimated from single-fibre voxels identified using the algorithm described in Tournier et al. (2013).

Table 6.1 Characteristics of the study group.

Characteristic	Whole cohort (n=50)	BSITD-III assessed (n=45)	p-value
Median (range) gestational age at birth (weeks)	30.4 (24.0-32.9)	30.6 (24.0-32.9)	>0.99
Median (range) postmenstrual age at scan (weeks)	42.1 (38.6- 47.1)	42.1 (38.6-46.1)	>0.99
Median (range) PMA at BSITD-III assessment corrected for prematurity (months)	N/A	20.2 (19.7-22.5)	>0.99
Median (range) birth weight (grams)	1202.5 (645- 1990)	1230 (645-1990)	>0.99
Mean (SD) birth weight z scores	-0.71 (0.876)	-0.71 (913)	>0.99
Median (range) days of ventilation (days)	0 (0-40)	0 (0-40)	>0.99
Bronchopulmonary dysplasia (no., %)	10 (20%)	8 (17.7%)	>0.99
Median (range) days of total parenteral nutrition (days)	6.5 (0-89)	7 (0-89)	>0.99
Rate of weight gain (grams per week)	164 (11-276)	163 (11-276)	>0.99
NEC requiring surgery (no, %)	1 (2%)	1 (2.2%)	>0.99
Chorioamnionitis (no., %)	2 (4%)	1 (2.2%)	>0.99
PDA requiring medical or surgical treatment (no., %)	1 (2%)	1 (2.2%)	>0.99
Median (range) index of multiple deprivation	14.9 (6.2-46.8)	14.7 (6.2-46.8)	>0.99

To calculate the isotropic CSF response function, voxels within the ventricles were delineated by manually drawing ROIs. The CSF and WM response functions were averaged across subjects and used to calculate each subject's FOD images.

#### **6.2.4 FBA**

##### **6.2.4.1 Registration**

Each subject's FOD image was mapped to an iteratively-refined, group-averaged template FOD image using nonlinear transformations (Raffelt et al., 2012a; Raffelt et al., 2011). FOD registration preserves the total FOD integral and the volume fractions of each fibre population (Raffelt et al., 2009).

##### **6.2.4.2 Fibre density**

At high diffusion-weightings, the extra-axonal water is strongly attenuated and the total radial diffusion signal is proportional to the intra-axonal water. The amplitude of the FOD is proportional to the radial diffusion signal and therefore provides a measure of the intra-axonal volume fraction of the fibres aligned with the fixel direction. FD was calculated for each fixel in each subject's warped FOD image. For each subject, the FOD lobes were segmented based on the peaks and troughs of the FOD. The peak of the FOD is the direction for which the FOD amplitude is at its maximum. The FD of each lobe was calculated by numerically integrating the FOD lobe over a hemisphere (Smith et al., 2013). It should be noted that when fibres are dispersed, a greater spread in orientations can correspond to greater fibre density without an increased peak amplitude. By calculating FD as the integral of the FOD this is taken into account. Fixels in each subject's warped FOD image were then reoriented to ensure orientation information remains anatomically consistent across voxels. Each FOD in the template was segmented. The template is a group average; therefore, it is representative of the fixels common to all subjects. This defines a fixel template mask within which the statistical analysis was performed. To achieve anatomical correspondence across subjects, an FD value from each subject's fixel is assigned to each corresponding fixel in the template mask. If a subject's fixel is more than 30° away from the template fixel, a value of zero was assigned.

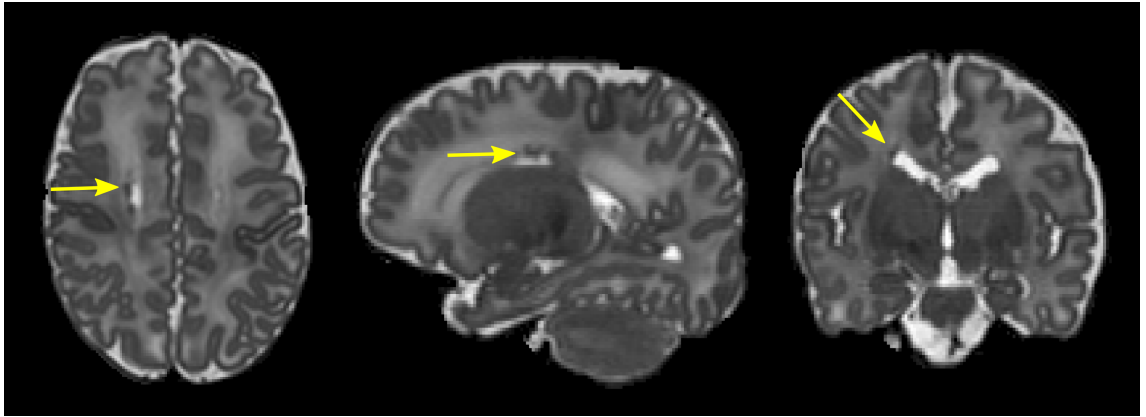


Figure 6.1 Axial, sagittal and coronal views of T2-weighted image of infant with small HPOI, indicated by the yellow arrows.

#### 6.2.4.3 Fibre cross-section

At each point, the nonlinear mapping of each subject's FOD image to template is given by the Jacobian matrix. The determinant of the Jacobian describes local expansion or contraction with respect to the template. FC is a measure of the cross-sectional change in direction perpendicular to the orientation of a fixel computed using the determinant of the Jacobian. FC is calculated using the warp from the template to the subject, therefore FC greater than 1 represents a larger fibre bundle in the subject than in the template.

#### 6.2.4.4 Fibre density and cross-section

FD and FC are combined to give a measure that is sensitive to both changes in microscopic density and macroscopic morphology. For each fixel, FDC is calculated by multiplying FD and FC.

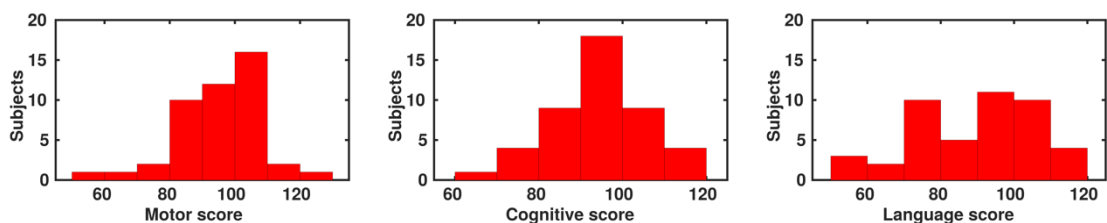


Figure 6.2 Histograms of motor, cognitive and language scores from the BSITD-III assessment

#### 6.2.4.5 Statistical analysis

Whole-brain probabilistic tractography was performed in the FOD template seeded from a whole-brain WM mask to produce a tractogram of 20 million streamlines. From this tractogram, a subset of 10 million streamlines was selected that best fit the diffusion signal using the SIFT algorithm (Smith et al., 2013). Connectivity-based fixel enhancement (CFE) was performed. CFE uses probabilistic tractography to establish structural connections between fixels. Connectivity between fixels is used to smooth fixel measures across connected fixels and for multiple comparisons correction by identifying connected clusters of fixels of significant effect, similar to that of threshold-free cluster enhancement (Smith and Nichols, 2009). Multiple comparisons correction was carried out using non-parametric permutation testing (Nichols and Holmes, 2002) with family-wise error rate (FWER) correction.

FBA was used to assess the relationship between fixel-derived measures and relevant perinatal risk factors. Regression analysis was carried out between FD, FC, FDC and the following;

- PMA (GA and sex as covariates),
- GA (PMA and sex as covariates),
- the number of days on mechanical ventilation (GA, PMA and sex as covariates),
- the number of days on total parenteral nutrition (TPN) (GA, PMA and sex as covariates),
- birth weight z scores (GA, PMA and sex as covariates),
- rate of weight gain per week (GA, PMA and sex as covariates)
- group differences between male and female infants (GA and PMA as covariates).

The effects of NEC, chorioamnionitis and treatment for patent ductus arteriosus were not investigated because too few subjects presented (see Table 6.1).

FBA was used to assess the relationship between fixel-derived measures at TEA and neurodevelopmental outcome at 20 months. Regression analysis was performed between FD, FC, FDC and BSITD-III scores for

- motor,
- cognitive
- language performance

with GA, PMA, socioeconomic status and sex as covariates. Socioeconomic status was defined by the index of multiple deprivation.

## **6.3 Results**

### **6.3.1 MRI findings**

Focal brain injury was observed on conventional MRI in three infants. One subject had a unilateral cerebellar haemorrhage in addition to germinal layer haemorrhage; one subject had a small unilateral haemorrhagic parenchymal infarct (Figure 6.1); and one subject had haemorrhage in the right temporal lobe, cerebellar haemorrhage, cerebellar hypotrophy and bilateral intraventricular haemorrhage.

### **6.3.2 Neurodevelopmental performance**

Of the 50 subjects, 45 were assessed using the BSITD-III. Four subjects were lost to follow up and one subject died from sudden infant death syndrome after discharge from the neonatal intensive care unit. The results for the BSITD-III scores are shown in Figure 6.2. The median (range) composite motor, cognitive and language scores were 94 (58-121), 95 (65-120) and 91 (53-115) respectively. There was no difference between the whole cohort (n=50) and the subset of subjects assessed using the BSITD-III (n=45) in any of the characteristics (p-values>0.99 for all characteristics).



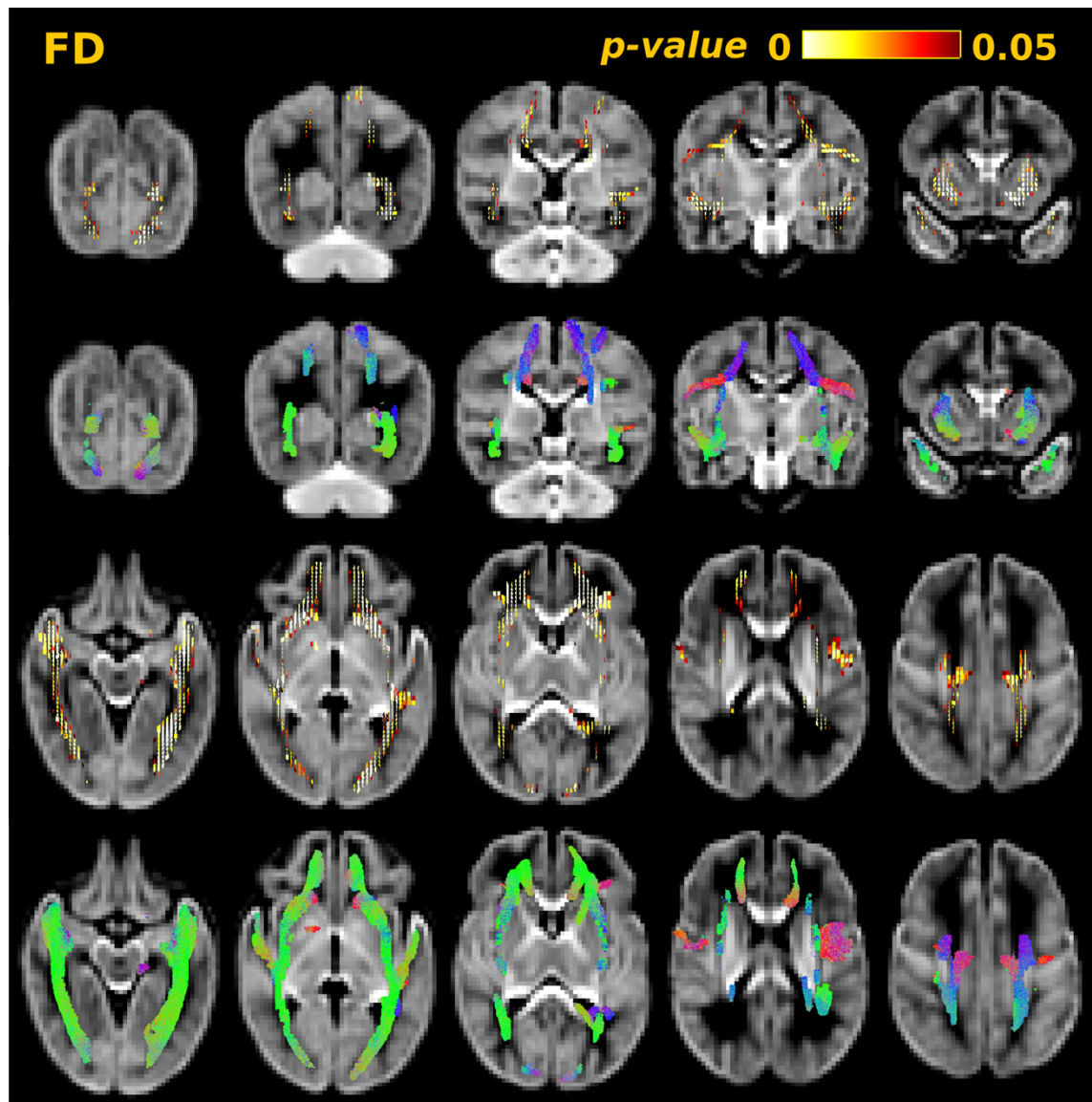


Figure 6.3 The results of fixel-based analysis assessing the relationship between FD and PMA at scan. The top and third rows show fixels with significant positive correlation (corrected  $p \leq 0.05$ ) between FD and PMA at scan. The second and bottom rows show the streamlines passing through significant fixels, coloured by direction (red: left-right; green: anterior-posterior; blue: inferior-superior).

### 6.3.3 Fixel-based analysis

#### 6.3.3.1 Relationship between fixel measures and perinatal risk factors

All significant results are bilateral, unless the hemisphere is explicitly stated.

##### 6.3.3.1.1 PMA at scan

PMA at scan was significantly correlated positively with FD, FC and FDC throughout the WM.

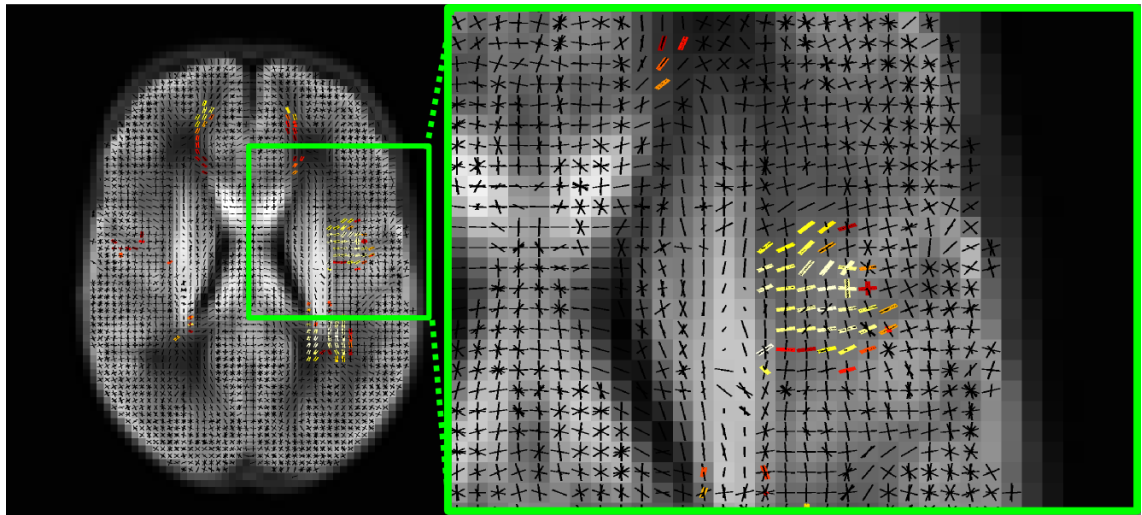


Figure 6.4 Coronal view of fixels showing significant positive correlation between FD and PMA at scan (red-yellow) overlaid on the template fixel mask (black) with a close-up of fixels projecting to the laterally to the cortex.

PMA at scan was correlated with FD in the forceps minor and forceps major, a small region of cortical projections from the middle of the body of the CC and lateral projections of the CC, the corona radiata, the IFOF, SLF, and ILF (Figure 6.3 and Figure 6.4).

There was a positive correlation between PMA and FC throughout the whole WM, including in the middle of the body of the CC and lateral projections of the CC, the forceps major, the anterior commissure, posterior commissure, CST, IFOF (except in the frontal lobe projects), SLF, ILF, cingulum, fornix, fixels within the thalamus, the cerebellum and pons (Figure 6.5 and Figure 6.6).

FDC was correlated with PMA in the middle of the body of the CC and the lateral projections of the CC, the forceps minor, forceps major, the anterior commissure, CST, IFOF, SLF, ILF, fixels within the thalamus and the cerebellum (Figure 6.7)

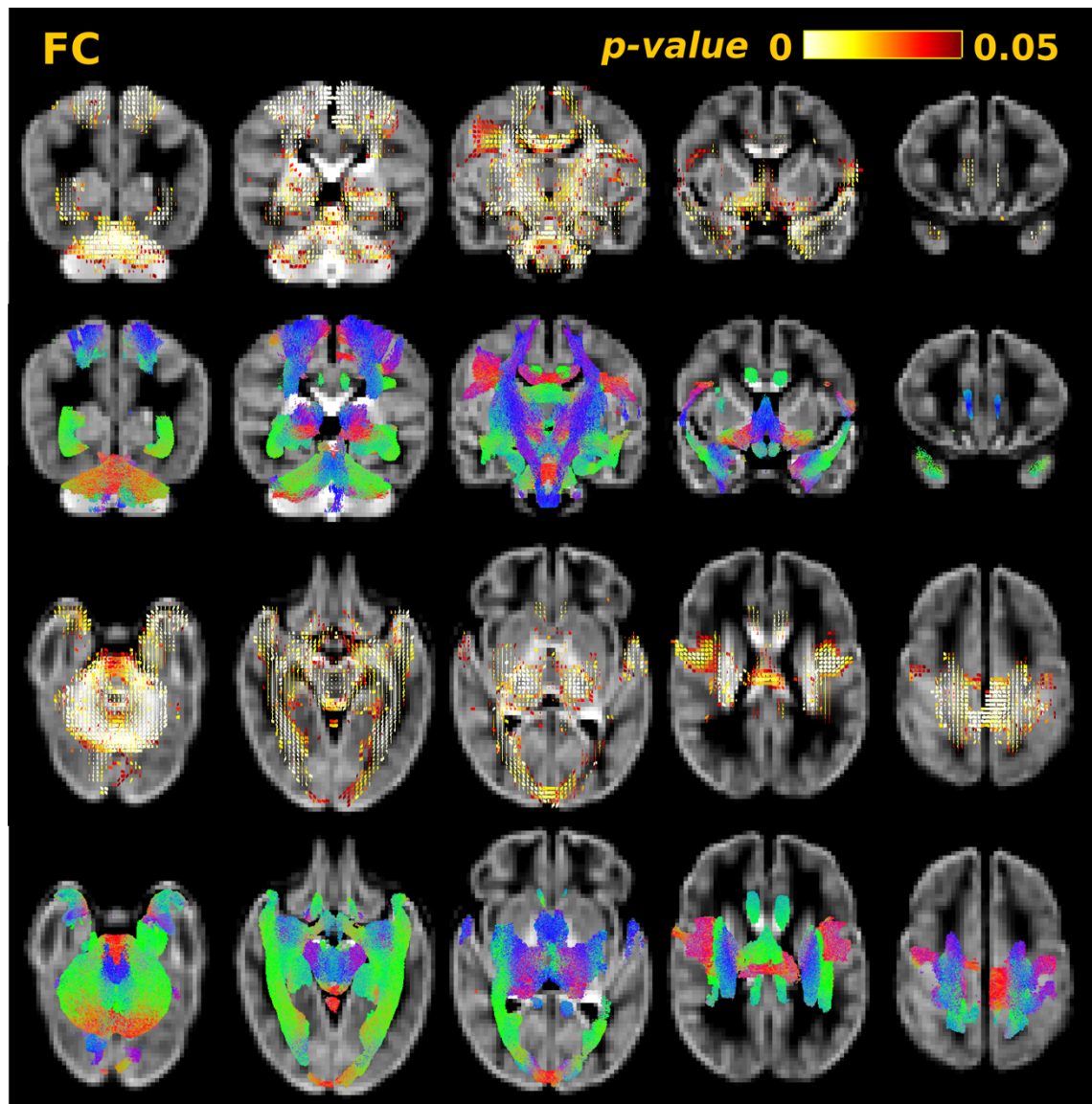


Figure 6.5 The results of fixel-based analysis assessing the relationship between FC and PMA at scan. The top and third rows show fixels with significant positive correlation (corrected  $p \leq 0.05$ ) between FC and PMA at scan. The second and bottom rows show the streamlines passing through significant fixels, coloured by direction (red: left-right; green: anterior-posterior; blue: inferior-superior).

#### 6.3.3.1.2 Gestational age at birth

GA at birth was significantly correlated positively with FD, FC and FDC.

GA at birth correlated with FD in the splenium and tapetum of the CC, the anterior commissure, and a small region in the left anterior IFOF (Figure 6.8)

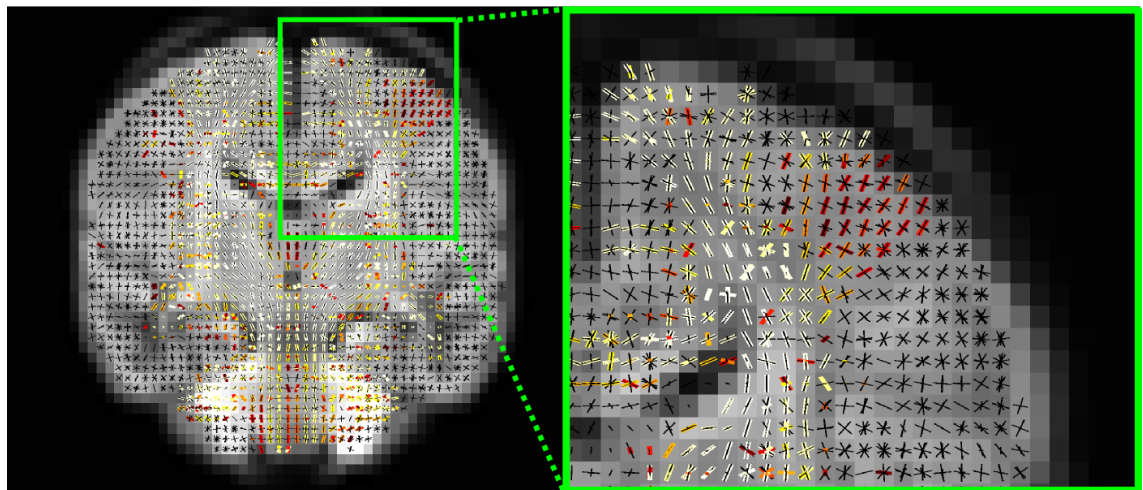


Figure 6.6 Coronal view of fixels showing significant positive correlation between FC and PMA at scan (red-yellow) overlaid on the template fixel mask (black) with a close-up of fixels projecting to the cortex. While multiple fixels within a voxel are identified as statistically significant, they are not the same value, with medial projections having a lower p-value than lateral projections.

GA was correlated more extensively with FC, namely in the genu and splenium of CC, the anterior commissure, the CST, IFOF, SLF, ILF, fornix, the cingulum (left > right), fixels within the thalamus, the cerebellum and the pons (Figure 6.9 and Figure 6.10)

FDC was correlated with GA in the genu, splenium and tapetum of the CC, the anterior commissure, the left CST inferior of the PLIC, and the middle-to-anterior regions of the IFOF and ILF, fornix and fixels within the thalamus (Figure 6.11).

#### 6.3.3.1.3 Days on mechanical ventilation

The number of days spent on mechanical ventilation were negatively correlated with all fixel measures.

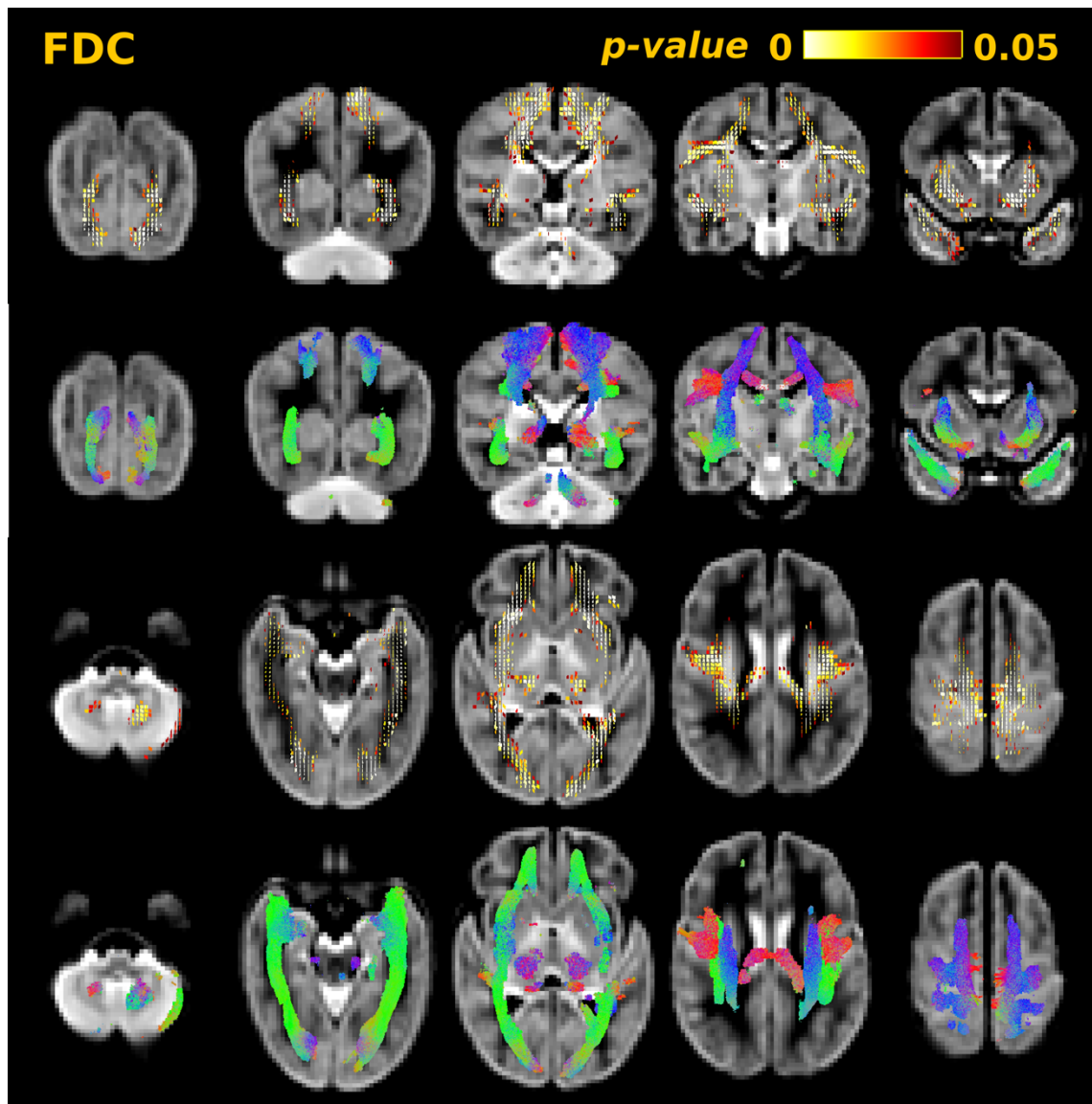


Figure 6.7 The results of fixel-based analysis assessing the relationship between FDC and PMA at scan. The top and third rows show fixels with significant positive correlation (corrected  $p \leq 0.05$ ) between FC and PMA at scan. The second and bottom rows show the streamlines passing through significant fixels, coloured by direction (red: left-right; green: anterior-posterior; blue: inferior-superior).

FD showed a negative correlation with number of days on mechanical ventilation in the cerebellum and the pons (Figure 6.12 and Figure 6.13).

FC showed negative correlation in the splenium and tapetum of the CC, the anterior commissure, CST, ALIC, the middle-to-anterior regions of the IFOF, fornix, fixels within the thalamus, cerebellum and pons (Figure 6.14 and Figure 6.15).



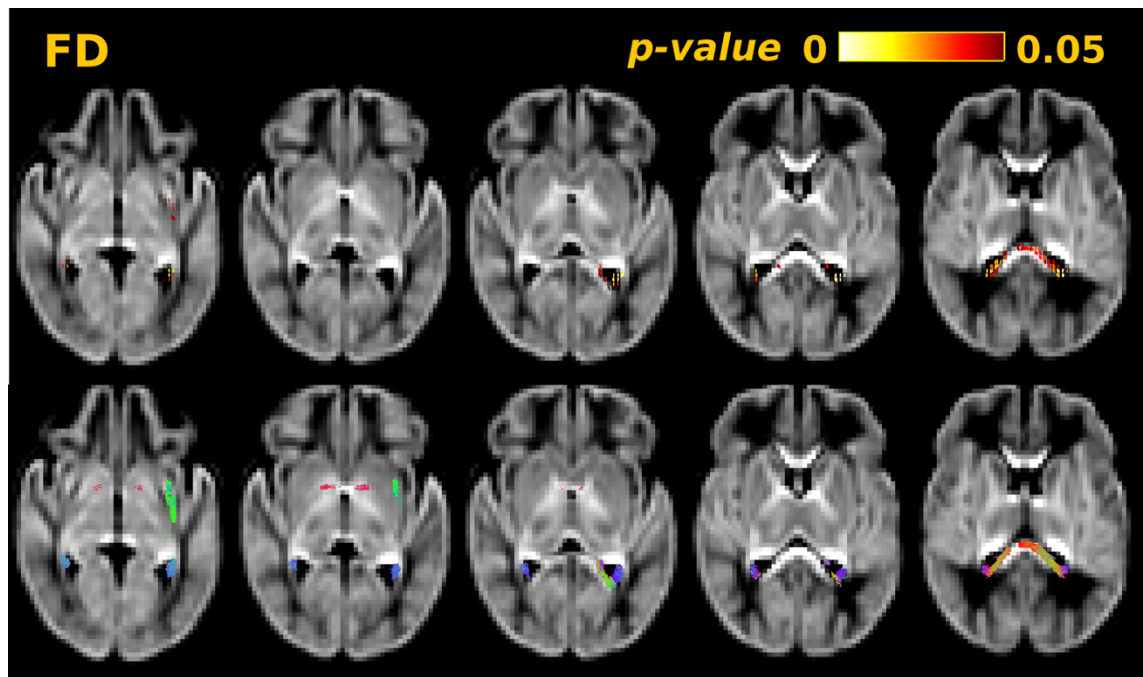


Figure 6.8 The results of fixel-based analysis assessing the relationship between FD and GA at birth. The top row shows fixels with significant positive correlation (corrected  $p \leq 0.05$ ) between FD and GA at birth. The bottom row shows the streamlines passing through significant fixels, coloured by direction (red: left-right; green: anterior-posterior; blue: inferior-superior).

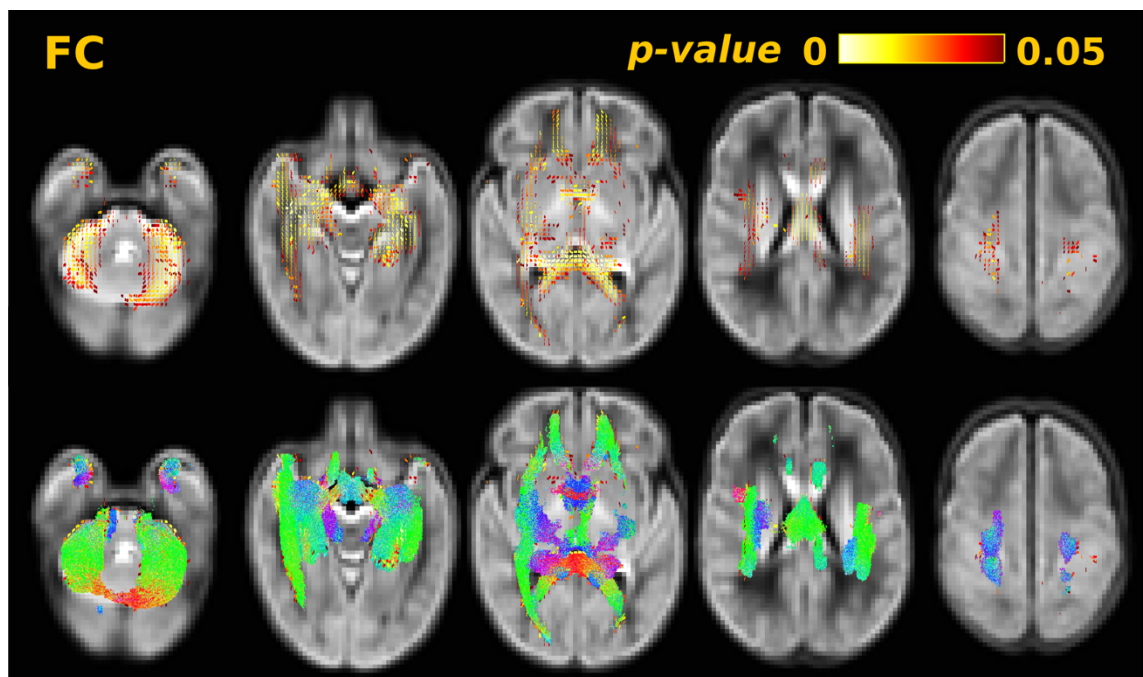


Figure 6.9 The results of fixel-based analysis assessing the relationship between FC and GA at birth. The top row shows fixels with significant positive correlation (corrected  $p \leq 0.05$ ) between FC and GA at birth. The bottom row shows the streamlines passing through significant fixels, coloured by direction (red: left-right; green: anterior-posterior; blue: inferior-superior).

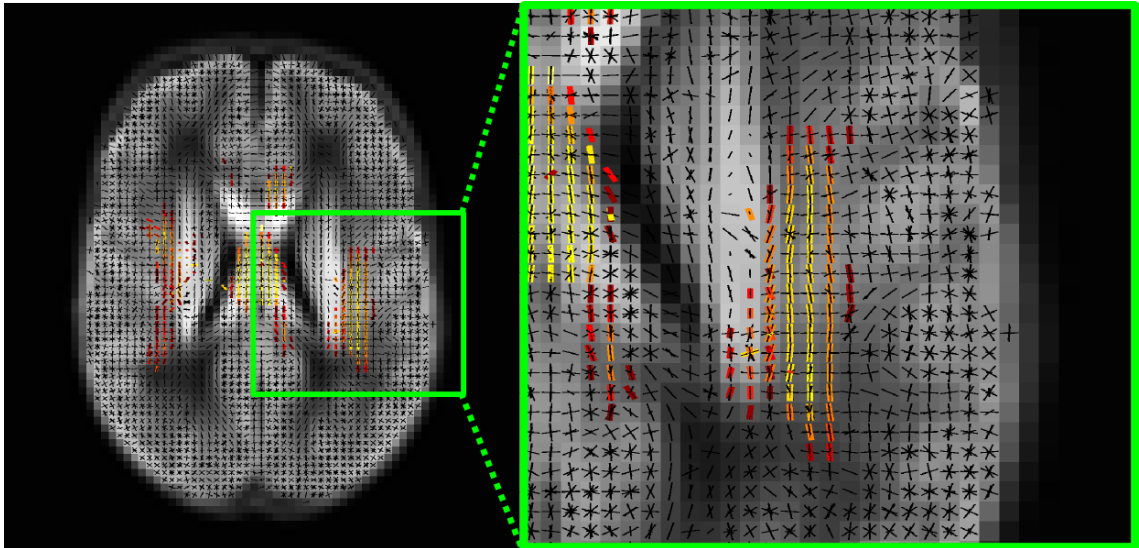


Figure 6.10 Axial view of fixels showing significant positive correlation between FC and GA at birth (red-yellow) overlaid on the fixel template mask (black) with a close-up of fixels within the centrum semiovale, identifying fixels within the SLF as statistically significant.

FDC showed negative correlation in the CST, the mid-ILF, the right fornix, the cerebellum and pons. The correlation in the left CST was only up to the level of the centrum semiovale, whereas on the right the correlation was present in the projections towards the cortex (Figure 6.16).

#### 6.3.3.1.4 Days on total parenteral nutrition

There were no significant correlations between FD, FDC and the number of days requiring TPN.

FC showed a negative correlation in the CST, up to the level of the centrum semiovale, and the cerebellum (Figure 6.17 and Figure 6.18).

#### 6.3.3.1.5 Birth weight

Birth weight z scores were not correlated with FD.

The correlation between birth weight z scores and FC was widespread throughout the WM. There were significant positive correlations in the genu, splenium, body and lateral projections of the CC, the anterior commissure, posterior commissure, CST, IFOF, SLF, ILF, cingulum, fornix, ALIC, the fixels within the thalamus, the cerebellum and pons (Figure 6.19 and Figure 6.20).

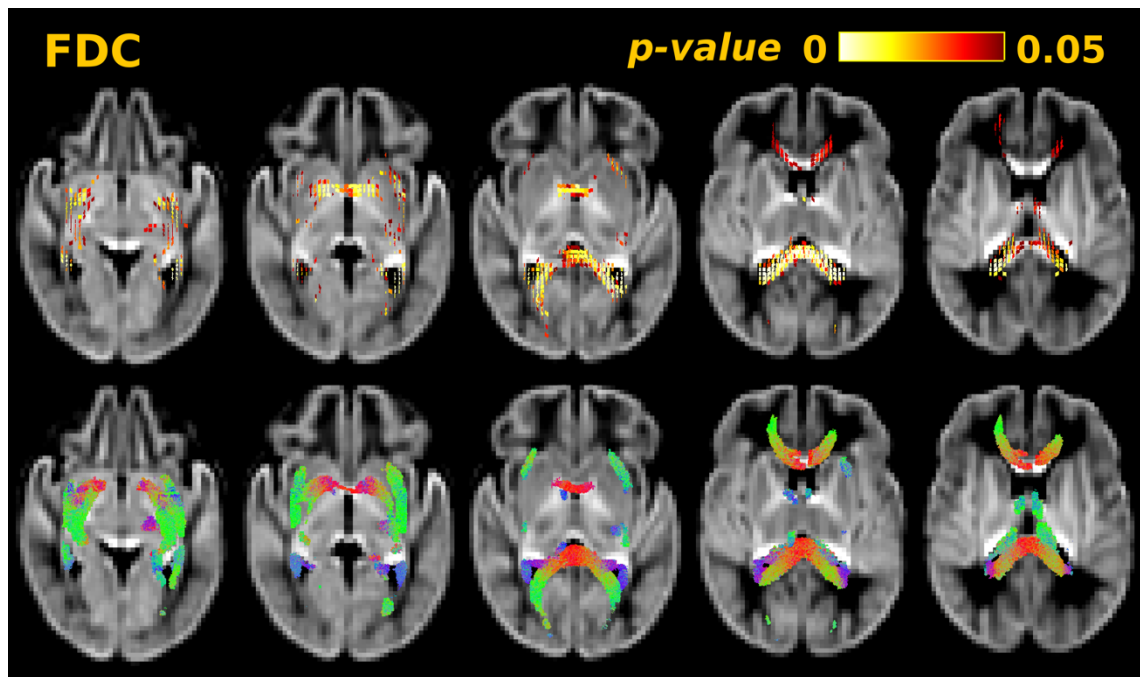


Figure 6.11 The results of fixel-based analysis assessing the relationship between FDC and GA at birth. The top row shows fixels with significant positive correlation (corrected  $p \leq 0.05$ ) between FDC and GA at birth. The bottom row shows the streamlines passing through significant fixels, coloured by direction (red: left-right; green: anterior-posterior; blue: inferior-superior).

There were significant positive correlations between birth weight z scores and FDC in the splenium and body of the CC, the anterior commissure, CST, IFOF, ILF, fornix and fixels within the thalamus (Figure 6.21).

#### 6.3.3.1.6 Rate of weight gain

The rate of weight gain per week showed no significant correlation with either FD, FC or FDC.

#### 6.3.3.1.7 Sex

There were no significant differences in FD and FDC between male and female subjects.

Male subjects showed higher FC in the splenium of the CC, CST, frontal lobe projections of the L IFOF/UNC, SLF, ILF, cingulum, fornix and cerebellum (Figure 6.22 and Figure 6.23)

There were no instances where female subjects had fixel measures significantly higher than male subjects.



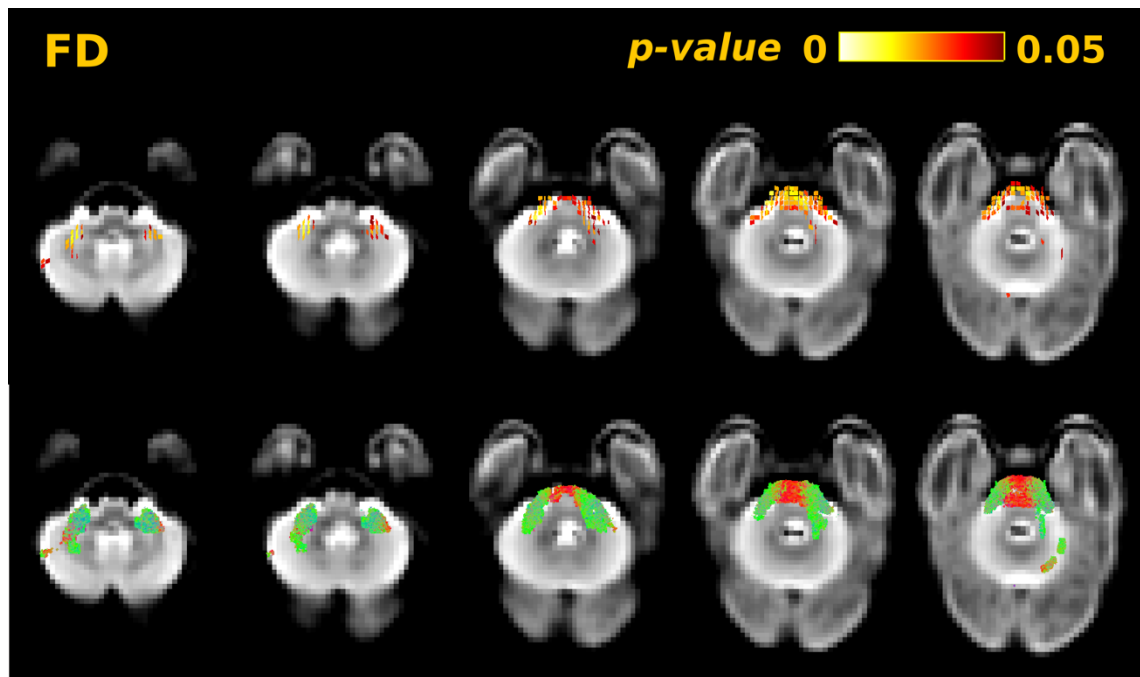


Figure 6.12 The results of fixel-based analysis assessing the relationship between FD and the number of days on mechanical ventilation. The top row shows fixels with significant negative correlation (corrected  $p \leq 0.05$ ) between FD and days on ventilation. The bottom row shows the streamlines passing through significant fixels, coloured by direction (red: left-right; green: anterior-posterior; blue: inferior-superior).

### 6.3.3.2 Relationship between fixel measures and developmental performance

#### 6.3.3.2.1 Motor performance

There was no significant correlation between motor performance and FD.

FC was significantly correlated positively with motor scores in the cerebellum and pons (Figure 6.24 and Figure 6.25), and FDC showed a positive correlation with motor performance in the splenium of the CC (Figure 6.26).

#### 6.3.3.2.2 Cognitive performance

There was no significant correlation between cognitive performance and FD.

There was significant positive correlation with FC in the splenium and tapetum of the CC, the anterior commissure and in a small region of the right ILF/IFOF (Figure 6.27).

FDC was correlated positively with cognitive scores in the splenium of the CC, a small region in the right CST and the ILF (Figure 6.28).

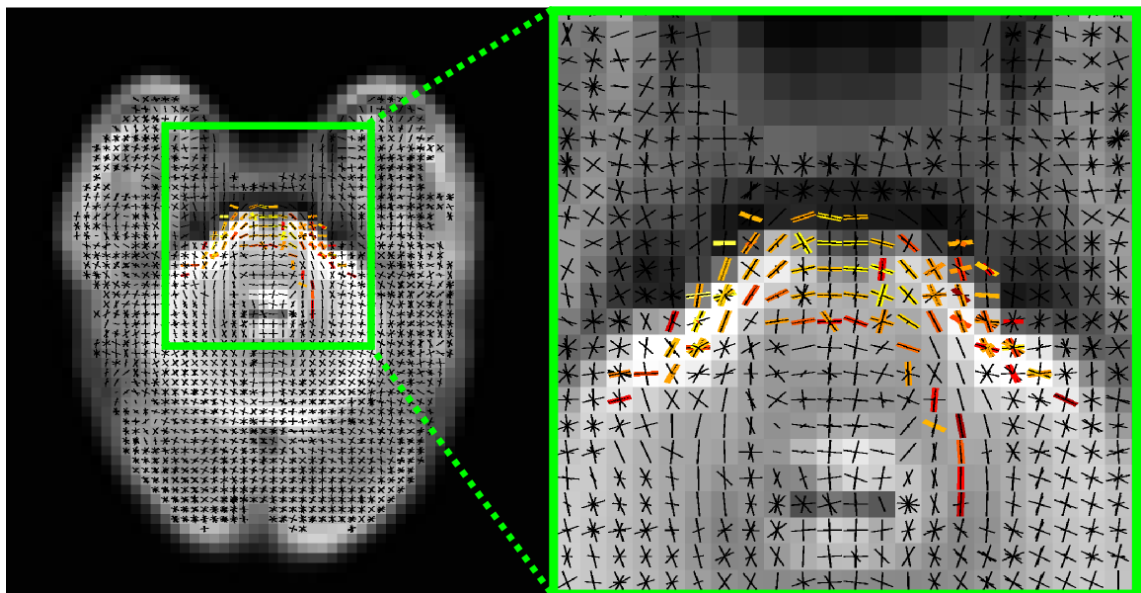


Figure 6.13 Axial view of fixels showing significant positive correlation between FD and the number of days on mechanical ventilation (red-yellow) overlaid on the fixel template mask (black) with a close-up of fixels within the cerebellum.

#### 6.3.3.2.3 Language performance

There was a significant positive correlation between language scores and FD in the splenium of the CC, a small region of fixels within the CC projecting from the middle of the body towards the cortex, and the ILF (Figure 6.29)

There was no correlation between language scores and FC.

FDC showed significant positive correlations with language scores in the genu, splenium and tapetum of the CC, in the same region of the middle of the body of the CC but also including fixels across the body and towards the cortex in both hemispheres, and in the ILF (Figure 6.30).

All the results from the FBA analysis are summarised in Table 2.

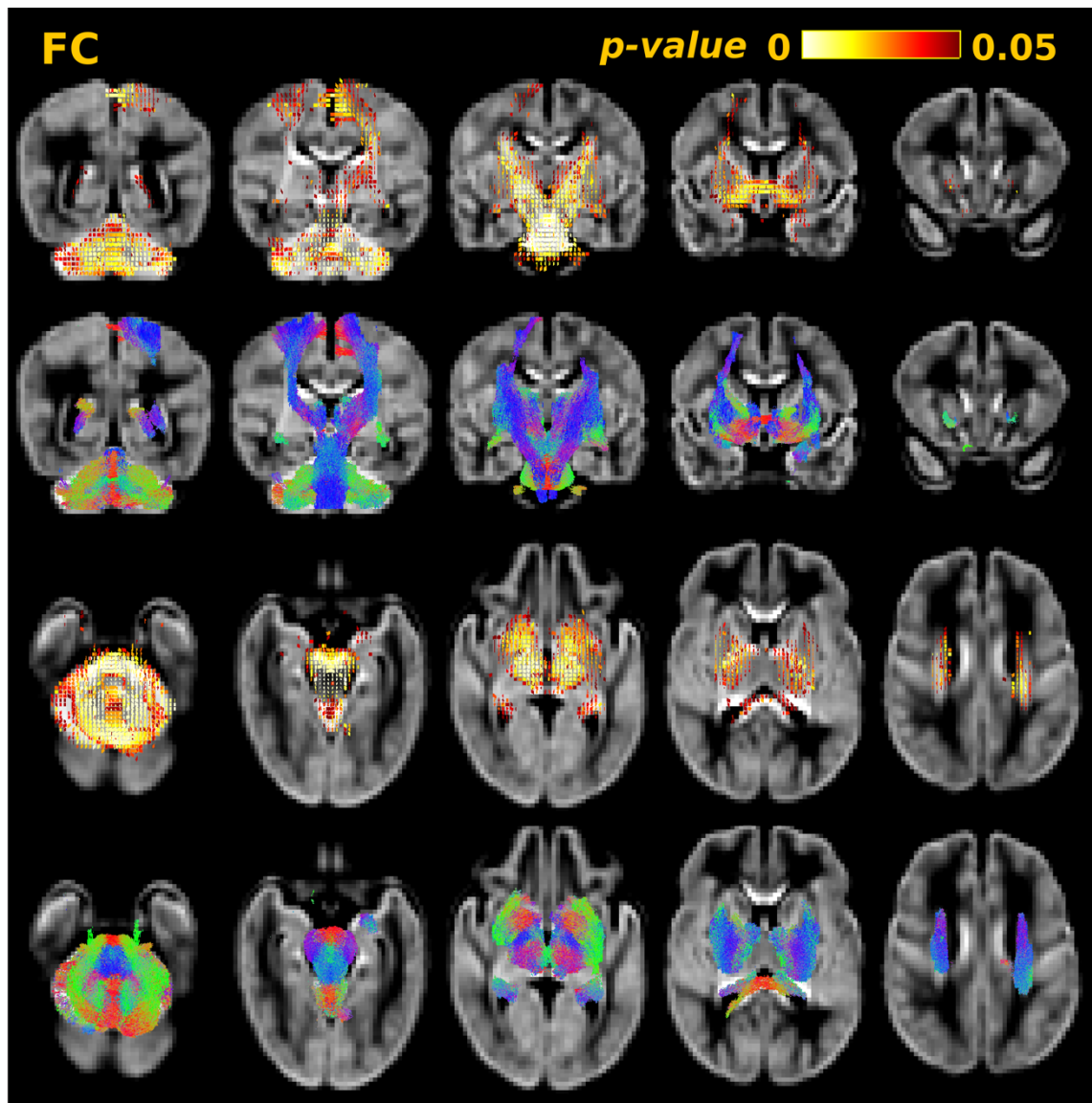


Figure 6.14 The results of fixel-based analysis assessing the relationship between FC and the number of days on mechanical ventilation. The top and third rows show fixels with significant negative correlation (corrected  $p \leq 0.05$ ) between FC and days on ventilation. The second and bottom rows show the streamlines passing through significant fixels, coloured by direction (red: left-right; green: anterior-posterior; blue: inferior-superior).

## 6.4 Discussion

This study demonstrates the feasibility of applying FBA to investigate WM properties in neonates, revealing associations between fibre population-specific measures of microstructural fibre density and regional cross-section of WM fasciculi and perinatal risk factors and neurodevelopmental performance. FD was calculated by integrating over the FOD lobe. As the amplitude of the FOD lobe is proportional to the restricted intra-axonal compartment, and contributions from the extra-cellular compartment are attenuated, FD provides a measure of

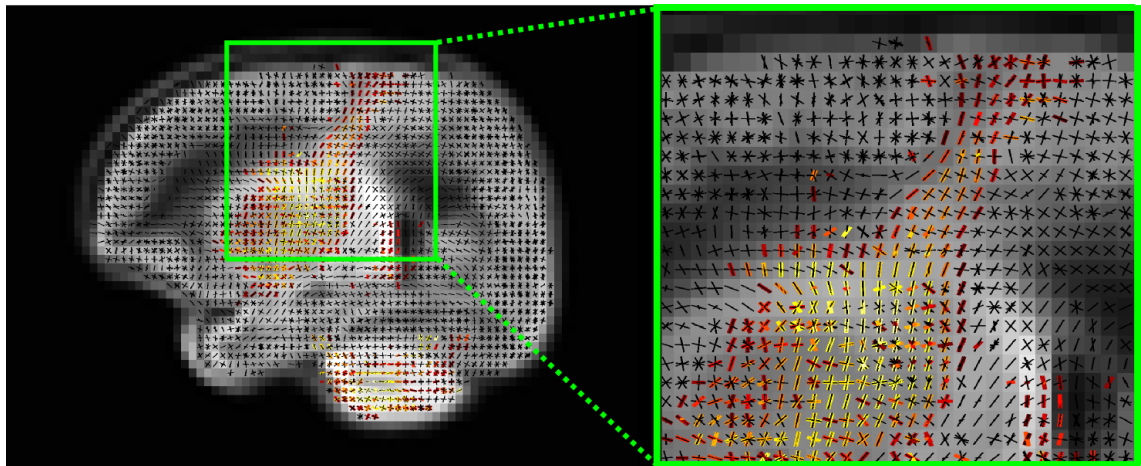


Figure 6.15 Sagittal view of the fixels showing significant positive negative between FC and the number of days on mechanical ventilation (red-yellow) overlaid on the template fixel mask (black) with a close-up demonstrating that, within the centrum semiovale, it is fibres from the CST that show a significant correlation with days on ventilation, and not association fibres or lateral projections of the CC.

within-voxel microstructural changes. FC was calculated from the determinant of the Jacobian matrices of the nonlinear deformations calculated during registration. FC provides a measure of the local expansion or contraction in WM bundles, across voxels, in the direction perpendicular to the main orientation of the fibre bundle. It should be noted that FC provides a measure of relative WM fibre-bundle macrostructural differences between subjects. It is calculated as the local change in fibre bundle cross-section with respect to the orientation of a fixel that occurs during registration but it is not an actual measure of a fibre bundle's cross-section. This makes the choice of template particularly important, which is defined as a study-specific group average in this study, so as not to introduce bias towards any particular subject or group. FDC was calculated by multiplying FC and FD, thereby providing a measure of change related to both tissue microstructure and fibre bundle morphology.

The correlations between variables of interest and FC were more widespread than correlations with FD, except for language performance. Indeed, there was no correlation between FD and days requiring TPN, birth weight z scores, motor scores and cognitive scores, and no significant differences in FD were found between male and female subjects. These results indicate that the variables studied here are more strongly associated with reductions in the cross-section of WM fasciculi rather than changes in WM microstructure.

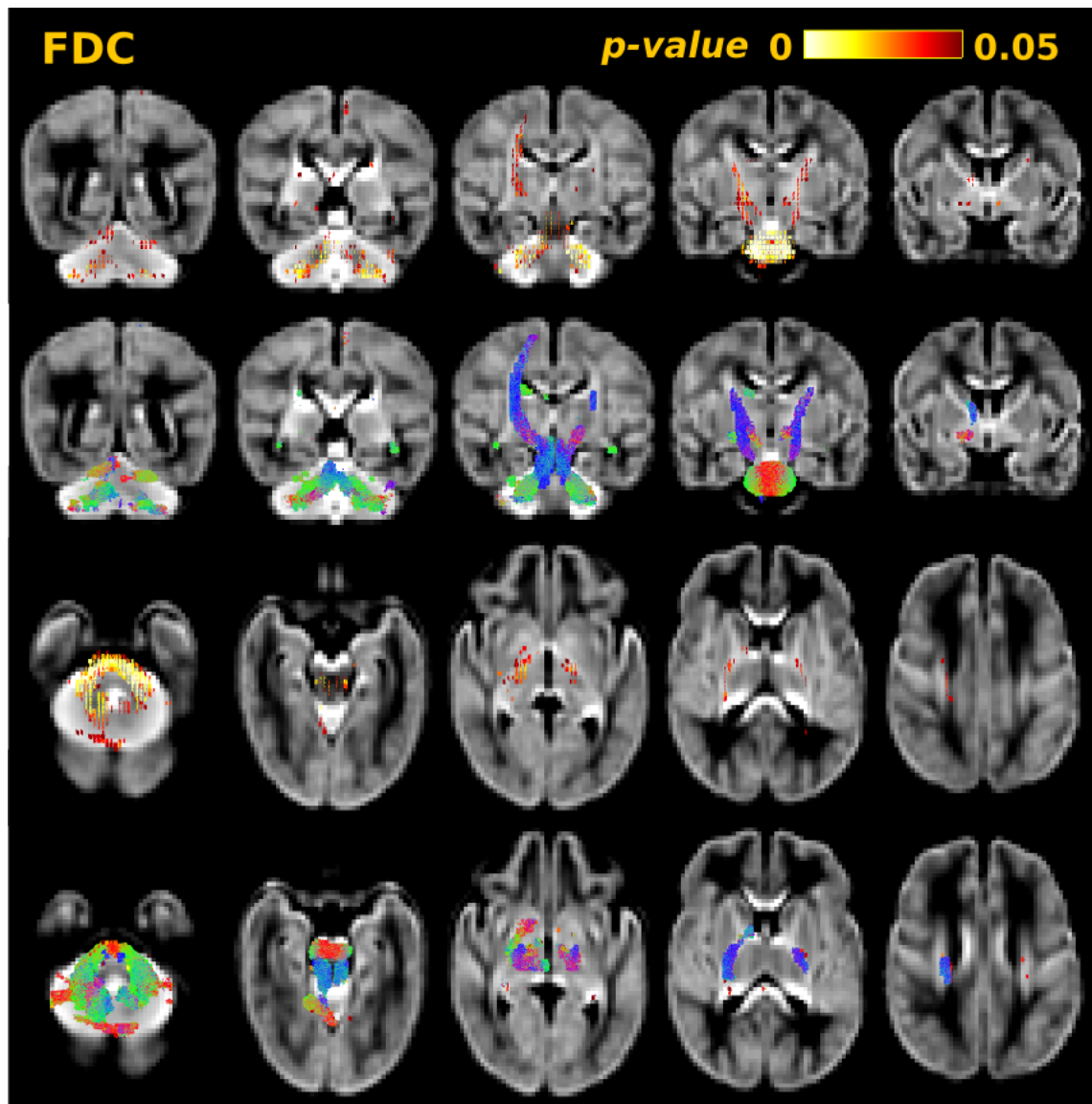


Figure 6.16 The results of fixel-based analysis assessing the relationship between FDC and the number of days on mechanical ventilation. The top and third rows show fixels with significant negative correlation (corrected  $p \leq 0.05$ ) between FDC and days on ventilation. The second and bottom rows show the streamlines passing through significant fixels, coloured by direction (red: left-right; green: anterior-posterior; blue: inferior-superior).

This study extends our knowledge of morphological changes associated with perinatal characteristics by demonstrating fibre-specific relationships. Previous volumetric studies investigated changes in total brain volume or tissue volumes. Using fixel-based measures it is possible to identify whether these changes are localised to specific fibre bundles or occur across the whole WM. This is of particular importance in regions of crossing fibres. In close-ups of the fixels within voxels containing multiple fibre populations it is clear that FBA enables fibre-bundle-specific inferences. For example, in Figure 6.15 a close-up of the centrum semiovale



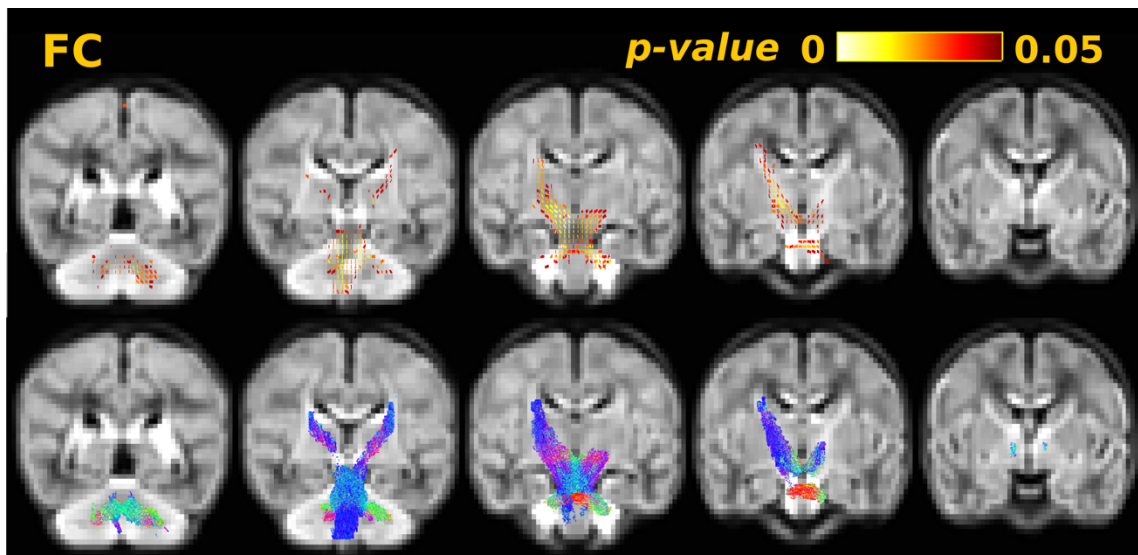


Figure 6.17 The results of fixel-based analysis assessing the relationship between FC and the number of days requiring total parenteral nutrition (TPN). The top row shows fixels with significant negative correlation (corrected  $p \leq 0.05$ ) between FC and days on TPN. The bottom row shows the streamlines passing through significant fixels, coloured by direction (red: left-right; green: anterior-posterior; blue: inferior-superior).

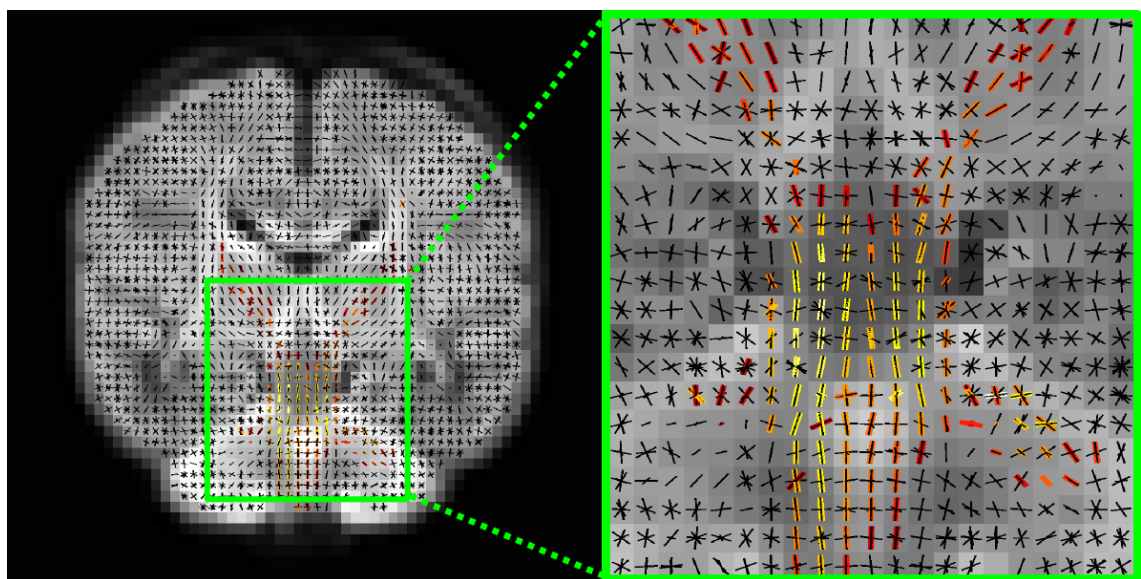


Figure 6.18 Coronal view of the fixels showing significant positive negative between FC and the number of days requiring total parenteral nutrition (TPN) (red-yellow) overlaid on the template fixel mask (black) with a close-up of a region of crossing fibres within the brain stem.

shows significant correlation between FC and days on mechanical ventilation. It can be observed that fixels belonging to the CST correlate with days spent on ventilation rather than any of the association fibres that traverse the region. By identifying which tracts are affected by given perinatal risk factors it could be possible to anticipate future developmental impairment by considering the functional pathways in which these tracts are involved.

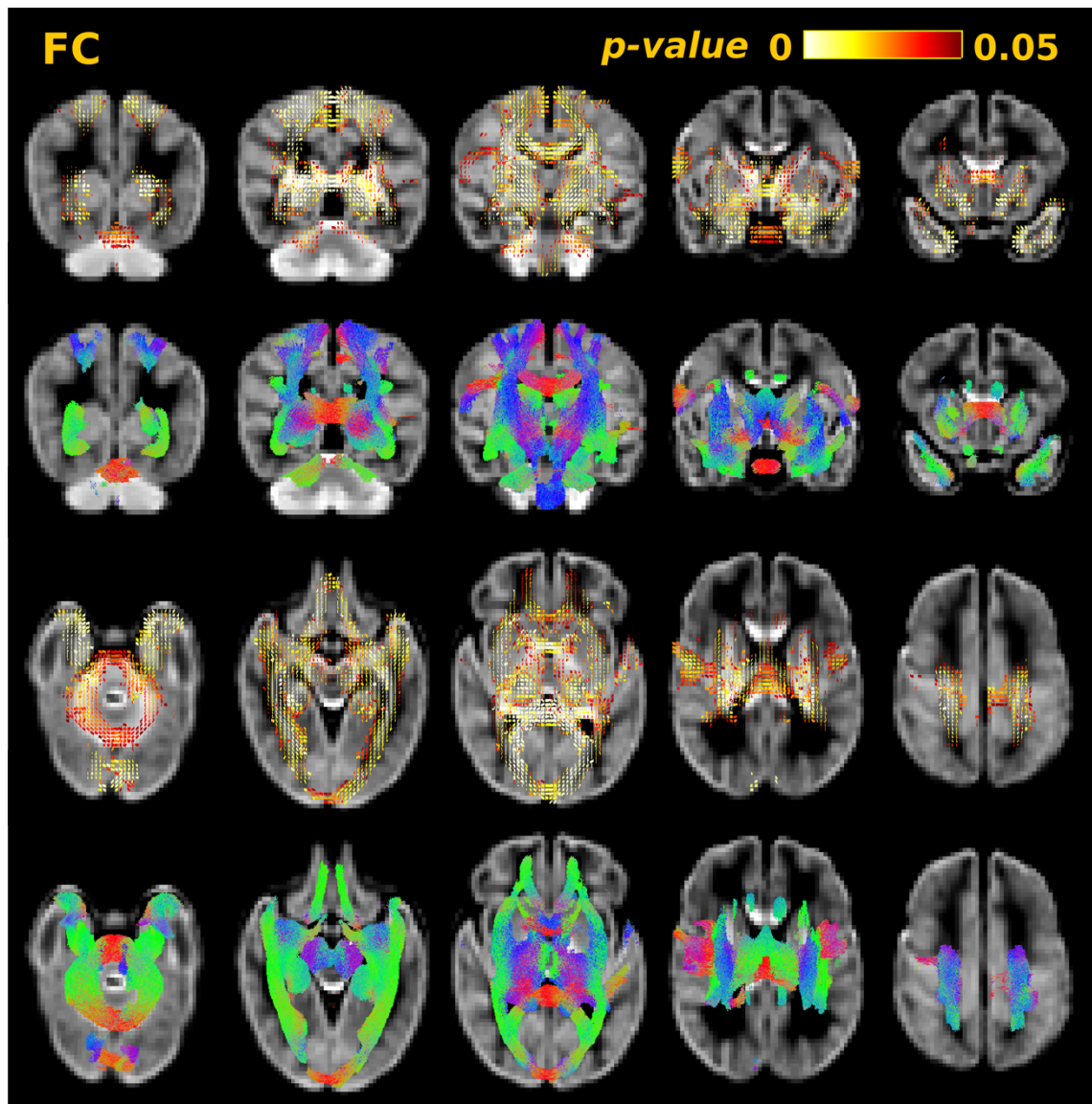


Figure 6.19 The results of fixel-based analysis assessing the relationship between FC and birth weight z scores. The top and third rows show fixels with significant positive correlation (corrected  $p \leq 0.05$ ) between FC and birth weight z scores. The second and bottom rows show the streamlines passing through significant fixels, coloured by direction (red: left-right; green: anterior-posterior; blue: inferior-superior).

However, a limitation of FBA is that it is not possible to identify the specific tract affected when multiple fibre populations from distinct fasciculi track through the same region in parallel trajectories. This is noticeable in the frontal and temporal WM, where it is not possible to make the distinction between the UNC and the projections of the ILF and IFOF.

The changes associated with PMA at scan were widespread throughout the WM. FD, FC and FDC measures showed significant positive correlations with age at scan. PMA at scan was positively correlated with FD throughout major WM tracts. Notably, there was no significant correlation between PMA and FD in the body of the CC, similar to results from Chapter 5, where

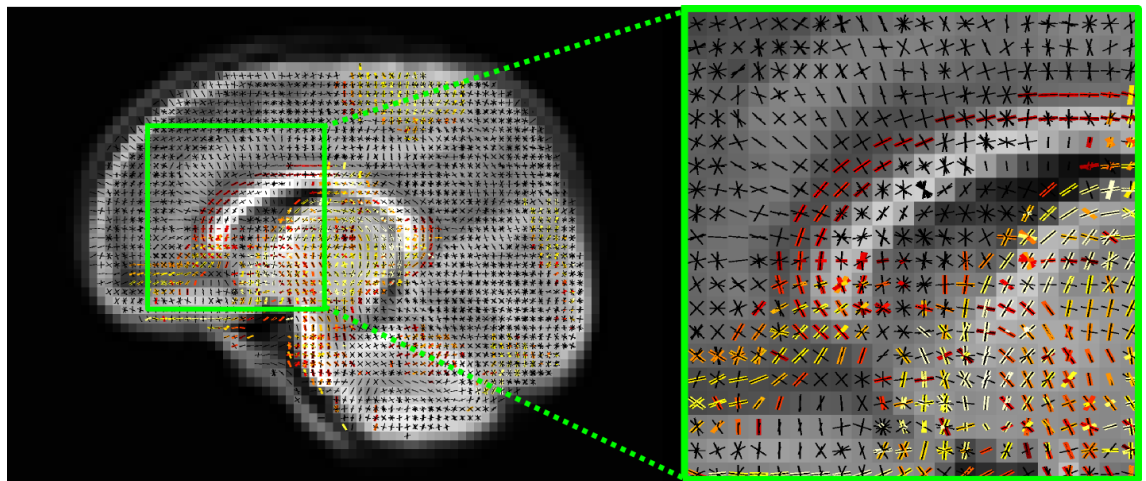


Figure 6.20 Sagittal view of fixels showing significant positive correlation between FC and birthweight z scores (red-yellow) overlaid on the fixel template mask (black) with a close-up within the cingulum.

no significant correlation was found between PMA and diffusion measures in the body of the CC. This supports the conclusion that the microstructural properties of the body of the CC are unchanging during this period. The correlation between PMA and FD is less extensive than the correlations between PMA and DTI measures found in the previous chapter. While FD and DTI measures all relate to the tissue microstructure, the cohort size in Chapter 5 was much greater than the cohort studied here. FC values were correlated positively with PMA at scan across the WM, demonstrating increases in WM fasciculi cross-section with maturation. These findings are consistent with previous volumetric studies based on conventional MRI which have identified linear increases in total brain volume and WM volume during the perinatal period. (Ajayi-Obe et al., 2000; Huppi et al., 1998b; Peterson et al., 2003).

GA at birth was correlated positively with FD in the splenium and tapetum of the CC, the anterior commissure and the left IFOF. As was discussed in Chapter 5, prematurity adversely affects WM microstructure. These findings demonstrate that commissural fibres in particular are vulnerable to disturbances in intra-axonal volume fraction. FC was correlated positively with GA at birth. The relationship was widespread across the WM. Previous studies have shown the preterm birth is associated with reduced tissue volumes and reduced overall brain volume (Inder et al., 2005; Srinivasan et al., 2006; Thompson et al., 2007). FBA demonstrates that this effect is widespread across WM fasciculi and not driven by localised changes.



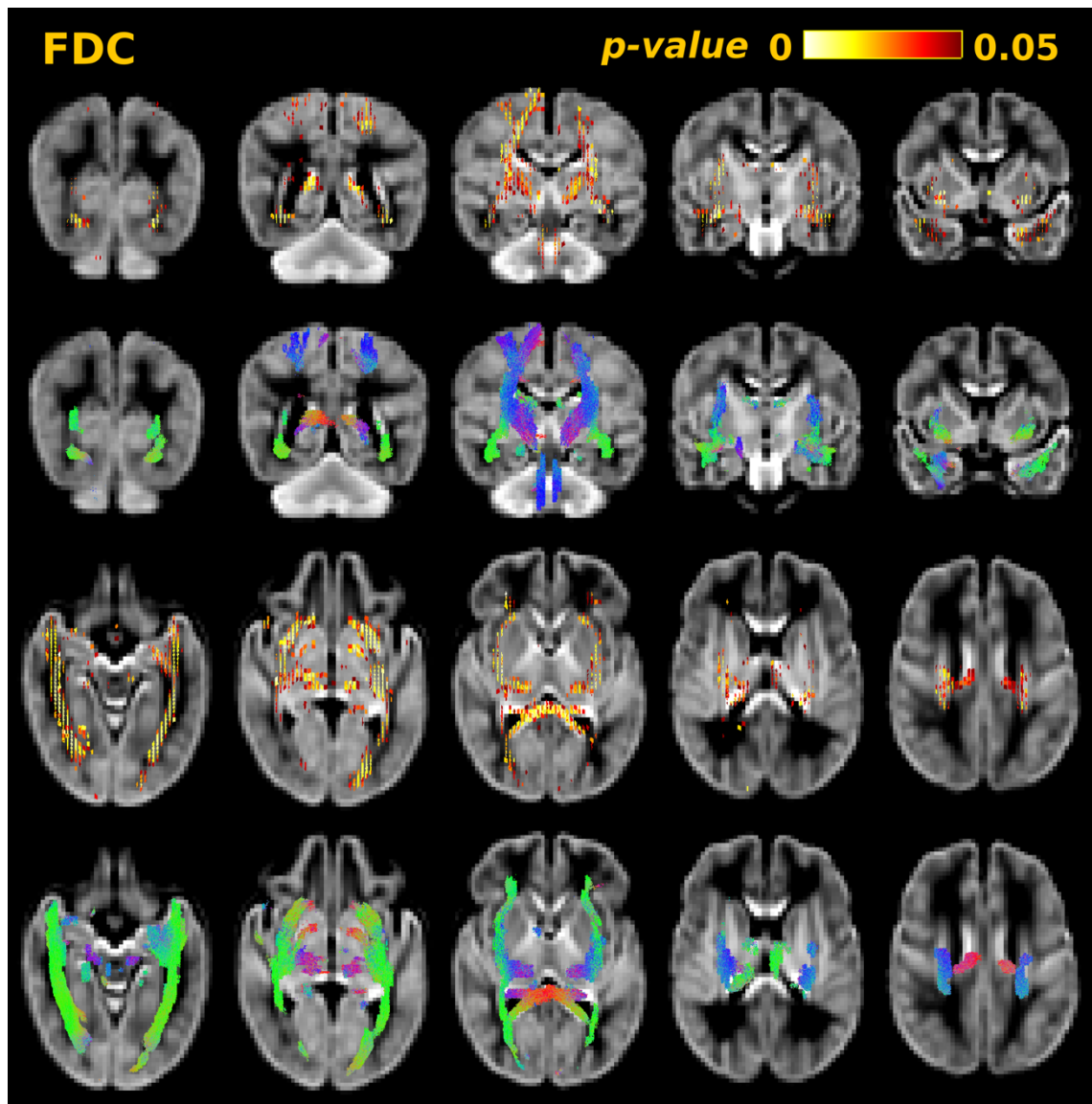


Figure 6.21 The results of fixel-based analysis assessing the relationship between FDC and birth weight z scores. The top and third rows show fixels with significant positive correlation (corrected  $p \leq 0.05$ ) between FDC and birth weight z scores. The second and bottom rows show the streamlines passing through significant fixels, coloured by direction (red: left-right; green: anterior-posterior; blue: inferior-superior).

Respiratory illness during the perinatal period has been associated with poor developmental outcome (Hansen et al., 2004; Short et al., 2003) and independent of prematurity at birth, is associated with WM microstructural abnormalities (Anjari et al., 2009; Ball et al., 2010) and reduced WM and cerebellar volumes in preterm infants (Argyropoulou et al., 2003; Boardman et al., 2007; Thompson et al., 2007) and preterm-born children (Reiss et al., 2004). FBA reveals that while days of ventilation had widespread effects on FC across the WM and cerebellum, microstructural changes as assessed by FD were localised to the cerebellum and pons. Cerebellar microstructural development in preterm infants has been not been well characterised. Brossard-Racine et al. (2017) reported counterintuitive increased FA and

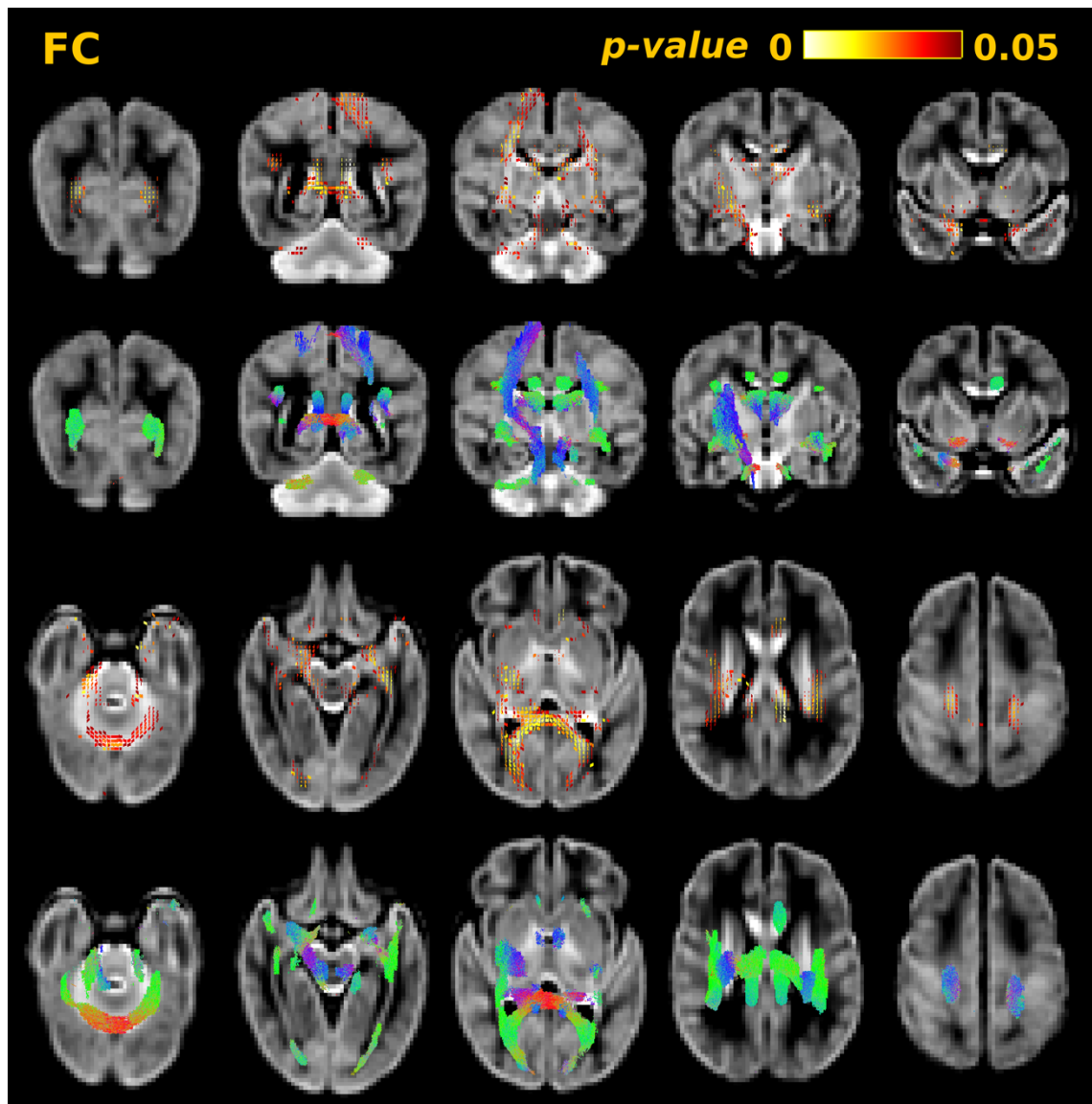


Figure 6.22 The results of fixel-based analysis assessing differences between male and female subjects. The top and third rows show fixels with FC significantly greater (corrected  $p \leq 0.05$ ) in male subjects than in female subjects. The second and bottom rows show the streamlines passing through significant fixels, coloured by direction (red: left-right; green: anterior-posterior; blue: inferior-superior).

reduced MD associated with compromised cardiorespiratory function in the dentate nucleus and WM abnormality scores in the vermis. This is most likely due the prevalence of crossing fibre regions, which have been demonstrated in fixed fetal brains using CSD tractography (Takahashi et al., 2014). This highlights the need for higher-order models in regions of complex fibre configurations, and specifically the cerebellum.

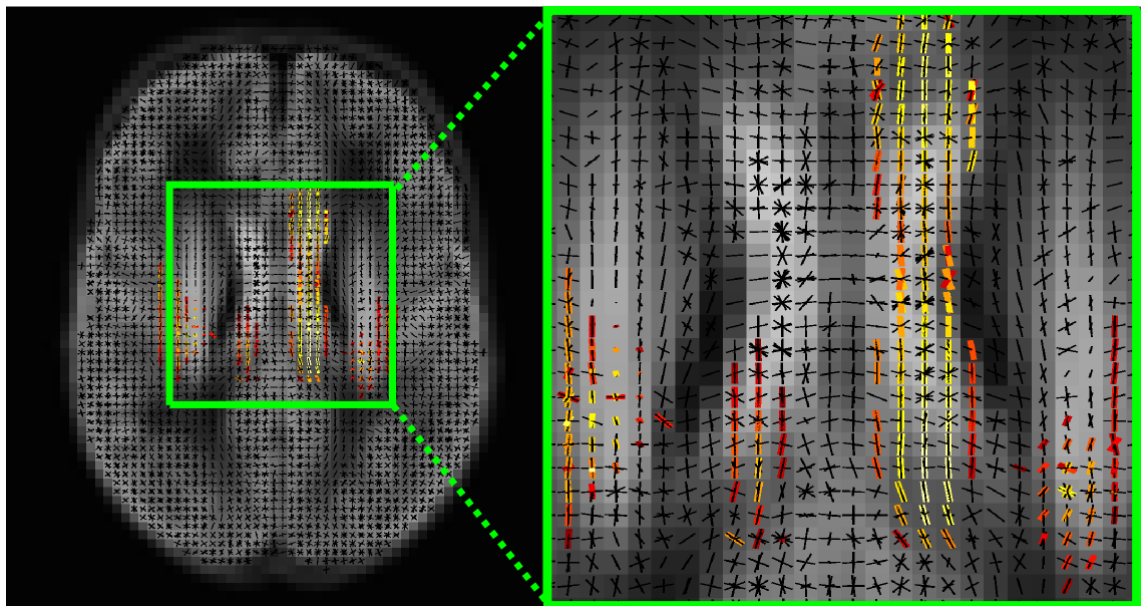


Figure 6.23 Axial view of the fixels showing significant differences in FC between male and female subjects (red-yellow) overlaid on the template fixel mask with a close-up of the fixels within the cingulum. The cingulum can be difficult to identify due to partial volume effects from the CC, however it is possible to distinguish the two using fixel-based analysis.

The relationship between TPN and fixel measures was also analysed. Gut immaturity in preterm infants can result in an inability to tolerate enteral feeds and therefore parenteral nutrition is required (Morgan, 2013). Nutritional deficits occur in infants who are dependent on parenteral nutrition (Clark et al., 2003; Dusick et al., 2003) and reduced energy and protein intake during the first week of life has been associated with impaired cognitive and motor performance (Stephens et al., 2009). Moreover, it is generally more critically ill infants who require TPN for longer (Ehrenkranz et al., 2011). Previous studies have shown parenteral nutrition is associated with WM and cerebellar abnormalities assessed qualitatively on conventional MRI (Brouwer et al., 2017) and that the cerebellum and hippocampus are particularly vulnerable to malnutrition (Levitsky and Strupp, 1995). FBA demonstrates a relative reduction in FC in the CST and cerebellum, and no changes in FD or FDC. Aberrant cerebellar and corticospinal morphology could impact both motor and cognitive function later on in life (Davis et al., 2010).

Birth weight z scores were correlated positively with FC and FDC across the WM, but no microstructural changes were observed. Birth weight is linearly associated with increased brain volume (Parikh et al., 2013; Xydis et al., 2013) and FBA demonstrates this effect is widespread throughout WM fasciculi.

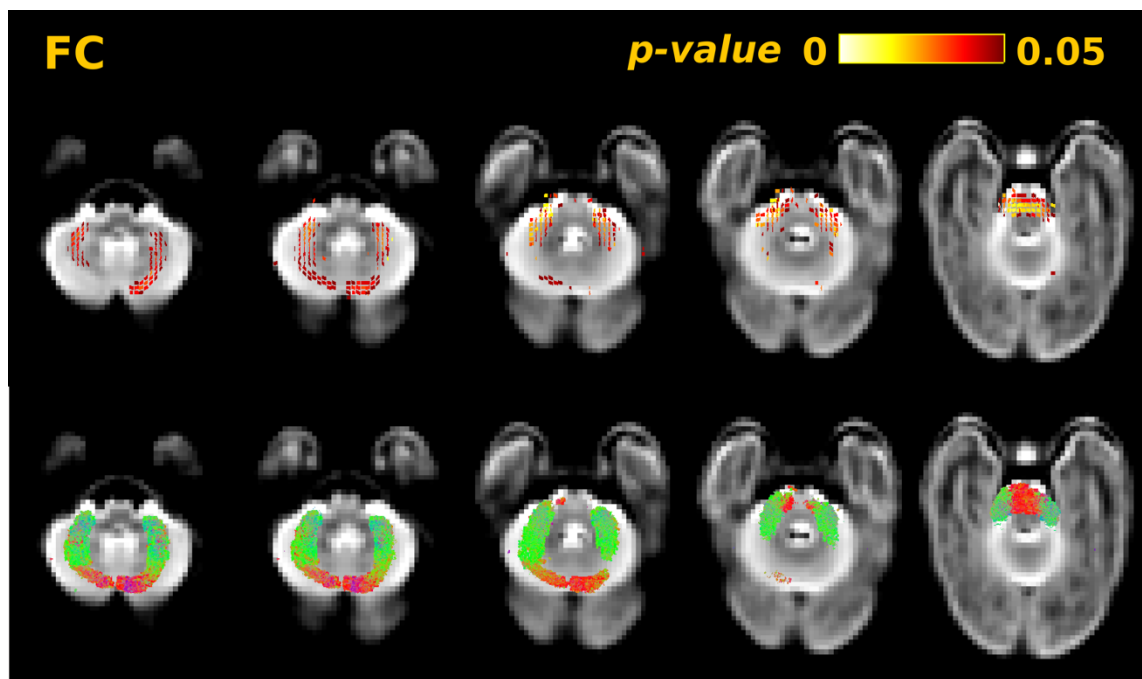


Figure 6.24 The results of fixel-based analysis assessing the relationship between FC and motor performance. The top row shows fixels with significant positive correlation (corrected  $p \leq 0.05$ ) between FC and motor scores from the BSITD-III. The bottom row shows the streamlines passing through significant fixels, coloured by direction (red: left-right; green: anterior-posterior; blue: inferior-superior).

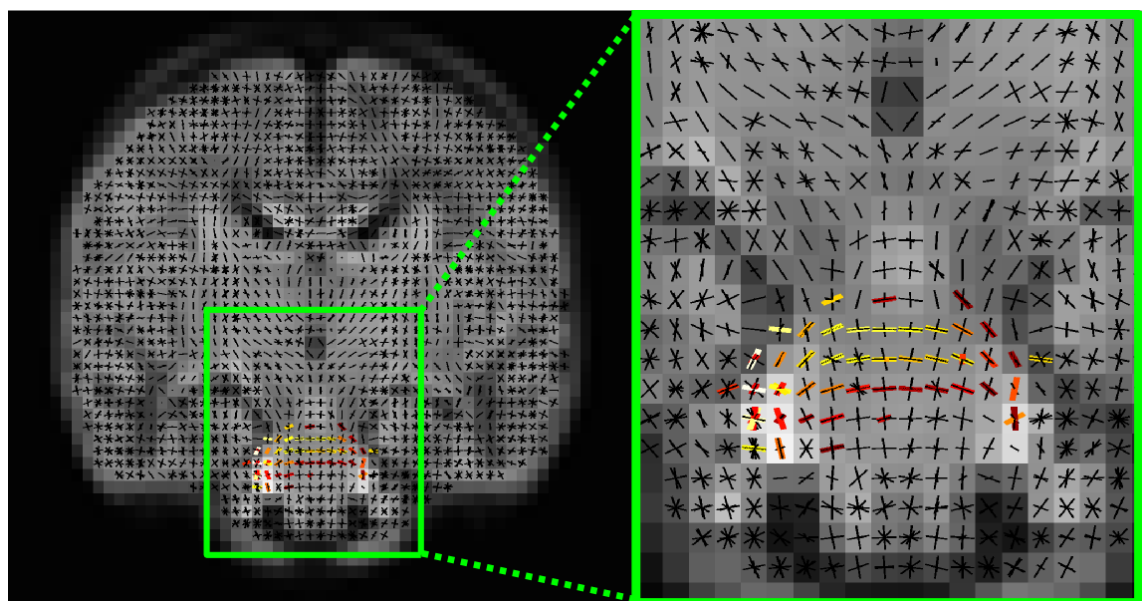


Figure 6.25 Coronal view of the fixel showing significant positive correlation between motor scores and FC (red-yellow) overlaid on the template fixel mask (black) with a close-up of the brainstem demonstrating that only fixels within the pons, and not the CST, are significantly correlated with motor scores.

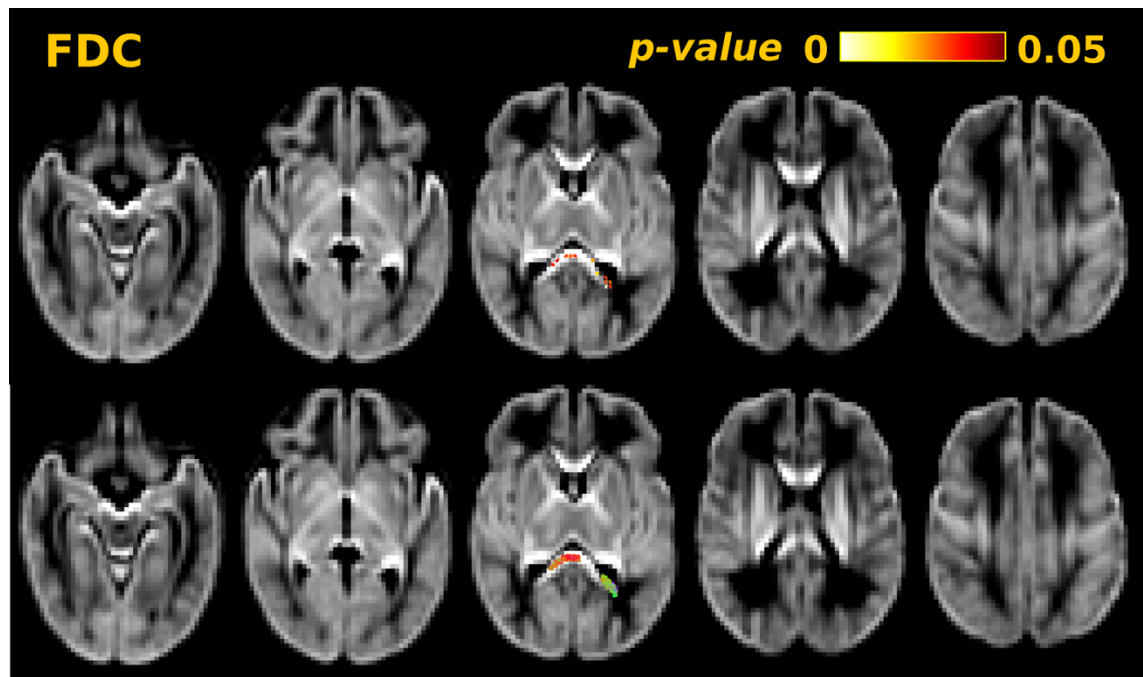


Figure 6.26 The results of fixel-based analysis assessing the relationship between FDC and motor performance. The top row shows fixels with significant positive correlation (corrected  $p \leq 0.05$ ) between FDC and motor scores from the BSITD-III. The bottom row shows the streamlines passing through significant fixels, coloured by direction (red: left-right; green: anterior-posterior; blue: inferior-superior).

Increased rate of weight gain during the perinatal period has been associated with improved neurodevelopmental scores (Ehrenkranz et al., 2006; Franz et al., 2009). However, rate of weight gain per week was not significantly correlated with any fixel measures. Rate of weight gain was calculated for the period between birth and the time of MRI scan. Rate of weight gain was linearly correlated with GA at birth (Pearson correlation = 0.38) and after correcting for GA no significant relationship remained.

Male sex has been implicated as a risk factor for poorer outcome in preterm infants (Hintz et al., 2006; Serenius et al., 2013; Wood et al., 2005). In this study, no microstructural differences were found between male and female subjects. A previous DTI study in a larger cohort ( $n=78$ ) have found lower FA in the splenium of the CC in preterm males than preterm females at TEA (Rose et al., 2009), however in a smaller cohorts ( $n=26$ ,  $n=29$ ,  $n=63$ ) (Anjari et al., 2007; Skiold et al., 2014; van Kooij et al., 2012b) no differences in diffusion measures were found. However, male infants had greater FC across the whole WM, consistent with previous studies of overall brain, WM and cerebellar volumes (Skiold et al., 2014; Thompson et al., 2007).



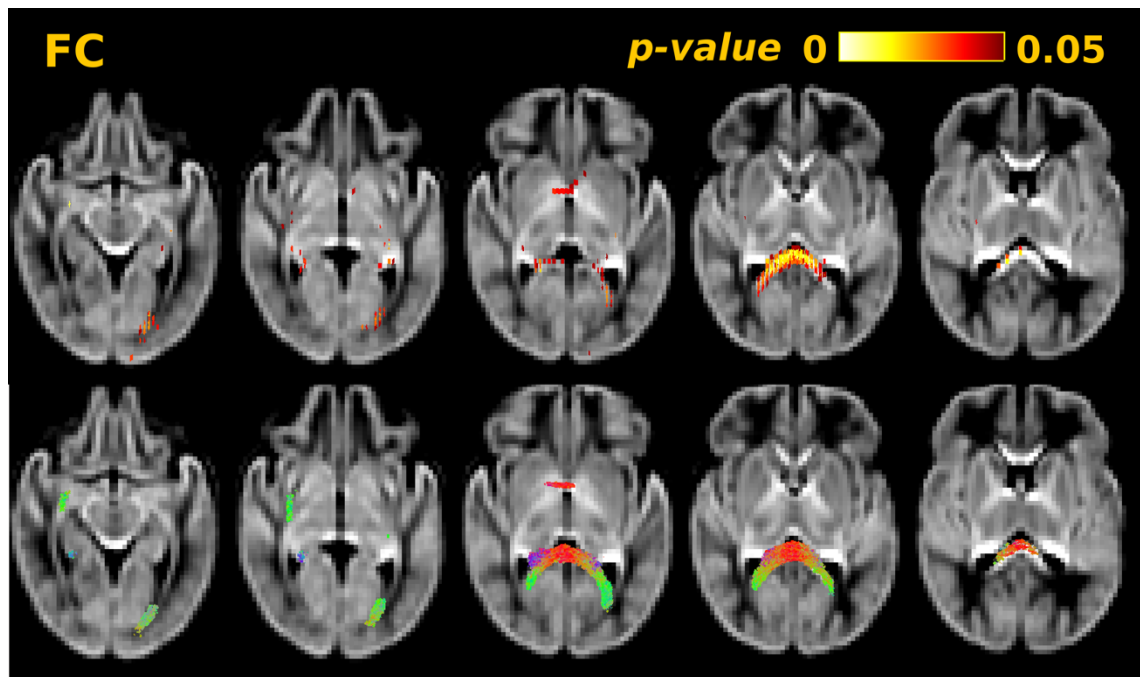


Figure 6.27 The results of fixel-based analysis assessing the relationship between FC and cognitive performance. The top row shows fixels with significant positive correlation (corrected  $p \leq 0.05$ ) between FC and cognitive scores from the BSITD-III. The bottom row shows the streamlines passing through significant fixels, coloured by direction (red: left-right; green: anterior-posterior; blue: inferior-superior).

A limitation of this study is that data regarding postnatal steroids treatment, ROP and postnatal infection or sepsis were not collected for this group and therefore their effects on the developing WM could not be studied.

Motor scores were correlated positively with FC in cerebellum. Cerebellar involvement in motor function is well-established (Evarts and Thach, 1969). Many of the studies exploring the role of the cerebellum in neurodevelopmental outcomes have been volumetric (Limperopoulos et al., 2010; Limperopoulos et al., 2005; Ranger et al., 2015; Srinivasan et al., 2006) or qualitative assessments of cerebellar injury (Haines et al., 2013; Limperopoulos et al., 2007; Messerschmidt et al., 2008). This demonstrates the relationship between the calibre of fibre bundles within the cerebellum and motor performance. More recently the role of the cerebellum in higher-order non-motor functions such as cognition and behaviour (Buckner, 2013; Schmahmann and Sherman, 1998) has been demonstrated. However, this study found no association between fixel measures in the cerebellum and cognitive scores.

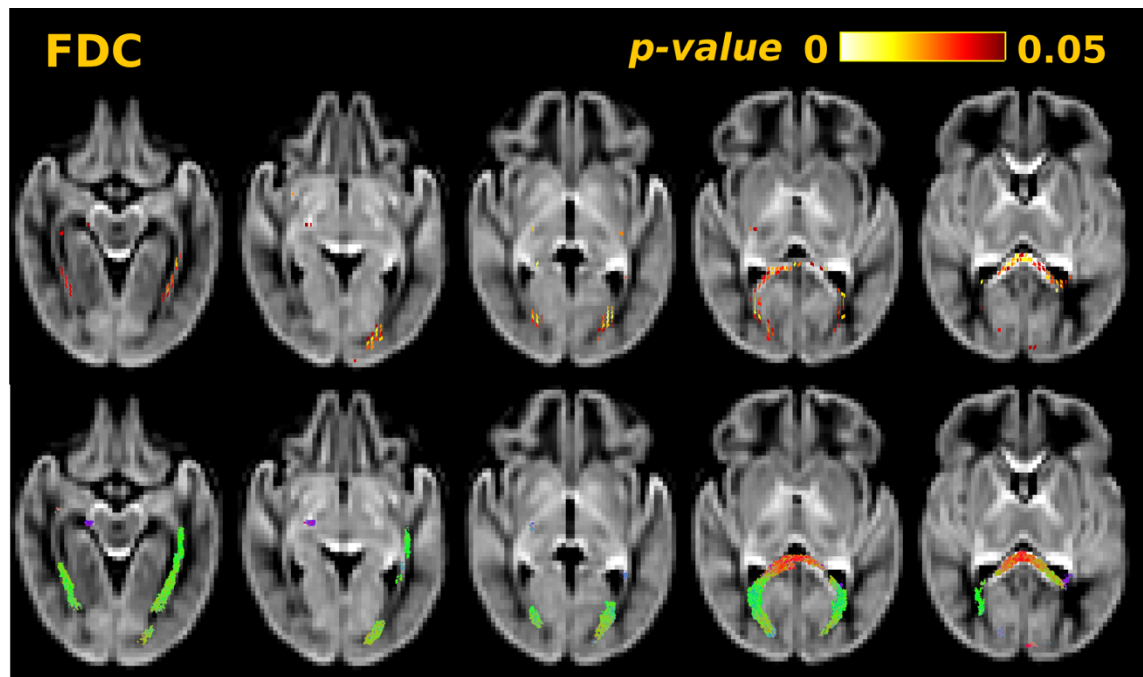


Figure 6.28 The results of fixel-based analysis assessing the relationship between FDC and cognitive performance. The top row shows fixels with significant positive correlation (corrected  $p \leq 0.05$ ) between FDC and cognitive scores from the BSITD-III. The bottom row shows the streamlines passing through significant fixels, coloured by direction (red: left-right; green: anterior-posterior; blue: inferior-superior).

Cognitive scores were correlated with FC in the CC and anterior commissure and with FDC in the CC and right CST. Both the CC and CST have been associated with cognitive performance in preterm infants in Chapter 5 and in other DTI studies (Duerden et al., 2015). Notably it is commissural fibres that demonstrate a significant correlation with cognitive performance, stressing the importance of inter-hemispheric connectivity. Moreover, this study highlights the importance of whole-brain analyses, as the anterior commissure is not often included in neonatal analyses.

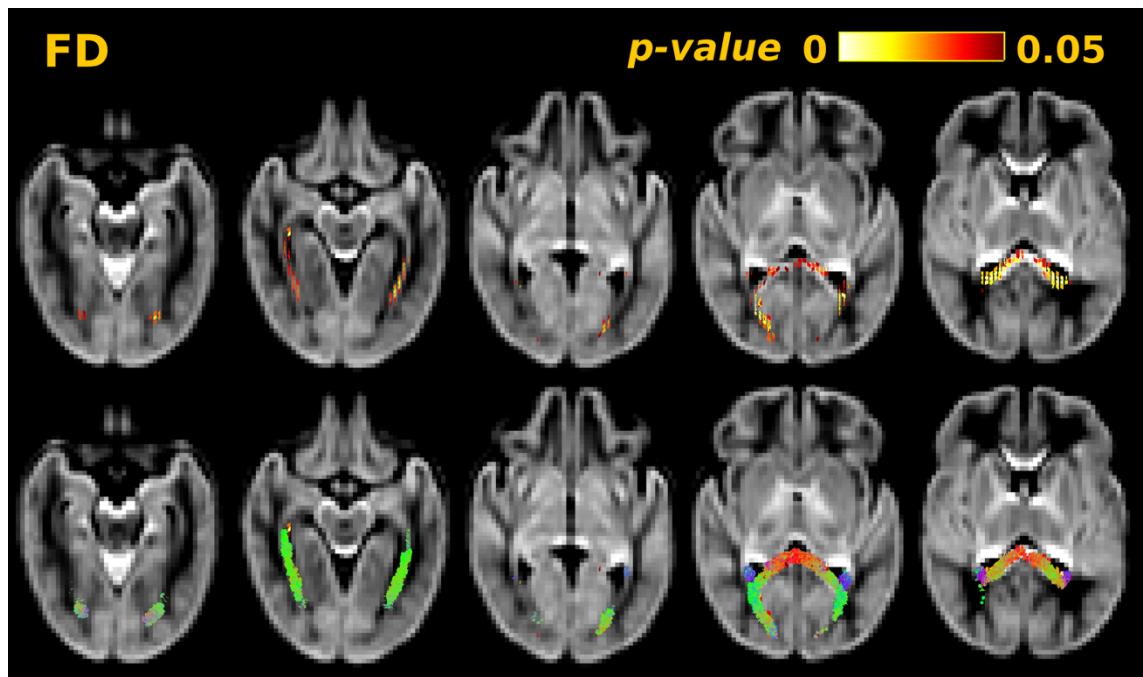


Figure 6.29 The results of fixel-based analysis assessing the relationship between FD and language performance. The top row shows fixels with significant positive correlation (corrected  $p \leq 0.05$ ) between FD and language scores from the BSITD-III. The bottom row shows the streamlines passing through significant fixels, coloured by direction (red: left-right; green: anterior-posterior; blue: inferior-superior).

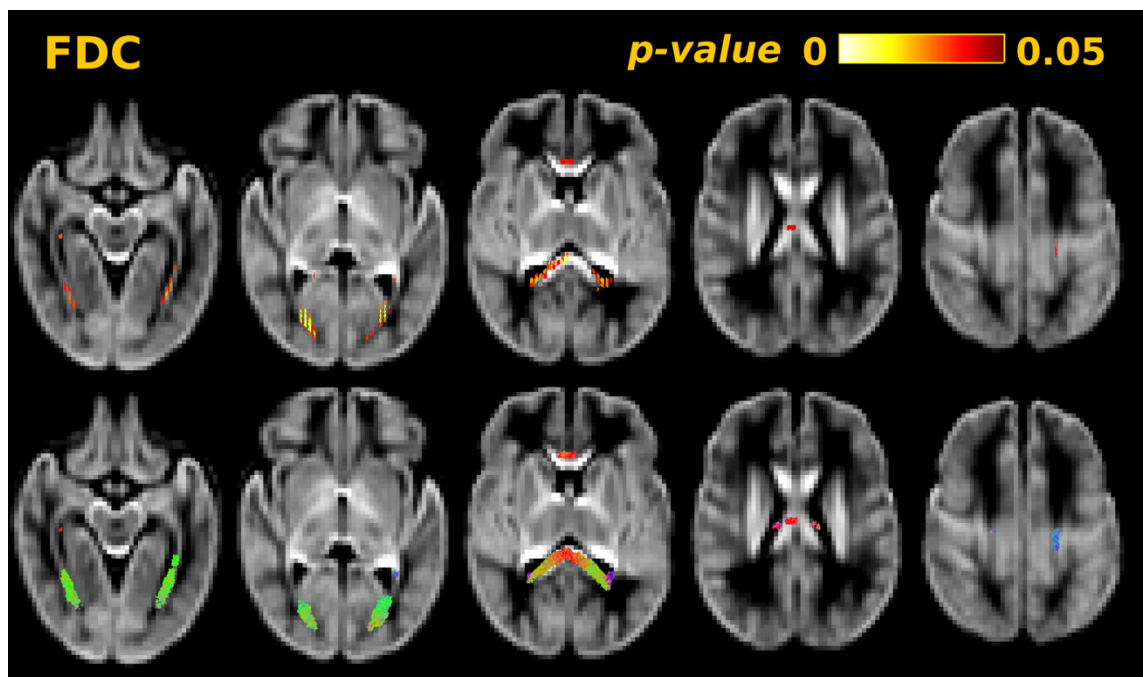


Figure 6.30 The results of fixel-based analysis assessing the relationship between FDC and language performance. The top row shows fixels with significant positive correlation (corrected  $p \leq 0.05$ ) between FDC and language scores from the BSITD-III. The bottom row shows the streamlines passing through significant fixels, coloured by direction (red: left-right; green: anterior-posterior; blue: inferior-superior).



Language performance was the only BSITD-III measure that showed a significant correlation with FD. Correlations were found in the ILF, the splenium of the CC, and a small region of fixels within the body of the CC projecting towards the cortex. These tracts have been shown to be involved in language and reading abilities in preterm-born children (Feldman et al., 2012). These findings suggest that language ability is more closely related to microstructural rather than morphological properties of WM, unlike motor or cognitive development. However, language and cognitive performance are closely related and it should be noted that regions showing significant correlation between FDC and cognitive scores and FDC and language scores overlap substantially.

## **6.5 Conclusions**

This chapter demonstrates the feasibility of applying FBA to the neonatal preterm population. This study identifies changes in fibre density and cross-section of specific fibre bundles within whole brain WM associated with maturation, perinatal risk factors and neurodevelopmental outcome.

Table 6.2 Summary of results from fixel-based analysis. All significant results are bilateral, unless the hemisphere is explicitly stated.

Variable of interest	FD	FC	FDC
PMA at scan	Forceps minor	Forceps major	Forceps minor
(positive correlation)	Forceps major	body CC	Forceps major
	Cortical projections	Lateral projections	body CC
	from body of CC	CC	Lateral projections
	Lateral projections	Anterior	CC
	CC	commissure	Anterior
	Corona radiata	Posterior	commissure
	IFOF	commissure	CST
	SLF	CST	IFOF
	ILF	IFOF	SLF
		SLF	ILF
		ILF	Fixels within the
		Cingulum	thalamus
		Fornix	Cerebellum
		Fixels within the	
		thalamus	
		Cerebellum	
		Pons	

Variable of interest	FD	FC	FDC
GA at birth (positive correlation)	splenium CC	genu CC	genu CC
	tapetum CC	splenium CC	splenium CC
	Anterior	Anterior	tapetum CC
	commissure	commissure	Anterior
	L IFOF	CST	commissure
		IFOF	L CST
		SLF	IFOF
		ILF	ILF
		Cingulum	Fornix
		Fornix	Fixels within the
		Fixels within the thalamus	thalamus
		Cerebellum	
		Pons	
Days on ventilation (negative correlation)	Cerebellum	splenium CC	CST
	Pons	tapetum CC	ILF
		Anterior	R Fornix
		commissure	Cerebellum
		CST	Pons
		IFOF	
		Fornix	
		ALIC	
		Fixels within the thalamus	
		Cerebellum	
		Pons	

Variable of interest	FD	FC	FDC
Days on total parenteral nutrition (negative correlation)	NS	CST  Cerebellum	NS
Birth weight z score (positive correlation)	NS	genu CC splenium CC body CC Lateral projections of CC Anterior commissure Posterior commissure ALIC CST IFOF SLF ILF Cingulum Fornix Fixels within the thalamus Cerebellum Pons	splenium CC body CC Lateral projections of CC Anterior commissure CST IFOF ILF Fornix Fixels within the thalamus
Rate of weight gain	NS	NS	NS

Variable of interest	FD	FC	FDC
Sex differences (male > female)	NS	splenium CC CST IFOF/UNC SLF Cingulum Fornix ILF Cerebellum	NS
Sex differences (female > male)	NS	NS	NS
Motor performance (positive correlation)	NS	Cerebellum Pons	splenium CC
Cognitive performance (positive correlation)	NS	splenium CC tapetum CC Anterior commissure R IFOF/ILF	splenium CC R CST ILF
Language performance (positive correlation)	splenium CC body CC ILF	NS	genu CC splenium CC tapetum CC body CC ILF

---

NS = not significant.

## Chapter 7 White matter in healthy term-born infants

This chapter studies WM lateralisation and maturation in term-born infants. While hemispheric WM asymmetries associated with functional specialisation have been demonstrated in adults, lateralisation has not been assessed within the perinatal period in healthy subjects. Furthermore, there are no studies characterising normal WM development in term infants using higher order diffusion models. In this chapter, TSA is combined with DTI, NODDI and fixel-derived measures and applied to state-of-the-art diffusion MRI data from the Developing Human Connectome Project to assess lateralisation and maturation in healthy term-born infants within the first four weeks of life. The results demonstrate little to no hemispheric differences in WM fasciculi, indicating that lateralisation emerges later in life. Regression analysis reveals a maturation pattern of decreasing diffusivity and increasing intracellular compartment and overall increases in WM fibre cross-section.

### 7.1 Introduction

Cerebral lateralisation is thought to be a key aspect of normal human development, arising from hereditary, genetic, developmental and experiential factors (Liu et al., 2009; Toga and Thompson, 2003). Typically, functional specialisation in the adult brain has been observed as left-hemispheric dominance for language and motor tasks, and right-hemispheric dominance for visuospatial attention (Badzakova-Trajkov et al., 2010; Barber et al., 2012; Cai et al., 2013; Heilman et al., 1983; Knecht et al., 2000; Schlerf et al., 2015; Whitehouse and Bishop, 2009). In addition, DTI studies have demonstrated asymmetries in WM fasciculi in children and adults. Higher FA in the left CST has been associated with right-handedness (Eluvathingal et al., 2007; Herve et al., 2009; Takao et al., 2011; Thiebaut de Schotten et al., 2011b; Westerhausen et al., 2007), and higher FA in the left arcuate fasciculus and SLF has been associated with language production (Buchel et al., 2004; Budisavljevic et al., 2015; Catani et al., 2007; Eluvathingal et al., 2007; Lebel and Beaulieu, 2009; Perlaki et al., 2013; Powell et al., 2006; Rodrigo et al., 2007; Takao et al., 2011), and visual-spatial attention has been associated with higher tract volumes in the right parieto-frontal SLF in right-handed adults (Thiebaut de Schotten et al., 2011a).

However, it remains unclear if such microstructural asymmetries are present at birth or emerge later in life. Functional MRI and event-related potential studies in infants have demonstrated higher activation in the left hemisphere in response to auditory stimuli (Dehaene-Lambertz, 2000; Dehaene-Lambertz et al., 2002; Dehaene-Lambertz et al., 2006; Pena et al., 2003) and studies in preterm neonates and foetuses have reported structural asymmetries in the Perisylvian region (Chi et al., 1977; Dubois et al., 2008b; Dubois et al., 2010; Habas et al., 2012; Leroy et al., 2015). DTI studies have found higher FA values in the left CST, SLF and arcuate fasciculus in preterm infants (Liu et al., 2010) and term-born infants aged 1-4 months (Dubois et al., 2009), and asymmetries of structural connectivity assessed using graph theoretical approaches in healthy neonates (Ratnarajah et al., 2013), however studies of WM lateralisation during the perinatal period in healthy term infants are lacking.

Furthermore, there are no studies characterising brain maturation in term-born infants beyond the DTI model. The Developing Human Connectome Project (dHCP) aims to deliver the first dynamic map of human brain connectivity from 20 to 44 weeks postconceptional age from well-characterized foetuses and newborn infants. Novel, optimised imaging methods developed for the dHCP (Hughes et al., 2016; Hutter et al., 2017) have produced neonatal MRI data of unprecedented quality. Applying advanced diffusion models, such as NODDI and fixel-derived measures, to state-of-the-art diffusion MRI data presents a unique opportunity to study normal human brain development. In this chapter, data from the first public release of imaging data from 40 dHCP subjects (Hughes et al., 2017) imaged within the first 4 weeks of life are studied to assess lateralisation and maturation in healthy term-born infants.

The aims of this chapter are to (i) investigate whether interhemispheric differences are present in WM fasciculi in healthy term-born neonates; and (ii) assess changes in the diffusion properties of WM fasciculi associated with increasing age using TSA and DTI, NODDI and fixel-derived measures. It is expected that diffusivities decrease and FA, FD, FC and neurite density, estimated by NODDI, will increase with increasing age.

## 7.2 Methods

### 7.2.1 Subjects

Infants were recruited and imaged at the Evelina Neonatal Imaging Centre, London, as part of the Developing Human Connectome Project. Informed parental consent was obtained for imaging and data release, and the study was approved by the UK Health Research Authority. The infants were imaged in natural sleep. 40 subjects from the first public data release were studied. Healthy subjects born at 36-41.6 (median 39.1) weeks GA were imaged within the first 4 weeks of life at 36.9-44.1 (median 39.4) weeks PMA. The subjects' perinatal characteristics are summarised in Table 1.

Table 7.1 The perinatal characteristics of the study group.

Perinatal characteristics	
Males, no. (%)	25 (62.5)
Median (range) gestational age at birth (weeks)	39.1 (36-41.6)
Median (range) postmenstrual age at scan (weeks)	39.4 (36.9-44.1)
Median (range) birth weight (grams)	2995 (2065-4100)
Median (range) weight at scan (grams)	3208 (1950-45)

### 7.2.2 Data Acquisition

All MR imaging data were acquired under the supervision of a paediatrician experienced in MR imaging procedures. Imaging was carried out on 3-Tesla Philips Achieva (running modified R3.2.2 software) using a dedicated neonatal imaging system using a neonatal 32 channel phased array head coil (Hughes et al., 2016). T1- and T2-weighted MR imaging was acquired with the following sequences parameters. T2-weighted and inversion recovery T1-weighted multi-slice fast spin-echo images were each acquired in sagittal and axial slice stacks with in-plane resolution  $0.8 \times 0.8 \text{ mm}^2$  and 1.6mm slices overlapped by 0.8mm. The rest of the parameters were – T2-weighted: TR=12000ms TE=156ms, SENSE factor 2.11 (axial) and 2.58 (sagittal); T1-weighted: TR=4795ms, TI=1740ms, TE=8.7ms, SENSE factor 2.27 (axial) and 2.66 (sagittal).

The sequence parameters for the dMRI data were as follows; a spherically optimized set of directions on 4 shells with b-values of  $400 \text{ s/mm}^2$ ,  $1000 \text{ s/mm}^2$  and  $2600 \text{ s/mm}^2$  in 64, 88 and 128 directions, respectively, and 20  $b=0 \text{ s/mm}^2$  images (Hutter et al., 2017) was split into 4 optimal



subsets (one per Phase Encoding Direction). These directions were then spread temporally taking motion and duty cycle considerations into account. A restart facility with user-selected set back from the break time point was used for additional motion and interruption robustness (Hutter et al., 2017). Acceleration of multiband 4, SENSE factor 1.2 and partial fourier 0.86 was used, acquired resolution 1.5x1.5mm, 3mm slices with 1.5mm overlap, TR=3800ms and TE=90ms. dMRI data was reconstructed using CG-SENSE including data-based Nyquist ghost estimation (Cordero Grande et al., 2016).

### 7.2.3 Image Processing

Structural MRI data were pre-processed by running bias field correction using the N4 algorithm (Tustison et al., 2010). The dMRI data were pre-processed by removal of motion-corrupted volumes using an automated detection approach (Kelly et al., 2017), PCA-based denoising (Veraart et al., 2016), distortion correction and outlier replacement (Andersson et al., 2016), bias field correction (Tustison et al., 2010) and intensity normalisation across datasets.

### 7.2.4 Estimation of microstructural features

#### 7.2.4.1 DTI

The diffusion tensor model was fitted for each subject, and FA, AD, MD and RD were calculated using *dwi2tensor* and *tensor2metric*, respectively, from the MRtrix3 package (Tournier et al., 2012).

#### 7.2.4.2 NODDI

The NODDI toolbox was used to fit the NODDI model and derive maps of estimated intracellular volume fraction,  $v_{ic}$ , orientation dispersion index (ODI), and isotropic water volume fraction,  $v_{iso}$ , for each subject. The range of values considered for the fraction of intracellular space used in the initialisation of the NODDI model fitting was lowered to 0-0.3 to better reflect the neonatal data. For voxels where the fitting did not converge, the fitting was repeated using AMICO (Daducci et al., 2015), a linearized version of NODDI, to provide initialization parameters (Batalle et al., 2017).

#### 7.2.4.3 Fixel-based measures

FOD images were computed for each subject using multi-shell multi-tissue CSD. Tissue-specific group-average response functions for WM and CSF were estimated using all 4 shells and FD and FC were calculated as described in Chapter 6.

Figure 7.1 shows the microstructural maps derived for a single representative subject.

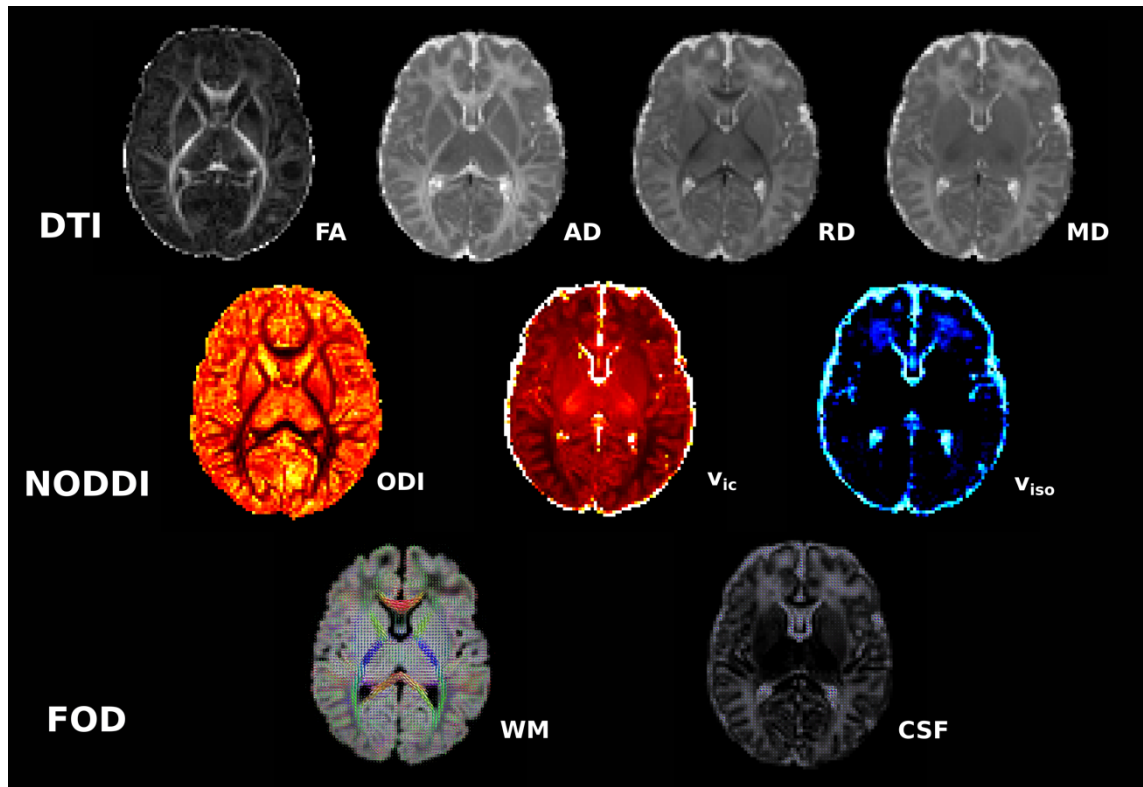


Figure 7.1 A representative subject from the study group, male infant born at 39.6 weeks and scanned at 39.9 weeks PMA. The top and middle rows show DTI and NODDI scalar maps in native space, the bottom row shows WM and CSF FODs overlaid on WM density and CSF density images, respectively.

#### 7.2.4.4 Brain volume estimation

T2-weighted images were brain extracted using BET (Smith, 2002) from FSL and segmented using the DRAW-EM algorithm (Makropoulos et al., 2014). Tissue segmentations of the cortical GM, deep GM, WM, brainstem and hippocampus and amygdala were summed to calculate brain tissue volumes.

## **7.2.5 Tract-specific analysis**

### **7.2.5.1 Registration**

To assess lateralisation, a symmetric template was created. Each subject's FOD image was flipped on the left-right axis. The native-orientation and flipped FOD images (80 images in total) were registered to an iteratively-refined, group-averaged template FOD image using nonlinear transformations (Raffelt et al., 2012a; Raffelt et al., 2011).

### **7.2.5.2 Tract segmentation and skeletonisation**

Whole-brain probabilistic tractography was performed in the FOD template, seeded from a whole-brain WM mask to produce a tractogram of 20 million streamlines. From this tractogram, a subset of 10 million streamlines was selected that best fit the diffusion signal using the SIFT algorithm (Smith et al., 2013). Tracts of interest were delineated using manually drawn regions of interest, as described in Chapter 4. The tracts delineated were the bilateral CST, IFOF, ILF, SLF, UNC and CC. The TSA continuous medial representation model was used to create tract-wise WM skeletons in the template, as described in Chapter 4. The results from the template tractography and TSA model fitting are shown in Figure 7.2.

### **7.2.5.3 Inter-hemispheric differences**

To investigate inter-hemispheric differences, for each subject, diffusion data from the both the left and right hemispheres were projected onto the same skeleton. For each subject, native space scalar maps of FA, AD, RD, MD,  $v_{ic}$ , and ODI were flipped along the left-right axis. The native-orientation and flipped scalar maps were warped to template space using the transformations from the registration of the native-orientation and flipped FODs, respectively. For each subject, DTI and NODDI measures from the native-orientation and flipped scalar maps were projected onto skeletons of the CC, CST, IFOF, ILF, SLF and UNC in the left hemisphere. By projecting the native and flipped images onto the same skeleton diffusion data from the left and right hemispheres is projected onto the same skeleton. As the CC traverses both hemispheres, a skeleton of just the left half of the CC was created (Figure 7.3) and diffusion data from both the left and right hemisphere were projected onto the partial skeleton.

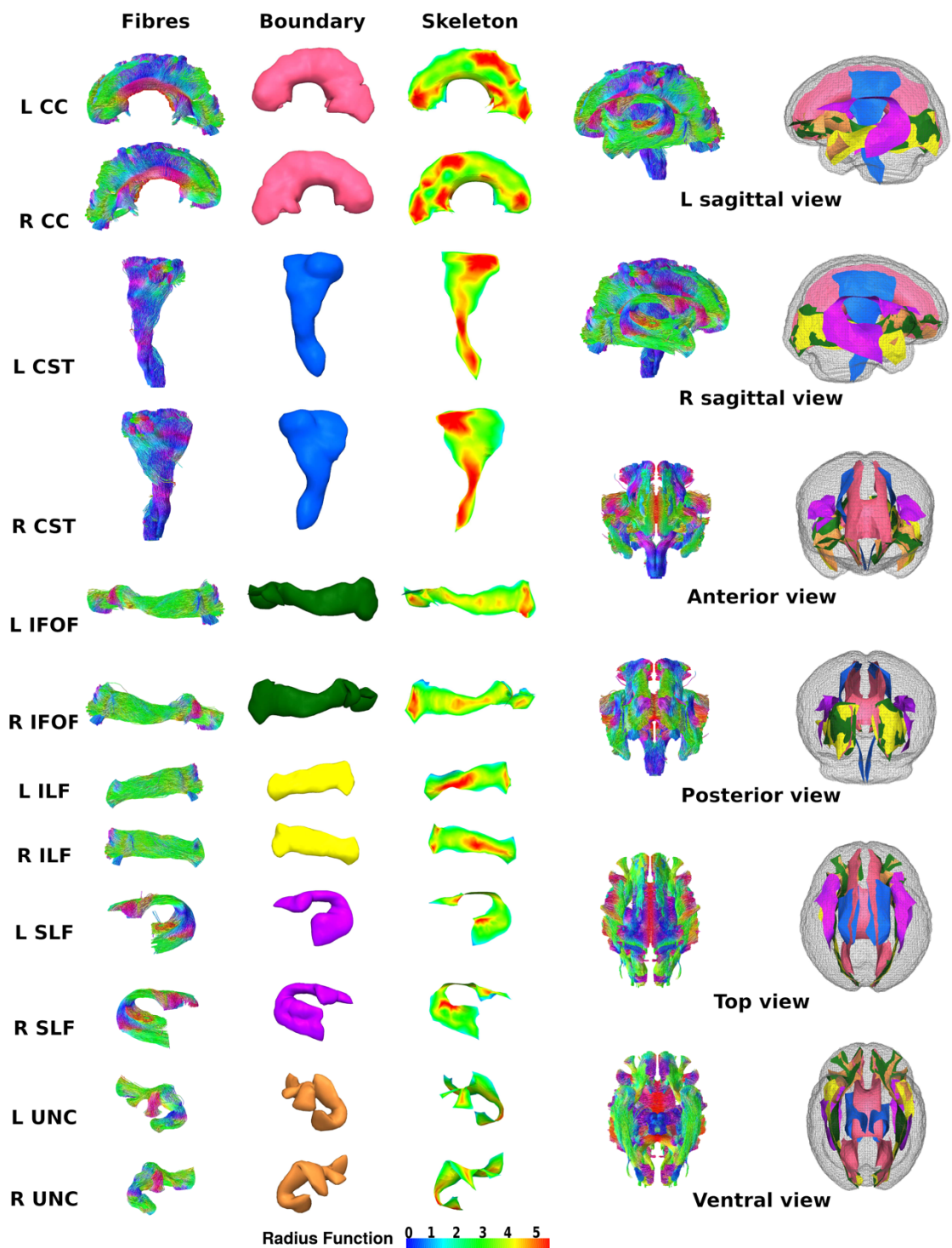


Figure 7.2 Template tractography and TSA model fitting results for the left and right CC, CST, IFO, ILF, SLF and UNC.

As FD and FC are estimated in template space no further transformation was needed. FD and FC values were estimated from native and flipped FODs. Of note, many voxels will contain multiple fibre populations. However, FD and FC values were extracted only from those fixels through which streamlines of the tracts of interest passed and these were projected onto the WM skeletons.

As described in Chapter 4, the TSA framework allows for two data projection strategies. In Chapters 4 and 5, the maximum-value strategy was employed to project DTI values from the voxel with the highest FA value onto the skeletons. In this study, the mean-value data projection strategy for TSA is used. For each point on the skeleton, the scalar parameter of interest was averaged along the direction of the normal to the skeleton within the skeleton boundary. The tractography carried out in the template produced thicker tracts with more fanning than the tractography results in previous chapters. This is due to the tractography algorithm – a probabilistic CSD algorithm, and a more mature cohort. Therefore, the mean value strategy was chosen to project a value more representative of the tract.

Interhemispheric asymmetries were assessed, correcting for multiple comparisons using non-parametric permutation-based suprathreshold cluster analysis (Nichols and Holmes, 2002) with family-wise error rate (FWER) correction. The same multiple comparisons strategy was used for the analysis in Sections 7.2.5.4 and 7.2.5.5.

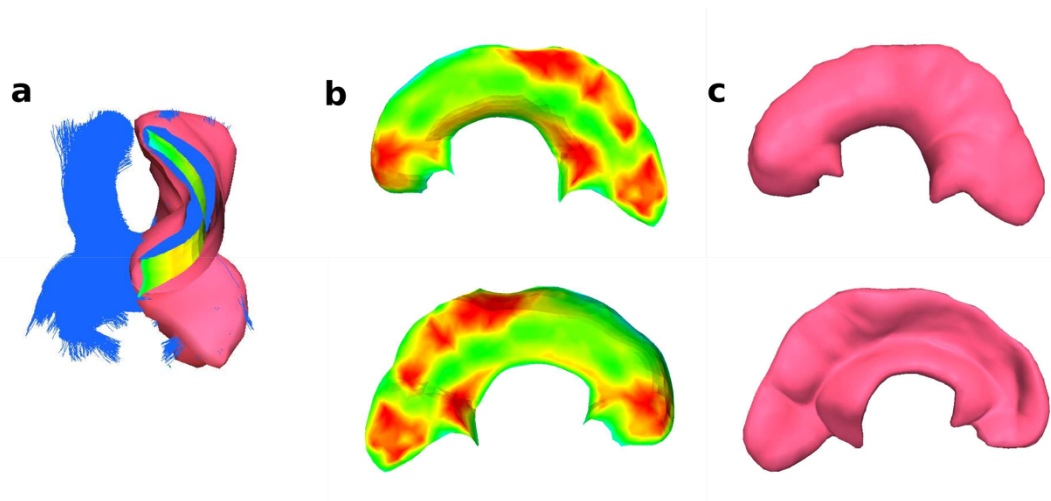


Figure 7.3 Unilateral skeleton for CC; (a) cross-sectional view of the CC tractography (blue), skeleton (green-yellow) and skeleton boundary (pink); (b) lateral (top) and medial (bottom) view of the CC skeleton; (c) lateral (top) and medial (bottom) view of the skeleton boundary.

#### 7.2.5.4 Changes in diffusion properties associated with increasing age

To investigate the changes in diffusion properties associated with increasing age, native-orientation maps of FA, AD, RD, MD,  $v_{ic}$ , ODI, FD and FC were projected onto WM skeletons of the CC, CST, IFOF, ILF, SLF and UNC bilaterally using the mean-value strategy. Linear regression analysis was carried out on the tract skeletons to assess the relationship between PMA at scan and FA, AD, RD, MD,  $v_{ic}$ , ODI, FD and FC.

#### 7.2.5.5 Differences between male and female subjects

As Chapter 5 demonstrated differences in FC between male and female subjects, differences in FA, AD, RD, MD,  $v_{ic}$ , ODI, FD, FC and brain tissue volume between male and female subjects were investigated, with PMA at scan as a covariate. Differences in brain volume calculated from the structural segmentations were assessed using a two-sample Kolmogorov-Smirnov test.

### 7.3 Results

#### 7.3.1 Average values

Group-average values for FA, AD, RD, MD,  $v_{ic}$ , ODI and FD for the CC, CST, IFOF, ILF, SLF and UNC bilaterally are shown in Figure 7.4 Sections 7.3.1.1-7.3.1.6 describe the distribution of group-averaged parameter values for each tract. Group-averaged values are not given for FC as FC can take on positive and negative values depending on the local expansion or contraction perpendicular to the fibre-bundle and averaging across all subjects provides values close to zero across whole tracts.

##### 7.3.1.1 CC

Group average parameters for the CC are shown in Figure 7.4. FA values in the CC were highest in the body and splenium, decreasing in the cortical projections. AD and RD were highest in the fibres adjacent to the body. MD was lowest in the posterior body and splenium and higher in the projections. ODI was lowest in the body and increased along the fibres fanning out towards the cortex.  $v_{ic}$  was highest in the body, genu and splenium, with lower, relatively uniform values across the projections. FD was highest in the splenium, and lower in the body of the CC, decreasing along the cortical projections towards the cortex.

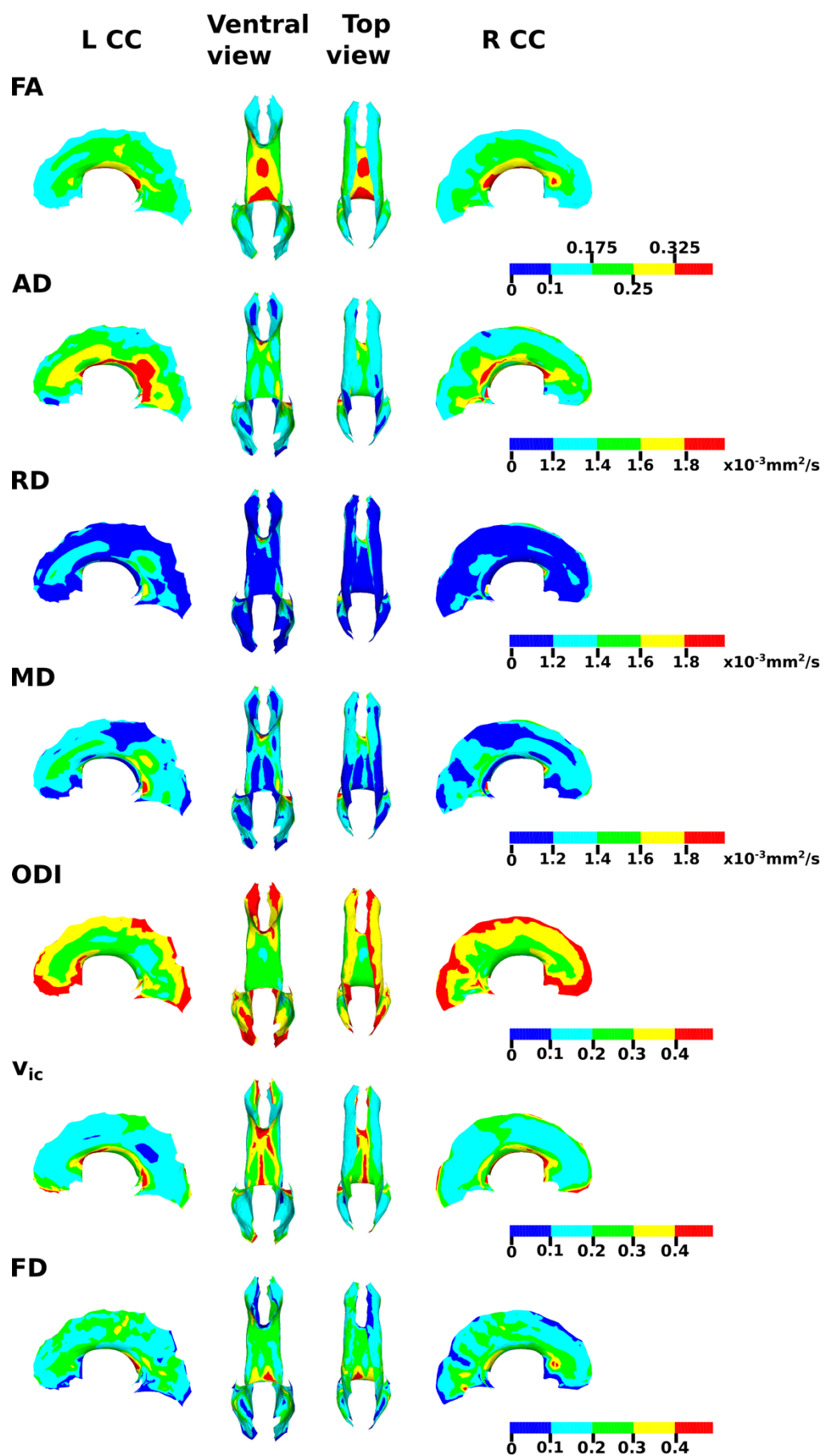


Figure 7.4 Group-averaged values for FA, AD, RD, MD,  $v_{ic}$ , ODI and FD for the CC.

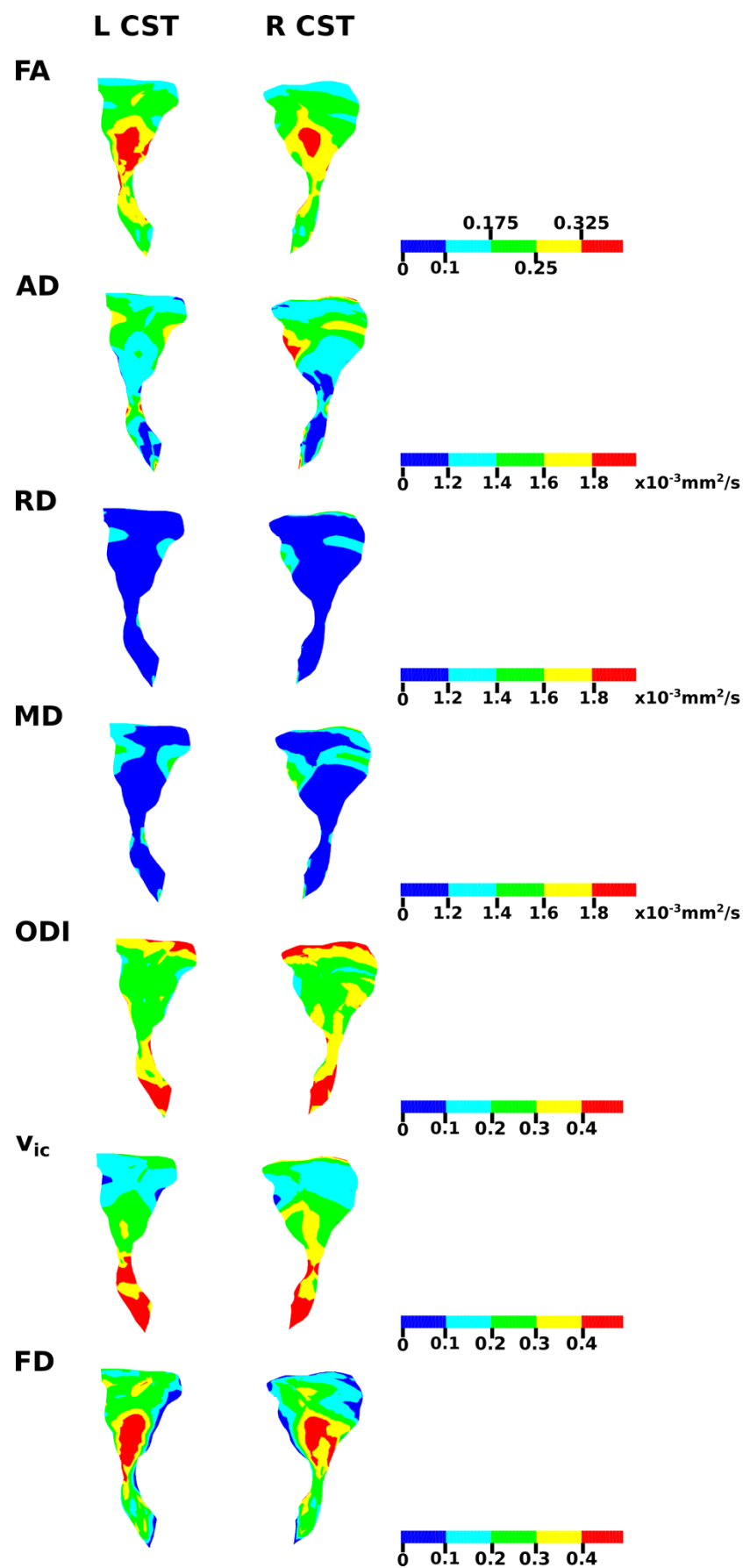


Figure 7.5 Group-averaged values for FA, AD, RD, MD,  $v_{ic}$ , ODI and FD for the CST.



### 7.3.1.2 CST

Group average parameter for the CST are shown in Figure 7.5. FA and FD were highest in the PLIC, decreasing in the inferior and superior directions. AD was lowest in the brainstem and PLIC, and highest in the centrum semiovale. RD and MD were relatively uniform and below  $1.2 \times 10^{-3} \text{mm}^2/\text{s}$  across the CST, with slightly higher values in the centrum semiovale. ODI was highest at the cortical WM-GM boundary and the brainstem, with lower values in PLIC and centrum semiovale.  $v_{ic}$  was highest in the brainstem, decreasing superiorly.

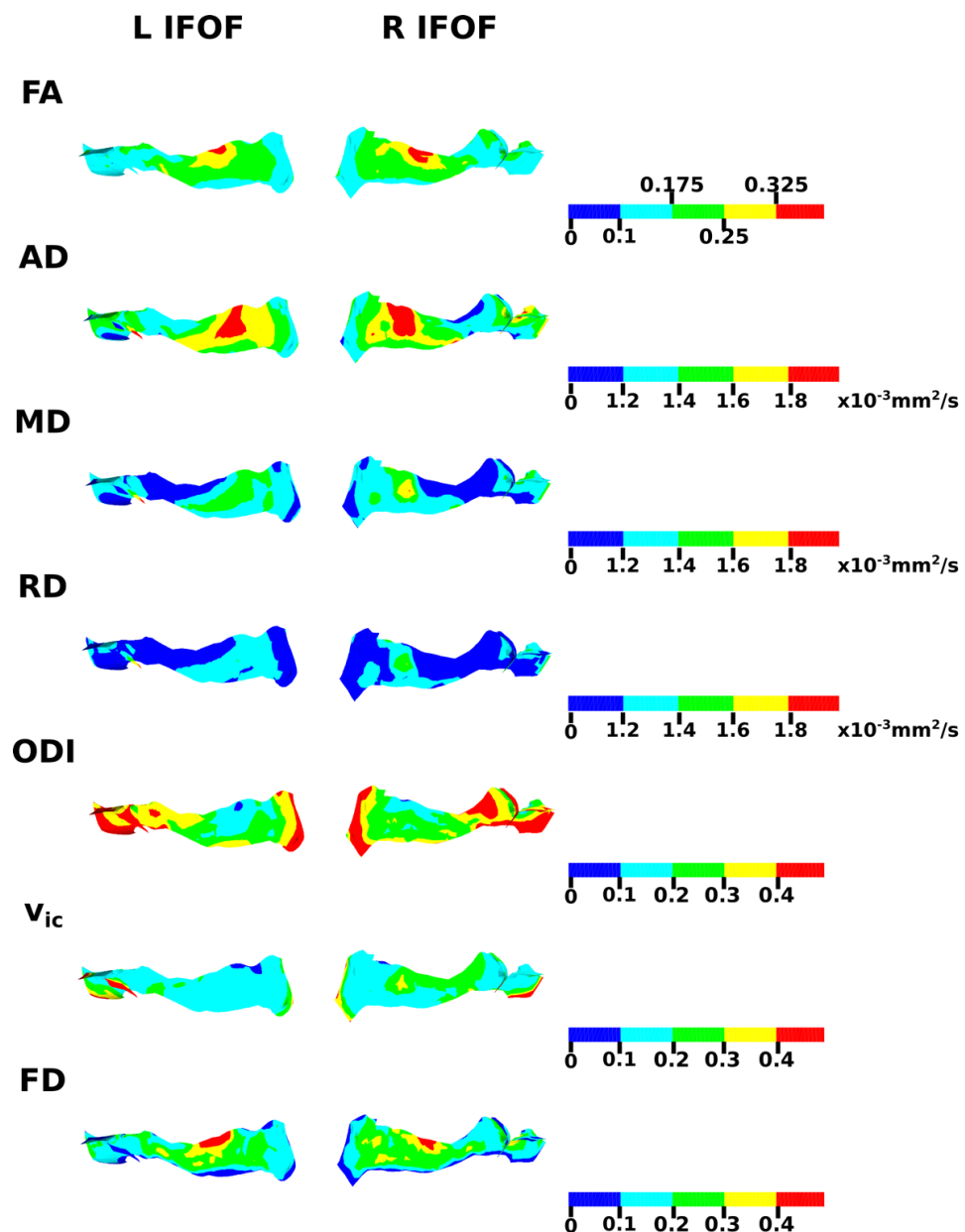


Figure 7.6 Group-averaged values for FA, AD, RD, MD,  $v_{ic}$ , ODI and FD for the IFOF.

### 7.3.1.3 IFOF

Group average parameter for the IFOF are shown in Figure 7.6. FA, AD and FD in the IFOF were highest in the occipital lobe, decreasing anteriorly and at the WM-GM boundary. Conversely, RD and MD were highest in the occipital lobe and frontal lobe projections, and lowest where the IFOF passes adjacent to the external capsule. ODI was lowest in the occipital lobe, increasing as the tract fanned out into the cortex.  $v_{ic}$  was between 0.1-0.2 across most of the tract.

### 7.3.1.4 ILF

Group average parameter for the ILF are shown in Figure 7.7. Similar to the IFOF, FA, AD and FD in the ILF peaked in the occipital lobe, decreasing anteriorly and posteriorly towards the WM-GM boundary. RD and MD were highest in the occipital lobe, where ODI values were lowest, and increased nearer the cortex.  $v_{ic}$  was between 0.1-0.2 throughout most of the tract.

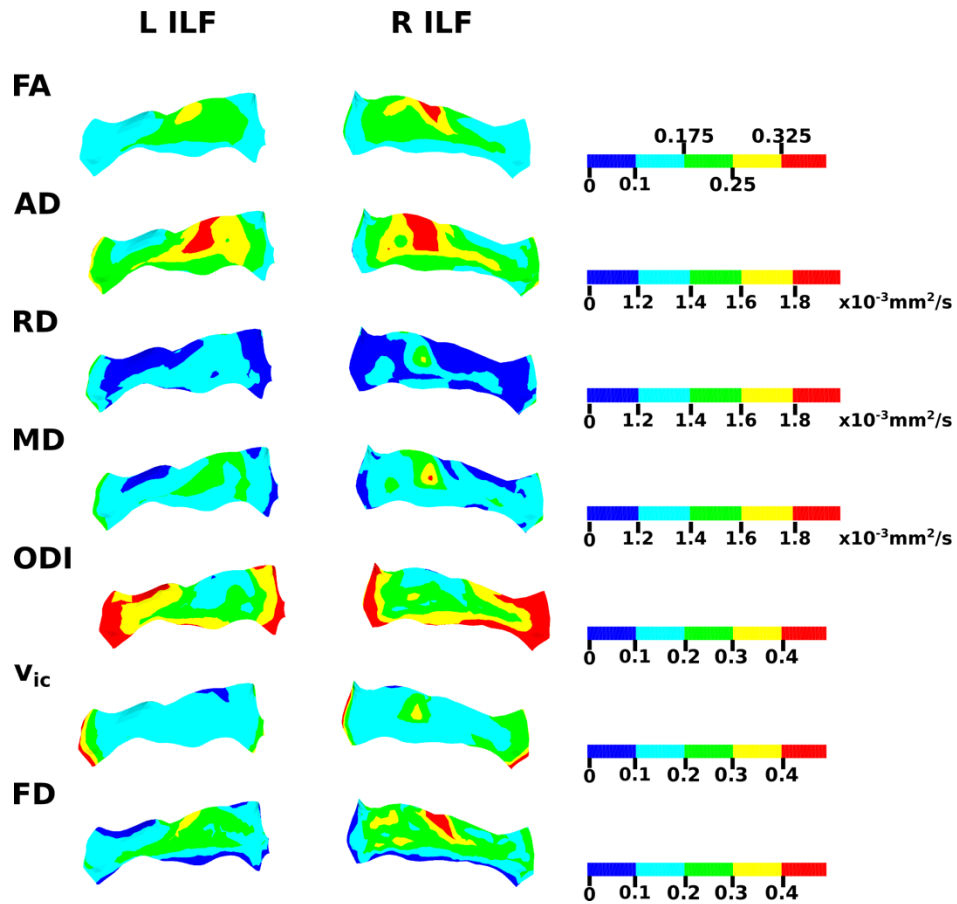


Figure 7.7 Group-averaged values for FA, AD, RD, MD,  $v_{ic}$ , ODI and FD for the ILF.

### 7.3.1.5 SLF

Group average parameter for the SLF are shown in Figure 7.8. FA was highest in the curved segment of the SLF and decreased as the tract fanned out into the parietal and temporal cortical GM. AD was highest in the curved segment and in the temporal lobe, with lower values in the parietal lobe. RD and MD were low in the parietal lobe, and higher in the temporal lobe. ODI was highest as the WM-GM boundary.  $v_{ic}$  and FD were relatively uniform throughout the tract.

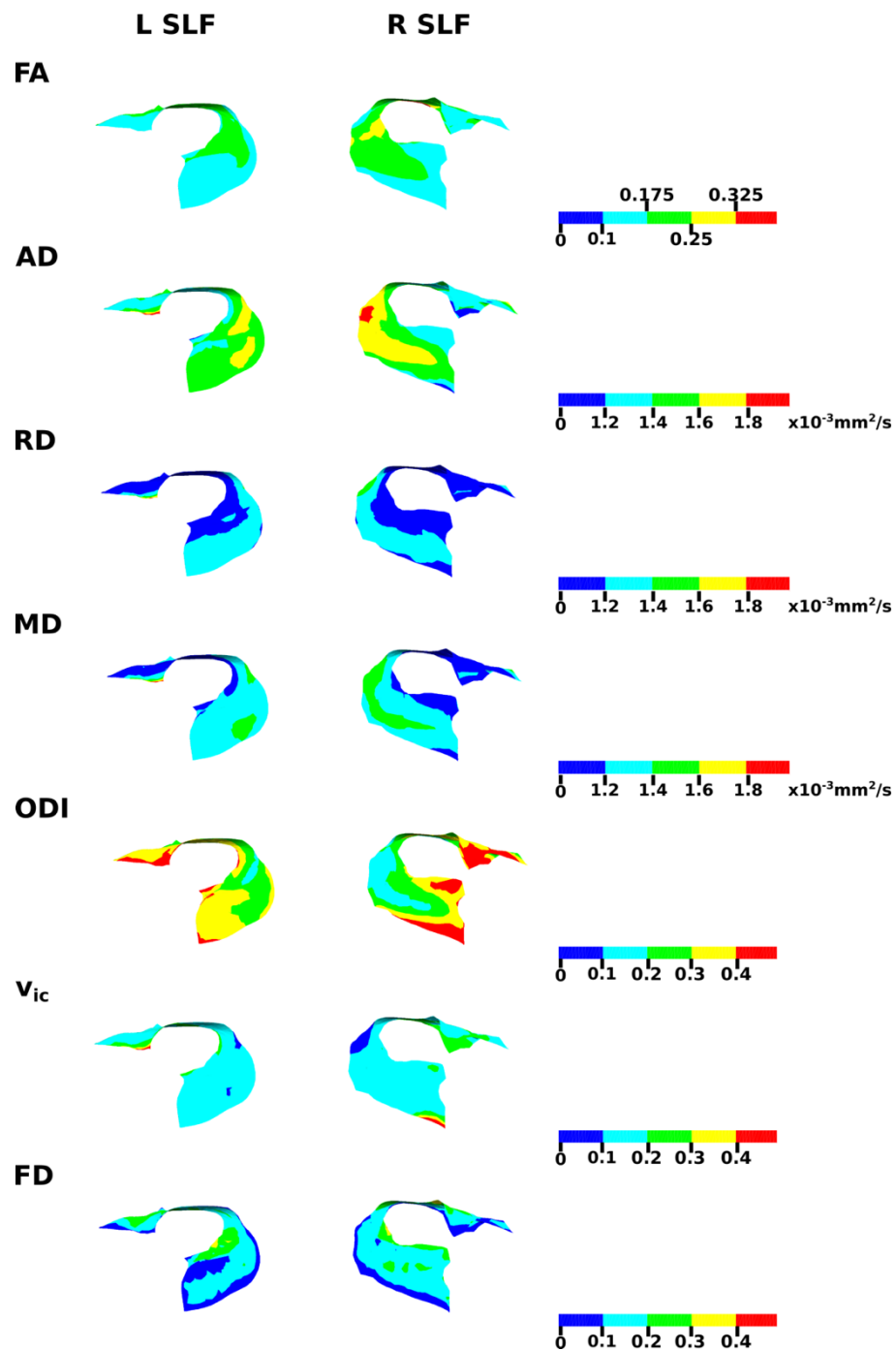


Figure 7.8 Group-averaged values for FA, AD, RD, MD,  $v_{ic}$ , ODI and FD for the SLF.

### 7.3.1.6 UNC

Group average parameter for the UNC are shown in Figure 7.9. FA, AD, RD and MD were relatively uniform though the tract, although diffusivities values were slightly higher in the temporal lobe. Out of all the tracts ODI was highest in the UNC, with values greater than 0.3 across the tract.  $v_{ic}$  was highest at the WM-GM boundary in the frontal and temporal lobes and lowest in the frontal lobe. FD was highest in the insular segment of the UNC and lower in the temporal and frontal lobes.

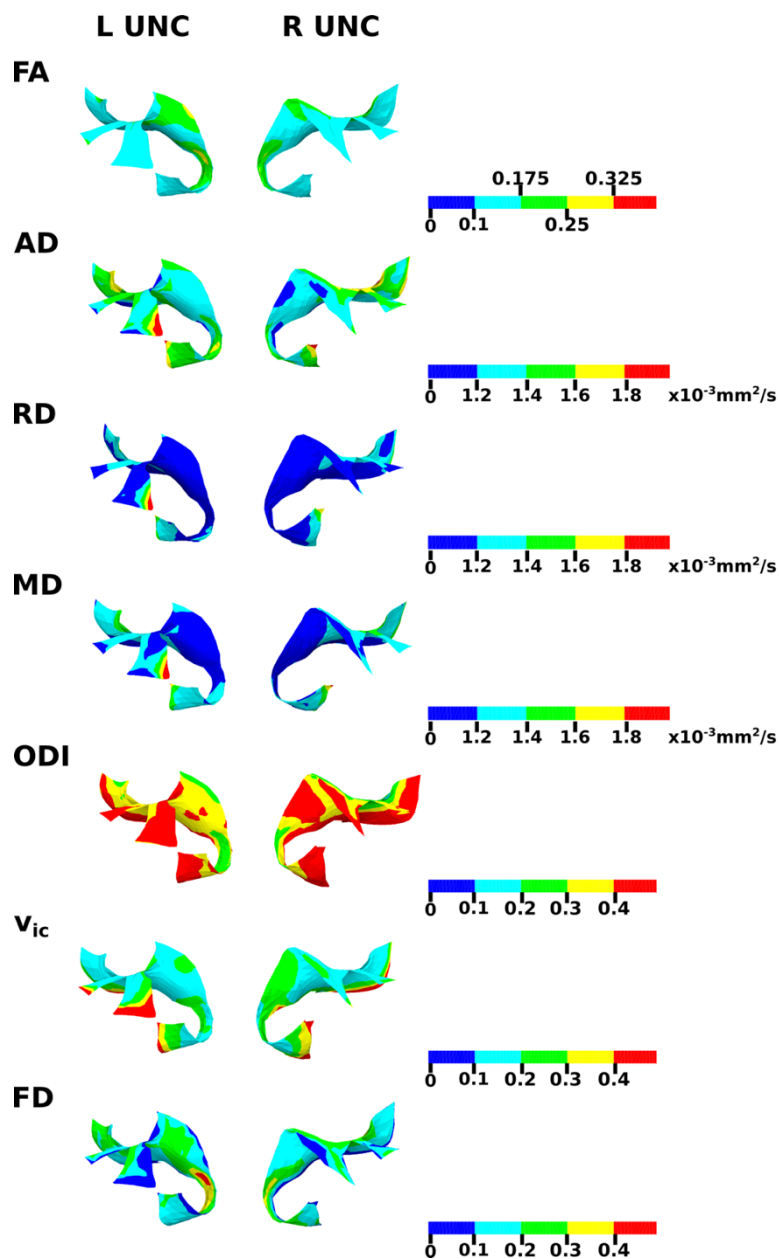


Figure 7.9 Group-averaged values for FA, AD, RD, MD,  $v_{ic}$ , ODI and FD for the UNC.

### 7.3.2 Inter-hemispheric asymmetries

Little to no significant differences were found between left and right tracts. Interhemispheric differences were limited to small regions within the SLF, ILF and IFOF, which comprised 1-1.5% of the vertices within each skeleton. Sections 7.3.2.1-7.3.2.3 summarise these findings.

#### 7.3.2.1 DTI metrics

AD, RD MD were significantly higher in a small region of the left hemisphere in the SLF. AD and MD were also significantly higher in a small region of the left ILF (Figure 7.10). FA was higher in the right SLF (Figure 7.11).

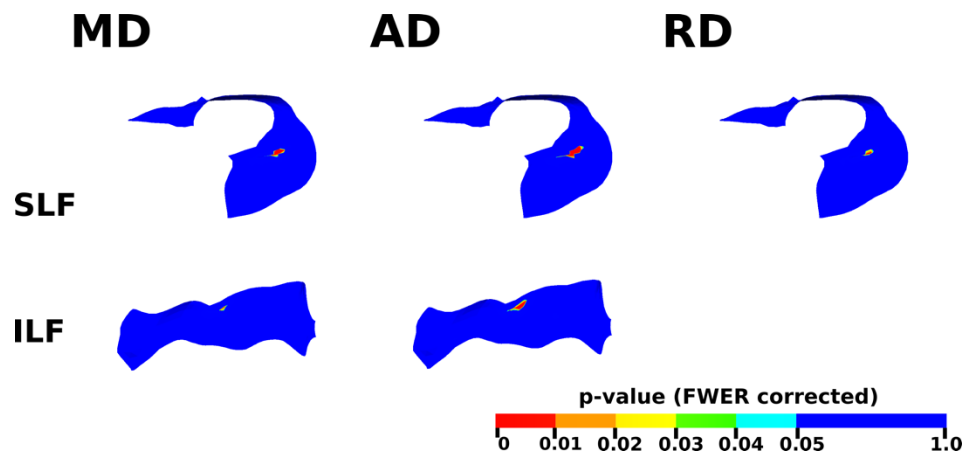


Figure 7.10 The regions where AD, RD and MD are greater in the left SLF and ILF (shown in red).

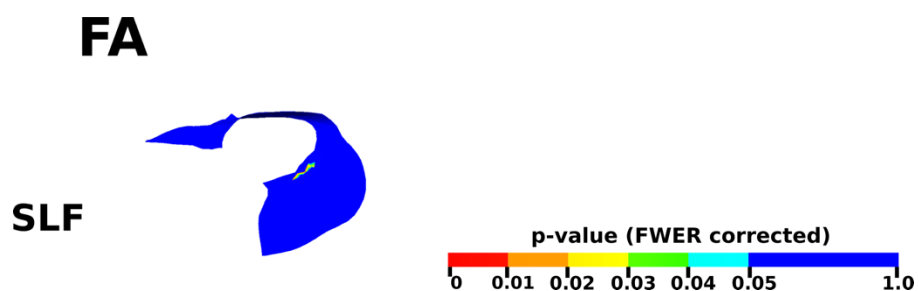


Figure 7.11 The region where FA is greater in the right SLF.

### 7.3.2.2 NODDI metrics

Both  $v_{ic}$  and ODI were significantly higher in a small region of the right SLF, overlapping with the regions of increased diffusivities in the left hemisphere. ODI was also higher in small regions of the right IFOF and ILF (Figure 7.12).

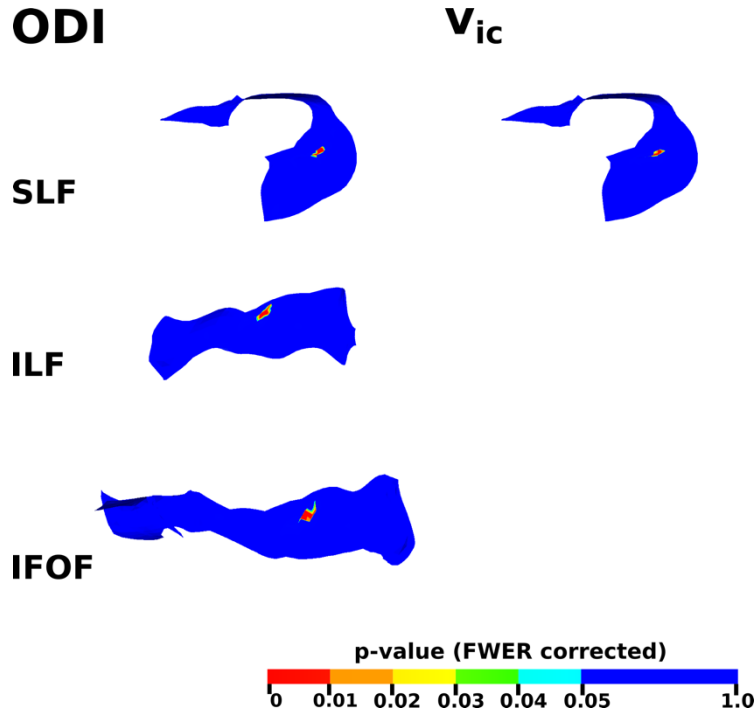


Figure 7.12 The regions where  $v_{ic}$  and ODI are greater in the right SLF, IFOF and ILF (shown in red).

### 7.3.2.3 Fixel-derived measures

There were no significant interhemispheric differences in FD or FC.

### 7.3.3 Changes in diffusion properties associated with increasing age

There was a significant decrease in diffusivities and increase in FA,  $v_{ic}$ , FD and FC with increasing PMA at scan across all tracts. There were no significant positive or negative correlations between PMA and ODI. Detailed descriptions of correlations between PMA and DTI, NODDI and fixel-derived parameters are given in Sections 7.3.3.1, 7.3.3.2, 7.3.3.3, respectively.

#### 7.3.3.1 DTI metrics

There was a significant positive correlation between PMA at scan and FA, and significant negative correlation between PMA and AD, RD and MD in the following regions; the cortical projections of

the CC, the CST between the PLIC and centrum semiovale, the IFOF, the ILF, the SLF and the UNC bilaterally (Figure 7.13 and Figure 7.20). The correlations between PMA and AD were less extensive than the correlations between PMA and FA, RD and MD. There were no negative correlations with FA and PMA, and no positive correlations PMA and AD, RD or MD.

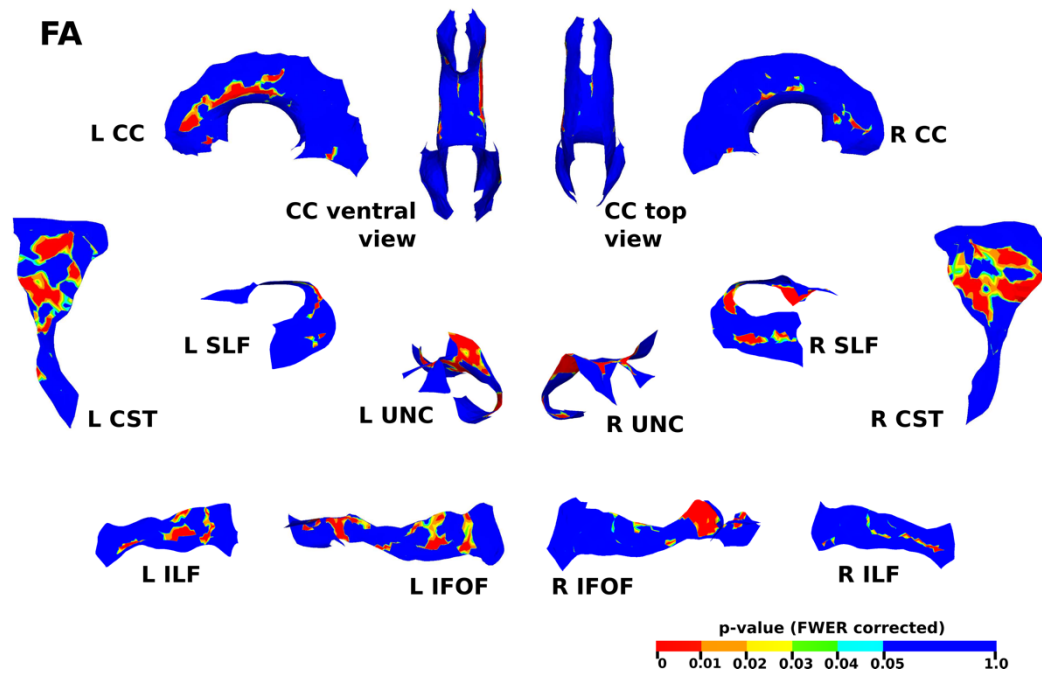


Figure 7.13 The results of the cluster analysis correlating PMA with FA at each point within the CC, CST, IFOF, ILF, SLF and UNC. Statistically significant regions of positive correlation are shown in red ( $p \leq 0.01$ ), orange ( $0.01 < p \leq 0.02$ ), yellow ( $0.02 < p \leq 0.03$ ), green ( $0.03 < p \leq 0.04$ ) and light blue ( $0.04 < p \leq 0.05$ ).

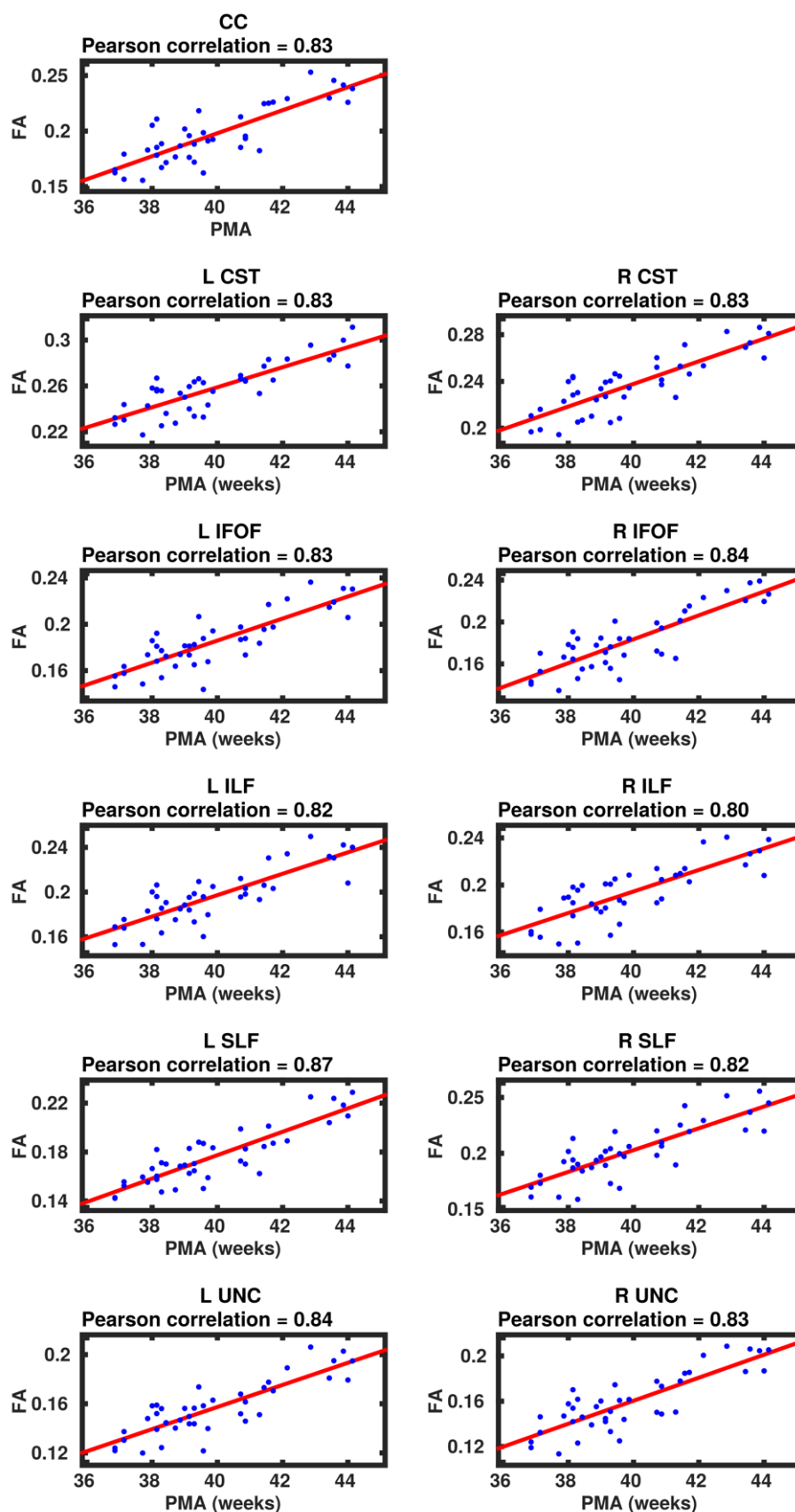


Figure 7.14 Scatter plots showing the linear relationship between FA and PMA from the regions showing significant correlation for the CC, CST, IFOF, ILF, SLF and UNC.



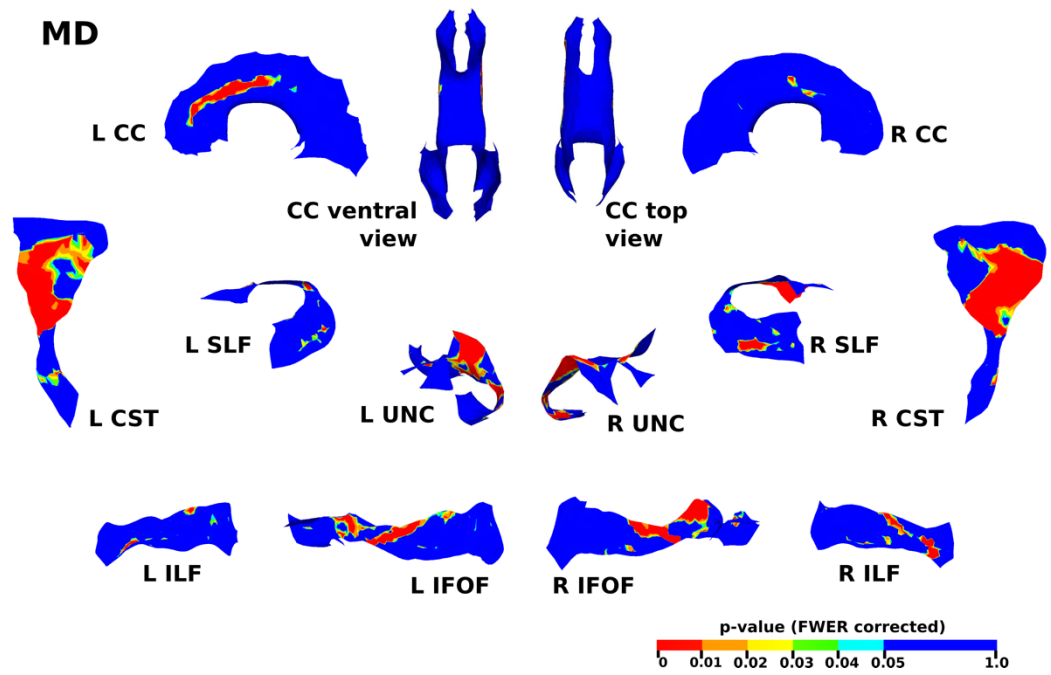


Figure 7.15 The results of the cluster analysis correlating PMA with MD at each point within the CC, CST, IFOF, ILF, SLF and UNC. Statistically significant regions of negative correlation are shown in red ( $p \leq 0.01$ ), orange ( $0.01 < p \leq 0.02$ ), yellow ( $0.02 < p \leq 0.03$ ), green ( $0.03 < p \leq 0.04$ ) and light blue ( $0.04 < p \leq 0.05$ ).

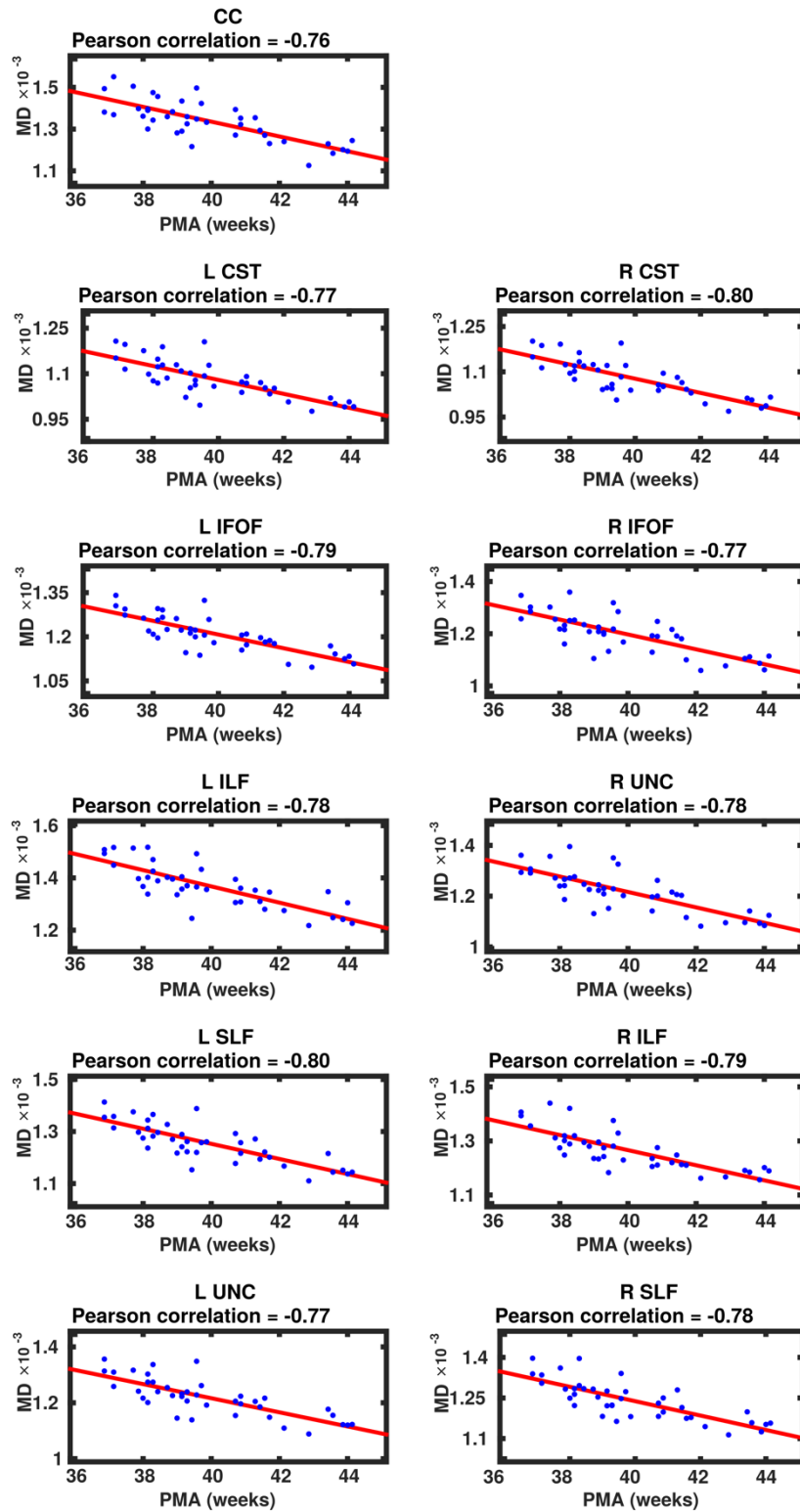


Figure 7.16 Scatter plots showing the linear relationship between MD and PMA from the regions showing significant correlation for the CC, CST, IFOF, ILF, SLF and UNC.

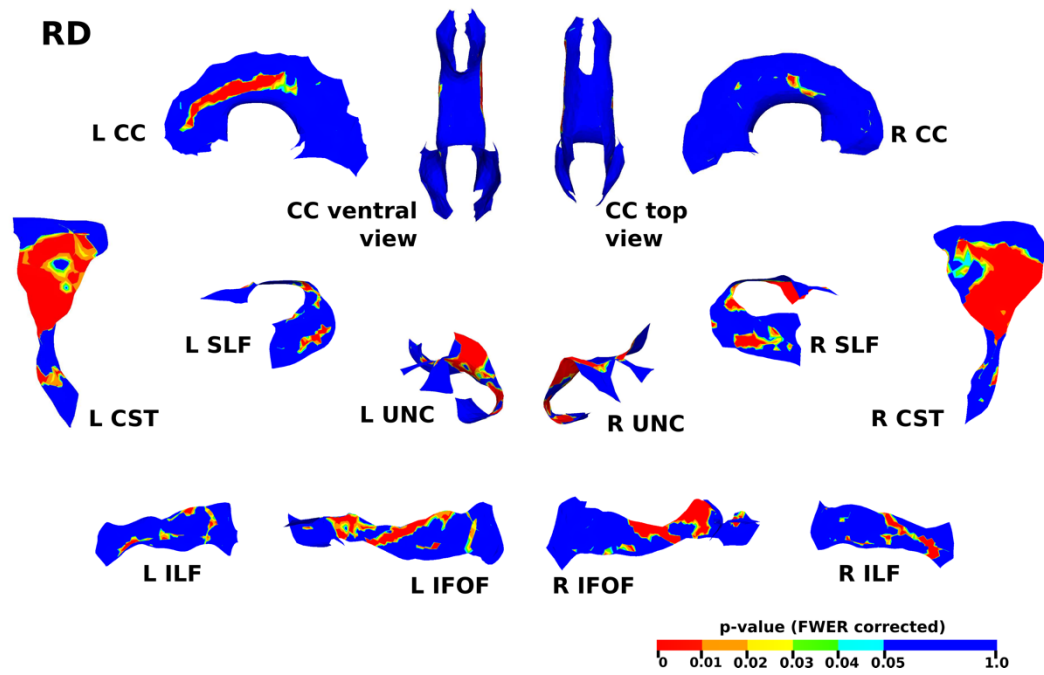


Figure 7.17 The results of the cluster analysis correlating PMA with RD at each point within the CC, CST, IFOF, ILF, SLF and UNC. Statistically significant regions of negative correlation are shown in red ( $p \leq 0.01$ ), orange ( $0.01 < p \leq 0.02$ ), yellow ( $0.02 < p \leq 0.03$ ), green ( $0.03 < p \leq 0.04$ ) and light blue ( $0.04 < p \leq 0.05$ ).

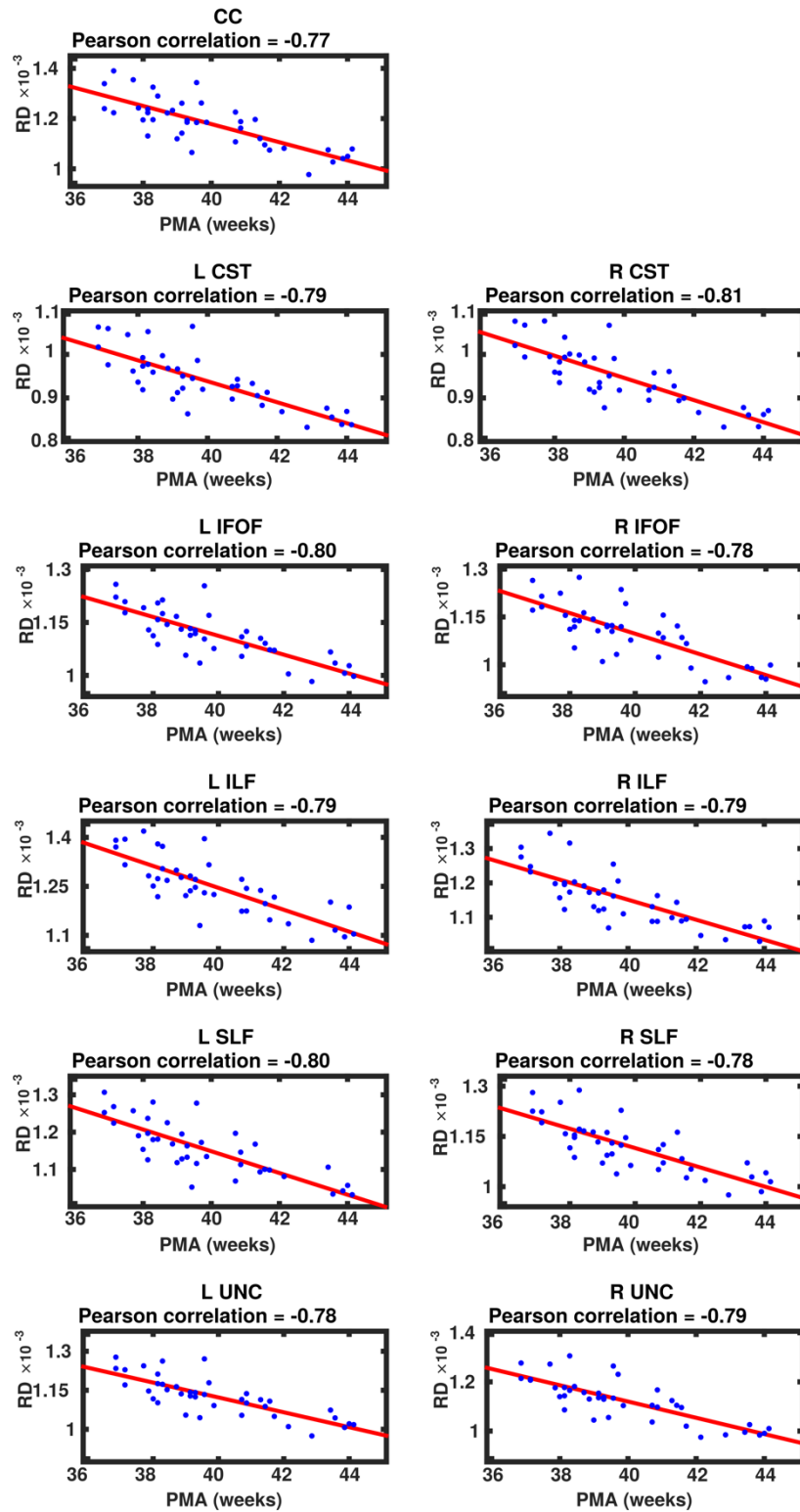


Figure 7.18 Scatter plots showing the linear relationship between RD and PMA from the regions showing significant correlation for the CC, CST, IFOF, ILF, SLF and UNC.

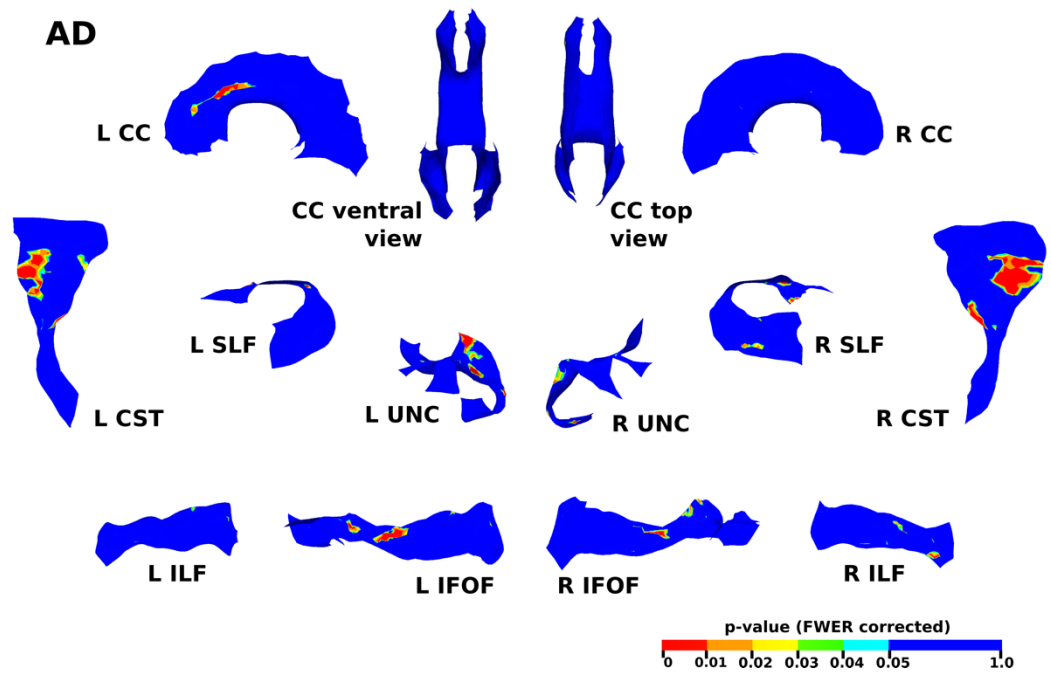


Figure 7.19 The results of the cluster analysis correlating PMA with AD at each point within the CC, CST, IFOF, ILF, SLF and UNC. Statistically significant regions of negative correlation are shown in red ( $p \leq 0.01$ ), orange ( $0.01 < p \leq 0.02$ ), yellow ( $0.02 < p \leq 0.03$ ), green ( $0.03 < p \leq 0.04$ ) and light blue ( $0.04 < p \leq 0.05$ ).

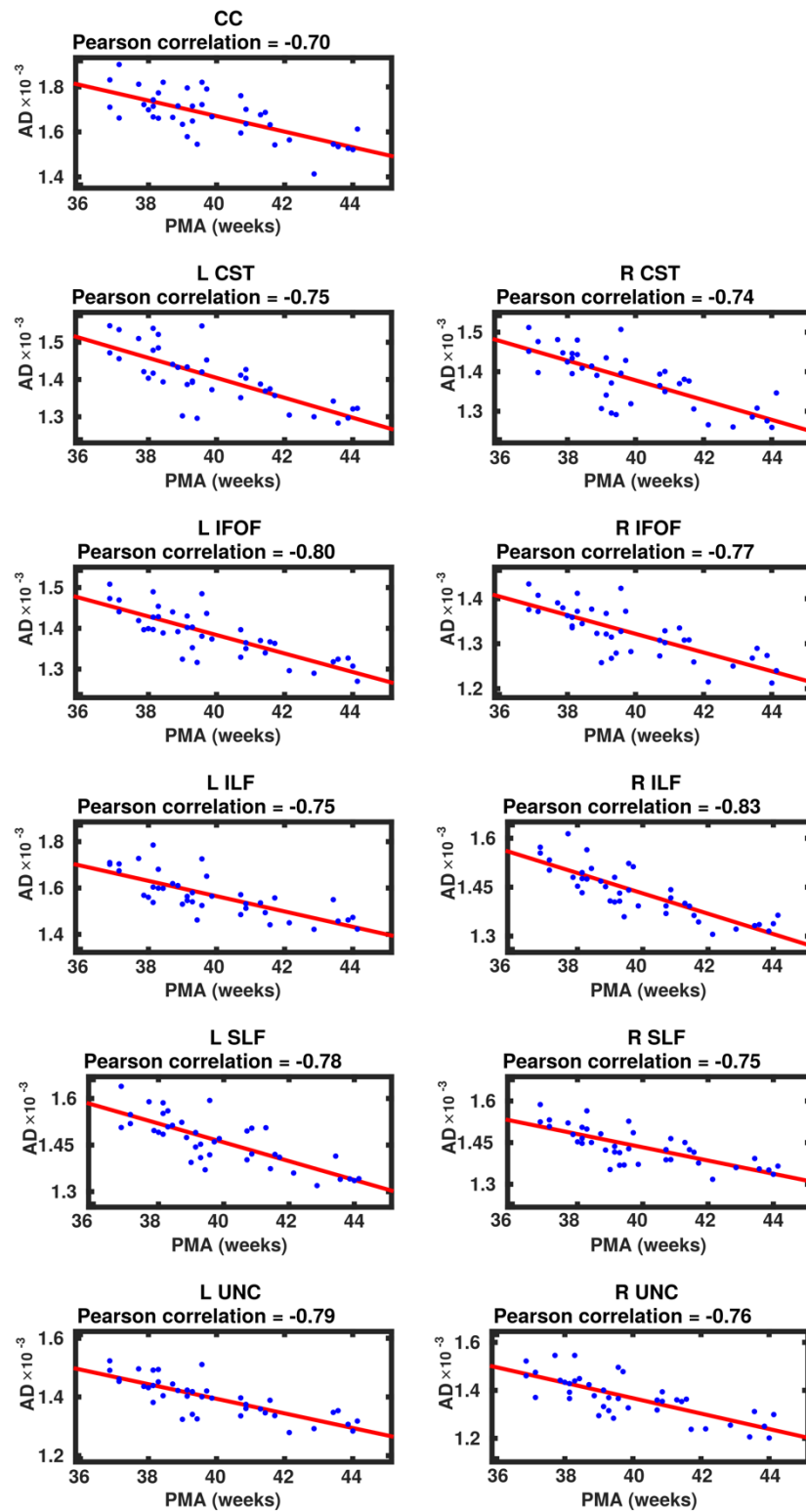


Figure 7.20 Scatter plots showing the linear relationship between AD and PMA from the regions showing significant correlation for the CC, CST, IFOF, ILF, SLF and UNC.

### 7.3.3.2 NODDI metrics

There was a significant positive correlation between  $v_{ic}$  and PMA at scan in a small region of the cortical projections of the CC, the CST between the PLIC and centrum semiovale, the IFOF where it passes adjacent to the external capsule, limited regions in the ILF, the parietal segment of the SLF, and the frontal lobe projections of the UNC bilaterally (Figure 7.21 and Figure 7.22). There were no negative correlations with  $v_{ic}$ . There were no significant correlations between ODI and PMA in any of the tracts, although, with the exception of the UNC, there was a slight positive trend across the tracts (Figure 7.23).

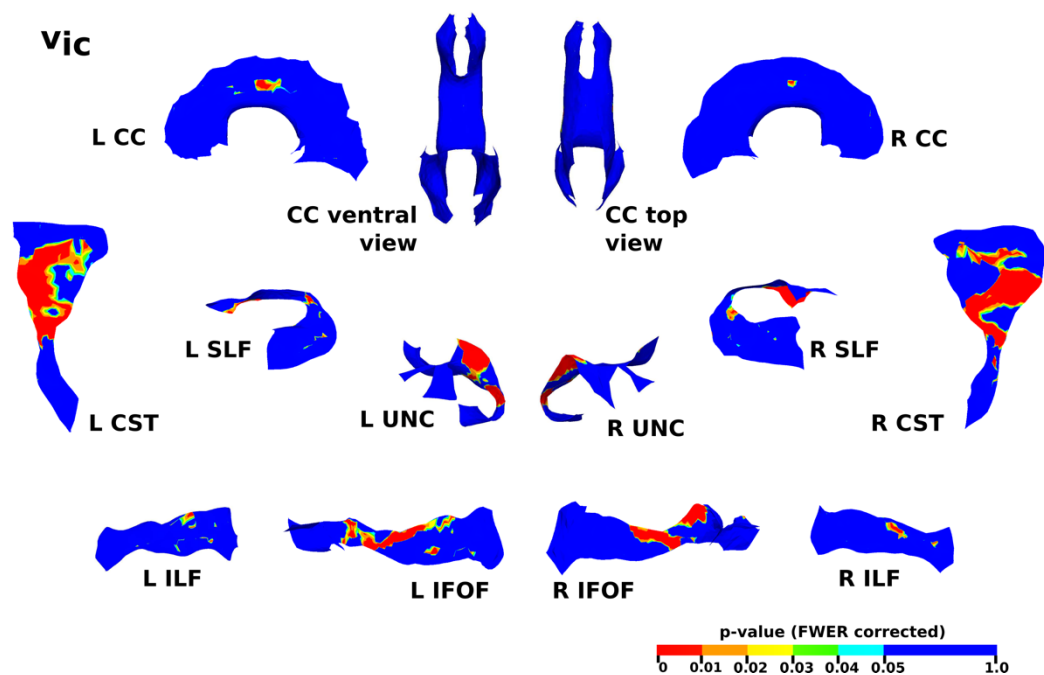


Figure 7.21 The results of the cluster analysis correlating PMA with  $v_{ic}$  at each point within the CC, CST, IFOF, ILF, SLF and UNC. Statistically significant regions of positive correlation are shown in red ( $p \leq 0.01$ ), orange ( $0.01 < p \leq 0.02$ ), yellow ( $0.02 < p \leq 0.03$ ), green ( $0.03 < p \leq 0.04$ ) and light blue ( $0.04 < p \leq 0.05$ ).

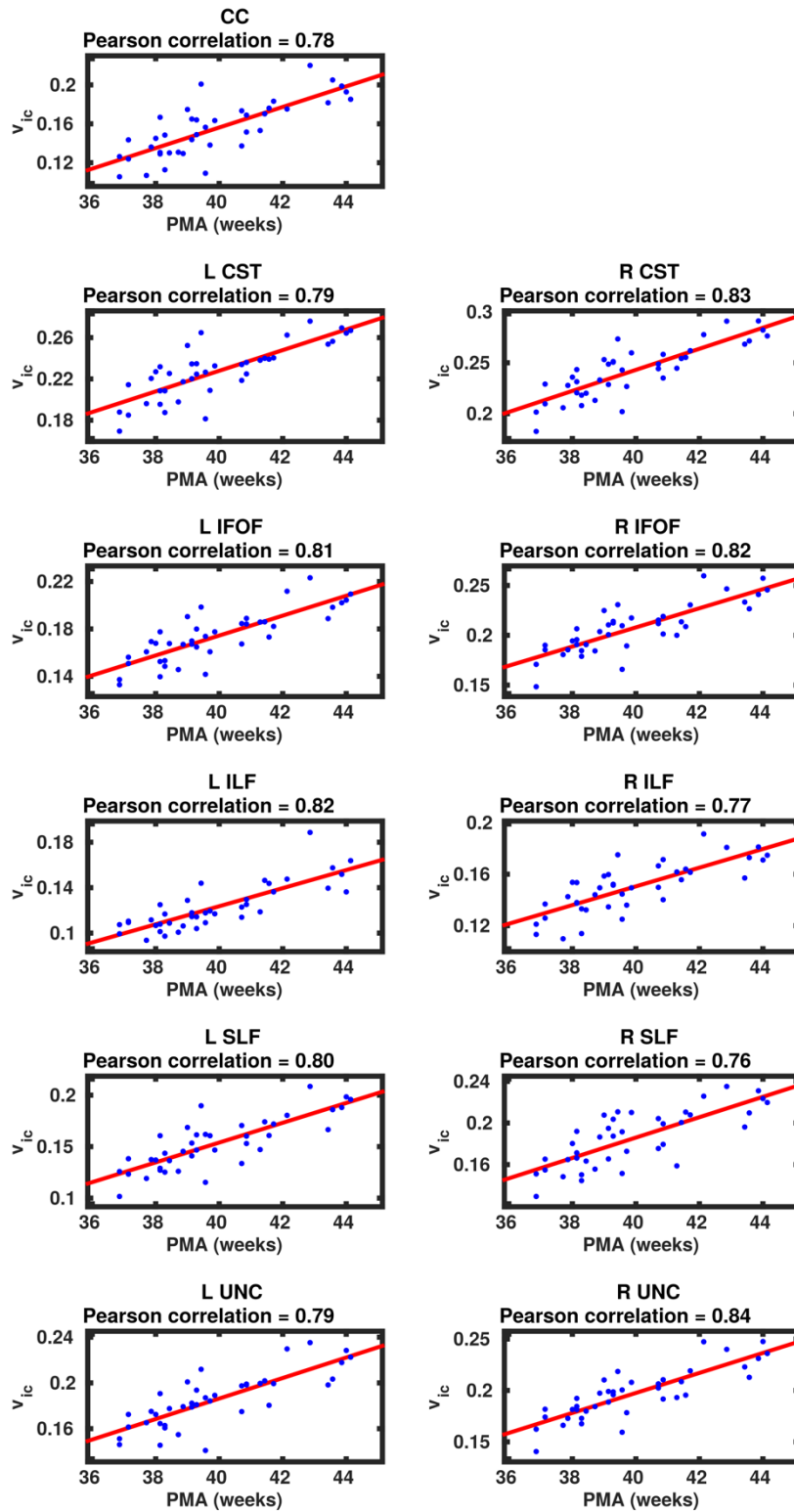


Figure 7.22 Scatter plots showing the linear relationship between  $v_{ic}$  and PMA from the regions showing significant correlation for the CC, CST, IFOF, ILF, SLF and UNC.



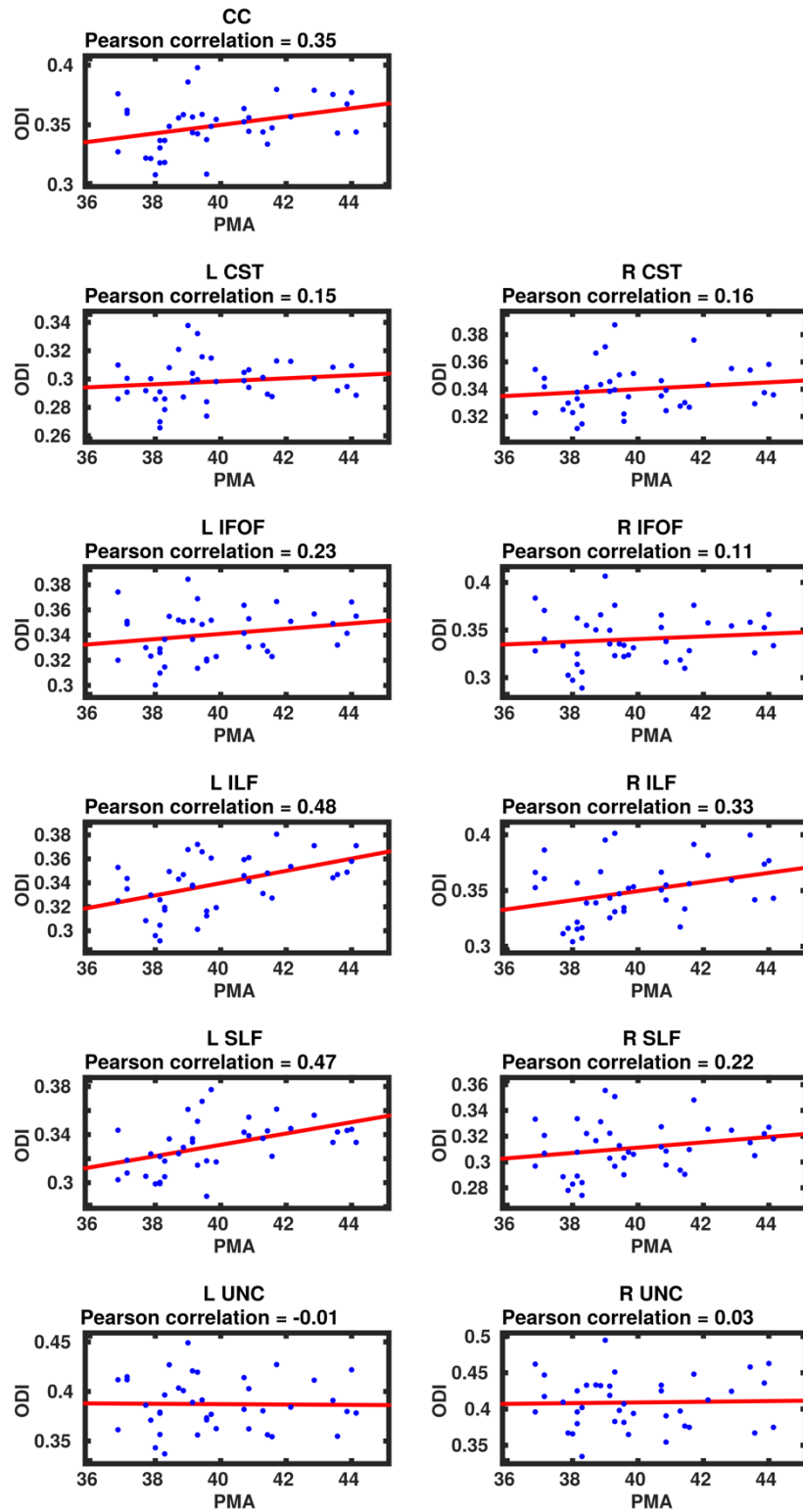


Figure 7.23 Scatter plots showing the relationship between ODI and PMA averaged over the whole tract skeleton for the CC, CST, IFOF, ILF, SLF and UNC. TSA found no statistically significant relationship was found between ODI and PMA

### 7.3.3.3 Fixel-derived measures

PMA at scan was significantly positively correlated with both FD and FC in the following regions; the cortical projections of the CC, the CST at the level of the centrum semiovale, the left IFOF and the anterior portion of the right IFOF, along the length of the ILF, limited regions in the SLF, and the frontal projections of the UNC bilaterally (Figure 7.24Figure 7.27).

### 7.3.4 Differences in diffusion properties between male and female subjects

There were no significant differences in any of the measures between male and female subjects.

The results from all the statistical analyses are summarised in Table 7.2.

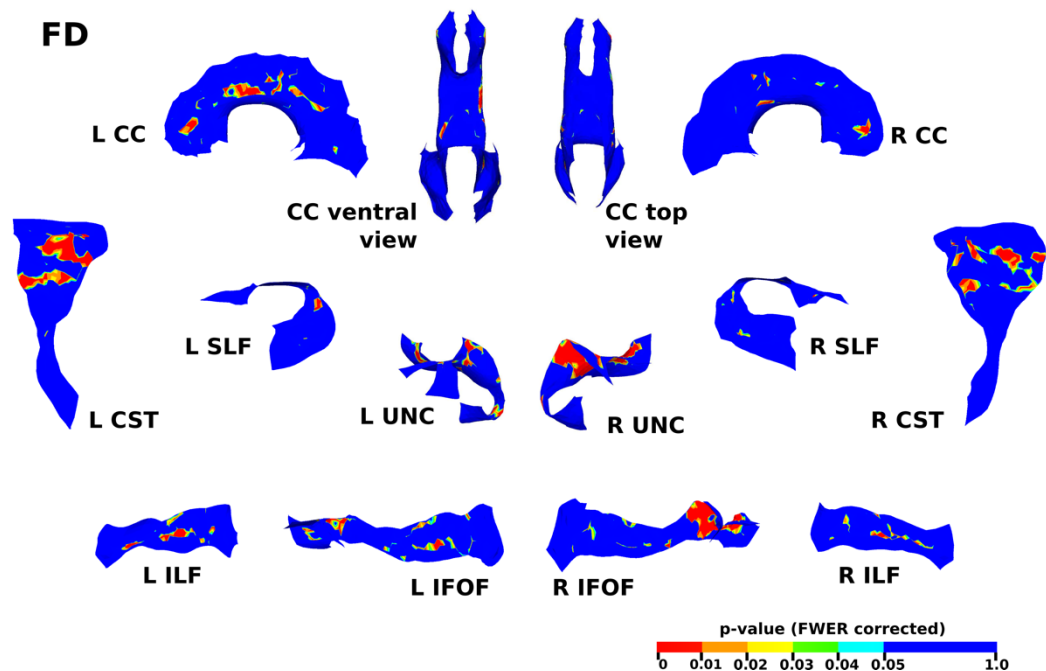


Figure 7.24 The results of the cluster analysis correlating PMA with FD at each point within the the CC, CST, IFOF, ILF, SLF and UNC. Statistically significant regions of positive correlation are shown in red ( $p \leq 0.01$ ), orange ( $0.01 < p \leq 0.02$ ), yellow ( $0.02 < p \leq 0.03$ ), green ( $0.03 < p \leq 0.04$ ) and light blue ( $0.04 < p \leq 0.05$ ).

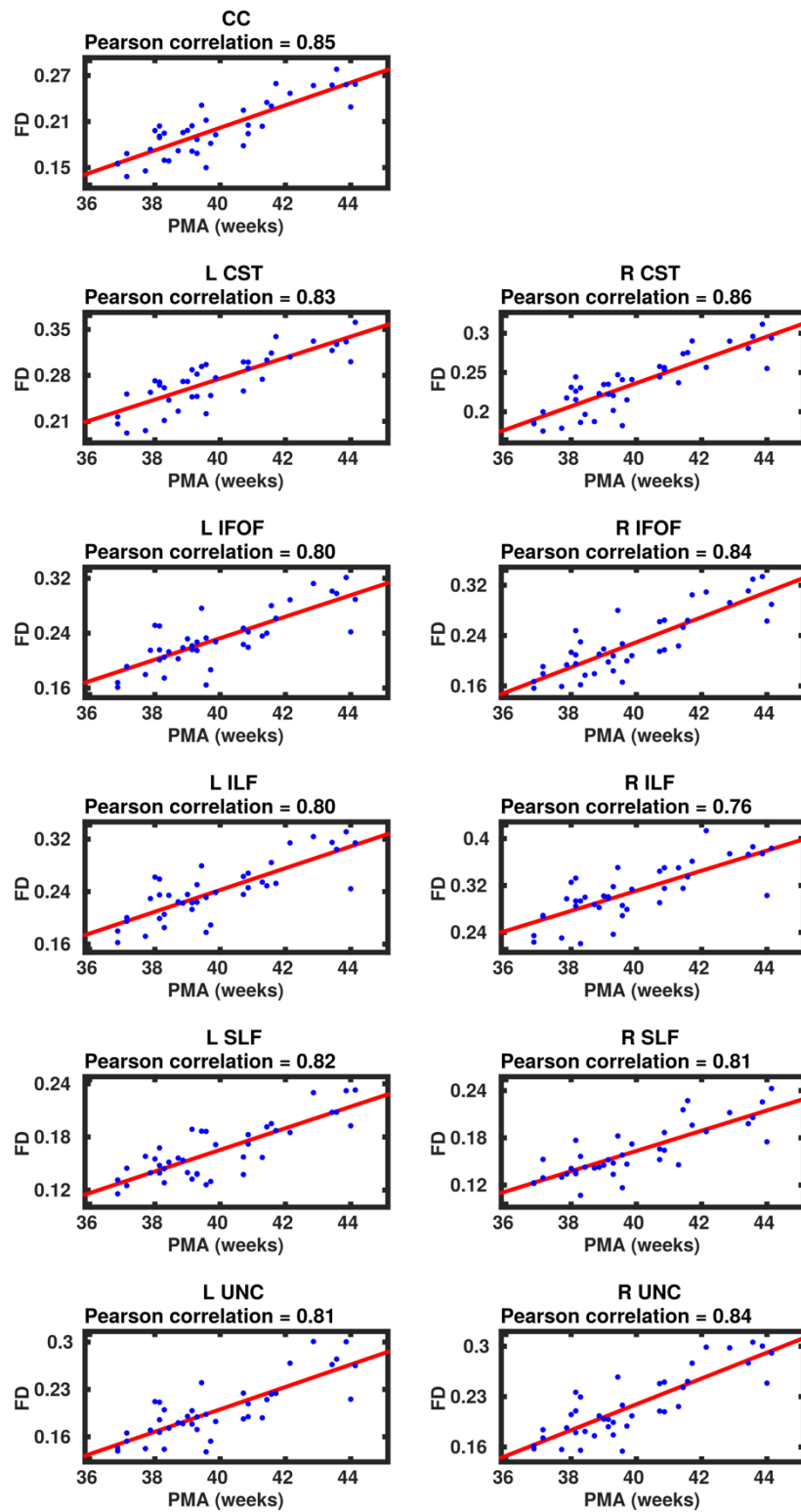


Figure 7.25 Scatter plots showing the linear relationship between FD and PMA from the regions showing significant correlation for the CC, CST, IFOF, ILF, SLF and UNC.

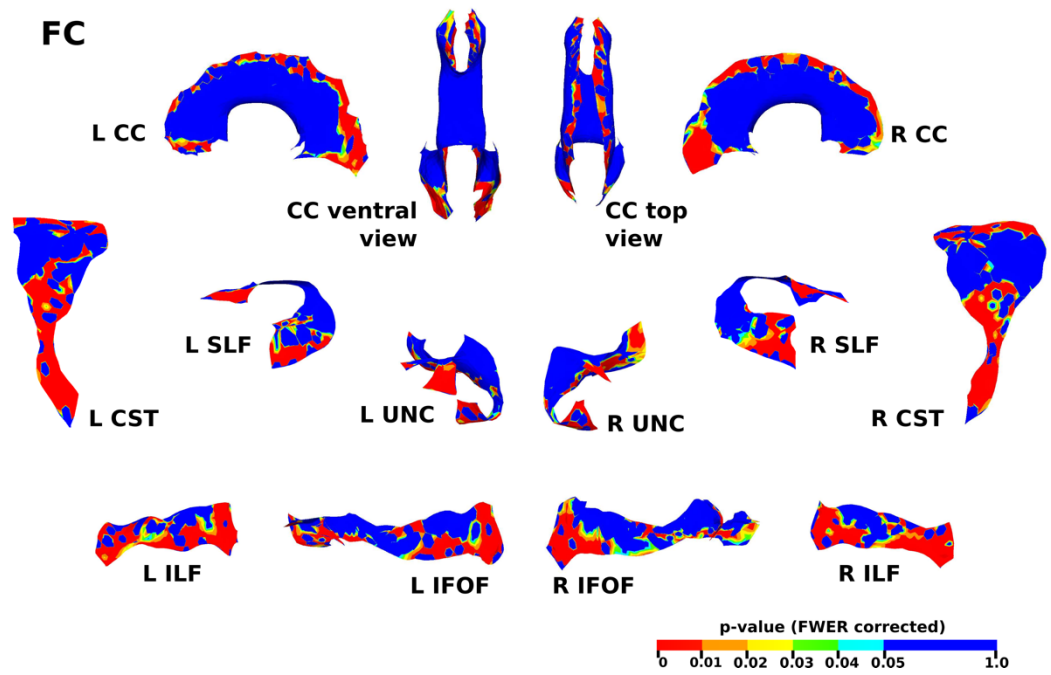


Figure 7.26 The results of the cluster analysis correlating PMA with FC at each point within the the CC, CST, IFOF, ILF, SLF and UNC. Statistically significant regions of positive correlation are shown in red ( $p \leq 0.01$ ), orange ( $0.01 < p \leq 0.02$ ), yellow ( $0.02 < p \leq 0.03$ ), green ( $0.03 < p \leq 0.04$ ) and light blue ( $0.04 < p \leq 0.05$ ).

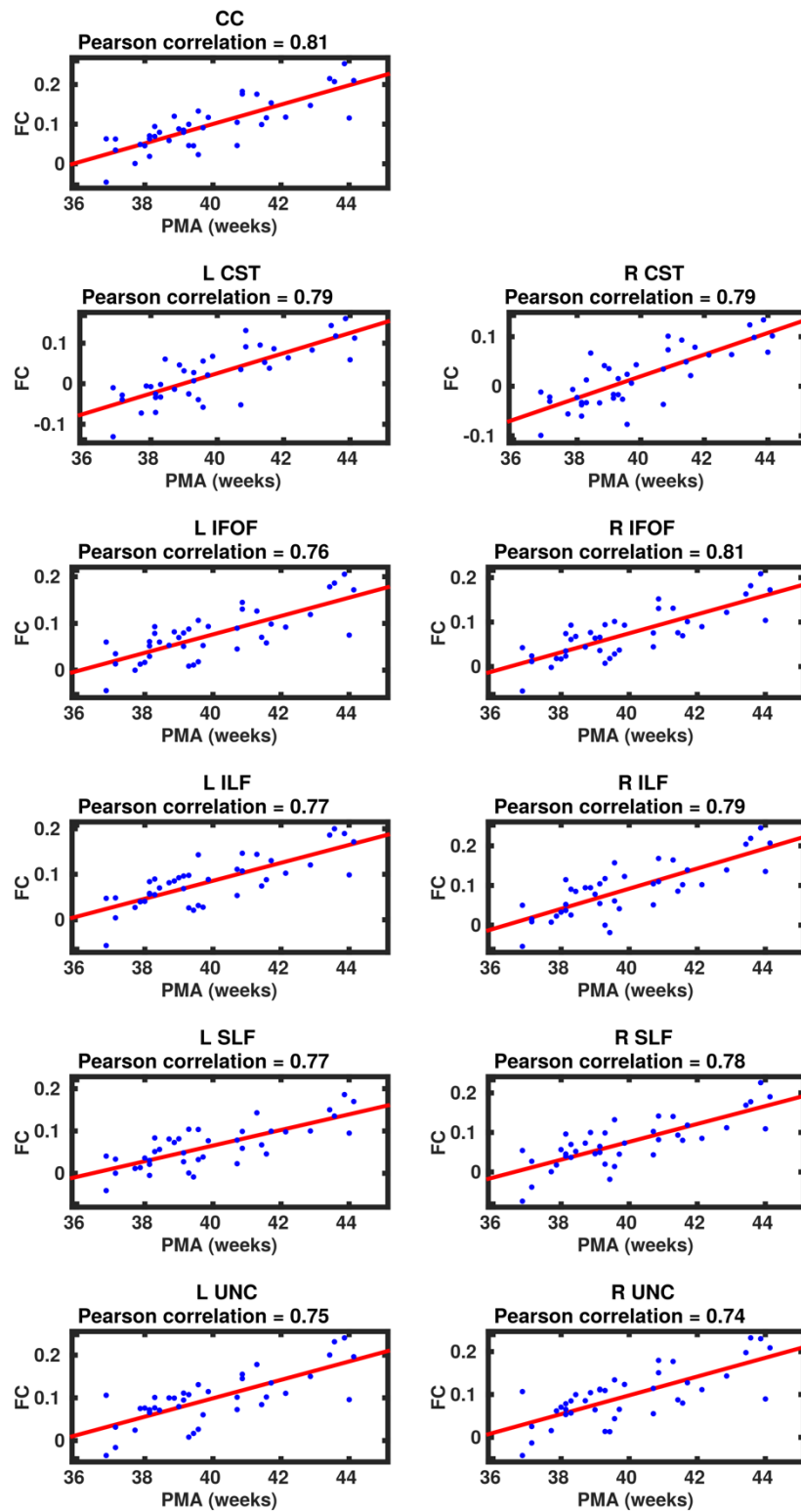


Figure 7.27 Scatter plots showing the linear relationship between FC and PMA from the regions showing significant correlation for the CC, CST, IFOF, ILF, SLF and UNC.

Table 7.2 Summary of results from tract-specific analysis. All significant results are bilateral.

Contrast	FA	MD	RD	AD	v <sub>ic</sub>	ODI	FD	FC
Left > right	NS	ILF	SLF	ILF	NS	NS	NS	NS
		SLF		SLF				
Left < right	SLF	NS	NS	NS	SLF	IFOF	NS	NS
						ILF		
						SLF		
Male > female	NS	NS	NS	NS	NS	NS	NS	NS
Male < female	NS	NS	NS	NS	NS	NS	NS	NS
Increasing	CC	CC	CC	CC	CC	NS	CC	CC
PMA at scan	CST	CST	CST	CST	CST		CST	CST
	IFOF	IFOF	IFOF	IFOF	IFOF		IFOF	IFOF
	ILF	ILF	ILF	ILF	ILF		ILF	ILF
	SLF	SLF	SLF	SLF	SLF		SLF	SLF
	UNC	UNC	UNC	UNC	UNC		UNC	UNC

## 7.4 Discussion

This chapter combines DTI, NODDI and fixel-derived parameters with TSA to assess lateralisation and maturation in subjects from the Developing Human Connectome Project. The limited spatial extent of hemispherical asymmetries found in this study indicate that the asymmetries observed in children and adults (Buchel et al., 2004; Catani et al., 2007; Eluvathingal et al., 2007; Herve et al., 2009; Johnson et al., 2014; Takao et al., 2011; Thiebaut de Schotten et al., 2011a; Thiebaut de Schotten et al., 2011b; Westerhausen et al., 2007) are acquired later in life and lateralisation of WM fibres bundles is not present at birth in healthy term neonates.

This study reports tract-specific normative values for DTI parameters and, for the first time, NODDI and fixel-derived measures for healthy term-born neonates. The group-averaged DTI values and increasing FA and decreasing diffusivities with increasing PMA at scan reported here concur with previous studies in term-born neonates (Akazawa et al., 2016; Bartha et al., 2007; Geng et al., 2012; Neil et al., 1998; Oishi et al., 2011) and the distributions of low and high values

observed in each tract is consistent with the pattern of along-tract DTI values reported in older typically-developing children (Goodlett et al., 2009; Johnson et al., 2014; Yeatman et al., 2012).

Group-averaged values for ODI demonstrate a pattern of increased dispersion in WM fasciculi near the WM-GM boundary. Dispersion in the frontal and temporal lobe projections of the UNC were markedly higher than in other tracts, most likely reflecting a high degree of fanning within the tract.  $v_{ic}$  was highest in the brainstem and PLIC, which are myelinated at birth (McArdle et al., 1987; Yakovlev and Lecours, 1967), and the body of the CC, a region of dense axonal packing. Increases in  $v_{ic}$  with increasing PMA reflect increases in the intracellular space most likely due to myelination or increasing axonal density. Increasing  $v_{ic}$  in the CST is most likely to reflect myelination, spreading superiorly and inferiorly along the tract from the PLIC. Increases in  $v_{ic}$  in the frontal lobe projections of the UNC are likely to be due increased axonal density, rather than myelination which begins around 1 year after birth in the frontal WM (Brody et al., 1987; Kinney et al., 1988). Similarly, the IFOF, ILF and SLF are unmyelinated at this time, therefore increases in  $v_{ic}$  are most likely due to increases in axonal density. Regions of  $v_{ic}$  increasing with increasing PMA at scan overlap with increases in FA. The absence of significant changes in ODI indicate that increases in FA are driven by increases in neurite density, rather than axonal coherence. These results are in agreement with findings in preterm infants (Batalle et al., 2017) and children aged 8-13 years (Mah et al., 2017).

The NODDI model (Zhang et al., 2012) has been applied previously to paediatric populations to study WM (Kunz et al., 2014; Melbourne et al., 2016), GM (Eaton-Rosen et al., 2015) and connectivity (Batalle et al., 2017) in preterm infants, and to a population of children born preterm to compare WM diffusion properties (Kelly et al., 2016), and to study GM and WM in healthy children and adolescents (Genc et al., 2017; Mah et al., 2017). Melbourne et al. (2016) demonstrated that  $v_{ic}$  increases in WM in preterm infants with increasing age, and similarly Genc et al. (2017) and Mah et al. (2017) reported a positive correlation between age and  $v_{ic}$  in children and adolescents, and weak or no changes, respectively, in ODI. Batalle et al. (2017) reported positive correlations between WM connectivity weighted by  $v_{ic}$  and negative correlations with WM connectivity weighted by  $1-ODI$ , a measure of WM coherence, in infants imaged between 25-46 weeks PMA, implying an increase in complexity and crossing fibres within the WM. These results

concur with the trend of ODI increasing with increasing PMA shown in Figure 7.24. ODI values reported for children aged 8-13 years (Mah et al., 2017) are lower than the values observed here. This suggests that changes in ODI do occur but over a different age range and possibly in a nonlinear trajectory.

Combining TSA and fixel-derived measures provides tract-specific measures of FD and FC, which are not possible within the standard FBA framework. FD values were found to be highest in regions comprising of mainly single fibres - in the body of the CC, the PLIC and the middle regions of the IFOF and ILF. Increases in FD were observed in all 11 tracts, overlapping with regions of increasing  $v_{ic}$ , supporting the interpretation of increasing axonal density. FC increased with PMA at scan in every tract, in agreement with previous studies reporting whole-brain WM volume increases after birth (Gilmore et al., 2007b; Knickmeyer et al., 2008; Makropoulos et al., 2016; Wang et al., 2012). This study demonstrates that increases in WM are driven by increases in fibre cross-section of the superficial WM.

In Chapter 6, preterm male subjects had greater FC than their female peers and it has been reported previously that term-born male neonates had greater intracranial volumes than female neonates (Gilmore et al., 2007b). In this cohort there was no significant difference in FC or brain tissue volume between male and female subjects. The differences reported by Gilmore et al. (2007b) were most likely driven by the 9% discrepancy in birth weight in male female subjects. The results here are supported by a larger study of 161 healthy infants by Qiu et al. (2013) which reported only a 2% difference in intracranial volume in a cohort with no significant differences in birth weight between male and female subjects.

Projecting fixel-derived measures onto the TSA skeleton does not exploit the whole-brain analysis capabilities of FBA. This is may be a disadvantage for exploratory studies without an a priori hypothesis. Indeed, Chapter 6 highlighted tracts that are often not included in WM microstructural analyses, such as the alterations in FC observed in the anterior commissure in relation to clinical risk factors and subsequent outcome. Nevertheless, a major benefit of this approach is the capacity to combine parameters from multiple models, in this case DTI, NODDI and fixel-derived measures, which provide complimentary information. The versatility of TSA means that in future studies, parameters from different modalities could also be combined, such as myelin-related



measures from quantitative T1 and T2 mapping, to provide a fuller characterisation of brain maturation.

## **7.5 Conclusions**

This chapter presents a novel method to analyse neonatal data using higher order diffusion models and TSA. Normative values of DTI, NODDI and fixel-derived measures and changes in these measures associated with maturation in the perinatal period are given for six major WM tracts. Analysis of high-quality diffusion MRI data from the Developing Human Connectome Project reveals that lateralisation of WM fasciculi is not present at birth in healthy term-born infants.

## Chapter 8 Summary and Future Directions

### 8.1 Key Findings

The aims of this thesis were to apply advanced dMRI analysis approaches to study brain development and preterm WM injury. TSA, NODDI, and FBA were applied to investigate the effects of perinatal risk factors on the developing brain in preterm infants; to explore the relationship between WM microstructure in the perinatal period and subsequent neurodevelopmental performance in preterm infants; and investigate brain maturation and lateralisation in healthy term-born infants using state-of-the-art diffusion data from the dHCP. The key findings from Chapters 4-7 are summarised below.

In Chapter 4, TSA, which creates surface skeleton representations of WM tracts for group analyses, was evaluated to assess this method's suitability for infant studies and to determine whether this approach offered any advantages over current widely-used analysis techniques. This evaluation demonstrated that TSA improved WM tract alignment over scalar-based registration by employing a tensor-based registration, and that the surface representations of tracts provided a close approximation of diffusion data derived from native space tractography.

In Chapter 5, TSA was applied to test the hypothesis that WM diffusion properties derived from DTI at TEA in a cohort of 407 preterm infants were associated with neurodevelopmental performance at 20 months, assessed using the BSITD-III. This analysis demonstrated anatomically-specific relationships between motor, cognitive and language performance and WM fasciculi. Higher motor and cognitive scores were associated with increased FA and decreased diffusivity in projection, commissural and association fibres, in agreement with previous studies (Counsell et al., 2008; Duerden et al., 2015; van Kooij et al., 2012b). These results suggest either that alterations in WM microstructure occur coincidentally in multiple tracts that independently modulate motor and cognitive functions, or that development of these two functional domains is related. There was little to no correlation between language performance and DTI metrics, in agreement with a previous TBSS study (Duerden et al., 2015). Conversely, Salvan et al. (2017) found FA in the arcuate fasciculus, derived from high b-value HARDI data using probabilistic CSD tractography, was positively correlated with language performance in preterm infants scanned at TEA and assessed at 2 years. The reasons for the differing results may be due to methodological

limitations of skeletonisation approaches based on low b-value and low angular resolution diffusion imaging, used in Chapter 5 and in the study by Duerden et al. (2015).

Given the limitations of DTI with respect to complex WM geometries, advanced imaging acquisition and analysis methods that correlate more specifically to tissue microstructure were applied to neonatal populations for the first time in Chapters 6 and 7. In Chapter 6, FBA was applied to a preterm neonatal cohort to test the hypothesis that perinatal risk factors adversely affect WM fasciculi, and further explore the association between WM and neurodevelopmental outcome. The diffusion tensor model is an inadequate representation of WM anatomy in voxels with multiple fibre populations. FBA (Raffelt et al., 2017) overcomes this limitation by calculating fixel-specific measures, where a fixel is a single fibre population within a voxel. FBA provides measures of the volume of the restricted intra-axonal compartment along the direction of a particular fibre population, given by FD, and relative changes in local WM fibre bundle cross-section, given by FC. Using this approach, it was possible to identify the distinct fibre populations within regions of crossing fibres associated with perinatal risk factors and developmental outcome at 20 months. Correlations between perinatal risk factors and FC were more widespread than correlations with FD, indicating a greater effect on WM fasciculi cross-section rather than microstructure. By identifying the tracts affected by given perinatal risk factors it could be possible to anticipate future developmental impairment by considering the functional pathways in which these tracts are involved. Motor and cognitive scores were positively correlated with FC in cerebellum and commissural fibres, respectively. In contrast, language was positively correlated with FD in the ILF and CC, but not with FC. These findings suggest that, unlike motor or cognitive abilities, language ability in the preterm population is more closely related to microstructural rather than morphological properties of WM fibres,

In Chapter 7, state-of-the-art dHCP data was analysed to investigate WM lateralisation and maturation in healthy term-born infants. While hemispheric asymmetries associated with functional specialisation have been demonstrated in adults (Buchel et al., 2004; Catani et al., 2007; Eluvathingal et al., 2007; Herve et al., 2009; Johnson et al., 2014; Takao et al., 2011; Thiebaut de Schotten et al., 2011a; Thiebaut de Schotten et al., 2011b; Westerhausen et al., 2007), lateralisation has not been assessed within the first four weeks of life in healthy subjects. Furthermore, there are no studies characterising normal WM development in term infants using

higher order diffusion models. The NODDI model (Zhang et al., 2012) has been previously applied in studies of preterm infants but has not been used in studies of normal brain development in healthy infants. NODDI characterises the morphology of neurites by estimating the orientation dispersion index (ODI) and provides a measure of neurite density,  $v_{ic}$ . TSA was combined with DTI, NODDI and fixel-derived metrics to assess interhemispheric differences and changes related to increasing age at scan. The results demonstrate little to no hemispheric differences in white matter fasciculi, indicating that lateralisation emerges later in life. The findings relating to WM maturation are in agreement with findings from previous DTI studies (Akazawa et al., 2016; Bartha et al., 2007; Geng et al., 2012; Neil et al., 1998; Oishi et al., 2011). However, the analysis of NODDI and fixel-derived measures produced novel findings demonstrating an increase in the intra-axonal compartment and in fibre cross-section with increasing age, with no significant changes in the dispersion of neurites.

## **8.2 Conclusions**

This thesis demonstrates the benefits of using TSA, NODDI and FBA for analysing neonatal dMRI data. These approaches provided more detailed characterisation of brain development in both term and preterm infants. The analysis carried out here reveals the adverse effects of perinatal risk factors on the developing brain; the relationship between WM microstructure in the perinatal period and subsequent neurodevelopmental performance in preterm infants; and normal development of cerebral WM in healthy infants with greater anatomical specificity than previously reported. These results may contribute to the development of quantitative measures that aim to identify infants at risk of developmental impairment and may be useful biomarkers for determining efficacy of potential therapies.

## **8.3 Future Work**

Summarised below are possible future directions for further investigations to extend the work presented in this thesis.

### **8.3.1 Multimodal imaging**

As was discussed in Chapter 7, the flexibility of TSA allows a number of quantitative imaging measures to be analysed. The work presented in this thesis could be extended to a multi-

parametric multimodal approach, including quantitative T1 and T2 data, which may be more sensitive to maturation-dependent changes than univariate analysis (Kulikova et al., 2015) and may improve the ability to discriminate between patient and control populations (Dean et al., 2017). Furthermore, while this thesis has focused on WM changes, future studies could combine quantitative measures from GM with WM measures derived from TSA and FBA, as proposed by Smith et al. (2017). Investigating how WM fasciculi influence GM structures, and vice versa, may provide additional insight into developmental changes and injury in the neonatal brain.

### **8.3.2 Future studies of neurodevelopment**

The long-term adverse effects of preterm birth underscore the importance of identifying early biomarkers of neurodevelopmental impairment. This thesis highlights the benefits of advanced dMRI techniques such as TSA, NODDI and FBA. The next step is to apply these techniques to high quality dMRI data in larger cohorts in combination with rich metadata, including genetics and behavioural information. Furthermore, these methods could be integrated into machine learning approaches, potentially moving beyond population studies and providing subject-specific predictions of neurodevelopmental outcome for vulnerable populations. Such analyses will be key to furthering our understanding of the environmental and biological factors influencing brain development and the pathophysiology of neurodevelopmental disorders.

## References

- Adams, E., Chau, V., Poskitt, K.J., Grunau, R.E., Synnes, A., Miller, S.P., 2010. Tractography-based quantitation of corticospinal tract development in premature newborns. *J Pediatr* 156, 882-888, 888 e881.
- Adams-Chapman, I., Stoll, B.J., 2006. Neonatal infection and long-term neurodevelopmental outcome in the preterm infant. *Curr Opin Infect Dis* 19, 290-297.
- Aeby, A., Liu, Y., De Tiege, X., Denolin, V., David, P., Baleriaux, D., Kavec, M., Metens, T., Van Bogaert, P., 2009. Maturation of thalamic radiations between 34 and 41 weeks' gestation: a combined voxel-based study and probabilistic tractography with diffusion tensor imaging. *AJNR Am J Neuroradiol* 30, 1780-1786.
- Ajayi-Obe, M., Saeed, N., Cowan, F.M., Rutherford, M.A., Edwards, A.D., 2000. Reduced development of cerebral cortex in extremely preterm infants. *Lancet* 356, 1162-1163.
- Akazawa, K., Chang, L., Yamakawa, R., Hayama, S., Buchthal, S., Alicata, D., Andres, T., Castillo, D., Oishi, K., Skranes, J., Ernst, T., Oishi, K., 2016. Probabilistic maps of the white matter tracts with known associated functions on the neonatal brain atlas: Application to evaluate longitudinal developmental trajectories in term-born and preterm-born infants. *Neuroimage* 128, 167-179.
- Alexander, D.C., 2005. Maximum entropy spherical deconvolution for diffusion MRI. *Inf Process Med Imaging* 19, 76-87.
- Alexander, D.C., 2008. A general framework for experiment design in diffusion MRI and its application in measuring direct tissue-microstructure features. *Magn Reson Med* 60, 439-448.
- Alexander, D.C., Hubbard, P.L., Hall, M.G., Moore, E.A., Ptito, M., Parker, G.J., Dyrby, T.B., 2010. Orientationally invariant indices of axon diameter and density from diffusion MRI. *Neuroimage* 52, 1374-1389.
- Allin, M., Walshe, M., Fern, A., Nosarti, C., Cuddy, M., Rifkin, L., Murray, R., Rushe, T., Wyatt, J., 2008. Cognitive maturation in preterm and term born adolescents. *J Neurol Neurosurg Psychiatry* 79, 381-386.
- Allin, M.P., Kontis, D., Walshe, M., Wyatt, J., Barker, G.J., Kanaan, R.A., McGuire, P., Rifkin, L., Murray, R.M., Nosarti, C., 2011. White matter and cognition in adults who were born preterm. *PLoS One* 6, e24525.
- Alshaikh, B., Yee, W., Lodha, A., Henderson, E., Yusuf, K., Sauve, R., 2014. Coagulase-negative staphylococcus sepsis in preterm infants and long-term neurodevelopmental outcome. *J Perinatol* 34, 125-129.
- Anblagan, D., Pataky, R., Evans, M.J., Telford, E.J., Serag, A., Sparrow, S., Piyasena, C., Semple, S.I., Wilkinson, A.G., Bastin, M.E., Boardman, J.P., 2016. Association between preterm brain injury and exposure to chorioamnionitis during fetal life. *Sci Rep* 6, 37932.
- Anderson, A.W., 2005. Measurement of fiber orientation distributions using high angular resolution diffusion imaging. *Magn Reson Med* 54, 1194-1206.
- Anderson, P.J., Doyle, L.W., 2006. Neurodevelopmental outcome of bronchopulmonary dysplasia. *Semin Perinatol* 30, 227-232.
- Andersson, J.L., Graham, M.S., Zsoldos, E., Sotiropoulos, S.N., 2016. Incorporating outlier detection and replacement into a non-parametric framework for movement and distortion correction of diffusion MR images. *Neuroimage* 141, 556-572.
- Andersson, J.L., Sotiropoulos, S.N., 2015. Non-parametric representation and prediction of single- and multi-shell diffusion-weighted MRI data using Gaussian processes. *Neuroimage* 122, 166-176.
- Andiman, S.E., Haynes, R.L., Trachtenberg, F.L., Billiards, S.S., Folkerth, R.D., Volpe, J.J., Kinney, H.C., 2010. The cerebral cortex overlying periventricular leukomalacia: analysis of pyramidal neurons. *Brain Pathol* 20, 803-814.

- Anjari, M., Counsell, S.J., Srinivasan, L., Allsop, J.M., Hajnal, J.V., Rutherford, M.A., Edwards, A.D., 2009. The association of lung disease with cerebral white matter abnormalities in preterm infants. *Pediatrics* 124, 268-276.
- Anjari, M., Srinivasan, L., Allsop, J.M., Hajnal, J.V., Rutherford, M.A., Edwards, A.D., Counsell, S.J., 2007. Diffusion tensor imaging with tract-based spatial statistics reveals local white matter abnormalities in preterm infants. *Neuroimage* 35, 1021-1027.
- Argyropoulou, M.I., Xydis, V., Drougia, A., Argyropoulou, P.I., Tzoufi, M., Bassounas, A., Andronikou, S., Efremidis, S.C., 2003. MRI measurements of the pons and cerebellum in children born preterm; associations with the severity of periventricular leukomalacia and perinatal risk factors. *Neuroradiology* 45, 730-734.
- Arzoumanian, Y., Mirmiran, M., Barnes, P.D., Woolley, K., Ariagno, R.L., Moseley, M.E., Fleisher, B.E., Atlas, S.W., 2003. Diffusion tensor brain imaging findings at term-equivalent age may predict neurologic abnormalities in low birth weight preterm infants. *AJNR Am J Neuroradiol* 24, 1646-1653.
- Ashburner, J., Friston, K.J., 2000. Voxel-based morphometry--the methods. *Neuroimage* 11, 805-821.
- Assaf, Y., Basser, P.J., 2005. Composite hindered and restricted model of diffusion (CHARMED) MR imaging of the human brain. *Neuroimage* 27, 48-58.
- Assaf, Y., Blumenfeld-Katzir, T., Yovel, Y., Basser, P.J., 2008. AxCaliber: a method for measuring axon diameter distribution from diffusion MRI. *Magn Reson Med* 59, 1347-1354.
- Assaf, Y., Freidlin, R.Z., Rohde, G.K., Basser, P.J., 2004. New modeling and experimental framework to characterize hindered and restricted water diffusion in brain white matter. *Magn Reson Med* 52, 965-978.
- Augustine, E.M., Spielman, D.M., Barnes, P.D., Sutcliffe, T.L., Dermon, J.D., Mirmiran, M., Clayton, D.B., Ariagno, R.L., 2008. Can magnetic resonance spectroscopy predict neurodevelopmental outcome in very low birth weight preterm infants? *J Perinatol* 28, 611-618.
- Avants, B.B., Epstein, C.L., Grossman, M., Gee, J.C., 2008. Symmetric diffeomorphic image registration with cross-correlation: evaluating automated labeling of elderly and neurodegenerative brain. *Med Image Anal* 12, 26-41.
- Bach, M., Laun, F.B., Leemans, A., Tax, C.M., Biessels, G.J., Stieltjes, B., Maier-Hein, K.H., 2014. Methodological considerations on tract-based spatial statistics (TBSS). *Neuroimage* 100, 358-369.
- Back, S.A., 2015. Brain Injury in the Preterm Infant: New Horizons for Pathogenesis and Prevention. *Pediatr Neurol* 53, 185-192.
- Back, S.A., Miller, S.P., 2014. Brain injury in premature neonates: A primary cerebral dysmaturation disorder? *Ann Neurol* 75, 469-486.
- Back, S.A., Tuohy, T.M., Chen, H., Wallingford, N., Craig, A., Struve, J., Luo, N.L., Banine, F., Liu, Y., Chang, A., Trapp, B.D., Bebo, B.F., Jr., Rao, M.S., Sherman, L.S., 2005. Hyaluronan accumulates in demyelinated lesions and inhibits oligodendrocyte progenitor maturation. *Nat Med* 11, 966-972.
- Badzakova-Trajkov, G., Haberling, I.S., Roberts, R.P., Corballis, M.C., 2010. Cerebral asymmetries: complementary and independent processes. *PLoS One* 5, e9682.
- Ball, G., Boardman, J.P., Rueckert, D., Aljabar, P., Arichi, T., Merchant, N., Gousias, I.S., Edwards, A.D., Counsell, S.J., 2012. The effect of preterm birth on thalamic and cortical development. *Cereb Cortex* 22, 1016-1024.
- Ball, G., Counsell, S.J., Anjari, M., Merchant, N., Arichi, T., Doria, V., Rutherford, M.A., Edwards, A.D., Rueckert, D., Boardman, J.P., 2010. An optimised tract-based spatial statistics protocol for neonates: applications to prematurity and chronic lung disease. *Neuroimage* 53, 94-102.
- Ball, G., Pazderova, L., Chew, A., Tusor, N., Merchant, N., Arichi, T., Allsop, J.M., Cowan, F.M., Edwards, A.D., Counsell, S.J., 2015. Thalamocortical Connectivity Predicts Cognition in Children Born Preterm. *Cereb Cortex* 25, 4310-4318.

- Ball, G., Srinivasan, L., Aljabar, P., Counsell, S.J., Durighel, G., Hajnal, J.V., Rutherford, M.A., Edwards, A.D., 2013. Development of cortical microstructure in the preterm human brain. *Proc Natl Acad Sci U S A* 110, 9541-9546.
- Ballabh, P., 2010. Intraventricular hemorrhage in premature infants: mechanism of disease. *Pediatr Res* 67, 1-8.
- Baraldi, E., Filippone, M., 2007. Chronic lung disease after premature birth. *N Engl J Med* 357, 1946-1955.
- Barazany, D., Basser, P.J., Assaf, Y., 2009. In vivo measurement of axon diameter distribution in the corpus callosum of rat brain. *Brain* 132, 1210-1220.
- Barber, A.D., Srinivasan, P., Joel, S.E., Caffo, B.S., Pekar, J.J., Mostofsky, S.H., 2012. Motor "dexterity"? Evidence that left hemisphere lateralization of motor circuit connectivity is associated with better motor performance in children. *Cereb Cortex* 22, 51-59.
- Barkovich, A.J., 2000. Concepts of myelin and myelination in neuroradiology. *AJNR Am J Neuroradiol* 21, 1099-1109.
- Barre, N., Morgan, A., Doyle, L.W., Anderson, P.J., 2011. Language abilities in children who were very preterm and/or very low birth weight: a meta-analysis. *J Pediatr* 158, 766-774 e761.
- Bartha, A.I., Yap, K.R., Miller, S.P., Jeremy, R.J., Nishimoto, M., Vigneron, D.B., Barkovich, A.J., Ferriero, D.M., 2007. The normal neonatal brain: MR imaging, diffusion tensor imaging, and 3D MR spectroscopy in healthy term neonates. *AJNR Am J Neuroradiol* 28, 1015-1021.
- Basser, P.J., 1995. Inferring microstructural features and the physiological state of tissues from diffusion-weighted images. *NMR Biomed* 8, 333-344.
- Basser, P.J., Mattiello, J., LeBihan, D., 1994. MR diffusion tensor spectroscopy and imaging. *Biophys J* 66, 259-267.
- Basser, P.J., Pajevic, S., Pierpaoli, C., Duda, J., Aldroubi, A., 2000. In vivo fiber tractography using DT-MRI data. *Magn Reson Med* 44, 625-632.
- Basser, P.J., Pierpaoli, C., 1996. Microstructural and physiological features of tissues elucidated by quantitative-diffusion-tensor MRI. *J Magn Reson B* 111, 209-219.
- Bassi, L., Chew, A., Merchant, N., Ball, G., Ramenghi, L., Boardman, J., Allsop, J.M., Doria, V., Arichi, T., Mosca, F., Edwards, A.D., Cowan, F.M., Rutherford, M.A., Counsell, S.J., 2011. Diffusion tensor imaging in preterm infants with punctate white matter lesions. *Pediatr Res* 69, 561-566.
- Bassi, L., Ricci, D., Volzone, A., Allsop, J.M., Srinivasan, L., Pai, A., Ribes, C., Ramenghi, L.A., Mercuri, E., Mosca, F., Edwards, A.D., Cowan, F.M., Rutherford, M.A., Counsell, S.J., 2008. Probabilistic diffusion tractography of the optic radiations and visual function in preterm infants at term equivalent age. *Brain* 131, 573-582.
- Batalle, D., Hughes, E.J., Zhang, H., Tournier, J.D., Tusor, N., Aljabar, P., Wali, L., Alexander, D.C., Hajnal, J.V., Nosarti, C., Edwards, A.D., Counsell, S.J., 2017. Early development of structural networks and the impact of prematurity on brain connectivity. *Neuroimage* 149, 379-392.
- Baumli, J.G., Meng, C., Daamen, M., Baumann, N., Busch, B., Bartmann, P., Wolke, D., Boecker, H., Wohlschlager, A., Sorg, C., Jaekel, J., 2017. The association of children's mathematic abilities with both adults' cognitive abilities and intrinsic fronto-parietal networks is altered in preterm-born individuals. *Brain Struct Funct* 222, 799-812.
- Bayless, S., Stevenson, J., 2007. Executive functions in school-age children born very prematurely. *Early Hum Dev* 83, 247-254.
- Beaulieu, C., 2002. The basis of anisotropic water diffusion in the nervous system - a technical review. *NMR Biomed* 15, 435-455.
- Beauport, L., Schneider, J., Faouzi, M., Hagmann, P., Huppi, P.S., Tolsa, J.F., Truttmann, A.C., Fischer Fumeaux, C.J., 2017. Impact of Early Nutritional Intake on Preterm Brain: A Magnetic Resonance Imaging Study. *J Pediatr* 181, 29-36 e21.
- Beck, S., Wojdyla, D., Say, L., Betran, A.P., Merialdi, M., Requejo, J.H., Rubens, C., Menon, R., Van Look, P.F., 2010. The worldwide incidence of preterm birth: a systematic review of maternal mortality and morbidity. *Bull World Health Organ* 88, 31-38.



- Behrens, T.E., Berg, H.J., Jbabdi, S., Rushworth, M.F., Woolrich, M.W., 2007. Probabilistic diffusion tractography with multiple fibre orientations: What can we gain? *Neuroimage* 34, 144-155.
- Behrens, T.E., Woolrich, M.W., Jenkinson, M., Johansen-Berg, H., Nunes, R.G., Clare, S., Matthews, P.M., Brady, J.M., Smith, S.M., 2003. Characterization and propagation of uncertainty in diffusion-weighted MR imaging. *Magn Reson Med* 50, 1077-1088.
- Bell, J.E., Becher, J.C., Wyatt, B., Keeling, J.W., McIntosh, N., 2005. Brain damage and axonal injury in a Scottish cohort of neonatal deaths. *Brain* 128, 1070-1081.
- Berger, A., Witt, A., Haiden, N., Kaider, A., Klebermasz, K., Fuiko, R., Langgartner, M., Pollak, A., 2009. Intrauterine infection with *Ureaplasma* species is associated with adverse neuromotor outcome at 1 and 2 years adjusted age in preterm infants. *J Perinat Med* 37, 72-78.
- Berman, J.I., Glass, H.C., Miller, S.P., Mukherjee, P., Ferriero, D.M., Barkovich, A.J., Vigneron, D.B., Henry, R.G., 2009. Quantitative fiber tracking analysis of the optic radiation correlated with visual performance in premature newborns. *AJNR Am J Neuroradiol* 30, 120-124.
- Berman, J.I., Mukherjee, P., Partridge, S.C., Miller, S.P., Ferriero, D.M., Barkovich, A.J., Vigneron, D.B., Henry, R.G., 2005. Quantitative diffusion tensor MRI fiber tractography of sensorimotor white matter development in premature infants. *Neuroimage* 27, 862-871.
- Bernstein, I.M., Horbar, J.D., Badger, G.J., Ohlsson, A., Golan, A., 2000. Morbidity and mortality among very-low-birth-weight neonates with intrauterine growth restriction. The Vermont Oxford Network. *Am J Obstet Gynecol* 182, 198-206.
- Bhutta, A.T., Cleves, M.A., Casey, P.H., Cradock, M.M., Anand, K.J., 2002. Cognitive and behavioral outcomes of school-aged children who were born preterm: a meta-analysis. *JAMA* 288, 728-737.
- Billiards, S.S., Haynes, R.L., Folkerth, R.D., Borenstein, N.S., Trachtenberg, F.L., Rowitch, D.H., Ligon, K.L., Volpe, J.J., Kinney, H.C., 2008. Myelin abnormalities without oligodendrocyte loss in periventricular leukomalacia. *Brain Pathol* 18, 153-163.
- Blakely, M.L., Lally, K.P., McDonald, S., Brown, R.L., Barnhart, D.C., Ricketts, R.R., Thompson, W.R., Scherer, L.R., Klein, M.D., Letton, R.W., Chwals, W.J., Touloukian, R.J., Kurkchubasche, A.G., Skinner, M.A., Moss, R.L., Hilfiker, M.L., Network, N.E.C.S.o.t.N.N.R., 2005. Postoperative outcomes of extremely low birth-weight infants with necrotizing enterocolitis or isolated intestinal perforation: a prospective cohort study by the NICHD Neonatal Research Network. *Ann Surg* 241, 984-989; discussion 989-994.
- Blencowe, H., Cousens, S., Oestergaard, M.Z., Chou, D., Moller, A.B., Narwal, R., Adler, A., Vera Garcia, C., Rohde, S., Say, L., Lawn, J.E., 2012. National, regional, and worldwide estimates of preterm birth rates in the year 2010 with time trends since 1990 for selected countries: a systematic analysis and implications. *Lancet* 379, 2162-2172.
- Bloch, F., 1946. Nuclear induction. *Phys. Rev.* 70, 460-474.
- Blondel, B., Macfarlane, A., Gissler, M., Breart, G., Zeitlin, J., Group, P.S., 2006. Preterm birth and multiple pregnancy in European countries participating in the PERISTAT project. *BJOG* 113, 528-535.
- Boardman, J.P., Counsell, S.J., Rueckert, D., Hajnal, J.V., Bhatia, K.K., Srinivasan, L., Kapellou, O., Aljabar, P., Dyet, L.E., Rutherford, M.A., Allsop, J.M., Edwards, A.D., 2007. Early growth in brain volume is preserved in the majority of preterm infants. *Ann Neurol* 62, 185-192.
- Boardman, J.P., Counsell, S.J., Rueckert, D., Kapellou, O., Bhatia, K.K., Aljabar, P., Hajnal, J., Allsop, J.M., Rutherford, M.A., Edwards, A.D., 2006. Abnormal deep grey matter development following preterm birth detected using deformation-based morphometry. *Neuroimage* 32, 70-78.
- Bolisetty, S., Dhawan, A., Abdel-Latif, M., Bajuk, B., Stack, J., Lui, K., New South, W., Australian Capital Territory Neonatal Intensive Care Units' Data, C., 2014. Intraventricular hemorrhage and neurodevelopmental outcomes in extreme preterm infants. *Pediatrics* 133, 55-62.
- Bonifacio, S.L., Glass, H.C., Chau, V., Berman, J.I., Xu, D., Brant, R., Barkovich, A.J., Poskitt, K.J., Miller, S.P., Ferriero, D.M., 2010. Extreme premature birth is not associated with impaired development of brain microstructure. *J Pediatr* 157, 726-732 e721.

- Bourgoin, L., Cipierre, C., Hauet, Q., Basset, H., Gournay, V., Roze, J.C., Flamant, C., Gascoin, G., 2016. Neurodevelopmental Outcome at 2 Years of Age according to Patent Ductus Arteriosus Management in Very Preterm Infants. *Neonatology* 109, 139-146.
- Braga, R.M., Roze, E., Ball, G., Merchant, N., Tusor, N., Arichi, T., Edwards, D., Rueckert, D., Counsell, S.J., 2015. Development of the Corticospinal and Callosal Tracts from Extremely Premature Birth up to 2 Years of Age. *PLoS One* 10, e0125681.
- Brody, B.A., Kinney, H.C., Kloman, A.S., Gilles, F.H., 1987. Sequence of central nervous system myelination in human infancy. I. An autopsy study of myelination. *J Neuropathol Exp Neurol* 46, 283-301.
- Brossard-Racine, M., Poretti, A., Murnick, J., Bouyssy-Kobar, M., McCarter, R., du Plessis, A.J., Limperopoulos, C., 2017. Cerebellar Microstructural Organization is Altered by Complications of Premature Birth: A Case-Control Study. *J Pediatr* 182, 28-33 e21.
- Brouwer, M.J., Kersbergen, K.J., van Kooij, B.J.M., Benders, M., van Haastert, I.C., Koopman-Esseboom, C., Neil, J.J., de Vries, L.S., Kidokoro, H., Inder, T.E., Groenendaal, F., 2017. Preterm brain injury on term-equivalent age MRI in relation to perinatal factors and neurodevelopmental outcome at two years. *PLoS One* 12, e0177128.
- Bruno, C.J., Bengani, S., Gomes, W.A., Brewer, M., Vega, M., Xie, X., Kim, M., Fuloria, M., 2017. MRI Differences Associated with Intrauterine Growth Restriction in Preterm Infants. *Neonatology* 111, 317-323.
- Buchel, C., Raedler, T., Sommer, M., Sach, M., Weiller, C., Koch, M.A., 2004. White matter asymmetry in the human brain: a diffusion tensor MRI study. *Cereb Cortex* 14, 945-951.
- Buckner, R.L., 2013. The cerebellum and cognitive function: 25 years of insight from anatomy and neuroimaging. *Neuron* 80, 807-815.
- Budisavljevic, S., Dell'Acqua, F., Rijdsdijk, F.V., Kane, F., Picchioni, M., McGuire, P., Touloupoulou, T., Georgiades, A., Kalidindi, S., Kravariti, E., Murray, R.M., Murphy, D.G., Craig, M.C., Catani, M., 2015. Age-Related Differences and Heritability of the Perisylvian Language Networks. *J Neurosci* 35, 12625-12634.
- Buser, J.R., Maire, J., Riddle, A., Gong, X., Nguyen, T., Nelson, K., Luo, N.L., Ren, J., Struve, J., Sherman, L.S., Miller, S.P., Chau, V., Henderson, G., Ballabh, P., Grafe, M.R., Back, S.A., 2012. Arrested preoligodendrocyte maturation contributes to myelination failure in premature infants. *Ann Neurol* 71, 93-109.
- Cai, Q., Van der Haegen, L., Brysbaert, M., 2013. Complementary hemispheric specialization for language production and visuospatial attention. *Proc Natl Acad Sci U S A* 110, E322-330.
- Card, D., Nossin-Manor, R., Moore, A.M., Raybaud, C., Sled, J.G., Taylor, M.J., 2013. Brain metabolite concentrations are associated with illness severity scores and white matter abnormalities in very preterm infants. *Pediatr Res* 74, 75-81.
- Catani, M., Allin, M.P., Husain, M., Pugliese, L., Mesulam, M.M., Murray, R.M., Jones, D.K., 2007. Symmetries in human brain language pathways correlate with verbal recall. *Proc Natl Acad Sci U S A* 104, 17163-17168.
- Chau, V., Brant, R., Poskitt, K.J., Tam, E.W., Synnes, A., Miller, S.P., 2012. Postnatal infection is associated with widespread abnormalities of brain development in premature newborns. *Pediatr Res* 71, 274-279.
- Chau, V., Poskitt, K.J., McFadden, D.E., Bowen-Roberts, T., Synnes, A., Brant, R., Sargent, M.A., Soulikias, W., Miller, S.P., 2009. Effect of chorioamnionitis on brain development and injury in premature newborns. *Ann Neurol* 66, 155-164.
- Chau, V., Synnes, A., Grunau, R.E., Poskitt, K.J., Brant, R., Miller, S.P., 2013. Abnormal brain maturation in preterm neonates associated with adverse developmental outcomes. *Neurology* 81, 2082-2089.
- Chen, J., Smith, L.E., 2007. Retinopathy of prematurity. *Angiogenesis* 10, 133-140.
- Chen, Z., Zhang, H., Yushkevich, P.A., Liu, M., Beaulieu, C., 2016. Maturation Along White Matter Tracts in Human Brain Using a Diffusion Tensor Surface Model Tract-Specific Analysis. *Front Neuroanat* 10, 9.

- Cheong, J.L., Thompson, D.K., Wang, H.X., Hunt, R.W., Anderson, P.J., Inder, T.E., Doyle, L.W., 2009. Abnormal white matter signal on MR imaging is related to abnormal tissue microstructure. *AJNR Am J Neuroradiol* 30, 623-628.
- Chi, J.G., Dooling, E.C., Gilles, F.H., 1977. Gyral development of the human brain. *Ann Neurol* 1, 86-93.
- Childs, A.M., Ramenghi, L.A., Cornette, L., Tanner, S.F., Arthur, R.J., Martinez, D., Levene, M.I., 2001. Cerebral maturation in premature infants: quantitative assessment using MR imaging. *AJNR Am J Neuroradiol* 22, 1577-1582.
- Claas, M.J., de Vries, L.S., Koopman, C., Uniken Venema, M.M., Eijssers, M.J., Bruinse, H.W., Verrijn Stuart, A.A., 2011. Postnatal growth of preterm born children  $\leq$  750g at birth. *Early Hum Dev* 87, 495-507.
- Clark, R.H., Wagner, C.L., Merritt, R.J., Bloom, B.T., Neu, J., Young, T.E., Clark, D.A., 2003. Nutrition in the neonatal intensive care unit: how do we reduce the incidence of extrauterine growth restriction? *J Perinatol* 23, 337-344.
- Conturo, T.E., Lori, N.F., Cull, T.S., Akbudak, E., Snyder, A.Z., Shimony, J.S., McKinstry, R.C., Burton, H., Raichle, M.E., 1999. Tracking neuronal fiber pathways in the living human brain. *Proc Natl Acad Sci U S A* 96, 10422-10427.
- Cooke, R.W., 2005. Perinatal and postnatal factors in very preterm infants and subsequent cognitive and motor abilities. *Arch Dis Child Fetal Neonatal Ed* 90, F60-63.
- Cordero Grande, L., Price, A., Hutter, J.M., Hughes, E., Hajnal, J.V., 2016. Comprehensive CG-SENSE reconstruction of SMS-EPI. conference abstracts of ISMRM.
- Cornette, L.G., Tanner, S.F., Ramenghi, L.A., Miall, L.S., Childs, A.M., Arthur, R.J., Martinez, D., Levene, M.I., 2002. Magnetic resonance imaging of the infant brain: anatomical characteristics and clinical significance of punctate lesions. *Arch Dis Child Fetal Neonatal Ed* 86, F171-177.
- Corouge, I., Fletcher, P.T., Joshi, S., Gouttard, S., Gerig, G., 2006. Fiber tract-oriented statistics for quantitative diffusion tensor MRI analysis. *Med Image Anal* 10, 786-798.
- Costeloe, K.L., Hennessy, E.M., Haider, S., Stacey, F., Marlow, N., Draper, E.S., 2012. Short term outcomes after extreme preterm birth in England: comparison of two birth cohorts in 1995 and 2006 (the EPICure studies). *BMJ* 345, e7976.
- Counsell, S.J., Allsop, J.M., Harrison, M.C., Larkman, D.J., Kennea, N.L., Kapellou, O., Cowan, F.M., Hajnal, J.V., Edwards, A.D., Rutherford, M.A., 2003a. Diffusion-weighted imaging of the brain in preterm infants with focal and diffuse white matter abnormality. *Pediatrics* 112, 1-7.
- Counsell, S.J., Dyet, L.E., Larkman, D.J., Nunes, R.G., Boardman, J.P., Allsop, J.M., Fitzpatrick, J., Srinivasan, L., Cowan, F.M., Hajnal, J.V., Rutherford, M.A., Edwards, A.D., 2007. Thalamo-cortical connectivity in children born preterm mapped using probabilistic magnetic resonance tractography. *Neuroimage* 34, 896-904.
- Counsell, S.J., Edwards, A.D., Chew, A.T., Anjari, M., Dyet, L.E., Srinivasan, L., Boardman, J.P., Allsop, J.M., Hajnal, J.V., Rutherford, M.A., Cowan, F.M., 2008. Specific relations between neurodevelopmental abilities and white matter microstructure in children born preterm. *Brain* 131, 3201-3208.
- Counsell, S.J., Kennea, N.L., Herlihy, A.H., Allsop, J.M., Harrison, M.C., Cowan, F.M., Hajnal, J.V., Edwards, B., Edwards, A.D., Rutherford, M.A., 2003b. T2 relaxation values in the developing preterm brain. *AJNR Am J Neuroradiol* 24, 1654-1660.
- Counsell, S.J., Shen, Y., Boardman, J.P., Larkman, D.J., Kapellou, O., Ward, P., Allsop, J.M., Cowan, F.M., Hajnal, J.V., Edwards, A.D., Rutherford, M.A., 2006. Axial and radial diffusivity in preterm infants who have diffuse white matter changes on magnetic resonance imaging at term-equivalent age. *Pediatrics* 117, 376-386.
- Daducci, A., Canales-Rodriguez, E.J., Zhang, H., Dyrby, T.B., Alexander, D.C., Thiran, J.P., 2015. Accelerated Microstructure Imaging via Convex Optimization (AMICO) from diffusion MRI data. *Neuroimage* 105, 32-44.
- Dammann, O., Leviton, A., 1997. Maternal intrauterine infection, cytokines, and brain damage in the preterm newborn. *Pediatr Res* 42, 1-8.

- Danks, M., Cherry, K., Burns, Y.R., Gray, P.H., 2017. Are behaviour problems in extremely low-birthweight children related to their motor ability? *Acta Paediatr* 106, 568-572.
- Davis, E.E., Pitchford, N.J., Jaspan, T., McArthur, D., Walker, D., 2010. Development of cognitive and motor function following cerebellar tumour injury sustained in early childhood. *Cortex* 46, 919-932.
- de Bruine, F.T., van den Berg-Huysmans, A.A., Leijser, L.M., Rijken, M., Steggerda, S.J., van der Grond, J., van Wezel-Meijler, G., 2011a. Clinical implications of MR imaging findings in the white matter in very preterm infants: a 2-year follow-up study. *Radiology* 261, 899-906.
- De Bruine, F.T., Van Wezel-Meijler, G., Leijser, L.M., Steggerda, S.J., Van Den Berg-Huysmans, A.A., Rijken, M., Van Buchem, M.A., Van Der Grond, J., 2013. Tractography of white-matter tracts in very preterm infants: a 2-year follow-up study. *Dev Med Child Neurol* 55, 427-433.
- de Bruine, F.T., van Wezel-Meijler, G., Leijser, L.M., van den Berg-Huysmans, A.A., van Steenis, A., van Buchem, M.A., van der Grond, J., 2011b. Tractography of developing white matter of the internal capsule and corpus callosum in very preterm infants. *Eur Radiol* 21, 538-547.
- de Graaf-Peters, V.B., Hadders-Algra, M., 2006. Ontogeny of the human central nervous system: what is happening when? *Early Hum Dev* 82, 257-266.
- de Groot, M., Vernooij, M.W., Klein, S., Ikram, M.A., Vos, F.M., Smith, S.M., Niessen, W.J., Andersson, J.L., 2013. Improving alignment in Tract-based spatial statistics: evaluation and optimization of image registration. *Neuroimage* 76, 400-411.
- de Kieviet, J.F., Piek, J.P., Aarnoudse-Moens, C.S., Oosterlaan, J., 2009. Motor development in very preterm and very low-birth-weight children from birth to adolescence: a meta-analysis. *JAMA* 302, 2235-2242.
- de Vries, L.S., Groenendaal, F., 2002. Neuroimaging in the preterm infant. *Ment Retard Dev Disabil Res Rev* 8, 273-280.
- Dean, D.C., 3rd, Lange, N., Travers, B.G., Prigge, M.B., Matsunami, N., Kellett, K.A., Freeman, A., Kane, K.L., Adluru, N., Tromp, D.P., Destiche, D.J., Samsin, D., Zielinski, B.A., Fletcher, P.T., Anderson, J.S., Froehlich, A.L., Leppert, M.F., Bigler, E.D., Lainhart, J.E., Alexander, A.L., 2017. Multivariate characterization of white matter heterogeneity in autism spectrum disorder. *Neuroimage Clin* 14, 54-66.
- Dean, D.C., 3rd, O'Muircheartaigh, J., Dirks, H., Travers, B.G., Adluru, N., Alexander, A.L., Deoni, S.C.L., 2016. Mapping an index of the myelin g-ratio in infants using magnetic resonance imaging. *Neuroimage* 132, 225-237.
- Dehaene-Lambertz, G., 2000. Cerebral specialization for speech and non-speech stimuli in infants. *J Cogn Neurosci* 12, 449-460.
- Dehaene-Lambertz, G., Dehaene, S., Hertz-Pannier, L., 2002. Functional neuroimaging of speech perception in infants. *Science* 298, 2013-2015.
- Dehaene-Lambertz, G., Hertz-Pannier, L., Dubois, J., 2006. Nature and nurture in language acquisition: anatomical and functional brain-imaging studies in infants. *Trends Neurosci* 29, 367-373.
- Dell'Acqua, F., Rizzo, G., Scifo, P., Clarke, R.A., Scotti, G., Fazio, F., 2007. A model-based deconvolution approach to solve fiber crossing in diffusion-weighted MR imaging. *IEEE Trans Biomed Eng* 54, 462-472.
- Dell'acqua, F., Scifo, P., Rizzo, G., Catani, M., Simmons, A., Scotti, G., Fazio, F., 2010. A modified damped Richardson-Lucy algorithm to reduce isotropic background effects in spherical deconvolution. *Neuroimage* 49, 1446-1458.
- Dell'Acqua, F., Simmons, A., Williams, S.C., Catani, M., 2013. Can spherical deconvolution provide more information than fiber orientations? Hindrance modulated orientational anisotropy, a true-tract specific index to characterize white matter diffusion. *Hum Brain Mapp* 34, 2464-2483.
- Delobel-Ayoub, M., Arnaud, C., White-Koning, M., Casper, C., Pierrat, V., Garel, M., Burguet, A., Roze, J.C., Matis, J., Picaud, J.C., Kaminski, M., Larroque, B., Group, E.S., 2009. Behavioral problems and cognitive performance at 5 years of age after very preterm birth: the EPIPAGE Study. *Pediatrics* 123, 1485-1492.
- Deoni, S.C., 2010. Quantitative relaxometry of the brain. *Top Magn Reson Imaging* 21, 101-113.

- Deoni, S.C., Dean, D.C., 3rd, O'Muirheartaigh, J., Dirks, H., Jerskey, B.A., 2012. Investigating white matter development in infancy and early childhood using myelin water fraction and relaxation time mapping. *Neuroimage* 63, 1038-1053.
- Deoni, S.C., Mercure, E., Blasi, A., Gasston, D., Thomson, A., Johnson, M., Williams, S.C., Murphy, D.G., 2011. Mapping infant brain myelination with magnetic resonance imaging. *J Neurosci* 31, 784-791.
- Descoteaux, M., Deriche, R., Knosche, T.R., Anwander, A., 2009. Deterministic and probabilistic tractography based on complex fibre orientation distributions. *IEEE Trans Med Imaging* 28, 269-286.
- Doyle, L.W., Cheong, J.L., Ehrenkranz, R.A., Halliday, H.L., 2017a. Early (< 8 days) systemic postnatal corticosteroids for prevention of bronchopulmonary dysplasia in preterm infants. *Cochrane Database Syst Rev* 10, CD001146.
- Doyle, L.W., Cheong, J.L., Ehrenkranz, R.A., Halliday, H.L., 2017b. Late (> 7 days) systemic postnatal corticosteroids for prevention of bronchopulmonary dysplasia in preterm infants. *Cochrane Database Syst Rev* 10, CD001145.
- Doyle, L.W., Roberts, G., Anderson, P.J., Victorian Infant Collaborative Study, G., 2010. Outcomes at age 2 years of infants < 28 weeks' gestational age born in Victoria in 2005. *J Pediatr* 156, 49-53 e41.
- Drobnjak, I., Zhang, H., Ianus, A., Kaden, E., Alexander, D.C., 2016. PGSE, OGSE, and sensitivity to axon diameter in diffusion MRI: Insight from a simulation study. *Magn Reson Med* 75, 688-700.
- Drobyshevsky, A., Bregman, J., Storey, P., Meyer, J., Prasad, P.V., Derrick, M., MacKendrick, W., Tan, S., 2007. Serial diffusion tensor imaging detects white matter changes that correlate with motor outcome in premature infants. *Dev Neurosci* 29, 289-301.
- Drost, F.J., Keunen, K., Moeskops, P., Claessens, N.H.P., van Kalken, F., Isgum, I., Voskuil-Kerkhof, E.S.M., Groenendaal, F., de Vries, L.S., Benders, M., Termote, J.U.M., 2018. Severe retinopathy of prematurity is associated with reduced cerebellar and brainstem volumes at term and neurodevelopmental deficits at 2 years. *Pediatr Res*.
- Dubois, J., Benders, M., Borradori-Tolsa, C., Cachia, A., Lazeyras, F., Ha-Vinh Leuchter, R., Sizonenko, S.V., Warfield, S.K., Mangin, J.F., Huppi, P.S., 2008a. Primary cortical folding in the human newborn: an early marker of later functional development. *Brain* 131, 2028-2041.
- Dubois, J., Benders, M., Cachia, A., Lazeyras, F., Ha-Vinh Leuchter, R., Sizonenko, S.V., Borradori-Tolsa, C., Mangin, J.F., Huppi, P.S., 2008b. Mapping the early cortical folding process in the preterm newborn brain. *Cereb Cortex* 18, 1444-1454.
- Dubois, J., Benders, M., Lazeyras, F., Borradori-Tolsa, C., Leuchter, R.H., Mangin, J.F., Huppi, P.S., 2010. Structural asymmetries of perisylvian regions in the preterm newborn. *Neuroimage* 52, 32-42.
- Dubois, J., Dehaene-Lambertz, G., Perrin, M., Mangin, J.F., Cointepas, Y., Duchesnay, E., Le Bihan, D., Hertz-Pannier, L., 2008c. Asynchrony of the early maturation of white matter bundles in healthy infants: quantitative landmarks revealed noninvasively by diffusion tensor imaging. *Hum Brain Mapp* 29, 14-27.
- Dubois, J., Hertz-Pannier, L., Cachia, A., Mangin, J.F., Le Bihan, D., Dehaene-Lambertz, G., 2009. Structural asymmetries in the infant language and sensori-motor networks. *Cereb Cortex* 19, 414-423.
- Dubois, J., Hertz-Pannier, L., Dehaene-Lambertz, G., Cointepas, Y., Le Bihan, D., 2006. Assessment of the early organization and maturation of infants' cerebral white matter fiber bundles: a feasibility study using quantitative diffusion tensor imaging and tractography. *Neuroimage* 30, 1121-1132.
- Dudink, J., Lequin, M., van Pul, C., Buijs, J., Conneman, N., van Goudoever, J., Govaert, P., 2007. Fractional anisotropy in white matter tracts of very-low-birth-weight infants. *Pediatr Radiol* 37, 1216-1223.
- Duerden, E.G., Foong, J., Chau, V., Branson, H., Poskitt, K.J., Grunau, R.E., Synnes, A., Zwicker, J.G., Miller, S.P., 2015. Tract-Based Spatial Statistics in Preterm-Born Neonates Predicts Cognitive and Motor Outcomes at 18 Months. *AJNR Am J Neuroradiol* 36, 1565-1571.

- Dusick, A.M., Poindexter, B.B., Ehrenkranz, R.A., Lemons, J.A., 2003. Growth failure in the preterm infant: can we catch up? *Semin Perinatol* 27, 302-310.
- Dyet, L.E., Kennea, N., Counsell, S.J., Maalouf, E.F., Ajayi-Obe, M., Duggan, P.J., Harrison, M., Allsop, J.M., Hajnal, J., Herlihy, A.H., Edwards, B., Laroche, S., Cowan, F.M., Rutherford, M.A., Edwards, A.D., 2006. Natural history of brain lesions in extremely preterm infants studied with serial magnetic resonance imaging from birth and neurodevelopmental assessment. *Pediatrics* 118, 536-548.
- Dyrby, T.B., Sogaard, L.V., Hall, M.G., Ptito, M., Alexander, D.C., 2013. Contrast and stability of the axon diameter index from microstructure imaging with diffusion MRI. *Magn Reson Med* 70, 711-721.
- Eaton-Rosen, Z., Melbourne, A., Orasanu, E., Cardoso, M.J., Modat, M., Bainbridge, A., Kendall, G.S., Robertson, N.J., Marlow, N., Ourselin, S., 2015. Longitudinal measurement of the developing grey matter in preterm subjects using multi-modal MRI. *Neuroimage* 111, 580-589.
- Eaton-Rosen, Z., Scherrer, B., Melbourne, A., Ourselin, S., Neil, J.J., Warfield, S.K., 2017. Investigating the maturation of microstructure and radial orientation in the preterm human cortex with diffusion MRI. *Neuroimage* 162, 65-72.
- Edden, R.A., Jones, D.K., 2011. Spatial and orientational heterogeneity in the statistical sensitivity of skeleton-based analyses of diffusion tensor MR imaging data. *J Neurosci Methods* 201, 213-219.
- Ehrenkranz, R.A., Das, A., Wrage, L.A., Poindexter, B.B., Higgins, R.D., Stoll, B.J., Oh, W., Eunice Kennedy Shriver National Institute of Child, H., Human Development Neonatal Research, N., 2011. Early nutrition mediates the influence of severity of illness on extremely LBW infants. *Pediatr Res* 69, 522-529.
- Ehrenkranz, R.A., Dusick, A.M., Vohr, B.R., Wright, L.L., Wrage, L.A., Poole, W.K., 2006. Growth in the neonatal intensive care unit influences neurodevelopmental and growth outcomes of extremely low birth weight infants. *Pediatrics* 117, 1253-1261.
- Eikenes, L., Lohaugen, G.C., Brubakk, A.M., Skranes, J., Haberg, A.K., 2011. Young adults born preterm with very low birth weight demonstrate widespread white matter alterations on brain DTI. *Neuroimage* 54, 1774-1785.
- Eluvathingal, T.J., Hasan, K.M., Kramer, L., Fletcher, J.M., Ewing-Cobbs, L., 2007. Quantitative diffusion tensor tractography of association and projection fibers in normally developing children and adolescents. *Cereb Cortex* 17, 2760-2768.
- Engelhardt, E., Inder, T.E., Alexopoulos, D., Dierker, D.L., Hill, J., Van Essen, D., Neil, J.J., 2015. Regional impairments of cortical folding in premature infants. *Ann Neurol* 77, 154-162.
- Evarts, E.V., Thach, W.T., 1969. Motor mechanisms of the CNS: cerebocerebellar interrelations. *Annu Rev Physiol* 31, 451-498.
- Ezz-Eldin, Z.M., Hamid, T.A., Youssef, M.R., Nabil Hel, D., 2015. Clinical Risk Index for Babies (CRIB II) Scoring System in Prediction of Mortality in Premature Babies. *J Clin Diagn Res* 9, SC08-11.
- Favrais, G., van de Looij, Y., Fleiss, B., Ramanantsoa, N., Bonnin, P., Stoltenburg-Didinger, G., Lacaud, A., Saliba, E., Dammann, O., Gallego, J., Sizonenko, S., Hagberg, H., Lelievre, V., Gressens, P., 2011. Systemic inflammation disrupts the developmental program of white matter. *Ann Neurol* 70, 550-565.
- Feldman, H.M., Lee, E.S., Yeatman, J.D., Yeom, K.W., 2012. Language and reading skills in school-aged children and adolescents born preterm are associated with white matter properties on diffusion tensor imaging. *Neuropsychologia* 50, 3348-3362.
- Ferizi, U., Schneider, T., Panagiotaki, E., Nedjati-Gilani, G., Zhang, H., Wheeler-Kingshott, C.A., Alexander, D.C., 2014. A ranking of diffusion MRI compartment models with in vivo human brain data. *Magn Reson Med* 72, 1785-1792.
- Forbes, K.P., Pipe, J.G., Bird, C.R., 2002. Changes in brain water diffusion during the 1st year of life. *Radiology* 222, 405-409.
- Forsey, J.T., Elmasry, O.A., Martin, R.P., 2009. Patent arterial duct. *Orphanet J Rare Dis* 4, 17.

- Franz, A.R., Pohlandt, F., Bode, H., Mihatsch, W.A., Sander, S., Kron, M., Steinmacher, J., 2009. Intrauterine, early neonatal, and postdischarge growth and neurodevelopmental outcome at 5.4 years in extremely preterm infants after intensive neonatal nutritional support. *Pediatrics* 123, e101-109.
- Gao, W., Lin, W., Chen, Y., Gerig, G., Smith, J.K., Jewells, V., Gilmore, J.H., 2009. Temporal and spatial development of axonal maturation and myelination of white matter in the developing brain. *AJNR Am J Neuroradiol* 30, 290-296.
- Gaser, C., Nenadic, I., Buchsbaum, B.R., Hazlett, E.A., Buchsbaum, M.S., 2001. Deformation-based morphometry and its relation to conventional volumetry of brain lateral ventricles in MRI. *Neuroimage* 13, 1140-1145.
- Genc, S., Malpas, C.B., Holland, S.K., Beare, R., Silk, T.J., 2017. Neurite density index is sensitive to age related differences in the developing brain. *Neuroimage* 148, 373-380.
- Geng, X., Gouttard, S., Sharma, A., Gu, H., Styner, M., Lin, W., Gerig, G., Gilmore, J.H., 2012. Quantitative tract-based white matter development from birth to age 2years. *Neuroimage* 61, 542-557.
- Geng, X., Gu, H., Shin, W., Ross, T.J., Yang, Y., 2010. Group-wise diffeomorphic diffusion tensor image registration. *Med Image Comput Comput Assist Interv* 13, 598-606.
- Gilmore, J.H., Lin, W., Corouge, I., Vetsa, Y.S., Smith, J.K., Kang, C., Gu, H., Hamer, R.M., Lieberman, J.A., Gerig, G., 2007a. Early postnatal development of corpus callosum and corticospinal white matter assessed with quantitative tractography. *AJNR Am J Neuroradiol* 28, 1789-1795.
- Gilmore, J.H., Lin, W., Prastawa, M.W., Looney, C.B., Vetsa, Y.S., Knickmeyer, R.C., Evans, D.D., Smith, J.K., Hamer, R.M., Lieberman, J.A., Gerig, G., 2007b. Regional gray matter growth, sexual dimorphism, and cerebral asymmetry in the neonatal brain. *J Neurosci* 27, 1255-1260.
- Glass, H.C., Bonifacio, S.L., Chau, V., Glidden, D., Poskitt, K., Barkovich, A.J., Ferriero, D.M., Miller, S.P., 2008. Recurrent postnatal infections are associated with progressive white matter injury in premature infants. *Pediatrics* 122, 299-305.
- Goldenberg, R.L., Culhane, J.F., Iams, J.D., Romero, R., 2008. Epidemiology and causes of preterm birth. *Lancet* 371, 75-84.
- Goldenberg, R.L., Hauth, J.C., Andrews, W.W., 2000. Intrauterine infection and preterm delivery. *N Engl J Med* 342, 1500-1507.
- Goodlett, C.B., Fletcher, P.T., Gilmore, J.H., Gerig, G., 2009. Group analysis of DTI fiber tract statistics with application to neurodevelopment. *Neuroimage* 45, S133-142.
- Goyen, T.A., Lui, K., 2002. Longitudinal motor development of "apparently normal" high-risk infants at 18 months, 3 and 5 years. *Early Hum Dev* 70, 103-115.
- Goyen, T.A., Lui, K., Woods, R., 1998. Visual-motor, visual-perceptual, and fine motor outcomes in very-low-birthweight children at 5 years. *Dev Med Child Neurol* 40, 76-81.
- Graham, E.M., Holcroft, C.J., Rai, K.K., Donohue, P.K., Allen, M.C., 2004. Neonatal cerebral white matter injury in preterm infants is associated with culture positive infections and only rarely with metabolic acidosis. *Am J Obstet Gynecol* 191, 1305-1310.
- Gravett, M.G., Rubens, C.E., Nunes, T.M., Group, G.R., 2010. Global report on preterm birth and stillbirth (2 of 7): discovery science. *BMC Pregnancy Childbirth* 10 Suppl 1, S2.
- Greene, M.M., Patra, K., Silvestri, J.M., Nelson, M.N., 2013. Re-evaluating preterm infants with the Bayley-III: patterns and predictors of change. *Res Dev Disabil* 34, 2107-2117.
- Groenendaal, F., Termote, J.U., van der Heide-Jalving, M., van Haastert, I.C., de Vries, L.S., 2010. Complications affecting preterm neonates from 1991 to 2006: what have we gained? *Acta Paediatr* 99, 354-358.
- Groeschel, S., Tournier, J.D., Northam, G.B., Baldeweg, T., Wyatt, J., Vollmer, B., Connelly, A., 2014. Identification and interpretation of microstructural abnormalities in motor pathways in adolescents born preterm. *Neuroimage* 87, 209-219.
- Groppi, M., Ricci, D., Bassi, L., Merchant, N., Doria, V., Arichi, T., Allsop, J.M., Ramenghi, L., Fox, M.J., Cowan, F.M., Counsell, S.J., Edwards, A.D., 2014. Development of the optic radiations and visual function after premature birth. *Cortex* 56, 30-37.

- Guarini, A., Sansavini, A., Fabbri, C., Alessandrini, R., Faldella, G., Karmiloff-Smith, A., 2009. Reconsidering the impact of preterm birth on language outcome. *Early Hum Dev* 85, 639-645.
- Guevara, P., Poupon, C., Riviere, D., Cointepas, Y., Descoteaux, M., Thirion, B., Mangin, J.F., 2011. Robust clustering of massive tractography datasets. *Neuroimage* 54, 1975-1993.
- Guo, T., Duerden, E.G., Adams, E., Chau, V., Branson, H.M., Chakravarty, M.M., Poskitt, K.J., Synnes, A., Grunau, R.E., Miller, S.P., 2017. Quantitative assessment of white matter injury in preterm neonates: Association with outcomes. *Neurology* 88, 614-622.
- Gupta, A., Poe, M.D., Styner, M.A., Panigrahy, A., Escolar, M.L., 2015. Regional differences in fiber tractography predict neurodevelopmental outcomes in neonates with infantile Krabbe disease. *Neuroimage Clin* 7, 792-798.
- Habas, P.A., Scott, J.A., Roosta, A., Rajagopalan, V., Kim, K., Rousseau, F., Barkovich, A.J., Glenn, O.A., Studholme, C., 2012. Early folding patterns and asymmetries of the normal human brain detected from in utero MRI. *Cereb Cortex* 22, 13-25.
- Hagmann, C.F., De Vita, E., Bainbridge, A., Gunny, R., Kapetanakis, A.B., Chong, W.K., Cady, E.B., Gadian, D.G., Robertson, N.J., 2009. T2 at MR imaging is an objective quantitative measure of cerebral white matter signal intensity abnormality in preterm infants at term-equivalent age. *Radiology* 252, 209-217.
- Hagmann, P., Jonasson, L., Maeder, P., Thiran, J.P., Wedeen, V.J., Meuli, R., 2006. Understanding diffusion MR imaging techniques: from scalar diffusion-weighted imaging to diffusion tensor imaging and beyond. *Radiographics* 26 Suppl 1, S205-223.
- Haines, K.M., Wang, W., Pierson, C.R., 2013. Cerebellar hemorrhagic injury in premature infants occurs during a vulnerable developmental period and is associated with wider neuropathology. *Acta Neuropathol Commun* 1, 69.
- Hajnal, J.V., Doran, M., Hall, A.S., Collins, A.G., Oatridge, A., Pennock, J.M., Young, I.R., Bydder, G.M., 1991. MR imaging of anisotropically restricted diffusion of water in the nervous system: technical, anatomic, and pathologic considerations. *J Comput Assist Tomogr* 15, 1-18.
- Hamrick, S.E., Miller, S.P., Leonard, C., Glidden, D.V., Goldstein, R., Ramaswamy, V., Piecuch, R., Ferriero, D.M., 2004. Trends in severe brain injury and neurodevelopmental outcome in premature newborn infants: the role of cystic periventricular leukomalacia. *J Pediatr* 145, 593-599.
- Hansen, B.M., Hoff, B., Uldall, P., Greisen, G., Kamper, J., Djernes, B., Hertel, J., Christensen, M.F., Andersen, E., Lillquist, K., Verder, H., Peitersen, B., Grytter, C., Agertoft, L., Andersen, E.A., Berg, A., Krag-Olsen, B., Sardeman, H., Jonsbo, F., Jorgensen, N.F., Christensen, N.C., Nielsen, F., Ebbesen, F., Pryds, O., Lange, A., Danish, E.G., 2004. Perinatal risk factors of adverse outcome in very preterm children: a role of initial treatment of respiratory insufficiency? *Acta Paediatr* 93, 185-189.
- Hasegawa, T., Yamada, K., Morimoto, M., Morioka, S., Tozawa, T., Isoda, K., Murakami, A., Chiyonobu, T., Tokuda, S., Nishimura, A., Nishimura, T., Hosoi, H., 2011. Development of corpus callosum in preterm infants is affected by the prematurity: in vivo assessment of diffusion tensor imaging at term-equivalent age. *Pediatr Res* 69, 249-254.
- Hay, W.W., Jr., 2013. Aggressive Nutrition of the Preterm Infant. *Curr Pediatr Rep* 1.
- Haynes, R.L., Folkerth, R.D., Keefe, R.J., Sung, I., Swzeda, L.I., Rosenberg, P.A., Volpe, J.J., Kinney, H.C., 2003. Nitrosative and oxidative injury to premyelinating oligodendrocytes in periventricular leukomalacia. *J Neuropathol Exp Neurol* 62, 441-450.
- Heilman, K.M., Watson, R.T., Bower, D., Valenstein, E., 1983. [Right hemisphere dominance for attention]. *Rev Neurol (Paris)* 139, 15-17.
- Hellstrom, A., Smith, L.E., Dammann, O., 2013. Retinopathy of prematurity. *Lancet* 382, 1445-1457.
- Hendson, L., Russell, L., Robertson, C.M., Liang, Y., Chen, Y., Abdalla, A., Lacaze-Masmonteil, T., 2011. Neonatal and neurodevelopmental outcomes of very low birth weight infants with histologic chorioamnionitis. *J Pediatr* 158, 397-402.
- Herve, P.Y., Leonard, G., Perron, M., Pike, B., Pitiot, A., Richer, L., Veillette, S., Pausova, Z., Paus, T., 2009. Handedness, motor skills and maturation of the corticospinal tract in the adolescent brain. *Hum Brain Mapp* 30, 3151-3162.



- Himpens, E., Van den Broeck, C., Oostra, A., Calders, P., Vanhaesebrouck, P., 2008. Prevalence, type, distribution, and severity of cerebral palsy in relation to gestational age: a meta-analytic review. *Dev Med Child Neurol* 50, 334-340.
- Hintz, S.R., Kendrick, D.E., Stoll, B.J., Vohr, B.R., Fanaroff, A.A., Donovan, E.F., Poole, W.K., Blakely, M.L., Wright, L., Higgins, R., Network, N.N.R., 2005. Neurodevelopmental and growth outcomes of extremely low birth weight infants after necrotizing enterocolitis. *Pediatrics* 115, 696-703.
- Hintz, S.R., Kendrick, D.E., Vohr, B.R., Kenneth Poole, W., Higgins, R.D., NICHD Neonatal Research, N., 2006. Gender differences in neurodevelopmental outcomes among extremely preterm, extremely-low-birthweight infants. *Acta Paediatr* 95, 1239-1248.
- Hornman, J., de Winter, A.F., Kerstjens, J.M., Bos, A.F., Reijneveld, S.A., 2016. Emotional and Behavioral Problems of Preterm and Full-Term Children at School Entry. *Pediatrics* 137.
- Howson, C.P., Kinney, M.V., McDougall, L., Lawn, J.E., Born Too Soon Preterm Birth Action, G., 2013. Born too soon: preterm birth matters. *Reprod Health* 10 Suppl 1, S1.
- Huang, H., Xue, R., Zhang, J., Ren, T., Richards, L.J., Yarowsky, P., Miller, M.I., Mori, S., 2009. Anatomical characterization of human fetal brain development with diffusion tensor magnetic resonance imaging. *J Neurosci* 29, 4263-4273.
- Huang, H., Zhang, J., Wakana, S., Zhang, W., Ren, T., Richards, L.J., Yarowsky, P., Donohue, P., Graham, E., van Zijl, P.C., Mori, S., 2006. White and gray matter development in human fetal, newborn and pediatric brains. *Neuroimage* 33, 27-38.
- Hughes, E.J., CorderoGrande, L., Murgasova, M., Hutter, J., Price, A., Santos Gomes, A., Allsop, J., Steinweg, J., Tusor, N., Wurie, J., BuenoConde, J., Tournier, J.D., Abaei, M., Counsell, S., Rutherford, M., Pietsch, M., Edwards, A.D., Hajnal, J.V., Fitzgibbon, S., Duff, E., Bastiani, M., Andersson, J., Jbabdi, S., Sotiropoulos, S., Jenkinson, M., Smith, S., Harrison, S.I., Griffanti, L., Wright, R., Bozek, J., Beckmann, C., Makropoulos, A., Robinson, E., Schuh, A., Passerat Palmbach, J., Lenz, G., Mortari, F., Tenev, T., Rueckert, D., 2017. The Developing Human Connectome: announcing the first release of open access neonatal brain imaging. 23rd Annual Meeting of the Organization for Human Brain Mapping.
- Hughes, E.J., Winchman, T., Padormo, F., Teixeira, R., Wurie, J., Sharma, M., Fox, M., Hutter, J., Cordero-Grande, L., Price, A.N., Allsop, J., Bueno-Conde, J., Tusor, N., Arichi, T., Edwards, A.D., Rutherford, M.A., Counsell, S.J., Hajnal, J.V., 2016. A dedicated neonatal brain imaging system. *Magn Reson Med*.
- Huppi, P.S., Maier, S.E., Peled, S., Zientara, G.P., Barnes, P.D., Jolesz, F.A., Volpe, J.J., 1998a. Microstructural development of human newborn cerebral white matter assessed in vivo by diffusion tensor magnetic resonance imaging. *Pediatr Res* 44, 584-590.
- Huppi, P.S., Murphy, B., Maier, S.E., Zientara, G.P., Inder, T.E., Barnes, P.D., Kikinis, R., Jolesz, F.A., Volpe, J.J., 2001. Microstructural brain development after perinatal cerebral white matter injury assessed by diffusion tensor magnetic resonance imaging. *Pediatrics* 107, 455-460.
- Huppi, P.S., Warfield, S., Kikinis, R., Barnes, P.D., Zientara, G.P., Jolesz, F.A., Tsuji, M.K., Volpe, J.J., 1998b. Quantitative magnetic resonance imaging of brain development in premature and mature newborns. *Ann Neurol* 43, 224-235.
- Hutter, J., Tournier, J.D., Price, A.N., Cordero-Grande, L., Hughes, E.J., Malik, S., Steinweg, J., Bastiani, M., Sotiropoulos, S.N., Jbabdi, S., Andersson, J., Edwards, A.D., Hajnal, J.V., 2017. Time-efficient and flexible design of optimized multishell HARDI diffusion. *Magn Reson Med*.
- Hyodo, R., Sato, Y., Ito, M., Sugiyama, Y., Ogawa, C., Kawai, H., Nakane, T., Saito, A., Hirakawa, A., Kidokoro, H., Natsume, J., Hayakawa, M., 2017. Magnetic resonance spectroscopy in preterm infants: association with neurodevelopmental outcomes. *Arch Dis Child Fetal Neonatal Ed*.
- Inder, T.E., Huppi, P.S., Warfield, S., Kikinis, R., Zientara, G.P., Barnes, P.D., Jolesz, F., Volpe, J.J., 1999. Periventricular white matter injury in the premature infant is followed by reduced cerebral cortical gray matter volume at term. *Ann Neurol* 46, 755-760.
- Inder, T.E., Warfield, S.K., Wang, H., Huppi, P.S., Volpe, J.J., 2005. Abnormal cerebral structure is present at term in premature infants. *Pediatrics* 115, 286-294.

- Inder, T.E., Wells, S.J., Mogridge, N.B., Spencer, C., Volpe, J.J., 2003. Defining the nature of the cerebral abnormalities in the premature infant: a qualitative magnetic resonance imaging study. *J Pediatr* 143, 171-179.
- Innocenti, G.M., Price, D.J., 2005. Exuberance in the development of cortical networks. *Nat Rev Neurosci* 6, 955-965.
- Jacobsson, B., Hagberg, G., Hagberg, B., Ladfors, L., Niklasson, A., Hagberg, H., 2002. Cerebral palsy in preterm infants: a population-based case-control study of antenatal and intrapartum risk factors. *Acta Paediatr* 91, 946-951.
- Janz-Robinson, E.M., Badawi, N., Walker, K., Bajuk, B., Abdel-Latif, M.E., Neonatal Intensive Care Units, N., 2015. Neurodevelopmental Outcomes of Premature Infants Treated for Patent Ductus Arteriosus: A Population-Based Cohort Study. *J Pediatr* 167, 1025-1032 e1023.
- Jary, S., De Carli, A., Ramenghi, L.A., Whitelaw, A., 2012. Impaired brain growth and neurodevelopment in preterm infants with posthaemorrhagic ventricular dilatation. *Acta Paediatr* 101, 743-748.
- Jenkinson, M., Beckmann, C.F., Behrens, T.E., Woolrich, M.W., Smith, S.M., 2012. *Fsl*. *Neuroimage* 62, 782-790.
- Jeurissen, B., Leemans, A., Tournier, J.D., Jones, D.K., Sijbers, J., 2013. Investigating the prevalence of complex fiber configurations in white matter tissue with diffusion magnetic resonance imaging. *Hum Brain Mapp* 34, 2747-2766.
- Jeurissen, B., Tournier, J.D., Dhollander, T., Connelly, A., Sijbers, J., 2014. Multi-tissue constrained spherical deconvolution for improved analysis of multi-shell diffusion MRI data. *Neuroimage* 103, 411-426.
- Jha, S.C., Meltzer-Brody, S., Steiner, R.J., Cornea, E., Woolson, S., Ahn, M., Verde, A.R., Hamer, R.M., Zhu, H., Styner, M., Gilmore, J.H., Knickmeyer, R.C., 2016. Antenatal depression, treatment with selective serotonin reuptake inhibitors, and neonatal brain structure: A propensity-matched cohort study. *Psychiatry Res* 253, 43-53.
- Johnson, R.T., Yeatman, J.D., Wandell, B.A., Buonocore, M.H., Amaral, D.G., Nordahl, C.W., 2014. Diffusion properties of major white matter tracts in young, typically developing children. *Neuroimage* 88, 143-154.
- Jones, D.K., 2003. Determining and visualizing uncertainty in estimates of fiber orientation from diffusion tensor MRI. *Magn Reson Med* 49, 7-12.
- Jones, D.K., 2008. Tractography gone wild: probabilistic fibre tracking using the wild bootstrap with diffusion tensor MRI. *IEEE Trans Med Imaging* 27, 1268-1274.
- Jones, D.K., Simmons, A., Williams, S.C., Horsfield, M.A., 1999. Non-invasive assessment of axonal fiber connectivity in the human brain via diffusion tensor MRI. *Magn Reson Med* 42, 37-41.
- Joseph, R.M., O'Shea, T.M., Allred, E.N., Heeren, T., Hirtz, D., Jara, H., Leviton, A., Kuban, K.C., Investigators, E.S., 2016. Neurocognitive and Academic Outcomes at Age 10 Years of Extremely Preterm Newborns. *Pediatrics* 137.
- Judas, M., Rados, M., Jovanov-Milosevic, N., Hrabac, P., Stern-Padovan, R., Kostovic, I., 2005. Structural, immunocytochemical, and mr imaging properties of periventricular crossroads of growing cortical pathways in preterm infants. *AJNR Am J Neuroradiol* 26, 2671-2684.
- Kaden, E., Kelm, N.D., Carson, R.P., Does, M.D., Alexander, D.C., 2016a. Multi-compartment microscopic diffusion imaging. *Neuroimage* 139, 346-359.
- Kaden, E., Kruggel, F., Alexander, D.C., 2016b. Quantitative mapping of the per-axon diffusion coefficients in brain white matter. *Magn Reson Med* 75, 1752-1763.
- Kady, S.M., Gardosi, J., 2004. Perinatal mortality and fetal growth restriction. *Best Pract Res Clin Obstet Gynaecol* 18, 397-410.
- Kapellou, O., Counsell, S.J., Kennea, N., Dyet, L., Saeed, N., Stark, J., Maalouf, E., Duggan, P., Ajayi-Obe, M., Hajnal, J., Allsop, J.M., Boardman, J., Rutherford, M.A., Cowan, F., Edwards, A.D., 2006. Abnormal cortical development after premature birth shown by altered allometric scaling of brain growth. *PLoS Med* 3, e265.

- Kaukola, T., Herva, R., Perhomaa, M., Paakko, E., Kingsmore, S., Vainionpaa, L., Hallman, M., 2006. Population cohort associating chorioamnionitis, cord inflammatory cytokines and neurologic outcome in very preterm, extremely low birth weight infants. *Pediatr Res* 59, 478-483.
- Keihaninejad, S., Ryan, N.S., Malone, I.B., Modat, M., Cash, D., Ridgway, G.R., Zhang, H., Fox, N.C., Ourselin, S., 2012. The importance of group-wise registration in tract based spatial statistics study of neurodegeneration: a simulation study in Alzheimer's disease. *PLoS One* 7, e45996.
- Keihaninejad, S., Zhang, H., Ryan, N.S., Malone, I.B., Modat, M., Cardoso, M.J., Cash, D.M., Fox, N.C., Ourselin, S., 2013. An unbiased longitudinal analysis framework for tracking white matter changes using diffusion tensor imaging with application to Alzheimer's disease. *Neuroimage* 72, 153-163.
- Kelly, C., Pietsch, M., Counsell, S.J., Tournier, J.D., 2017. Transfer learning and convolutional neural net fusion for motion artefact detection. 25th Annual Meeting of the International Society of Magnetic Resonance in Medicine, Honolulu, HI, USA.
- Kelly, C.E., Thompson, D.K., Chen, J., Leemans, A., Adamson, C.L., Inder, T.E., Cheong, J.L., Doyle, L.W., Anderson, P.J., 2016. Axon density and axon orientation dispersion in children born preterm. *Hum Brain Mapp* 37, 3080-3102.
- Kendall, G.S., Melbourne, A., Johnson, S., Price, D., Bainbridge, A., Gunny, R., Huertas-Ceballos, A., Cady, E.B., Ourselin, S., Marlow, N., Robertson, N.J., 2014. White matter NAA/Cho and Cho/Cr ratios at MR spectroscopy are predictive of motor outcome in preterm infants. *Radiology* 271, 230-238.
- Kersbergen, K.J., Benders, M.J., Groenendaal, F., Koopman-Esseboom, C., Nievelstein, R.A., van Haastert, I.C., de Vries, L.S., 2014a. Different patterns of punctate white matter lesions in serially scanned preterm infants. *PLoS One* 9, e108904.
- Kersbergen, K.J., de Vries, L.S., Groenendaal, F., van Haastert, I.C., Chew, A.T., Makropoulos, A., Dawson, S.L., Cowan, F.M., Benders, M.J., Counsell, S.J., 2015. Corticospinal Tract Injury Precedes Thalamic Volume Reduction in Preterm Infants with Cystic Periventricular Leukomalacia. *J Pediatr* 167, 260-268 e263.
- Kersbergen, K.J., Leemans, A., Groenendaal, F., van der Aa, N.E., Viergever, M.A., de Vries, L.S., Benders, M.J., 2014b. Microstructural brain development between 30 and 40 weeks corrected age in a longitudinal cohort of extremely preterm infants. *Neuroimage* 103, 214-224.
- Kesler, S.R., Ment, L.R., Vohr, B., Pajot, S.K., Schneider, K.C., Katz, K.H., Ebbitt, T.B., Duncan, C.C., Makuch, R.W., Reiss, A.L., 2004. Volumetric analysis of regional cerebral development in preterm children. *Pediatr Neurol* 31, 318-325.
- Khwaja, O., Volpe, J.J., 2008. Pathogenesis of cerebral white matter injury of prematurity. *Arch Dis Child Fetal Neonatal Ed* 93, F153-161.
- Kidokoro, H., Neil, J.J., Inder, T.E., 2013. New MR imaging assessment tool to define brain abnormalities in very preterm infants at term. *AJNR Am J Neuroradiol* 34, 2208-2214.
- Kinney, H.C., Brody, B.A., Kloman, A.S., Gilles, F.H., 1988. Sequence of central nervous system myelination in human infancy. II. Patterns of myelination in autopsied infants. *J Neuropathol Exp Neurol* 47, 217-234.
- Klebermass-Schrehof, K., Czaba, C., Olischar, M., Fuiko, R., Waldhoer, T., Rona, Z., Pollak, A., Weninger, M., 2012. Impact of low-grade intraventricular hemorrhage on long-term neurodevelopmental outcome in preterm infants. *Childs Nerv Syst* 28, 2085-2092.
- Klein, A., Andersson, J., Ardekani, B.A., Ashburner, J., Avants, B., Chiang, M.C., Christensen, G.E., Collins, D.L., Gee, J., Hellier, P., Song, J.H., Jenkinson, M., Lepage, C., Rueckert, D., Thompson, P., Vercauteren, T., Woods, R.P., Mann, J.J., Parsey, R.V., 2009. Evaluation of 14 nonlinear deformation algorithms applied to human brain MRI registration. *Neuroimage* 46, 786-802.
- Klevebro, S., Lundgren, P., Hammar, U., Smith, L.E., Bottai, M., Domellof, M., Lofqvist, C., Hallberg, B., Hellstrom, A., 2016. Cohort study of growth patterns by gestational age in preterm infants developing morbidity. *BMJ Open* 6, e012872.
- Knecht, S., Drager, B., Deppe, M., Bobe, L., Lohmann, H., Floel, A., Ringelstein, E.B., Henningsen, H., 2000. Handedness and hemispheric language dominance in healthy humans. *Brain* 123 Pt 12, 2512-2518.

- Knickmeyer, R.C., Gouttard, S., Kang, C., Evans, D., Wilber, K., Smith, J.K., Hamer, R.M., Lin, W., Gerig, G., Gilmore, J.H., 2008. A structural MRI study of human brain development from birth to 2 years. *J Neurosci* 28, 12176-12182.
- Knight, M.J., Smith-Collins, A., Newell, S., Denbow, M., Kauppinen, R.A., 2018. Cerebral White Matter Maturation Patterns in Preterm Infants: An MRI T2 Relaxation Anisotropy and Diffusion Tensor Imaging Study. *J Neuroimaging* 28, 86-94.
- Kobaly, K., Schluchter, M., Minich, N., Friedman, H., Taylor, H.G., Wilson-Costello, D., Hack, M., 2008. Outcomes of extremely low birth weight (<1 kg) and extremely low gestational age (<28 weeks) infants with bronchopulmonary dysplasia: effects of practice changes in 2000 to 2003. *Pediatrics* 121, 73-81.
- Kostovic, I., Jovanov-Milosevic, N., 2006. The development of cerebral connections during the first 20-45 weeks' gestation. *Semin Fetal Neonatal Med* 11, 415-422.
- Kostovic, I., Jovanov-Milosevic, N., Rados, M., Sedmak, G., Benjak, V., Kostovic-Srzentic, M., Vasung, L., Culjat, M., Rados, M., Huppi, P., Judas, M., 2014a. Perinatal and early postnatal reorganization of the subplate and related cellular compartments in the human cerebral wall as revealed by histological and MRI approaches. *Brain Struct Funct* 219, 231-253.
- Kostovic, I., Judas, M., 2006. Prolonged coexistence of transient and permanent circuitry elements in the developing cerebral cortex of fetuses and preterm infants. *Dev Med Child Neurol* 48, 388-393.
- Kostovic, I., Judas, M., 2010. The development of the subplate and thalamocortical connections in the human foetal brain. *Acta Paediatr* 99, 1119-1127.
- Kostovic, I., Judas, M., Rados, M., Hrabac, P., 2002. Laminar organization of the human fetal cerebrum revealed by histochemical markers and magnetic resonance imaging. *Cereb Cortex* 12, 536-544.
- Kostovic, I., Kostovic-Srzentic, M., Benjak, V., Jovanov-Milosevic, N., Rados, M., 2014b. Developmental dynamics of radial vulnerability in the cerebral compartments in preterm infants and neonates. *Front Neurol* 5, 139.
- Krishnan, M.L., Dyet, L.E., Boardman, J.P., Kapellou, O., Allsop, J.M., Cowan, F., Edwards, A.D., Rutherford, M.A., Counsell, S.J., 2007. Relationship between white matter apparent diffusion coefficients in preterm infants at term-equivalent age and developmental outcome at 2 years. *Pediatrics* 120, e604-609.
- Kuklisova-Murgasova, M., Aljabar, P., Srinivasan, L., Counsell, S.J., Doria, V., Serag, A., Gousias, I.S., Boardman, J.P., Rutherford, M.A., Edwards, A.D., Hajnal, J.V., Rueckert, D., 2011. A dynamic 4D probabilistic atlas of the developing brain. *Neuroimage* 54, 2750-2763.
- Kulikova, S., Hertz-Pannier, L., Dehaene-Lambertz, G., Buzmakov, A., Poupon, C., Dubois, J., 2015. Multi-parametric evaluation of the white matter maturation. *Brain Struct Funct* 220, 3657-3672.
- Kunz, N., Zhang, H., Vasung, L., O'Brien, K.R., Assaf, Y., Lazeyras, F., Alexander, D.C., Huppi, P.S., 2014. Assessing white matter microstructure of the newborn with multi-shell diffusion MRI and biophysical compartment models. *Neuroimage* 96, 288-299.
- Lahra, M.M., Beeby, P.J., Jeffery, H.E., 2009a. Intrauterine inflammation, neonatal sepsis, and chronic lung disease: a 13-year hospital cohort study. *Pediatrics* 123, 1314-1319.
- Lahra, M.M., Beeby, P.J., Jeffery, H.E., 2009b. Maternal versus fetal inflammation and respiratory distress syndrome: a 10-year hospital cohort study. *Arch Dis Child Fetal Neonatal Ed* 94, F13-16.
- Lahra, M.M., Jeffery, H.E., 2004. A fetal response to chorioamnionitis is associated with early survival after preterm birth. *Am J Obstet Gynecol* 190, 147-151.
- Lampinen, B., Szczepankiewicz, F., Martensson, J., van Westen, D., Sundgren, P.C., Nilsson, M., 2017. Neurite density imaging versus imaging of microscopic anisotropy in diffusion MRI: A model comparison using spherical tensor encoding. *Neuroimage* 147, 517-531.
- Larroque, B., Ancel, P.Y., Marret, S., Marchand, L., Andre, M., Arnaud, C., Pierrat, V., Roze, J.C., Messer, J., Thiriez, G., Burguet, A., Picaud, J.C., Breart, G., Kaminski, M., group, E.S., 2008. Neurodevelopmental disabilities and special care of 5-year-old children born before 33 weeks of gestation (the EPIPAGE study): a longitudinal cohort study. *Lancet* 371, 813-820.

- Larroque, B., Marret, S., Ancel, P.Y., Arnaud, C., Marpeau, L., Supernant, K., Pierrat, V., Roze, J.C., Matis, J., Cambonie, G., Burguet, A., Andre, M., Kaminski, M., Breart, G., Group, E.S., 2003. White matter damage and intraventricular hemorrhage in very preterm infants: the EPIPAGE study. *J Pediatr* 143, 477-483.
- Laule, C., Kozlowski, P., Leung, E., Li, D.K., Mackay, A.L., Moore, G.R., 2008. Myelin water imaging of multiple sclerosis at 7 T: correlations with histopathology. *Neuroimage* 40, 1575-1580.
- Laule, C., Leung, E., Li, D.K., Traboulsee, A.L., Paty, D.W., MacKay, A.L., Moore, G.R., 2006. Myelin water imaging in multiple sclerosis: quantitative correlations with histopathology. *Mult Scler* 12, 747-753.
- Lauterbur, P.C., 1973. Image formation by induced local interactions. Examples employing nuclear magnetic resonance. 1973. *Clin Orthop Relat Res*, 3-6.
- Lebel, C., Beaulieu, C., 2009. Lateralization of the arcuate fasciculus from childhood to adulthood and its relation to cognitive abilities in children. *Hum Brain Mapp* 30, 3563-3573.
- Lebel, C., Walker, L., Leemans, A., Phillips, L., Beaulieu, C., 2008. Microstructural maturation of the human brain from childhood to adulthood. *Neuroimage* 40, 1044-1055.
- Lee, I., Neil, J.J., Huettner, P.C., Smyser, C.D., Rogers, C.E., Shimony, J.S., Kidokoro, H., Mysorekar, I.U., Inder, T.E., 2014. The impact of prenatal and neonatal infection on neurodevelopmental outcomes in very preterm infants. *J Perinatol* 34, 741-747.
- Lee, J.D., Park, H.J., Park, E.S., Oh, M.K., Park, B., Rha, D.W., Cho, S.R., Kim, E.Y., Park, J.Y., Kim, C.H., Kim, D.G., Park, C.I., 2011. Motor pathway injury in patients with periventricular leucomalacia and spastic diplegia. *Brain* 134, 1199-1210.
- Lee, S.J., Steiner, R.J., Luo, S., Neale, M.C., Styner, M., Zhu, H., Gilmore, J.H., 2015. Quantitative tract-based white matter heritability in twin neonates. *Neuroimage* 111, 123-135.
- Lefebvre, F., Mazurier, E., Tessier, R., 2005. Cognitive and educational outcomes in early adulthood for infants weighing 1000 grams or less at birth. *Acta Paediatr* 94, 733-740.
- Leijser, L.M., de Bruine, F.T., Steggerda, S.J., van der Grond, J., Walther, F.J., van Wezel-Meijler, G., 2009. Brain imaging findings in very preterm infants throughout the neonatal period: part I. Incidences and evolution of lesions, comparison between ultrasound and MRI. *Early Hum Dev* 85, 101-109.
- Lemmers, P.M., Benders, M.J., D'Ascenzo, R., Zethof, J., Alderliesten, T., Kersbergen, K.J., Isgum, I., de Vries, L.S., Groenendaal, F., van Bel, F., 2016. Patent Ductus Arteriosus and Brain Volume. *Pediatrics* 137.
- Leow, A.D., Klunder, A.D., Jack, C.R., Jr., Toga, A.W., Dale, A.M., Bernstein, M.A., Britson, P.J., Gunter, J.L., Ward, C.P., Whitwell, J.L., Borowski, B.J., Fleisher, A.S., Fox, N.C., Harvey, D., Kornak, J., Schuff, N., Studholme, C., Alexander, G.E., Weiner, M.W., Thompson, P.M., Study, A.P.P., 2006. Longitudinal stability of MRI for mapping brain change using tensor-based morphometry. *Neuroimage* 31, 627-640.
- Leroy, F., Cai, Q., Bogart, S.L., Dubois, J., Coulon, O., Monzalvo, K., Fischer, C., Glasel, H., Van der Haegen, L., Benezit, A., Lin, C.P., Kennedy, D.N., Ihara, A.S., Hertz-Pannier, L., Moutard, M.L., Poupon, C., Brysbaert, M., Roberts, N., Hopkins, W.D., Mangin, J.F., Dehaene-Lambertz, G., 2015. New human-specific brain landmark: the depth asymmetry of superior temporal sulcus. *Proc Natl Acad Sci U S A* 112, 1208-1213.
- Levitsky, D.A., Strupp, B.J., 1995. Malnutrition and the brain: changing concepts, changing concerns. *J Nutr* 125, 2212S-2220S.
- Li, X., Gao, J., Wang, M., Zheng, J., Li, Y., Hui, E.S., Wan, M., Yang, J., 2017. Characterization of Extensive Microstructural Variations Associated with Punctate White Matter Lesions in Preterm Neonates. *AJNR Am J Neuroradiol* 38, 1228-1234.
- Limperopoulos, C., Bassan, H., Gauvreau, K., Robertson, R.L., Jr., Sullivan, N.R., Benson, C.B., Avery, L., Stewart, J., Soul, J.S., Ringer, S.A., Volpe, J.J., duPlessis, A.J., 2007. Does cerebellar injury in premature infants contribute to the high prevalence of long-term cognitive, learning, and behavioral disability in survivors? *Pediatrics* 120, 584-593.
- Limperopoulos, C., Chilingaryan, G., Guizard, N., Robertson, R.L., Du Plessis, A.J., 2010. Cerebellar injury in the premature infant is associated with impaired growth of specific cerebral regions. *Pediatr Res* 68, 145-150.

- Limperopoulos, C., Soul, J.S., Gauvreau, K., Huppi, P.S., Warfield, S.K., Bassan, H., Robertson, R.L., Volpe, J.J., du Plessis, A.J., 2005. Late gestation cerebellar growth is rapid and impeded by premature birth. *Pediatrics* 115, 688-695.
- Lin, P.W., Stoll, B.J., 2006. Necrotising enterocolitis. *Lancet* 368, 1271-1283.
- Lin, Y., Okumura, A., Hayakawa, F., Kato, K., Kuno, T., Watanabe, K., 2001. Quantitative evaluation of thalami and basal ganglia in infants with periventricular leukomalacia. *Dev Med Child Neurol* 43, 481-485.
- Lind, A., Parkkola, R., Lehtonen, L., Munck, P., Maunu, J., Lapinleimu, H., Haataja, L., Group, P.S., 2011. Associations between regional brain volumes at term-equivalent age and development at 2 years of age in preterm children. *Pediatr Radiol* 41, 953-961.
- Lindstrom, K., Winblad, B., Haglund, B., Hjern, A., 2007. Preterm infants as young adults: a Swedish national cohort study. *Pediatrics* 120, 70-77.
- Liu, H., Stuffelbeam, S.M., Sepulcre, J., Hedden, T., Buckner, R.L., 2009. Evidence from intrinsic activity that asymmetry of the human brain is controlled by multiple factors. *Proc Natl Acad Sci U S A* 106, 20499-20503.
- Liu, Y., Aeby, A., Baleriaux, D., David, P., Absil, J., De Maertelaer, V., Van Bogaert, P., Avni, F., Metens, T., 2012. White matter abnormalities are related to microstructural changes in preterm neonates at term-equivalent age: a diffusion tensor imaging and probabilistic tractography study. *AJNR Am J Neuroradiol* 33, 839-845.
- Liu, Y., Baleriaux, D., Kavec, M., Metens, T., Absil, J., Denolin, V., Pardou, A., Avni, F., Van Bogaert, P., Aeby, A., 2010. Structural asymmetries in motor and language networks in a population of healthy preterm neonates at term equivalent age: a diffusion tensor imaging and probabilistic tractography study. *Neuroimage* 51, 783-788.
- Lodha, A., Sauve, R., Bhandari, V., Tang, S., Christianson, H., Bhandari, A., Amin, H., Singhal, N., 2014. Need for supplemental oxygen at discharge in infants with bronchopulmonary dysplasia is not associated with worse neurodevelopmental outcomes at 3 years corrected age. *PLoS One* 9, e90843.
- Lodygensky, G.A., Rademaker, K., Zimine, S., Gex-Fabry, M., Lieftink, A.F., Lazeyras, F., Groenendaal, F., de Vries, L.S., Huppi, P.S., 2005. Structural and functional brain development after hydrocortisone treatment for neonatal chronic lung disease. *Pediatrics* 116, 1-7.
- Longo, S., Bollani, L., Decembrino, L., Di Comite, A., Angelini, M., Stronati, M., 2013. Short-term and long-term sequelae in intrauterine growth retardation (IUGR). *J Matern Fetal Neonatal Med* 26, 222-225.
- Luu, T.M., Vohr, B.R., Allan, W., Schneider, K.C., Ment, L.R., 2011. Evidence for catch-up in cognition and receptive vocabulary among adolescents born very preterm. *Pediatrics* 128, 313-322.
- Maas, L.C., Mukherjee, P., Carballido-Gamio, J., Veeraraghavan, S., Miller, S.P., Partridge, S.C., Henry, R.G., Barkovich, A.J., Vigneron, D.B., 2004. Early laminar organization of the human cerebrum demonstrated with diffusion tensor imaging in extremely premature infants. *Neuroimage* 22, 1134-1140.
- Madan, J.C., Kendrick, D., Hagadorn, J.I., Frantz, I.D., 3rd, National Institute of Child, H., Human Development Neonatal Research, N., 2009. Patent ductus arteriosus therapy: impact on neonatal and 18-month outcome. *Pediatrics* 123, 674-681.
- Mah, A., Geeraert, B., Lebel, C., 2017. Detailing neuroanatomical development in late childhood and early adolescence using NODDI. *PLoS One* 12, e0182340.
- Makropoulos, A., Aljabar, P., Wright, R., Huning, B., Merchant, N., Arichi, T., Tusor, N., Hajnal, J.V., Edwards, A.D., Counsell, S.J., Rueckert, D., 2016. Regional growth and atlasing of the developing human brain. *Neuroimage* 125, 456-478.
- Makropoulos, A., Gousias, I.S., Ledig, C., Aljabar, P., Serag, A., Hajnal, J.V., Edwards, A.D., Counsell, S.J., Rueckert, D., 2014. Automatic whole brain MRI segmentation of the developing neonatal brain. *IEEE Trans Med Imaging* 33, 1818-1831.
- Mangham, L.J., Petrou, S., Doyle, L.W., Draper, E.S., Marlow, N., 2009. The cost of preterm birth throughout childhood in England and Wales. *Pediatrics* 123, e312-327.

- Marlow, N., Hennessy, E.M., Bracewell, M.A., Wolke, D., Group, E.P.S., 2007. Motor and executive function at 6 years of age after extremely preterm birth. *Pediatrics* 120, 793-804.
- Marlow, N., Rose, A.S., Rands, C.E., Draper, E.S., 2005a. Neuropsychological and educational problems at school age associated with neonatal encephalopathy. *Arch Dis Child Fetal Neonatal Ed* 90, F380-387.
- Marlow, N., Wolke, D., Bracewell, M.A., Samara, M., Group, E.P.S., 2005b. Neurologic and developmental disability at six years of age after extremely preterm birth. *N Engl J Med* 352, 9-19.
- McArdle, C.B., Richardson, C.J., Nicholas, D.A., Mirfakhraee, M., Hayden, C.K., Amparo, E.G., 1987. Developmental features of the neonatal brain: MR imaging. Part I. Gray-white matter differentiation and myelination. *Radiology* 162, 223-229.
- Melbourne, A., Eaton-Rosen, Z., Orasanu, E., Price, D., Bainbridge, A., Cardoso, M.J., Kendall, G.S., Robertson, N.J., Marlow, N., Ourselin, S., 2016. Longitudinal development in the preterm thalamus and posterior white matter: MRI correlations between diffusion weighted imaging and T2 relaxometry. *Hum Brain Mapp* 37, 2479-2492.
- Menon, R., 2008. Spontaneous preterm birth, a clinical dilemma: etiologic, pathophysiologic and genetic heterogeneities and racial disparity. *Acta Obstet Gynecol Scand* 87, 590-600.
- Merhar, S.L., Ramos, Y., Meinzen-Derr, J., Kline-Fath, B.M., 2014. Brain magnetic resonance imaging in infants with surgical necrotizing enterocolitis or spontaneous intestinal perforation versus medical necrotizing enterocolitis. *J Pediatr* 164, 410-412 e411.
- Messerschmidt, A., Fuiko, R., Prayer, D., Brugger, P.C., Boltshauser, E., Zoder, G., Sterniste, W., Weber, M., Birnbacher, R., 2008. Disrupted cerebellar development in preterm infants is associated with impaired neurodevelopmental outcome. *Eur J Pediatr* 167, 1141-1147.
- Milgrom, J., Newnham, C., Anderson, P.J., Doyle, L.W., Gemmill, A.W., Lee, K., Hunt, R.W., Bear, M., Inder, T., 2010. Early sensitivity training for parents of preterm infants: impact on the developing brain. *Pediatr Res* 67, 330-335.
- Miller, S.P., Cozzio, C.C., Goldstein, R.B., Ferriero, D.M., Partridge, J.C., Vigneron, D.B., Barkovich, A.J., 2003. Comparing the diagnosis of white matter injury in premature newborns with serial MR imaging and transfontanel ultrasonography findings. *AJNR Am J Neuroradiol* 24, 1661-1669.
- Miller, S.P., Ferriero, D.M., Leonard, C., Piecuch, R., Glidden, D.V., Partridge, J.C., Perez, M., Mukherjee, P., Vigneron, D.B., Barkovich, A.J., 2005. Early brain injury in premature newborns detected with magnetic resonance imaging is associated with adverse early neurodevelopmental outcome. *J Pediatr* 147, 609-616.
- Miller, S.P., Vigneron, D.B., Henry, R.G., Bohland, M.A., Ceppi-Cozzio, C., Hoffman, C., Newton, N., Partridge, J.C., Ferriero, D.M., Barkovich, A.J., 2002. Serial quantitative diffusion tensor MRI of the premature brain: development in newborns with and without injury. *J Magn Reson Imaging* 16, 621-632.
- Moffett, J.R., Ross, B., Arun, P., Madhavarao, C.N., Namboodiri, A.M., 2007. N-Acetylaspartate in the CNS: from neurodiagnostics to neurobiology. *Prog Neurobiol* 81, 89-131.
- Moore, T., Hennessy, E.M., Myles, J., Johnson, S.J., Draper, E.S., Costeloe, K.L., Marlow, N., 2012. Neurological and developmental outcome in extremely preterm children born in England in 1995 and 2006: the EPICure studies. *BMJ* 345, e7961.
- Morgan, C., 2013. Early amino acid administration in very preterm infants: Too little, too late or too much, too soon? *Semin Fetal Neonatal Med*.
- Mori, S., Crain, B.J., Chacko, V.P., van Zijl, P.C., 1999. Three-dimensional tracking of axonal projections in the brain by magnetic resonance imaging. *Ann Neurol* 45, 265-269.
- Mori, S., van Zijl, P.C., 2002. Fiber tracking: principles and strategies - a technical review. *NMR Biomed* 15, 468-480.
- Morita, T., Morimoto, M., Yamada, K., Hasegawa, T., Morioka, S., Kidowaki, S., Moroto, M., Yamashita, S., Maeda, H., Chiyonobu, T., Tokuda, S., Hosoi, H., 2015. Low-grade intraventricular hemorrhage disrupts cerebellar white matter in preterm infants: evidence from diffusion tensor imaging. *Neuroradiology* 57, 507-514.

Moseley, M.E., Cohen, Y., Kucharczyk, J., Mintorovitch, J., Asgari, H.S., Wendland, M.F., Tsuruda, J., Norman, D., 1990. Diffusion-weighted MR imaging of anisotropic water diffusion in cat central nervous system. *Radiology* 176, 439-445.

Muglia, L.J., Katz, M., 2010. The enigma of spontaneous preterm birth. *N Engl J Med* 362, 529-535.

Mukherjee, P., Miller, J.H., Shimony, J.S., Philip, J.V., Nehra, D., Snyder, A.Z., Conturo, T.E., Neil, J.J., McKinstry, R.C., 2002. Diffusion-tensor MR imaging of gray and white matter development during normal human brain maturation. *AJNR Am J Neuroradiol* 23, 1445-1456.

Murakami, A., Morimoto, M., Yamada, K., Kizu, O., Nishimura, A., Nishimura, T., Sugimoto, T., 2008. Fiber-tracking techniques can predict the degree of neurologic impairment for periventricular leukomalacia. *Pediatrics* 122, 500-506.

Murphy, B.P., Inder, T.E., Rooks, V., Taylor, G.A., Anderson, N.J., Mogridge, N., Horwood, L.J., Volpe, J.J., 2002. Posthaemorrhagic ventricular dilatation in the premature infant: natural history and predictors of outcome. *Arch Dis Child Fetal Neonatal Ed* 87, F37-41.

Murray, A.L., Thompson, D.K., Pascoe, L., Leemans, A., Inder, T.E., Doyle, L.W., Anderson, J.F., Anderson, P.J., 2016. White matter abnormalities and impaired attention abilities in children born very preterm. *Neuroimage* 124, 75-84.

Murray, C.J., Vos, T., Lozano, R., Naghavi, M., Flaxman, A.D., Michaud, C., Ezzati, M., Shibuya, K., Salomon, J.A., Abdalla, S., Aboyans, V., Abraham, J., Ackerman, I., Aggarwal, R., Ahn, S.Y., Ali, M.K., Alvarado, M., Anderson, H.R., Anderson, L.M., Andrews, K.G., Atkinson, C., Baddour, L.M., Bahalim, A.N., Barker-Collo, S., Barrero, L.H., Bartels, D.H., Basanez, M.G., Baxter, A., Bell, M.L., Benjamin, E.J., Bennett, D., Bernabe, E., Bhalla, K., Bhandari, B., Bikbov, B., Bin Abdulhak, A., Birbeck, G., Black, J.A., Blencowe, H., Blore, J.D., Blyth, F., Bolliger, I., Bonaventure, A., Boufous, S., Bourne, R., Boussinesq, M., Braithwaite, T., Brayne, C., Bridgett, L., Brooker, S., Brooks, P., Brugha, T.S., Bryan-Hancock, C., Bucello, C., Buchbinder, R., Buckle, G., Budke, C.M., Burch, M., Burney, P., Burstein, R., Calabria, B., Campbell, B., Canter, C.E., Carabin, H., Carapetis, J., Carmona, L., Cella, C., Charlson, F., Chen, H., Cheng, A.T., Chou, D., Chugh, S.S., Coffeng, L.E., Colan, S.D., Colquhoun, S., Colson, K.E., Condon, J., Connor, M.D., Cooper, L.T., Corriere, M., Cortinovis, M., de Vaccaro, K.C., Couser, W., Cowie, B.C., Criqui, M.H., Cross, M., Dabhadkar, K.C., Dahiya, M., Dahodwala, N., Damsere-Derry, J., Danaei, G., Davis, A., De Leo, D., Degenhardt, L., Dellavalle, R., Delossantos, A., Denenberg, J., Derrett, S., Des Jarlais, D.C., Dharmaratne, S.D., Dherani, M., Diaz-Torne, C., Dolk, H., Dorsey, E.R., Driscoll, T., Duber, H., Ebel, B., Edmond, K., Elbaz, A., Ali, S.E., Erskine, H., Erwin, P.J., Espindola, P., Ewoigbokhan, S.E., Farzadfar, F., Feigin, V., Felson, D.T., Ferrari, A., Ferri, C.P., Fevre, E.M., Finucane, M.M., Flaxman, S., Flood, L., Foreman, K., Forouzanfar, M.H., Fowkes, F.G., Fransen, M., Freeman, M.K., Gabbe, B.J., Gabriel, S.E., Gakidou, E., Ganatra, H.A., Garcia, B., Gaspari, F., Gillum, R.F., Gmel, G., Gonzalez-Medina, D., Gosselin, R., Grainger, R., Grant, B., Groeger, J., Guillemin, F., Gunnell, D., Gupta, R., Haagsma, J., Hagan, H., Halasa, Y.A., Hall, W., Haring, D., Haro, J.M., Harrison, J.E., Havmoeller, R., Hay, R.J., Higashi, H., Hill, C., Hoen, B., Hoffman, H., Hotez, P.J., Hoy, D., Huang, J.J., Ibeanusi, S.E., Jacobsen, K.H., James, S.L., Jarvis, D., Jasrasaria, R., Jayaraman, S., Johns, N., Jonas, J.B., Karthikeyan, G., Kassebaum, N., Kawakami, N., Keren, A., Khoo, J.P., King, C.H., Knowlton, L.M., Kobusingye, O., Koranteng, A., Krishnamurthi, R., Laden, F., Laloo, R., Laslett, L.L., Lathlean, T., Leasher, J.L., Lee, Y.Y., Leigh, J., Levinson, D., Lim, S.S., Limb, E., Lin, J.K., Lipnick, M., Lipshultz, S.E., Liu, W., Loane, M., Ohno, S.L., Lyons, R., Mabweijano, J., MacIntyre, M.F., Malekzadeh, R., Mallinger, L., Manivannan, S., Marcenes, W., March, L., Margolis, D.J., Marks, G.B., Marks, R., Matsumori, A., Matzopoulos, R., Mayosi, B.M., McAnulty, J.H., McDermott, M.M., McGill, N., McGrath, J., Medina-Mora, M.E., Meltzer, M., Mensah, G.A., Merriman, T.R., Meyer, A.C., Miglioli, V., Miller, M., Miller, T.R., Mitchell, P.B., Mock, C., Mocumbi, A.O., Moffitt, T.E., Mokdad, A.A., Monasta, L., Montico, M., Moradi-Lakeh, M., Moran, A., Morawska, L., Mori, R., Murdoch, M.E., Mwaniki, M.K., Naidoo, K., Nair, M.N., Naldi, L., Narayan, K.M., Nelson, P.K., Nelson, R.G., Nevitt, M.C., Newton, C.R., Nolte, S., Norman, P., Norman, R., O'Donnell, M., O'Hanlon, S., Olives, C., Omer, S.B., Ortblad, K., Osborne, R., Ozgediz, D., Page, A., Pahari, B., Pandian, J.D., Rivero, A.P., Patten, S.B., Pearce, N., Padilla, R.P., Perez-Ruiz, F., Perico, N., Pesudovs, K., Phillips, D., Phillips, M.R., Pierce, K., Pion, S., Polanczyk, G.V., Polinder, S., Pope, C.A., 3rd, Popova, S., Porrini, E., Pourmalek, F., Prince, M., Pullan, R.L., Ramaiah, K.D., Ranganathan, D., Razavi, H., Regan, M., Rehm, J.T., Rein, D.B., Remuzzi, G., Richardson, K., Rivara, F.P., Roberts, T., Robinson, C., De Leon, F.R., Ronfani, L., Room, R., Rosenfeld, L.C., Rushton, L., Sacco, R.L., Saha, S., Sampson, U., Sanchez-Riera, L., Sanman, E., Schwebel, D.C., Scott, J.G., Segui-Gomez, M., Shahraz, S., Shepard, D.S., Shin, H., Shivakoti, R., Singh, D., Singh, G.M., Singh, J.A., Singleton, J., Sleet,



- D.A., Sliwa, K., Smith, E., Smith, J.L., Stapelberg, N.J., Steer, A., Steiner, T., Stolk, W.A., Stovner, L.J., Sudfeld, C., Syed, S., Tamburlini, G., Tavakkoli, M., Taylor, H.R., Taylor, J.A., Taylor, W.J., Thomas, B., Thomson, W.M., Thurston, G.D., Tleyjeh, I.M., Tonelli, M., Towbin, J.A., Truelsen, T., Tsilimbaris, M.K., Ubeda, C., Undurraga, E.A., van der Werf, M.J., van Os, J., Vavilala, M.S., Venketasubramanian, N., Wang, M., Wang, W., Watt, K., Weatherall, D.J., Weinstock, M.A., Weintraub, R., Weisskopf, M.G., Weissman, M.M., White, R.A., Whiteford, H., Wiebe, N., Wiersma, S.T., Wilkinson, J.D., Williams, H.C., Williams, S.R., Witt, E., Wolfe, F., Woolf, A.D., Wulf, S., Yeh, P.H., Zaidi, A.K., Zheng, Z.J., Zonies, D., Lopez, A.D., AlMazroa, M.A., Memish, Z.A., 2012. Disability-adjusted life years (DALYs) for 291 diseases and injuries in 21 regions, 1990-2010: a systematic analysis for the Global Burden of Disease Study 2010. *Lancet* 380, 2197-2223.
- Nagasunder, A.C., Kinney, H.C., Bluml, S., Tavaré, C.J., Rosser, T., Gilles, F.H., Nelson, M.D., Panigrahy, A., 2011. Abnormal microstructure of the atrophic thalamus in preterm survivors with periventricular leukomalacia. *AJNR Am J Neuroradiol* 32, 185-191.
- Natarajan, G., Pappas, A., Shankaran, S., Kendrick, D.E., Das, A., Higgins, R.D., Laptook, A.R., Bell, E.F., Stoll, B.J., Newman, N., Hale, E.C., Bara, R., Walsh, M.C., 2012. Outcomes of extremely low birth weight infants with bronchopulmonary dysplasia: impact of the physiologic definition. *Early Hum Dev* 88, 509-515.
- Neil, J.J., Shiran, S.I., McKinstry, R.C., Schefft, G.L., Snyder, A.Z., Almli, C.R., Akbudak, E., Aronovitz, J.A., Miller, J.P., Lee, B.C., Conturo, T.E., 1998. Normal brain in human newborns: apparent diffusion coefficient and diffusion anisotropy measured by using diffusion tensor MR imaging. *Radiology* 209, 57-66.
- Nichols, T.E., Holmes, A.P., 2002. Nonparametric permutation tests for functional neuroimaging: a primer with examples. *Hum Brain Mapp* 15, 1-25.
- Nilsson, M., Lasic, S., Drobnyak, I., Topgaard, D., Westin, C.F., 2017. Resolution limit of cylinder diameter estimation by diffusion MRI: The impact of gradient waveform and orientation dispersion. *NMR Biomed*.
- Nishida, M., Makris, N., Kennedy, D.N., Vangel, M., Fischl, B., Krishnamoorthy, K.S., Caviness, V.S., Grant, P.E., 2006. Detailed semiautomated MRI based morphometry of the neonatal brain: preliminary results. *Neuroimage* 32, 1041-1049.
- Nosarti, C., Al-Asady, M.H., Frangou, S., Stewart, A.L., Rifkin, L., Murray, R.M., 2002. Adolescents who were born very preterm have decreased brain volumes. *Brain* 125, 1616-1623.
- Nosarti, C., Giouroukou, E., Micali, N., Rifkin, L., Morris, R.G., Murray, R.M., 2007. Impaired executive functioning in young adults born very preterm. *J Int Neuropsychol Soc* 13, 571-581.
- Nossin-Manor, R., Card, D., Morris, D., Noormohamed, S., Shroff, M.M., Whyte, H.E., Taylor, M.J., Sled, J.G., 2013. Quantitative MRI in the very preterm brain: assessing tissue organization and myelination using magnetization transfer, diffusion tensor and T(1) imaging. *Neuroimage* 64, 505-516.
- Nossin-Manor, R., Card, D., Raybaud, C., Taylor, M.J., Sled, J.G., 2015. Cerebral maturation in the early preterm period-A magnetization transfer and diffusion tensor imaging study using voxel-based analysis. *Neuroimage* 112, 30-42.
- O'Donnell, L.J., Westin, C.F., Golby, A.J., 2009. Tract-based morphometry for white matter group analysis. *Neuroimage* 45, 832-844.
- O'Gorman, R.L., Bucher, H.U., Held, U., Koller, B.M., Huppi, P.S., Hagmann, C.F., Swiss, E.P.O.N.T.G., 2015. Tract-based spatial statistics to assess the neuroprotective effect of early erythropoietin on white matter development in preterm infants. *Brain* 138, 388-397.
- Oishi, K., Mori, S., Donohue, P.K., Ernst, T., Anderson, L., Buchthal, S., Faria, A., Jiang, H., Li, X., Miller, M.I., van Zijl, P.C., Chang, L., 2011. Multi-contrast human neonatal brain atlas: application to normal neonate development analysis. *Neuroimage* 56, 8-20.
- Padilla, N., Alexandrou, G., Blennow, M., Lagercrantz, H., Aden, U., 2015. Brain Growth Gains and Losses in Extremely Preterm Infants at Term. *Cereb Cortex* 25, 1897-1905.
- Padilla, N., Falcon, C., Sanz-Cortes, M., Figueras, F., Bargallo, N., Crispi, F., Eixarch, E., Arranz, A., Botet, F., Gratacos, E., 2011. Differential effects of intrauterine growth restriction on brain structure and development in preterm infants: a magnetic resonance imaging study. *Brain Res* 1382, 98-108.

- Padilla, N., Junque, C., Figueras, F., Sanz-Cortes, M., Bargallo, N., Arranz, A., Donaire, A., Figueras, J., Gratacos, E., 2014. Differential vulnerability of gray matter and white matter to intrauterine growth restriction in preterm infants at 12 months corrected age. *Brain Res* 1545, 1-11.
- Panagiotaki, E., Schneider, T., Siow, B., Hall, M.G., Lythgoe, M.F., Alexander, D.C., 2012. Compartment models of the diffusion MR signal in brain white matter: a taxonomy and comparison. *Neuroimage* 59, 2241-2254.
- Pandit, A.S., Ball, G., Edwards, A.D., Counsell, S.J., 2013. Diffusion magnetic resonance imaging in preterm brain injury. *Neuroradiology* 55 Suppl 2, 65-95.
- Pandit, A.S., Robinson, E., Aljabar, P., Ball, G., Gousias, I.S., Wang, Z., Hajnal, J.V., Rueckert, D., Counsell, S.J., Montana, G., Edwards, A.D., 2014. Whole-brain mapping of structural connectivity in infants reveals altered connection strength associated with growth and preterm birth. *Cereb Cortex* 24, 2324-2333.
- Pangelinan, M.M., Zhang, G., VanMeter, J.W., Clark, J.E., Hatfield, B.D., Haufler, A.J., 2011. Beyond age and gender: relationships between cortical and subcortical brain volume and cognitive-motor abilities in school-age children. *Neuroimage* 54, 3093-3100.
- Pannek, K., Guzzetta, A., Colditz, P.B., Rose, S.E., 2012. Diffusion MRI of the neonate brain: acquisition, processing and analysis techniques. *Pediatr Radiol* 42, 1169-1182.
- Pannek, K., Hatzigeorgiou, X., Colditz, P.B., Rose, S., 2013. Assessment of structural connectivity in the preterm brain at term equivalent age using diffusion MRI and T2 relaxometry: a network-based analysis. *PLoS One* 8, e68593.
- Pannek, K., Mathias, J.L., Bigler, E.D., Brown, G., Taylor, J.D., Rose, S., 2010. An automated strategy for the delineation and parcellation of commissural pathways suitable for clinical populations utilising high angular resolution diffusion imaging tractography. *Neuroimage* 50, 1044-1053.
- Papile, L.A., Burstein, J., Burstein, R., Koffler, H., 1978. Incidence and evolution of subependymal and intraventricular hemorrhage: a study of infants with birth weights less than 1,500 gm. *J Pediatr* 92, 529-534.
- Parikh, N.A., Kennedy, K.A., Lasky, R.E., Tyson, J.E., 2015. Neurodevelopmental Outcomes of Extremely Preterm Infants Randomized to Stress Dose Hydrocortisone. *PLoS One* 10, e0137051.
- Parikh, N.A., Lasky, R.E., Kennedy, K.A., McDavid, G., Tyson, J.E., 2013. Perinatal factors and regional brain volume abnormalities at term in a cohort of extremely low birth weight infants. *PLoS One* 8, e62804.
- Park, H.J., Kubicki, M., Shenton, M.E., Guimond, A., McCarley, R.W., Maier, S.E., Kikinis, R., Jolesz, F.A., Westin, C.F., 2003. Spatial normalization of diffusion tensor MRI using multiple channels. *Neuroimage* 20, 1995-2009.
- Parker, G.D., Marshall, D., Rosin, P.L., Drage, N., Richmond, S., Jones, D.K., 2013. A pitfall in the reconstruction of fibre ODFs using spherical deconvolution of diffusion MRI data. *Neuroimage* 65, 433-448.
- Parker, G.J., Alexander, D.C., 2005. Probabilistic anatomical connectivity derived from the microscopic persistent angular structure of cerebral tissue. *Philos Trans R Soc Lond B Biol Sci* 360, 893-902.
- Parker, G.J., Haroon, H.A., Wheeler-Kingshott, C.A., 2003. A framework for a streamline-based probabilistic index of connectivity (PICO) using a structural interpretation of MRI diffusion measurements. *J Magn Reson Imaging* 18, 242-254.
- Partridge, S.C., Mukherjee, P., Henry, R.G., Miller, S.P., Berman, J.I., Jin, H., Lu, Y., Glenn, O.A., Ferriero, D.M., Barkovich, A.J., Vigneron, D.B., 2004. Diffusion tensor imaging: serial quantitation of white matter tract maturity in premature newborns. *Neuroimage* 22, 1302-1314.
- Patra, K., Greene, M.M., Silvestri, J.M., 2015. Neurodevelopmental impact of hydrocortisone exposure in extremely low birth weight infants: outcomes at 1 and 2 years. *J Perinatol* 35, 77-81.
- Patra, K., Wilson-Costello, D., Taylor, H.G., Mercuri-Minich, N., Hack, M., 2006. Grades I-II intraventricular hemorrhage in extremely low birth weight infants: effects on neurodevelopment. *J Pediatr* 149, 169-173.

- Paus, T., Collins, D.L., Evans, A.C., Leonard, G., Pike, B., Zijdenbos, A., 2001. Maturation of white matter in the human brain: a review of magnetic resonance studies. *Brain Res Bull* 54, 255-266.
- Pecheva, D., Yushkevich, P., Batalle, D., Hughes, E., Aljabar, P., Wurie, J., Hajnal, J.V., Edwards, A.D., Alexander, D.C., Counsell, S.J., Zhang, H., 2017. A tract-specific approach to assessing white matter in preterm infants. *Neuroimage* 157, 675-694.
- Pena, M., Maki, A., Kovacic, D., Dehaene-Lambertz, G., Koizumi, H., Bouquet, F., Mehler, J., 2003. Sounds and silence: an optical topography study of language recognition at birth. *Proc Natl Acad Sci U S A* 100, 11702-11705.
- Perlaki, G., Horvath, R., Orsi, G., Aradi, M., Auer, T., Varga, E., Kantor, G., Altbacker, A., John, F., Doczi, T., Komoly, S., Kovacs, N., Schwarcz, A., Janszky, J., 2013. White-matter microstructure and language lateralization in left-handers: a whole-brain MRI analysis. *Brain Cogn* 82, 319-328.
- Peterson, B.S., Anderson, A.W., Ehrenkranz, R., Staib, L.H., Tageldin, M., Colson, E., Gore, J.C., Duncan, C.C., Makuch, R., Ment, L.R., 2003. Regional brain volumes and their later neurodevelopmental correlates in term and preterm infants. *Pediatrics* 111, 939-948.
- Peterson, B.S., Vohr, B., Staib, L.H., Cannistraci, C.J., Dolberg, A., Schneider, K.C., Katz, K.H., Westerveld, M., Sparrow, S., Anderson, A.W., Duncan, C.C., Makuch, R.W., Gore, J.C., Ment, L.R., 2000. Regional brain volume abnormalities and long-term cognitive outcome in preterm infants. *JAMA* 284, 1939-1947.
- Pierpaoli, C., Basser, P.J., 1996. Toward a quantitative assessment of diffusion anisotropy. *Magn Reson Med* 36, 893-906.
- Pierson, C.R., Folkerth, R.D., Billiards, S.S., Trachtenberg, F.L., Drinkwater, M.E., Volpe, J.J., Kinney, H.C., 2007. Gray matter injury associated with periventricular leukomalacia in the premature infant. *Acta Neuropathol* 114, 619-631.
- Pieterman, K., Batalle, D., Dudink, J., Tournier, J.D., Hughes, E.J., Barnett, M., Benders, M.J., Edwards, A.D., Hoebeek, F.E., Counsell, S.J., 2017. Cerebello-cerebral connectivity in the developing brain. *Brain Struct Funct* 222, 1625-1634.
- Platt, M.J., Cans, C., Johnson, A., Surman, G., Topp, M., Torrioli, M.G., Krageloh-Mann, I., 2007. Trends in cerebral palsy among infants of very low birthweight (<1500 g) or born prematurely (<32 weeks) in 16 European centres: a database study. *Lancet* 369, 43-50.
- Plunkett, J., Muglia, L.J., 2008. Genetic contributions to preterm birth: implications from epidemiological and genetic association studies. *Ann Med* 40, 167-195.
- Poupon, C., Clark, C.A., Frouin, V., Regis, J., Bloch, I., Le Bihan, D., Mangin, J., 2000. Regularization of diffusion-based direction maps for the tracking of brain white matter fascicles. *Neuroimage* 12, 184-195.
- Powell, H.W., Parker, G.J., Alexander, D.C., Symms, M.R., Boulby, P.A., Wheeler-Kingshott, C.A., Barker, G.J., Noppeney, U., Koepp, M.J., Duncan, J.S., 2006. Hemispheric asymmetries in language-related pathways: a combined functional MRI and tractography study. *Neuroimage* 32, 388-399.
- Purcell, E.M., Torrey, H.C., Pound, R.V., 1946. Resonance absorption by nuclear magnetic moments in a solid. *Phys. Rev.* 69, 37-38.
- Qiu, A., Fortier, M.V., Bai, J., Zhang, X., Chong, Y.S., Kwek, K., Saw, S.M., Godfrey, K.M., Gluckman, P.D., Meaney, M.J., 2013. Morphology and microstructure of subcortical structures at birth: a large-scale Asian neonatal neuroimaging study. *Neuroimage* 65, 315-323.
- Radic, J.A., Vincer, M., McNeely, P.D., 2015a. Outcomes of intraventricular hemorrhage and posthemorrhagic hydrocephalus in a population-based cohort of very preterm infants born to residents of Nova Scotia from 1993 to 2010. *J Neurosurg Pediatr* 15, 580-588.
- Radic, J.A., Vincer, M., McNeely, P.D., 2015b. Temporal trends of intraventricular hemorrhage of prematurity in Nova Scotia from 1993 to 2012. *J Neurosurg Pediatr* 15, 573-579.
- Raffelt, D., Tournier, J.D., Crozier, S., Connelly, A., Salvado, O., 2012a. Reorientation of fiber orientation distributions using apodized point spread functions. *Magn Reson Med* 67, 844-855.

- Raffelt, D., Tournier, J.D., Fripp, J., Crozier, S., Connelly, A., Salvado, O., 2009. Spatial normalization of high angular resolution diffusion imaging data using fiber orientation distributions. *Proceedings of International Society for Magnetic Resonance in Medicine*.
- Raffelt, D., Tournier, J.D., Fripp, J., Crozier, S., Connelly, A., Salvado, O., 2011. Symmetric diffeomorphic registration of fibre orientation distributions. *Neuroimage* 56, 1171-1180.
- Raffelt, D., Tournier, J.D., Rose, S., Ridgway, G.R., Henderson, R., Crozier, S., Salvado, O., Connelly, A., 2012b. Apparent Fibre Density: a novel measure for the analysis of diffusion-weighted magnetic resonance images. *Neuroimage* 59, 3976-3994.
- Raffelt, D.A., Tournier, J.D., Smith, R.E., Vaughan, D.N., Jackson, G., Ridgway, G.R., Connelly, A., 2017. Investigating white matter fibre density and morphology using fixel-based analysis. *Neuroimage* 144, 58-73.
- Ramenghi, L.A., Fumagalli, M., Righini, A., Bassi, L., Groppo, M., Parazzini, C., Bianchini, E., Triulzi, F., Mosca, F., 2007. Magnetic resonance imaging assessment of brain maturation in preterm neonates with punctate white matter lesions. *Neuroradiology* 49, 161-167.
- Ranger, M., Zwicker, J.G., Chau, C.M., Park, M.T., Chakravarthy, M.M., Poskitt, K., Miller, S.P., Bjornson, B.H., Tam, E.W., Chau, V., Synnes, A.R., Grunau, R.E., 2015. Neonatal Pain and Infection Relate to Smaller Cerebellum in Very Preterm Children at School Age. *J Pediatr* 167, 292-298 e291.
- Ratnarajah, N., Rifkin-Graboi, A., Fortier, M.V., Chong, Y.S., Kwek, K., Saw, S.M., Godfrey, K.M., Gluckman, P.D., Meaney, M.J., Qiu, A., 2013. Structural connectivity asymmetry in the neonatal brain. *Neuroimage* 75, 187-194.
- Rees, C.M., Pierro, A., Eaton, S., 2007. Neurodevelopmental outcomes of neonates with medically and surgically treated necrotizing enterocolitis. *Arch Dis Child Fetal Neonatal Ed* 92, F193-198.
- Reid, S.M., Carlin, J.B., Reddihough, D.S., 2011. Rates of cerebral palsy in Victoria, Australia, 1970 to 2004: has there been a change? *Dev Med Child Neurol* 53, 907-912.
- Reidy, N., Morgan, A., Thompson, D.K., Inder, T.E., Doyle, L.W., Anderson, P.J., 2013. Impaired language abilities and white matter abnormalities in children born very preterm and/or very low birth weight. *J Pediatr* 162, 719-724.
- Reilly, S., Wake, M., Ukoumunne, O.C., Bavin, E., Prior, M., Cini, E., Conway, L., Eadie, P., Bretherton, L., 2010. Predicting language outcomes at 4 years of age: findings from Early Language in Victoria Study. *Pediatrics* 126, e1530-1537.
- Reiss, A.L., Kesler, S.R., Vohr, B., Duncan, C.C., Katz, K.H., Pajot, S., Schneider, K.C., Makuch, R.W., Ment, L.R., 2004. Sex differences in cerebral volumes of 8-year-olds born preterm. *J Pediatr* 145, 242-249.
- Repka, M.X., 2002. Ophthalmological problems of the premature infant. *Ment Retard Dev Disabil Res Rev* 8, 249-257.
- Resch, B., Vollaard, E., Maurer, U., Haas, J., Rosegger, H., Muller, W., 2000. Risk factors and determinants of neurodevelopmental outcome in cystic periventricular leukomalacia. *Eur J Pediatr* 159, 663-670.
- Rezaie, P., Dean, A., 2002. Periventricular leukomalacia, inflammation and white matter lesions within the developing nervous system. *Neuropathology* 22, 106-132.
- Robinson, E.C., Hammers, A., Ericsson, A., Edwards, A.D., Rueckert, D., 2010. Identifying population differences in whole-brain structural networks: a machine learning approach. *Neuroimage* 50, 910-919.
- Rodrigo, S., Naggara, O., Oppenheim, C., Golestani, N., Poupon, C., Cointepas, Y., Mangin, J.F., Le Bihan, D., Meder, J.F., 2007. Human subinsular asymmetry studied by diffusion tensor imaging and fiber tracking. *AJNR Am J Neuroradiol* 28, 1526-1531.
- Rogers, C.E., Smyser, T., Smyser, C.D., Shimony, J., Inder, T.E., Neil, J.J., 2016. Regional white matter development in very preterm infants: perinatal predictors and early developmental outcomes. *Pediatr Res* 79, 87-95.
- Rogers, E.E., Hintz, S.R., 2016. Early neurodevelopmental outcomes of extremely preterm infants. *Semin Perinatol* 40, 497-509.

- Rohlfing, T., 2012. Image similarity and tissue overlaps as surrogates for image registration accuracy: widely used but unreliable. *IEEE Trans Med Imaging* 31, 153-163.
- Roine, T., Jeurissen, B., Perrone, D., Aelterman, J., Leemans, A., Philips, W., Sijbers, J., 2014. Isotropic non-white matter partial volume effects in constrained spherical deconvolution. *Front Neuroinform* 8, 28.
- Rose, J., Butler, E.E., Lamont, L.E., Barnes, P.D., Atlas, S.W., Stevenson, D.K., 2009. Neonatal brain structure on MRI and diffusion tensor imaging, sex, and neurodevelopment in very-low-birthweight preterm children. *Dev Med Child Neurol* 51, 526-535.
- Rose, J., Mirmiran, M., Butler, E.E., Lin, C.Y., Barnes, P.D., Kermoian, R., Stevenson, D.K., 2007. Neonatal microstructural development of the internal capsule on diffusion tensor imaging correlates with severity of gait and motor deficits. *Dev Med Child Neurol* 49, 745-750.
- Rose, J., Vassar, R., Cahill-Rowley, K., Guzman, X.S., Stevenson, D.K., Barnea-Goraly, N., 2014. Brain microstructural development at near-term age in very-low-birth-weight preterm infants: an atlas-based diffusion imaging study. *Neuroimage* 86, 244-256.
- Rose, S.E., Hatzigeorgiou, X., Strudwick, M.W., Durbridge, G., Davies, P.S., Colditz, P.B., 2008. Altered white matter diffusion anisotropy in normal and preterm infants at term-equivalent age. *Magn Reson Med* 60, 761-767.
- Roze, E., Harris, P.A., Ball, G., Elorza, L.Z., Braga, R.M., Allsop, J.M., Merchant, N., Porter, E., Arichi, T., Edwards, A.D., Rutherford, M.A., Cowan, F.M., Counsell, S.J., 2012. Tractography of the corticospinal tracts in infants with focal perinatal injury: comparison with normal controls and to motor development. *Neuroradiology* 54, 507-516.
- Rueckert, D., Sonoda, L.I., Hayes, C., Hill, D.L., Leach, M.O., Hawkes, D.J., 1999. Nonrigid registration using free-form deformations: application to breast MR images. *IEEE Trans Med Imaging* 18, 712-721.
- Rutherford, M.A., Pennock, J.M., Counsell, S.J., Mercuri, E., Cowan, F.M., Dubowitz, L.M., Edwards, A.D., 1998. Abnormal magnetic resonance signal in the internal capsule predicts poor neurodevelopmental outcome in infants with hypoxic-ischemic encephalopathy. *Pediatrics* 102, 323-328.
- Rutherford, M.A., Supramaniam, V., Ederies, A., Chew, A., Bassi, L., Groppo, M., Anjari, M., Counsell, S., Ramenghi, L.A., 2010. Magnetic resonance imaging of white matter diseases of prematurity. *Neuroradiology* 52, 505-521.
- Saigal, S., Doyle, L.W., 2008. An overview of mortality and sequelae of preterm birth from infancy to adulthood. *Lancet* 371, 261-269.
- Saliba, E., Marret, S., 2001. Cerebral white matter damage in the preterm infant: pathophysiology and risk factors. *Semin Neonatol* 6, 121-133.
- Salvan, P., Tournier, J.D., Batalle, D., Falconer, S., Chew, A., Kennea, N., Aljabar, P., Dehaene-Lambertz, G., Arichi, T., Edwards, A.D., Counsell, S.J., 2017. Language ability in preterm children is associated with arcuate fasciculi microstructure at term. *Hum Brain Mapp*.
- Scherrer, B., Schwartzman, A., Taquet, M., Sahin, M., Prabhu, S.P., Warfield, S.K., 2016. Characterizing brain tissue by assessment of the distribution of anisotropic microstructural environments in diffusion-compartment imaging (DIAMOND). *Magn Reson Med* 76, 963-977.
- Schlapbach, L.J., Aebischer, M., Adams, M., Natalucci, G., Bonhoeffer, J., Latzin, P., Nelle, M., Bucher, H.U., Latal, B., Swiss Neonatal, N., Follow-Up, G., 2011. Impact of sepsis on neurodevelopmental outcome in a Swiss National Cohort of extremely premature infants. *Pediatrics* 128, e348-357.
- Schlerf, J.E., Galea, J.M., Spampinato, D., Celnik, P.A., 2015. Laterality Differences in Cerebellar-Motor Cortex Connectivity. *Cereb Cortex* 25, 1827-1834.
- Schmahmann, J.D., Sherman, J.C., 1998. The cerebellar cognitive affective syndrome. *Brain* 121 ( Pt 4), 561-579.
- Schwarz, C.G., Reid, R.I., Gunter, J.L., Senjem, M.L., Przybelski, S.A., Zuk, S.M., Whitwell, J.L., Vemuri, P., Josephs, K.A., Kantarci, K., Thompson, P.M., Petersen, R.C., Jack, C.R., Jr., Alzheimer's Disease Neuroimaging, I., 2014. Improved DTI registration allows voxel-based analysis that outperforms tract-based spatial statistics. *Neuroimage* 94, 65-78.

- Scott, J.A., Habas, P.A., Kim, K., Rajagopalan, V., Hamzelou, K.S., Corbett-Detig, J.M., Barkovich, A.J., Glenn, O.A., Studholme, C., 2011. Growth trajectories of the human fetal brain tissues estimated from 3D reconstructed in utero MRI. *Int J Dev Neurosci* 29, 529-536.
- Serenius, F., Ewald, U., Farooqi, A., Fellman, V., Hafstrom, M., Hellgren, K., Marsal, K., Ohlin, A., Olhager, E., Stjernqvist, K., Stromberg, B., Aden, U., Kallen, K., Extremely Preterm Infants in Sweden Study, G., 2016. Neurodevelopmental Outcomes Among Extremely Preterm Infants 6.5 Years After Active Perinatal Care in Sweden. *JAMA Pediatr* 170, 954-963.
- Serenius, F., Kallen, K., Blennow, M., Ewald, U., Fellman, V., Holmstrom, G., Lindberg, E., Lundqvist, P., Marsal, K., Norman, M., Olhager, E., Stigson, L., Stjernqvist, K., Vollmer, B., Stromberg, B., Group, E., 2013. Neurodevelopmental outcome in extremely preterm infants at 2.5 years after active perinatal care in Sweden. *JAMA* 309, 1810-1820.
- Shah, D.K., Anderson, P.J., Carlin, J.B., Pavlovic, M., Howard, K., Thompson, D.K., Warfield, S.K., Inder, T.E., 2006. Reduction in cerebellar volumes in preterm infants: relationship to white matter injury and neurodevelopment at two years of age. *Pediatr Res* 60, 97-102.
- Shah, P., Kaciroti, N., Richards, B., Oh, W., Lumeng, J.C., 2016. Developmental Outcomes of Late Preterm Infants From Infancy to Kindergarten. *Pediatrics* 138.
- Shih, M.T., Singh, A.K., Wang, A.M., Patel, S., 2004. Brain lesions with elevated lactic acid peaks on magnetic resonance spectroscopy. *Curr Probl Diagn Radiol* 33, 85-95.
- Short, E.J., Klein, N.K., Lewis, B.A., Fulton, S., Eisengart, S., Kercsmar, C., Baley, J., Singer, L.T., 2003. Cognitive and academic consequences of bronchopulmonary dysplasia and very low birth weight: 8-year-old outcomes. *Pediatrics* 112, e359.
- Sie, L.T., Hart, A.A., van Hof, J., de Groot, L., Lems, W., Lafeber, H.N., Valk, J., van der Knaap, M.S., 2005. Predictive value of neonatal MRI with respect to late MRI findings and clinical outcome. A study in infants with periventricular densities on neonatal ultrasound. *Neuropediatrics* 36, 78-89.
- Skiold, B., Alexandrou, G., Padilla, N., Blennow, M., Vollmer, B., Aden, U., 2014. Sex differences in outcome and associations with neonatal brain morphology in extremely preterm children. *J Pediatr* 164, 1012-1018.
- Skiold, B., Horsch, S., Hallberg, B., Engstrom, M., Nagy, Z., Mosskin, M., Blennow, M., Aden, U., 2010. White matter changes in extremely preterm infants, a population-based diffusion tensor imaging study. *Acta Paediatr* 99, 842-849.
- Skiold, B., Vollmer, B., Bohm, B., Hallberg, B., Horsch, S., Mosskin, M., Lagercrantz, H., Aden, U., Blennow, M., 2012. Neonatal magnetic resonance imaging and outcome at age 30 months in extremely preterm infants. *J Pediatr* 160, 559-566 e551.
- Skranes, J., Lohaugen, G.C., Martinussen, M., Indredavik, M.S., Dale, A.M., Haraldseth, O., Vangberg, T.R., Brubakk, A.M., 2009. White matter abnormalities and executive function in children with very low birth weight. *Neuroreport* 20, 263-266.
- Skranes, J., Vangberg, T.R., Kulseng, S., Indredavik, M.S., Evensen, K.A., Martinussen, M., Dale, A.M., Haraldseth, O., Brubakk, A.M., 2007. Clinical findings and white matter abnormalities seen on diffusion tensor imaging in adolescents with very low birth weight. *Brain* 130, 654-666.
- Slattery, C.F., Zhang, J., Paterson, R.W., Foulkes, A.J.M., Carton, A., Macpherson, K., Mancini, L., Thomas, D.L., Modat, M., Toussaint, N., Cash, D.M., Thornton, J.S., Henley, S.M.D., Crutch, S.J., Alexander, D.C., Ourselin, S., Fox, N.C., Zhang, H., Schott, J.M., 2017. ApoE influences regional white-matter axonal density loss in Alzheimer's disease. *Neurobiol Aging* 57, 8-17.
- Smith, R.E., Raffelt, D., Vaughan, D.N., Calamante, F., Connelly, A., 2017. Toward interrogating relationships between grey and white matter measures using Fixel Track-Weighted Imaging and Fixel-Based Analysis. 25th Annual Meeting of the International Society of Magnetic Resonance in Medicine, Honolulu, HI, USA.
- Smith, R.E., Tournier, J.D., Calamante, F., Connelly, A., 2012. Anatomically-constrained tractography: improved diffusion MRI streamlines tractography through effective use of anatomical information. *Neuroimage* 62, 1924-1938.
- Smith, R.E., Tournier, J.D., Calamante, F., Connelly, A., 2013. SIFT: Spherical-deconvolution informed filtering of tractograms. *Neuroimage* 67, 298-312.
- Smith, S.M., 2002. Fast robust automated brain extraction. *Hum Brain Mapp* 17, 143-155.

- Smith, S.M., Jenkinson, M., Johansen-Berg, H., Rueckert, D., Nichols, T.E., Mackay, C.E., Watkins, K.E., Ciccarelli, O., Cader, M.Z., Matthews, P.M., Behrens, T.E., 2006. Tract-based spatial statistics: voxelwise analysis of multi-subject diffusion data. *Neuroimage* 31, 1487-1505.
- Smith, S.M., Nichols, T.E., 2009. Threshold-free cluster enhancement: addressing problems of smoothing, threshold dependence and localisation in cluster inference. *Neuroimage* 44, 83-98.
- Smithers-Sheedy, H., McIntyre, S., Gibson, C., Meehan, E., Scott, H., Goldsmith, S., Watson, L., Badawi, N., Walker, K., Novak, I., Blair, E., Australian Cerebral Palsy Register, G., 2016. A special supplement: findings from the Australian Cerebral Palsy Register, birth years 1993 to 2006. *Dev Med Child Neurol* 58 Suppl 2, 5-10.
- Soria-Pastor, S., Padilla, N., Zubiaurre-Elorza, L., Ibarretxe-Bilbao, N., Botet, F., Costas-Moragas, C., Falcon, C., Bargallo, N., Mercader, J.M., Junque, C., 2009. Decreased regional brain volume and cognitive impairment in preterm children at low risk. *Pediatrics* 124, e1161-1170.
- Spencer-Smith, M.M., Spittle, A.J., Lee, K.J., Doyle, L.W., Anderson, P.J., 2015. Bayley-III Cognitive and Language Scales in Preterm Children. *Pediatrics* 135, e1258-1265.
- Spittle, A.J., Boyd, R.N., Inder, T.E., Doyle, L.W., 2009. Predicting motor development in very preterm infants at 12 months' corrected age: the role of qualitative magnetic resonance imaging and general movements assessments. *Pediatrics* 123, 512-517.
- Spittle, A.J., Walsh, J.M., Potter, C., McInnes, E., Olsen, J.E., Lee, K.J., Anderson, P.J., Doyle, L.W., Cheong, J.L., 2017. Neurobehaviour at term-equivalent age and neurodevelopmental outcomes at 2 years in infants born moderate-to-late preterm. *Dev Med Child Neurol* 59, 207-215.
- Srinivasan, L., Allsop, J., Counsell, S.J., Boardman, J.P., Edwards, A.D., Rutherford, M., 2006. Smaller cerebellar volumes in very preterm infants at term-equivalent age are associated with the presence of supratentorial lesions. *AJNR Am J Neuroradiol* 27, 573-579.
- Srinivasan, L., Dutta, R., Counsell, S.J., Allsop, J.M., Boardman, J.P., Rutherford, M.A., Edwards, A.D., 2007. Quantification of deep gray matter in preterm infants at term-equivalent age using manual volumetry of 3-tesla magnetic resonance images. *Pediatrics* 119, 759-765.
- Stanisz, G.J., Szafer, A., Wright, G.A., Henkelman, R.M., 1997. An analytical model of restricted diffusion in bovine optic nerve. *Magn Reson Med* 37, 103-111.
- Stephens, B.E., Walden, R.V., Gargus, R.A., Tucker, R., McKinley, L., Mance, M., Nye, J., Vohr, B.R., 2009. First-week protein and energy intakes are associated with 18-month developmental outcomes in extremely low birth weight infants. *Pediatrics* 123, 1337-1343.
- Stikov, N., Campbell, J.S., Stroh, T., Lavelee, M., Frey, S., Novek, J., Nuara, S., Ho, M.K., Bedell, B.J., Dougherty, R.F., Leppert, I.R., Boudreau, M., Narayanan, S., Duval, T., Cohen-Adad, J., Picard, P.A., Gasecka, A., Cote, D., Pike, G.B., 2015. In vivo histology of the myelin g-ratio with magnetic resonance imaging. *Neuroimage* 118, 397-405.
- Stoll, B.J., Hansen, N., Fanaroff, A.A., Wright, L.L., Carlo, W.A., Ehrenkranz, R.A., Lemons, J.A., Donovan, E.F., Stark, A.R., Tyson, J.E., Oh, W., Bauer, C.R., Korones, S.B., Shankaran, S., Laptook, A.R., Stevenson, D.K., Papile, L.A., Poole, W.K., 2002a. Changes in pathogens causing early-onset sepsis in very-low-birth-weight infants. *N Engl J Med* 347, 240-247.
- Stoll, B.J., Hansen, N., Fanaroff, A.A., Wright, L.L., Carlo, W.A., Ehrenkranz, R.A., Lemons, J.A., Donovan, E.F., Stark, A.R., Tyson, J.E., Oh, W., Bauer, C.R., Korones, S.B., Shankaran, S., Laptook, A.R., Stevenson, D.K., Papile, L.A., Poole, W.K., 2002b. Late-onset sepsis in very low birth weight neonates: the experience of the NICHD Neonatal Research Network. *Pediatrics* 110, 285-291.
- Stoll, B.J., Hansen, N.I., Adams-Chapman, I., Fanaroff, A.A., Hintz, S.R., Vohr, B., Higgins, R.D., National Institute of Child, H., Human Development Neonatal Research, N., 2004. Neurodevelopmental and growth impairment among extremely low-birth-weight infants with neonatal infection. *JAMA* 292, 2357-2365.
- Stoll, B.J., Hansen, N.I., Bell, E.F., Walsh, M.C., Carlo, W.A., Shankaran, S., Laptook, A.R., Sanchez, P.J., Van Meurs, K.P., Wyckoff, M., Das, A., Hale, E.C., Ball, M.B., Newman, N.S., Schibler, K., Poindexter, B.B., Kennedy, K.A., Cotten, C.M., Watterberg, K.L., D'Angio, C.T., DeMauro, S.B., Truog, W.E., Devaskar, U., Higgins, R.D., Eunice Kennedy Shriver National Institute of Child, H., Human Development Neonatal Research, N., 2015. Trends in Care

- Practices, Morbidity, and Mortality of Extremely Preterm Neonates, 1993-2012. *JAMA* 314, 1039-1051.
- Suarez, R.O., Commowick, O., Prabhu, S.P., Warfield, S.K., 2012. Automated delineation of white matter fiber tracts with a multiple region-of-interest approach. *Neuroimage* 59, 3690-3700.
- Takahashi, E., Folkerth, R.D., Galaburda, A.M., Grant, P.E., 2012. Emerging cerebral connectivity in the human fetal brain: an MR tractography study. *Cereb Cortex* 22, 455-464.
- Takahashi, E., Hayashi, E., Schmahmann, J.D., Grant, P.E., 2014. Development of cerebellar connectivity in human fetal brains revealed by high angular resolution diffusion tractography. *Neuroimage* 96, 326-333.
- Takao, H., Abe, O., Yamasue, H., Aoki, S., Sasaki, H., Kasai, K., Yoshioka, N., Ohtomo, K., 2011. Gray and white matter asymmetries in healthy individuals aged 21-29 years: a voxel-based morphometry and diffusion tensor imaging study. *Hum Brain Mapp* 32, 1762-1773.
- Tam, E.W., Ferriero, D.M., Xu, D., Berman, J.I., Vigneron, D.B., Barkovich, A.J., Miller, S.P., 2009. Cerebellar development in the preterm neonate: effect of supratentorial brain injury. *Pediatr Res* 66, 102-106.
- Tam, E.W., Miller, S.P., Studholme, C., Chau, V., Glidden, D., Poskitt, K.J., Ferriero, D.M., Barkovich, A.J., 2011. Differential effects of intraventricular hemorrhage and white matter injury on preterm cerebellar growth. *J Pediatr* 158, 366-371.
- Thiebaut de Schotten, M., Dell'Acqua, F., Forkel, S.J., Simmons, A., Vergani, F., Murphy, D.G., Catani, M., 2011a. A lateralized brain network for visuospatial attention. *Nat Neurosci* 14, 1245-1246.
- Thiebaut de Schotten, M., Ffytche, D.H., Bizzi, A., Dell'Acqua, F., Allin, M., Walshe, M., Murray, R., Williams, S.C., Murphy, D.G., Catani, M., 2011b. Atlasing location, asymmetry and inter-subject variability of white matter tracts in the human brain with MR diffusion tractography. *Neuroimage* 54, 49-59.
- Thompson, D.K., Inder, T.E., Faggian, N., Johnston, L., Warfield, S.K., Anderson, P.J., Doyle, L.W., Egan, G.F., 2011. Characterization of the corpus callosum in very preterm and full-term infants utilizing MRI. *Neuroimage* 55, 479-490.
- Thompson, D.K., Inder, T.E., Faggian, N., Warfield, S.K., Anderson, P.J., Doyle, L.W., Egan, G.F., 2012. Corpus callosum alterations in very preterm infants: perinatal correlates and 2 year neurodevelopmental outcomes. *Neuroimage* 59, 3571-3581.
- Thompson, D.K., Warfield, S.K., Carlin, J.B., Pavlovic, M., Wang, H.X., Bear, M., Kean, M.J., Doyle, L.W., Egan, G.F., Inder, T.E., 2007. Perinatal risk factors altering regional brain structure in the preterm infant. *Brain* 130, 667-677.
- Thomsen, C., Henriksen, O., Ring, P., 1987. In vivo measurement of water self diffusion in the human brain by magnetic resonance imaging. *Acta Radiol* 28, 353-361.
- Toga, A.W., Thompson, P.M., 2003. Mapping brain asymmetry. *Nat Rev Neurosci* 4, 37-48.
- Tolsa, C.B., Zimine, S., Warfield, S.K., Freschi, M., Sancho Rossignol, A., Lazeyras, F., Hanquinet, S., Pfizenmaier, M., Huppi, P.S., 2004. Early alteration of structural and functional brain development in premature infants born with intrauterine growth restriction. *Pediatr Res* 56, 132-138.
- Tomblin, J.B., Harrison, M., Ambrose, S.E., Walker, E.A., Oleson, J.J., Moeller, M.P., 2015. Language Outcomes in Young Children with Mild to Severe Hearing Loss. *Ear Hear* 36 Suppl 1, 76S-91S.
- Torrance, H.L., Bloemen, M.C., Mulder, E.J., Nikkels, P.G., Derks, J.B., de Vries, L.S., Visser, G.H., 2010. Predictors of outcome at 2 years of age after early intrauterine growth restriction. *Ultrasound Obstet Gynecol* 36, 171-177.
- Tournier, J.-D., Calamante, F., Connelly, A., 2012. MRtrix: Diffusion tractography in crossing fiber regions. *International Journal of Imaging Systems and Technology* 22, 53-66.
- Tournier, J.D., Calamante, F., Connelly, A., 2007. Robust determination of the fibre orientation distribution in diffusion MRI: non-negativity constrained super-resolved spherical deconvolution. *Neuroimage* 35, 1459-1472.



- Tournier, J.D., Calamante, F., Connelly, A., 2013. Determination of the appropriate b value and number of gradient directions for high-angular-resolution diffusion-weighted imaging. *NMR Biomed* 26, 1775-1786.
- Tournier, J.D., Calamante, F., Gadian, D.G., Connelly, A., 2003. Diffusion-weighted magnetic resonance imaging fibre tracking using a front evolution algorithm. *Neuroimage* 20, 276-288.
- Tournier, J.D., Calamante, F., Gadian, D.G., Connelly, A., 2004. Direct estimation of the fiber orientation density function from diffusion-weighted MRI data using spherical deconvolution. *Neuroimage* 23, 1176-1185.
- Tournier, J.D., Mori, S., Leemans, A., 2011. Diffusion tensor imaging and beyond. *Magn Reson Med* 65, 1532-1556.
- Travis, K.E., Adams, J.N., Ben-Shachar, M., Feldman, H.M., 2015. Decreased and Increased Anisotropy along Major Cerebral White Matter Tracts in Preterm Children and Adolescents. *PLoS One* 10, e0142860.
- Tuch, D.S., Reese, T.G., Wiegell, M.R., Makris, N., Belliveau, J.W., Wedeen, V.J., 2002. High angular resolution diffusion imaging reveals intravoxel white matter fiber heterogeneity. *Magn Reson Med* 48, 577-582.
- Tusor, N., Benders, M.J., Counsell, S.J., Nongena, P., Ederies, M.A., Falconer, S., Chew, A., Gonzalez-Cinca, N., Hajnal, J.V., Gangadharan, S., Chatzi, V., Kersbergen, K.J., Kennea, N., Azzopardi, D.V., Edwards, A.D., 2017. Punctate White Matter Lesions Associated With Altered Brain Development And Adverse Motor Outcome In Preterm Infants. *Sci Rep* 7, 13250.
- Tusor, N., Wusthoff, C., Smee, N., Merchant, N., Arichi, T., Allsop, J.M., Cowan, F.M., Azzopardi, D., Edwards, A.D., Counsell, S.J., 2012. Prediction of neurodevelopmental outcome after hypoxic-ischemic encephalopathy treated with hypothermia by diffusion tensor imaging analyzed using tract-based spatial statistics. *Pediatr Res* 72, 63-69.
- Tustison, N.J., Avants, B.B., Cook, P.A., Zheng, Y., Egan, A., Yushkevich, P.A., Gee, J.C., 2010. N4ITK: improved N3 bias correction. *IEEE Trans Med Imaging* 29, 1310-1320.
- van Haastert, I.C., Groenendaal, F., Uiterwaal, C.S., Termote, J.U., van der Heide-Jalving, M., Eijssermans, M.J., Gorter, J.W., Helders, P.J., Jongmans, M.J., de Vries, L.S., 2011. Decreasing incidence and severity of cerebral palsy in prematurely born children. *J Pediatr* 159, 86-91 e81.
- Van Hecke, W., Leemans, A., D'Agostino, E., De Backer, S., Vandervliet, E., Parizel, P.M., Sijbers, J., 2007. Nonrigid coregistration of diffusion tensor images using a viscous fluid model and mutual information. *IEEE Trans Med Imaging* 26, 1598-1612.
- Van Hecke, W., Leemans, A., De Backer, S., Jeurissen, B., Parizel, P.M., Sijbers, J., 2010. Comparing isotropic and anisotropic smoothing for voxel-based DTI analyses: A simulation study. *Hum Brain Mapp* 31, 98-114.
- Van Hecke, W., Leemans, A., Sage, C.A., Emsell, L., Veraart, J., Sijbers, J., Sunaert, S., Parizel, P.M., 2011. The effect of template selection on diffusion tensor voxel-based analysis results. *Neuroimage* 55, 566-573.
- Van Kooij, B.J., Benders, M.J., Anbeek, P., Van Haastert, I.C., De Vries, L.S., Groenendaal, F., 2012a. Cerebellar volume and proton magnetic resonance spectroscopy at term, and neurodevelopment at 2 years of age in preterm infants. *Dev Med Child Neurol* 54, 260-266.
- van Kooij, B.J., de Vries, L.S., Ball, G., van Haastert, I.C., Benders, M.J., Groenendaal, F., Counsell, S.J., 2012b. Neonatal tract-based spatial statistics findings and outcome in preterm infants. *AJNR Am J Neuroradiol* 33, 188-194.
- van Kooij, B.J., van Pul, C., Benders, M.J., van Haastert, I.C., de Vries, L.S., Groenendaal, F., 2011. Fiber tracking at term displays gender differences regarding cognitive and motor outcome at 2 years of age in preterm infants. *Pediatr Res* 70, 626-632.
- van Pul, C., van Kooij, B.J., de Vries, L.S., Benders, M.J., Vilanova, A., Groenendaal, F., 2012. Quantitative fiber tracking in the corpus callosum and internal capsule reveals microstructural abnormalities in preterm infants at term-equivalent age. *AJNR Am J Neuroradiol* 33, 678-684.
- Vasileiadis, G.T., Gelman, N., Han, V.K., Williams, L.A., Mann, R., Bureau, Y., Thompson, R.T., 2004. Uncomplicated intraventricular hemorrhage is followed by reduced cortical volume at near-term age. *Pediatrics* 114, e367-372.

- Vasung, L., Lepage, C., Rados, M., Pletikos, M., Goldman, J.S., Richiardi, J., Raguz, M., Fisch-Gomez, E., Karama, S., Huppi, P.S., Evans, A.C., Kostovic, I., 2016. Quantitative and Qualitative Analysis of Transient Fetal Compartments during Prenatal Human Brain Development. *Front Neuroanat* 10, 11.
- Veraart, J., Novikov, D.S., Christiaens, D., Ades-Aron, B., Sijbers, J., Fieremans, E., 2016. Denoising of diffusion MRI using random matrix theory. *Neuroimage* 142, 394-406.
- Verde, A.R., Budin, F., Berger, J.B., Gupta, A., Farzinfar, M., Kaiser, A., Ahn, M., Johnson, H., Matsui, J., Hazlett, H.C., Sharma, A., Goodlett, C., Shi, Y., Gouttard, S., Vachet, C., Piven, J., Zhu, H., Gerig, G., Styner, M., 2014. UNC-Utah NA-MIC framework for DTI fiber tract analysis. *Front Neuroinform* 7, 51.
- Vinall, J., Grunau, R.E., Brant, R., Chau, V., Poskitt, K.J., Synnes, A.R., Miller, S.P., 2013. Slower postnatal growth is associated with delayed cerebral cortical maturation in preterm newborns. *Sci Transl Med* 5, 168ra168.
- Vohr, B., 2014. Speech and language outcomes of very preterm infants. *Semin Fetal Neonatal Med* 19, 78-83.
- Vohr, B., Jodoin-Krauzyk, J., Tucker, R., Johnson, M.J., Topol, D., Ahlgren, M., 2008. Early language outcomes of early-identified infants with permanent hearing loss at 12 to 16 months of age. *Pediatrics* 122, 535-544.
- Vohr, B.R., 2016. Language and hearing outcomes of preterm infants. *Semin Perinatol* 40, 510-519.
- Vohr, B.R., Wright, L.L., Dusick, A.M., Mele, L., Verter, J., Steichen, J.J., Simon, N.P., Wilson, D.C., Broyles, S., Bauer, C.R., Delaney-Black, V., Yolton, K.A., Fleisher, B.E., Papile, L.A., Kaplan, M.D., 2000. Neurodevelopmental and functional outcomes of extremely low birth weight infants in the National Institute of Child Health and Human Development Neonatal Research Network, 1993-1994. *Pediatrics* 105, 1216-1226.
- Vollmer, B., Lundequist, A., Martensson, G., Nagy, Z., Lagercrantz, H., Smedler, A.C., Forssberg, H., 2017. Correlation between white matter microstructure and executive functions suggests early developmental influence on long fibre tracts in preterm born adolescents. *PLoS One* 12, e0178893.
- Volpe, J.J., 2001. Neurobiology of periventricular leukomalacia in the premature infant. *Pediatr Res* 50, 553-562.
- Volpe, J.J., 2003. Cerebral white matter injury of the premature infant-more common than you think. *Pediatrics* 112, 176-180.
- Volpe, J.J., 2009a. Brain injury in premature infants: a complex amalgam of destructive and developmental disturbances. *Lancet Neurol* 8, 110-124.
- Volpe, J.J., 2009b. The encephalopathy of prematurity--brain injury and impaired brain development inextricably intertwined. *Semin Pediatr Neurol* 16, 167-178.
- Volpe, J.J., Kinney, H.C., Jensen, F.E., Rosenberg, P.A., 2011. The developing oligodendrocyte: key cellular target in brain injury in the premature infant. *Int J Dev Neurosci* 29, 423-440.
- Wagenaar, N., Chau, V., Groenendaal, F., Kersbergen, K.J., Poskitt, K.J., Grunau, R.E., Synnes, A., Duerden, E.G., de Vries, L.S., Miller, S.P., Benders, M.J., 2017. Clinical Risk Factors for Punctate White Matter Lesions on Early Magnetic Resonance Imaging in Preterm Newborns. *J Pediatr* 182, 34-40 e31.
- Wakana, S., Caprihan, A., Panzenboeck, M.M., Fallon, J.H., Perry, M., Gollub, R.L., Hua, K., Zhang, J., Jiang, H., Dubey, P., Blitz, A., van Zijl, P., Mori, S., 2007. Reproducibility of quantitative tractography methods applied to cerebral white matter. *Neuroimage* 36, 630-644.
- Wang, L., Shi, F., Yap, P.T., Gilmore, J.H., Lin, W., Shen, D., 2012. 4D multi-modality tissue segmentation of serial infant images. *PLoS One* 7, e44596.
- Wang, Y., Gupta, A., Liu, Z., Zhang, H., Escobar, M.L., Gilmore, J.H., Gouttard, S., Fillard, P., Maltbie, E., Gerig, G., Styner, M., 2011. DTI registration in atlas based fiber analysis of infantile Krabbe disease. *Neuroimage* 55, 1577-1586.

- Watkin, P., McCann, D., Law, C., Mullee, M., Petrou, S., Stevenson, J., Worsfold, S., Yuen, H.M., Kennedy, C., 2007. Language ability in children with permanent hearing impairment: the influence of early management and family participation. *Pediatrics* 120, e694-701.
- Webb, S., Munro, C.A., Midha, R., Stanis, G.J., 2003. Is multicomponent T2 a good measure of myelin content in peripheral nerve? *Magn Reson Med* 49, 638-645.
- Westerhausen, R., Huster, R.J., Kreuder, F., Wittling, W., Schweiger, E., 2007. Corticospinal tract asymmetries at the level of the internal capsule: is there an association with handedness? *Neuroimage* 37, 379-386.
- Wheeler-Kingshott, C.A., Cercignani, M., 2009. About "axial" and "radial" diffusivities. *Magn Reson Med* 61, 1255-1260.
- Whitehouse, A.J., Bishop, D.V., 2009. Hemispheric division of function is the result of independent probabilistic biases. *Neuropsychologia* 47, 1938-1943.
- Williams, J., Lee, K.J., Anderson, P.J., 2010. Prevalence of motor-skill impairment in preterm children who do not develop cerebral palsy: a systematic review. *Dev Med Child Neurol* 52, 232-237.
- Wimberger, D.M., Roberts, T.P., Barkovich, A.J., Prayer, L.M., Moseley, M.E., Kucharczyk, J., 1995. Identification of "premyelination" by diffusion-weighted MRI. *J Comput Assist Tomogr* 19, 28-33.
- Wisnowski, J.L., Ceschin, R.C., Choi, S.Y., Schmithorst, V.J., Painter, M.J., Nelson, M.D., Bluml, S., Panigrahy, A., 2015. Reduced thalamic volume in preterm infants is associated with abnormal white matter metabolism independent of injury. *Neuroradiology* 57, 515-525.
- Wojkowska-Mach, J., Rozanska, A., Borszewska-Kornacka, M., Domanska, J., Gadzinowski, J., Gulczynska, E., Helwich, E., Kordek, A., Pawlik, D., Szczapa, J., Heczko, P.B., 2014. Necrotising enterocolitis in preterm infants: epidemiology and antibiotic consumption in the Polish neonatology network neonatal intensive care units in 2009. *PLoS One* 9, e92865.
- Wolke, D., Meyer, R., 1999. Cognitive status, language attainment, and prereading skills of 6-year-old very preterm children and their peers: the Bavarian Longitudinal Study. *Dev Med Child Neurol* 41, 94-109.
- Wolke, D., Samara, M., Bracewell, M., Marlow, N., Group, E.P.S., 2008. Specific language difficulties and school achievement in children born at 25 weeks of gestation or less. *J Pediatr* 152, 256-262.
- Wood, N.S., Costeloe, K., Gibson, A.T., Hennessy, E.M., Marlow, N., Wilkinson, A.R., Group, E.P.S., 2005. The EPICure study: associations and antecedents of neurological and developmental disability at 30 months of age following extremely preterm birth. *Arch Dis Child Fetal Neonatal Ed* 90, F134-140.
- Woods, P.L., Rieger, I., Wocadlo, C., Gordon, A., 2014. Predicting the outcome of specific language impairment at five years of age through early developmental assessment in preterm infants. *Early Hum Dev* 90, 613-619.
- Woodward, L.J., Anderson, P.J., Austin, N.C., Howard, K., Inder, T.E., 2006. Neonatal MRI to predict neurodevelopmental outcomes in preterm infants. *N Engl J Med* 355, 685-694.
- Woodward, L.J., Edgin, J.O., Thompson, D., Inder, T.E., 2005. Object working memory deficits predicted by early brain injury and development in the preterm infant. *Brain* 128, 2578-2587.
- Wu, Y.W., 2002. Systematic review of chorioamnionitis and cerebral palsy. *Ment Retard Dev Disabil Res Rev* 8, 25-29.
- Wu, Y.W., Colford, J.M., Jr., 2000. Chorioamnionitis as a risk factor for cerebral palsy: A meta-analysis. *JAMA* 284, 1417-1424.
- Wu, Y.W., Escobar, G.J., Grether, J.K., Croen, L.A., Greene, J.D., Newman, T.B., 2003. Chorioamnionitis and cerebral palsy in term and near-term infants. *JAMA* 290, 2677-2684.
- Xu, D., Bonifacio, S.L., Charlton, N.N., C, P.V., Lu, Y., Ferriero, D.M., Vigneron, D.B., Barkovich, A.J., 2011. MR spectroscopy of normative premature newborns. *J Magn Reson Imaging* 33, 306-311.
- Xu, D., Mori, S., Shen, D., van Zijl, P.C., Davatzikos, C., 2003. Spatial normalization of diffusion tensor fields. *Magn Reson Med* 50, 175-182.

- Xydis, V., Drougia, A., Giapros, V., Argyropoulou, M., Andronikou, S., 2013. Brain growth in preterm infants is affected by the degree of growth restriction at birth. *J Matern Fetal Neonatal Med* 26, 673-679.
- Yakovlev, P., Lecours, A., 1967. The myelinogenetic cycles of regional maturation of the brain. *Retional Development of the Brain Early in Life*. Blackwell Scientific Publications, 67.
- Yeatman, J.D., Dougherty, R.F., Myall, N.J., Wandell, B.A., Feldman, H.M., 2012. Tract profiles of white matter properties: automating fiber-tract quantification. *PLoS One* 7, e49790.
- Yeo, B.T., Vercauteren, T., Fillard, P., Peyrat, J.M., Pennec, X., Golland, P., Ayache, N., Clatz, O., 2009. DT-REFinD: diffusion tensor registration with exact finite-strain differential. *IEEE Trans Med Imaging* 28, 1914-1928.
- Young, J.M., Morgan, B.R., Whyte, H.E., Lee, W., Smith, M.L., Raybaud, C., Shroff, M.M., Sled, J.G., Taylor, M.J., 2016. Longitudinal Study of White Matter Development and Outcomes in Children Born Very Preterm. *Cereb Cortex*.
- Yushkevich, P.A., Zhang, H., Simon, T.J., Gee, J.C., 2008. Structure-specific statistical mapping of white matter tracts. *Neuroimage* 41, 448-461.
- Yushkevich, P.A., Zhang, H.G., 2013. Deformable modeling using a 3D boundary representation with quadratic constraints on the branching structure of the Blum skeleton. *Inf Process Med Imaging* 23, 280-291.
- Zacharia, A., Zimine, S., Lovblad, K.O., Warfield, S., Thoeny, H., Ozdoba, C., Bossi, E., Kreis, R., Boesch, C., Schroth, G., Huppi, P.S., 2006. Early assessment of brain maturation by MR imaging segmentation in neonates and premature infants. *AJNR Am J Neuroradiol* 27, 972-977.
- Zalesky, A., 2011. Moderating registration misalignment in voxelwise comparisons of DTI data: a performance evaluation of skeleton projection. *Magn Reson Imaging* 29, 111-125.
- Zhang, H., Avants, B.B., Yushkevich, P.A., Woo, J.H., Wang, S., McCluskey, L.F., Elman, L.B., Melhem, E.R., Gee, J.C., 2007. High-dimensional spatial normalization of diffusion tensor images improves the detection of white matter differences: an example study using amyotrophic lateral sclerosis. *IEEE Trans Med Imaging* 26, 1585-1597.
- Zhang, H., Awate, S.P., Das, S.R., Woo, J.H., Melhem, E.R., Gee, J.C., Yushkevich, P.A., 2010a. A tract-specific framework for white matter morphometry combining macroscopic and microscopic tract features. *Med Image Anal* 14, 666-673.
- Zhang, H., Hubbard, P.L., Parker, G.J., Alexander, D.C., 2011. Axon diameter mapping in the presence of orientation dispersion with diffusion MRI. *Neuroimage* 56, 1301-1315.
- Zhang, H., Schneider, T., Wheeler-Kingshott, C.A., Alexander, D.C., 2012. NODDI: practical in vivo neurite orientation dispersion and density imaging of the human brain. *Neuroimage* 61, 1000-1016.
- Zhang, H., Yushkevich, P.A., Alexander, D.C., Gee, J.C., 2006. Deformable registration of diffusion tensor MR images with explicit orientation optimization. *Med Image Anal* 10, 764-785.
- Zhang, Y., Inder, T.E., Neil, J.J., Dierker, D.L., Alexopoulos, D., Anderson, P.J., Van Essen, D.C., 2015. Cortical structural abnormalities in very preterm children at 7 years of age. *Neuroimage* 109, 469-479.
- Zhang, Y., Zhang, J., Oishi, K., Faria, A.V., Jiang, H., Li, X., Akhter, K., Rosa-Neto, P., Pike, G.B., Evans, A., Toga, A.W., Woods, R., Mazziotta, J.C., Miller, M.I., van Zijl, P.C., Mori, S., 2010b. Atlas-guided tract reconstruction for automated and comprehensive examination of the white matter anatomy. *Neuroimage* 52, 1289-1301.